The Dissertation Committee for Seng Keat Yeoh certifies that this is the approved version of the following dissertation:

On Understanding the Physics and Source Conditions of the Enceladus South Polar Plume via Numerical Simulation

Committee:

David B. Goldstein, Co-Supervisor

Philip L. Varghese, Co-Supervisor

Deborah A. Levin

Laurence M. Trafton

Jack H. Waite, Jr.

On Understanding the Physics and Source Conditions of the Enceladus South Polar Plume via Numerical Simulation

by

Seng Keat Yeoh, B.S.E.M.E.; M.S.E.

Dissertation

Presented to the Faculty of the Graduate School of

The University of Texas at Austin

in Partial Fulfillment

of the Requirements

for the Degree of

Doctor of Philosophy

The University of Texas at Austin

May 2015

To my beloved family and friends

Acknowledgements

First, I would like to thank my co-advisors, Prof. David Goldstein and Prof. Philip Varghese, not only for their guidance and supervision but also for their patience and support throughout the course of my graduate education. Both professors are always available and willing to discuss research. Even after having spent many years in the business and accumulated a breadth of knowledge, they continue to be driven by their curiosity and desire to know more. As an aspiring young engineer and scientist, they have been an inspiration to me.

I would also like to thank Dr. Laurence Trafton for providing valuable insights and suggestions during our weekly group meetings. Being the only astronomer in the group, he is ever ready to explain and clarify various concepts in astronomy to me. I am also grateful to the other members on my committee, Prof. Deborah Levin and Dr. Hunter Waite, for reading my dissertation and offering helpful comments and advice that have improved the work significantly.

Part of this work is a collaboration with a group at the University of Illinois at Urbana-Champaign (formerly at Pennsylvania State University). I would like to thank them, particularly Prof. Levin, Dr. Zheng Li and Rohit Dhariwal, for the fruitful discussions over countless teleconferences and phone calls and also for supplying the input needed for some of the simulations in this work.

I have benefited greatly from productive discussions with Prof. Andrew Ingersoll at Caltech, Prof. Jürgen Schmidt at University of Oulu and Mark Perry at the Applied Physics Laboratory (at Johns Hopkins University). Moreover, I wish to thank Ben Teolis at Southwest Research Institute and Yaxue Dong at the Laboratory for Atmospheric and

Space Physics (at University of Colorado at Boulder) for providing me with some of the Cassini *in-situ* data sets.

I also thank my past and present colleagues at the Computational Fluid Physics Laboratory: Aaron Morris, Andrew Walker, Bénédicte Stewart, Chris Moore, Kelly Stephani, James Strand, William McDoniel, William Hoey, Kyle Higdon, Jeff Chu, Jared Berg, Parvathy Prem, Peter Clarke, Aaron Hawkins, Justin Lamb, Scott Drews, Charles Doolittle and Arjun Sharma. Special thanks go to Aaron Morris, Andrew Walker, Bénédicte Stewart and Chris Moore for showing me the ropes to the in-house DSMC code when I first started. I am also thankful to several undergraduate students with whom I was able to work on this project: Benjamin Hanna, Justin Kizer and Todd Chapman.

I am grateful to all my friends and professors whom I have gotten to know during graduate school, without whom my experience in graduate school would not have been that enriching, enjoyable and fun. I would also like to express my gratitude to my church family for their love and support throughout my stay in Austin.

I also wish to acknowledge the help and support provided by the administrative staff at the Department of Aerospace Engineering and Engineering Mechanics. In particular, I would like to thank Tina Woods for her willingness to help address my questions concerning graduate school rules and protocols, Therese Larson for helping with room reservations, Scott Messec for offering tech support, and Geetha Rajagopal for taking care of my reimbursements and other logistical matters.

This work would not have been possible without funding and computational resources. Funding for this work was provided by the NASA Cassini Data Analysis Program (CDAP) grants NNX08AP77G and NNX10AF10G. Massively parallel computations for this work were performed on the supercomputers at the Texas Advanced Computing Center (TACC).

Lastly, my sincere and heartfelt gratitude to my parents. Without them, I would not have made it this far. They have provided my brother and me with food and shelter and have worked tirelessly to put both of us through school. I love them dearly and cannot thank them enough for their sacrifices.

On Understanding the Physics and Source Conditions of the Enceladus South Polar Plume via Numerical Simulation

Seng Keat Yeoh, Ph.D.

The University of Texas at Austin, 2015

Co-Supervisors: David B. Goldstein and Philip L. Varghese

Enceladus, a tiny moon of Saturn, is found to be geologically active. In 2005, Cassini detected an anomalously warm region and a plume, consisting of mostly water vapor and ice grains, at its south pole. The plume has far-reaching effects on the Saturnian system and offers clues into the moon's interior, particularly as to whether liquid water exists underground. Consequently, understanding the physics and source conditions of the plume is crucial, which is the focus of this work.

The plume is not only two-phase but also multi-regime in nature and can be divided into three distinct regions: a subsurface region, a collisional near-field and a free-molecular far-field. To study it, a hybrid model of the plume, which treats each region separately, is constructed. Two subsurface models are considered. Using the resulting vent conditions from these models, the plume is propagated from the surface vents out to several Enceladus radii using the direct simulation Monte Carlo (DSMC) method in the near-field and a free-molecular model in the far-field.

The model is used to examine the plume flow, with and without grains. Collisions are found to be important in various processes, including grain condensation and flow acceleration. Since collision rates drop away from the vent, they must be high enough at the vent to enable significant condensation to occur and the gas to accelerate to the

maximum speed possible by allowing energy stored in internal modes to be converted into translational energy as the gas expands. When slower grains are present, however, they may decelerate and push the gas out more laterally. Moreover, grains may form a thick column and restrict the free expansion of the gas. Smaller grains have greater and more extensive effects on the gas, but are also more strongly affected by the gas. Their motions decouple from the gas motions higher above the vent. They are also more likely to spread with the gas and be accelerated to the gas speeds.

By constraining the plume far-field using Cassini data, the H_2O and grain production rates from the plume are estimated to be ~100–1000 kg/s and < 10 kg/s respectively, which agree with other estimates. Based on fit results, the gas jets appear to be narrow, suggesting high Mach numbers at the vents.

Table of Contents

List of Important Symbols

α	vent grain-to-gas velocity ratio (see definition in Chapter 5)
β_0	initial grain salt mass fraction (at the vent)
β_f	final grain salt mass fraction
γ	ratio of specific heats
Γ_{grain}	grain volume fraction (see definition in Appendix A)
δ_{gas}	spreading angle of gas jet (see definition in Section 5.4)
δ_{grain}	spreading angle of grain jet (see definition in Section 5.4)
Δr_{grain}	maximum growth in grain radius due to condensation *above* vents
Δt, Δx	timestep and grid sizes respectively
ξ_b	fraction of gas molecules traveling *opposite* of direction of mean gas motion for a gas in equilibrium
ζ	collision rate per unit volume
ζ_{vent}	collision rate per unit volume at the vent
λ	local gas mean free path
λ_{vent}	gas mean free path at the vent
μ	gas dynamic viscosity
ρ	gas density ($\triangleq n \times m$)
ρ_{ice}	ice density (~920 kg/m^3)
ρ_{grain}	grain density ($= \rho_{ice}$)
σ_i	error bar associated with each data point of *in-situ* measurements
τ_{coll}	local mean collision time
τ_F	characteristic flow timescale (see definition in Section 5.3)
τ_V	grain momentum response or acceleration timescale (see definition in Section 5.3)
φ	vent grain-to-gas mass flow rate ratio (see definition in Chapter 5)
χ_i	mass fraction of species i in a mixture
ψ	local mass concentration of grains relative to gas (see definition in Section 6.2)

c'	molecular thermal or peculiar speed
C_D	drag coefficient
$c_{p,grain}$	grain specific heat capacity (~2.11 kJ/kg-K[1])
$d_{Enc\text{-}S}$	mean orbital radius of Enceladus around Saturn (~238,020 km)
D_{vent}, A_{vent}	vent diameter and area respectively
D_{throat}	throat diameter (of a subsurface channel)
e_{rot}	molecular rotational energy
f_{num}	number of real particles per computational particle
g_{Enc}	Enceladus surface gravity (~0.113 m/s^2)
G	gravitational constant (~6.6738×10^{-11} m^3 kg^{-1} s^{-2})
h	height of simulation domain
$h_{decoupl}$	grain decoupling height
k_b	Boltzmann constant (~1.3806×10^{-23} J/K)
Kn	local Knudsen number (see definition in Section 3.3.1)
Kn_{grain}	grain Knudsen number (see definition in Section 3.3.3)
Kn_{vent}	vent Knudsen number (see definition in Section 4.1)
L	gradient-based length scale (see definition in Section 3.3.1)
m	mass of H_2O molecule (~2.99×10^{-26} kg)
m_{grain}	grain mass
$\dot{m}_{vent}$	gas mass flow rate at the vent
$\dot{M}_{esc}$	total rate of escaping grain mass from Enceladus
$\dot{M}_{grain}$	total grain mass production rate from Enceladus
Ma	local Mach number
Ma_n	Mach number normal to a surface
Ma_{vent}	Mach number at the vent
n	gas number density
n_{bg}	background density (see Section 7.1.3)

n_{grain}, T_{grain}	grain number density and temperature respectively
n_{vent}	gas number density at the vent
N_{dof}	number of rotational degrees of freedom
p	local gas pressure
p_{vap}	H_2O equilibrium vapor pressure over ice
r_0	initial grain radius
r_f	final grain radius
r_{flyby}	altitude of spacecraft from surface of Enceladus
r_{grain}	grain radius
r_{init}	initial radial position of gas molecule in the vent
r_{max}	maximum grain radius that can be launched to escape speeds (see definition in Section 5.5)
R	horizontal distance from vent centerline
Re_{rel}	relative Reynolds number (see definition in Section 5.3)
R_{Enc}	Enceladus radius (~252.1 km)
R_H	Enceladus Hill sphere radius (~948 km)
R_{H2O}	gas constant for H_2O (~462 J/kg-K)
R_S	Saturn radius (~60,330 km)
R_{vent}	vent radius ($D_{vent}/2$)
s_{Jet}	strength of individual jet (see Section 7.1.1)
$s_{Jet,tot}$	total (sum) strength of *all* jets
s_{glb}	strength of global source (see Section 7.1.2)
St_V	Stokes number (see definition in Section 5.3)
T_0, p_0, ρ_0	stagnation conditions at the source (temperature, pressure and density)
T_{tr}, T_{rot}	gas translational and rotational temperatures respectively (see definitions in Section 4.2)
T_{vent}	gas temperature at the vent
T_{wall}	temperature of channel wall from computational subsurface model

U, V	horizontal and vertical velocity components respectively (for gas and grains)
V_{esc}	two-body escape speed from Enceladus (~240 m/s) (see definition in Section 4.2)
$\boldsymbol{V_{grad}}$	gas velocity component along density gradient (see definition in Section 5.3)
V_{init}	grain initial velocity at the vent
$\boldsymbol{V_{mol}}$	molecular velocity
V_{max}	maximum grain speed (see definition in Section 5.5)
V_n, V_t, V_{az}	normal, tangential and azimuthal components of molecular velocity respectively (see definition in Section 4.6)
V_{ult}	ultimate speed of adiabatic expansion (see definition in Section 4.2)
w	width of simulation domain
Z	altitude from surface
Z^*	normalized altitude (Z/D_{vent})
Z_{FM}	altitude at which flow becomes free-molecular

[1]This value is for ice at 273 K, which is higher than 1.4 kJ/kg-K for ice at 50 K (Fukusako, 1990). As a result, the grains can store 33% more energy than they are supposed to, but the effects should be minimal.

List of Tables

List of Figures

Chapter 1.

Introduction

1.1. MOTIVATION

Surprisingly, Enceladus, a tiny moon of Saturn with a diameter of ~504 km, has been found to be geologically active (Porco *et al.*, 2006; Spencer *et al.*, 2006). The Cassini spacecraft observed a relatively warm south polar region with an anomalously high emission of heat in 2005 (Spencer *et al.*, 2006). In addition, multiple instruments onboard detected a large plume consisting of mostly water vapor and tiny icy grains over the region (Dougherty *et al.*, 2006; Hansen *et al.*, 2006; Spahn *et al.*, 2006b; Tokar *et al.*, 2006; Waite *et al.*, 2006). This plume is responsible for several phenomena in the Saturnian system.

Saturn's large but tenuous E ring, which is composed of icy grains with a narrow size distribution (Horanyi *et al.*, 1992; Nicholson *et al.*, 1996; Pang *et al.*, 1984; Showalter *et al.*, 1991), is mainly being fed by the plume. The unusual vertical structure of the E ring (Hillier *et al.*, 2007; Showalter *et al.*, 1991), which increases in thickness with distance from Saturn but has a local minimum at the orbit of Enceladus, results from the ejection dynamics of the grains from the localized south polar source on Enceladus (Kempf *et al.*, 2008). Moreover, the large torus of neutral water molecules and their dissociation products (O, OH and H) that populates the inner magnetosphere of Saturn (Cassidy and Johnson, 2010; Esposito *et al.*, 2005; Johnson *et al.*, 1989, 2006) is produced by the plume, albeit indirectly. The plume is directly responsible for a much narrower torus consisting primarily of water molecules (Johnson *et al.*, 2006), which interacts with the Saturnian magnetospheric plasma to produce the larger torus. The Enceladus plume is also a major source of water group ions (Tokar *et al.*, 2006) and a sink of low-energy electrons (Jones *et al.*, 2006) for the Saturnian magnetospheric plasma.

The effects of the plume extend beyond changing the populations of grains, neutrals and charged particles in the Saturnian environment. The plume also alters the appearance of several Saturnian moons. The five moons located in the densest portion of the E ring—Mimas, Tethys, Dione, Rhea and Enceladus itself—are among the brightest objects in the solar system (Verbiscer *et al.*, 2007). Grains from the E ring, which is mainly supplied by the plume, impact the surfaces of these moons and produce ejecta that return to coat the surfaces with fresh bright material. Additionally, for Enceladus, most of the icy grains in the plume do not escape but fall back immediately to form the very bright plains in its south polar region (Porco *et al.*, 2006). The plume also provides a valuable window into the interior of Enceladus, especially as to whether or not liquid water exists below the surface (Pang *et al.*, 1984; Porco *et al.*, 2006; Showalter *et al.*, 1991). Liquid water, if present, together with the anomalous heat source at its south pole, would make Enceladus favorable for life (McKay *et al.*, 2008; Parkinson *et al.*, 2008).

Consequently, the plume, the Saturnian system and the interior of Enceladus are all inextricably linked. To understand the Saturnian system and to determine if liquid water exists on Enceladus, it is crucial that the plume is modeled accurately and its physics is understood properly. Many models of the gas component exist, ranging from analytical models (Dong *et al.*, 2011; Saur *et al.*, 2008; Tenishev *et al.*, 2010) to computational models (Burger *et al.*, 2007; Smith *et al.*, 2010; Tian *et al.*, 2007; Waite *et al.*, 2006). The grain component has also been the subject of substantial modeling effort (Degruyter and Manga, 2011; Ingersoll and Ewald, 2011; Kempf *et al.*, 2010; Postberg *et al.*, 2011; Schmidt *et al.*, 2008; Spahn *et al.*, 2006b). However, none of these models has properly treated the two-phase expansion of the plume flow from the sources on the surface into vacuum, which is important.

1.2. OBJECTIVES

The main objective of this work is to construct a plume model that properly treats the two-phase expansion process of the plume flow from the sources into vacuum. In such an expansion process, the flow passes through multiple regimes, from nearly continuum close to the sources, where the density is high and the flow is collisional, to free-molecular at higher altitudes, where the density has dropped so much that collisions have effectively ceased. Non-equilibrium effects also become important, e.g. the freezing of the molecular internal energy modes. Furthermore, the presence of grains complicates matters as interaction between gas and grains may be significant depending on their relative amounts. The direct simulation Monte Carlo (DSMC) method (Bird, 1994) is suitable for modeling such complex flows and is used to simulate the expansion process of the plume flow in this work. The DSMC method uses computational particles to represent the motions, collisions and internal states of real particles in a flow. To model the gas-grain interaction, a two-way coupling method, i.e. gas and grains exchange momentum and energy, is implemented (Burt and Boyd, 2004; Gallis *et al.*, 2001). The specific DSMC solver used in this work is an in-house code that has been applied to a broad range of flow scenarios, including planetary plumes and atmospheres, cometary impacts, and lunar dust dispersals by lander rocket plumes.

Using the DSMC model, we study the important physics associated with the expansion of the plume flow from the sources into vacuum, which occurs in the near-field directly above the surface. First, we investigate the physics of the expansion process in the absence of grains (only gas). Then, we examine the physics of the expansion process in the presence of grains, with emphasis on the interaction between gas and grains. A parametric study is conducted to analyze several phenomena pertaining to the gas-grain interaction during the expansion process.

As the flow becomes free-molecular, a planetary-scale free-molecular model takes the DSMC output and continues to propagate the plume into the far-field where several Cassini data sets are available to provide constraints on the modeling. Particles execute ballistic trajectories in this regime. For this model, the simulation domains extend beyond the Hill sphere of Enceladus and the timescales of interest are comparable to the rotational and orbital periods of Enceladus (~33 hours for both). As a result, the gravitational fields of both Saturn and Enceladus as well as the Coriolis and centrifugal forces due to the rotation of Enceladus and its orbit around Saturn become important and are included in this model.

By constraining our results using the Cassini *in-situ* data in the far-field, we attempt to deduce certain properties of the plume, such as the H_2O and grain production rates and the source conditions. Various estimates from observations and modeling range from ~100 kg/s to ~1000 kg/s for the H_2O production rate and from a few kg/s to hundreds of kg/s for the grain production rate, thus the production rates are not yet well constrained. The most likely hypothesis for the plume generation mechanism is that a subsurface reservoir of liquid water exists and is connected to the surface via narrow channels through which water vapor and ice grains escape to form the plume. In this work, we explore this hypothesis by considering two subsurface models. These models are used to generate boundary conditions for our hybrid DSMC/free-molecular model, which we then use to propagate the resulting flow into the far-field. To assess the validity of the subsurface models, we constrain the resulting plume far-field using the Cassini *in-situ* data.

1.3. OVERVIEW OF DISSERTATION

Chapter 2 provides a literature review of the Saturnian system, Enceladus and its south polar activity, particularly the thermal anomaly and the plume, as they relate to this

work. Here, the implications of the plume on the Saturnian system, which are mentioned briefly above, are discussed in greater detail. In addition, the different hypotheses for the plume generation mechanisms and the plume modeling efforts by others are summarized.

Chapter 3 describes how the hybrid DSMC/free-molecular model of the plume is constructed and how the simulation results are converted into a format that can directly be constrained using the Cassini *in-situ* data in the far-field. Here, the methods employed and their implementations as well as the physical processes included are presented. Moreover, the two different subsurface models considered are discussed. The Cassini *in-situ* data used as constraints are also shown.

Chapter 4 discusses the important physical processes associated with the expansion process of the plume flow from the vent into vacuum in the *absence* of grains (only gas). Results from DSMC simulations are presented here. The topics discussed include the transition in flow regime, non-equilibrium effects, condensation grain growth, and the effects of near-field collisions on the far-field, particularly on the molecular velocities as the flow becomes free-molecular.

Chapter 5 discusses the important physical processes associated with the expansion process of the plume flow in the *presence* of grains. Results from DSMC simulations based on a parametric study involving grain size, grain-to-gas mass flow rate ratio at the vent (a measure of grain mass loading), and velocity difference between the gas and the grains at the vent are presented here. The topics discussed include the effects of grains on the gas both in the near-field and the far-field, the decoupling of grain motion from gas motion, and the spreading and acceleration of the grains by the gas.

Chapter 6 discusses the simulation results from the more complex computational subsurface model. The subsurface flow simulations and results were generated by our collaborators (Li, Z., Dhariwal, R., and Levin, D.). First, the flowfield in the subsurface

channel is examined. Next, the resulting collisional near-field from the surface vent out to higher altitudes where the flow becomes free-molecular is investigated.

Chapter 7 presents the results from constraining the far-field of the plume model to the Cassini *in-situ* data. In particular, the results from the fits to the E2, E3, E5 and E7 INMS H_2O density distributions and E2 CDA grain density distribution are discussed. A sensitivity analysis to the different vent conditions used is also presented. Moreover, estimates of H_2O and grain production rates from the plume based on the fits are given.

Chapter 8 summarizes the important conclusions from this work as well as dicusses several considerations in taking this work forward.

Chapter 2.

Literature Review

This chapter provides an overview on the Saturnian system, Enceladus and its plume as they relate to this work. A short introduction to Enceladus and the discovery of the plume and its implications are presented. Next, the characteristics of the plume (e.g. composition and structure) and the thermal anomaly observed at Enceladus' south pole are discussed. Then, a review of the various hypotheses on the plume source is provided. Finally, prior modeling work done on the plume and the gas and grain environments near Enceladus are summarized.

2.1. Enceladus and the South Polar Region

Enceladus is a tiny moon of Saturn, with a mean radius, $R_{Enc} \approx 252.1$ km. It is tidally locked to Saturn, with an orbital period of ~1.37 days (~33 hours) and an orbital eccentricity of ~0.0047 which is excited by a 2:1 mean motion resonance with Dione (Hurford *et al.*, 2007). Its mean orbital distance from Saturn is ~238,020 km or ~3.95 Saturn radii ($R_S \approx 60{,}330$ km), which puts it between Mimas and Tethys and within Saturn's vast but tenuous E ring. With a mean visual geometric albedo of ~1.4 (Verbiscer *et al.*, 2007), Enceladus is one of the brightest objects in the solar system. The surface of Enceladus is diverse and can be divided into several distinct geological provinces (Porco *et al.*, 2006; Smith *et al.*, 1981), as shown in Figure 2.1a. The oldest provinces are heavily cratered while the younger provinces are relatively crater-free and contain ridges, fractures and troughs scattered across their surfaces. The surface distribution of grains also varies across the provinces, with the smallest grains in the oldest provinces and the largest grains in the younger provinces (Jaumann *et al.*, 2008). The surface of Enceladus is dominated by

pure water ice except near the south pole where traces of light organics and CO_2 are present (Brown *et al.*, 2006).

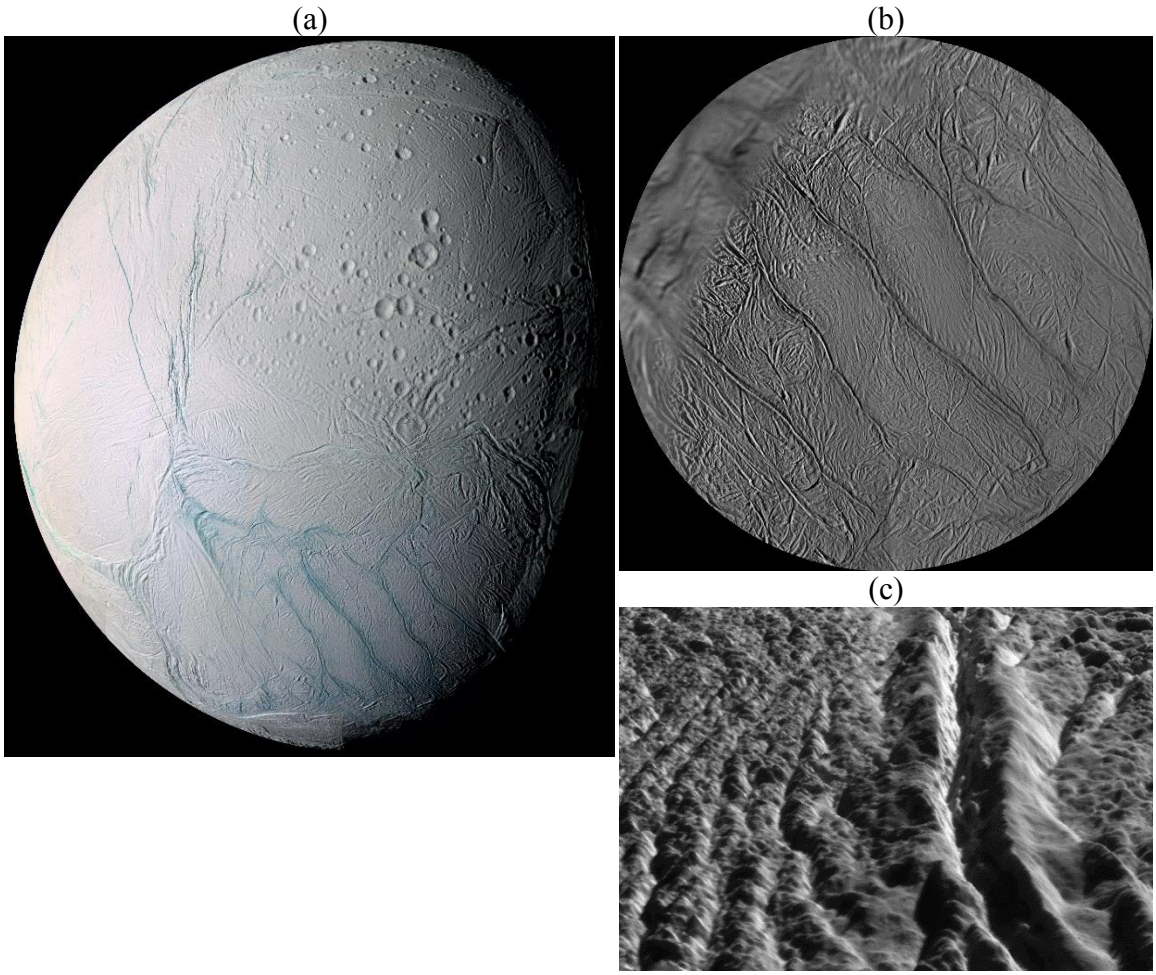

Figure 2.1. (a) False-color mosaic of Enceladus, revealing diverse terrains. The four Tiger Stripes can be seen in the south polar region (bottom right). (*Image PIA06254, courtesy of National Aeronautics and Space Administration (NASA)/Jet Propulsion Laboratory (JPL)/Space Science Institute (SSI)*). (b) Polar stereographic projection of south polar region, showing the Tiger Stripes. The south pole is located right at the center and Saturn is located towards the top of the image. (*Image PIA08419, courtesy of NASA/JPL/SSI*). (c) Close-up view of the Damascus Sulcus, with relief exaggerated ~10× for clarity. (*Image PIA12207, courtesy of NASA/JPL/SSI /Universities Space Research Association (USRA)/Lunar and Planetary Institute (LPI)*).

Most intriguing is the south polar region located below latitude 55°S. This region is relatively young, unusually bright and relatively free of craters, indicating recent tectonic and resurfacing activity. Four prominent, nearly parallel, linear features, called the "Tiger Stripes", extend across the region, as shown in Figure 2.1b. From bottom left to top right in Figure 2.1b, the names of the Tiger Stripes (in order) are Alexandria, Cairo, Baghdad and Damascus. As shown in Figure 2.1c, each Tiger Stripe is actually a linear depression on the surface and is on the average ~500 m deep, ~130 km long and ~2 km wide lined with ridges that are ~100 m high on each side (Porco *et al.*, 2006).

2.2. DISCOVERY OF SOUTH POLAR ACTIVITY AND PLUME

In 2005, the Cassini spacecraft discovered a geologically active region at the south pole of Enceladus (Porco *et al.*, 2006; Spencer *et al.*, 2006). During its third and closest flyby that year (E2 flyby), the Composite Infrared Spectrometer (CIRS) picked up an anomalously warm south polar region exhibiting elevated brightness temperatures and emitting several gigawatts of thermal radiation (Spencer *et al.*, 2006), as shown in Figure 2.2a. Other instruments onboard also detected a two-phase plume over the south polar region, as shown in Figure 2.2b. Gas density data collected by the Ion and Neutral Mass Spectrometer (INMS) indicated a plume dominated by water (~90%) (Waite *et al.*, 2006). The INMS water density distribution along the E2 flyby is shown in Figure 2.2c. Stellar occultation observations by the Ultraviolet Imaging Spectrograph (UVIS) suggested the localized nature of the plume as a tenuous atmosphere was detected only during the ingress when the instrument line-of-sight passed over the south polar region but not during the egress (Hansen *et al.*, 2006), as shown in Figure 2.2d. Magnetic field perturbations detected by the Cassini Magnetometer (MAG) (Dougherty *et al.*, 2006) and strong deflections in Saturn's corotating magnetospheric plasma flow measured by the Cassini Plasma

Spectrometer (CAPS) near Enceladus (Tokar *et al.*, 2006) further corroborated the existence of the south polar plume. Moreover, the asymmetry in the dust impact rates measured by the Cosmic Dust Analyzer (CDA) with respect to closest approach (CA), as shown in Figure 2.2c, pointed to a localized south polar source of grains found in the plume and Saturn's E ring (Spahn *et al.*, 2006b).

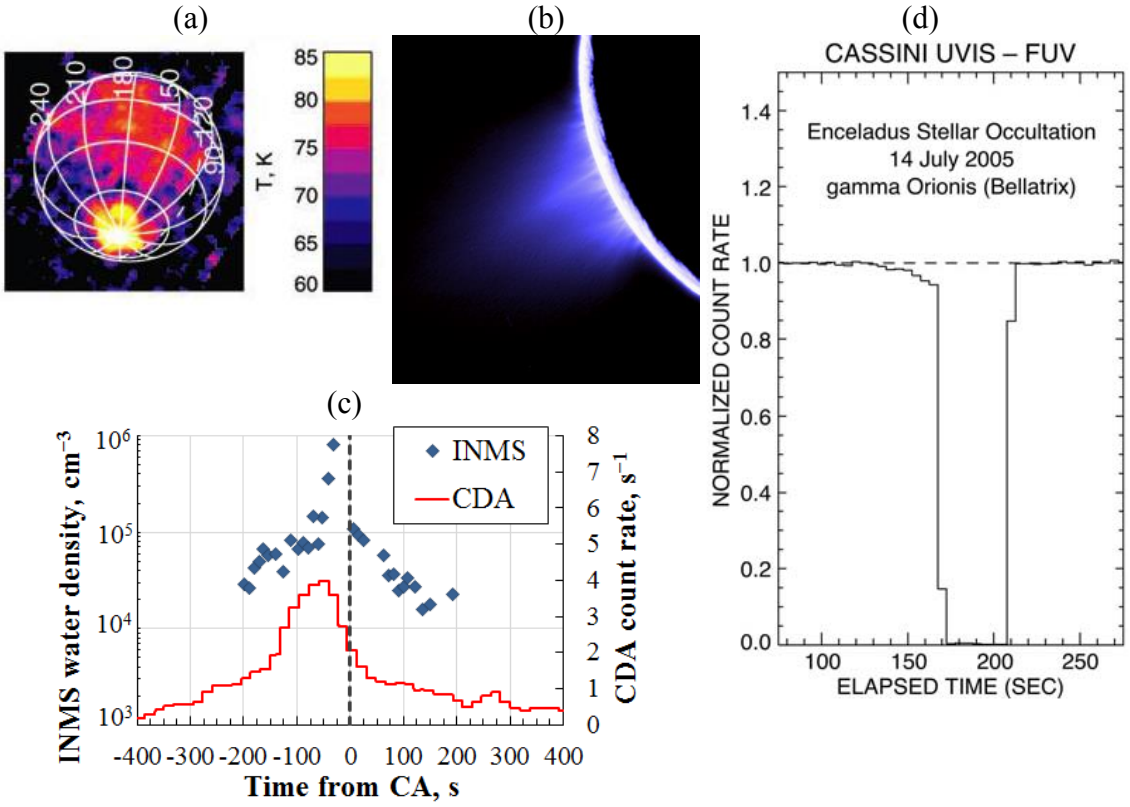

Figure 2.2. (a) CIRS brightness temperature image of Enceladus in the mid-infrared spectrum, showing a warm south polar region. (*From Spencer et al. (2006), courtesy of John Spencer*). (b) False-color image of south polar plume, enhanced to reveal individual jets in the plume. (*Image PIA08386, courtesy of NASA/JPL/SSI*). (c) INMS water density and CDA count rate ($r_{grain} \geq 1.6$ μm) versus time from CA along the E2 trajectory. (*Adapted from Waite et al. (2006) and Spahn et al. (2006b)*). (d) UVIS starlight signal of γ-Orionis versus time. Signal is zero when the star is behind Enceladus. Gradual drop of signal during ingress is due to the attenuation of starlight by the plume at the south pole. (*From Hansen et al. (2006), courtesy of Candice Hansen*).

2.3. IMPLICATIONS OF THE ENCELADUS PLUME

The Enceladus plume plays a major role in shaping the Saturnian system and is responsible for some of the phenomena observed, both directly as well as indirectly. While many questions were answered with the discovery of the plume, new ones were also raised.

2.3.1. E Ring

Enceladus has long been speculated to be the main source of Saturn's E-ring grains (Baum *et al.*, 1981) before the discovery of the plume finally confirmed it. The E ring is vast and tenuous, extending from ~3R_S to at least 8R_S, and spans the orbits of several Saturnian icy moons, including Mimas, Enceladus, Tethys, Dione and Rhea, as shown schematically in Figure 2.3a. It has an unusual vertical profile, with a thickness that increases from ~6000 km at ~3R_S to ~15,000 km at ~8R_S, with a local minimum of ~4000 km at the orbit of Enceladus at ~4R_S (Hillier *et al.*, 2007; Showalter *et al.*, 1991). Moreover, the densest region in the E ring does not occur at the orbit of Enceladus but is located slightly outwards (by at least 0.05R_S) (Kempf *et al.*, 2008). The vertical extent of the E ring at the orbit of Enceladus is related to the ejection dynamics of grains from Enceladus (Kempf *et al.*, 2008). Enceladus can be seen embedded within the E ring as well as feeding material into it in Figures 2.3b and 2.3c.

The E-ring grains have a narrow size distribution, with grain radii, r_{grain}, ranging from 0.3 μm to 3 μm (Horanyi *et al.*, 1992; Nicholson *et al.*, 1996; Pang *et al.*, 1984; Showalter *et al.*, 1991). While the E-ring grains are mainly composed of water ice, they can be categorized into three distinct populations: (i) pure water ice grains, (ii) ice grains containing significant amounts of organic compounds and/or silicate minerals, and (iii) ice grains rich in sodium (~0.5–2% by mass) (Hillier *et al.*, 2007; Postberg *et al.*, 2008, 2009). The composition of the E-ring grains may provide a clue to their production mechanism on Enceladus, which may in turn reveal the subsurface conditions on Enceladus.

(a)

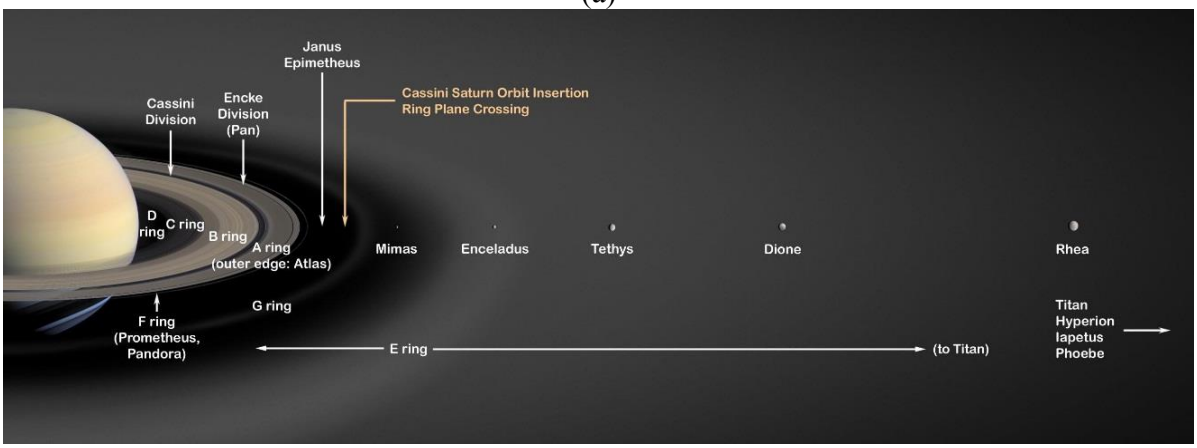

(b) (c)

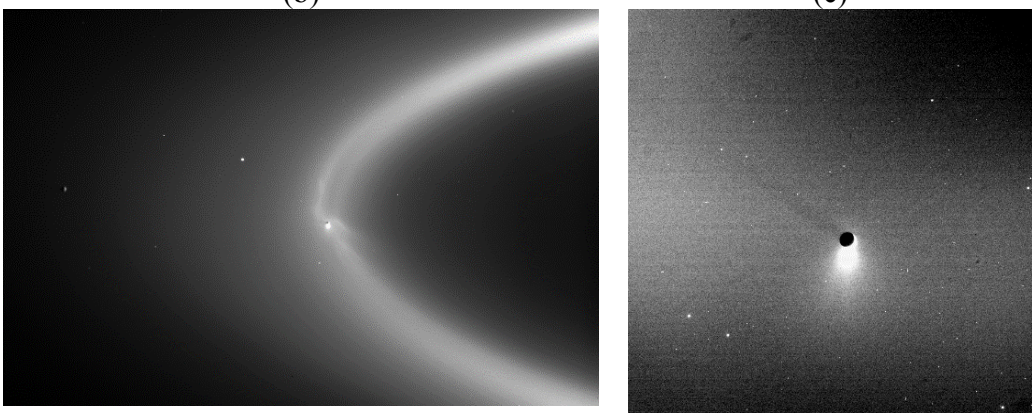

Figure 2.3. (a) Schematic of the Saturnian system, showing the location of the E ring. (*Image PIA03550, courtesy of NASA/JPL*). (b) A portion of the E ring, showing wispy "fingers" of bright, icy material extending from Enceladus (small black dot near the center). This image was taken in the visible spectrum by ISS at high phase angles. Also seen here is a region devoid of material left by Enceladus as it orbits Saturn. (*Image PIA08321, courtesy of NASA/JPL/SSI*). (c) Enceladus (black dot) embedded within the E ring. The plume shines brightly below Enceladus in the image. (*Image PIA08921, courtesy of NASA/JPL/SSI*).

2.3.2. Surface Morphology of Enceladus and Other Saturnian Moons

Based on Hubble Space Telescope (HST) observations at true opposition, the mean visual geometric albedos of Mimas, Enceladus, Tethys, Dione and Rhea, which are icy

moons embedded in the densest portions of the E ring, were estimated to be close to one or greater (Verbiscer *et al.*, 2007). In comparison, the mean visual geometric albedos of most icy moons in the outer solar system range from 0.2 to 0.4. The high albedos of these embedded moons may have resulted from hypervelocity impacts of E-ring grains, most of which originate from the plume, with the surfaces of these moons. Ejecta from such impacts would return to coat the surfaces of these moons with icy materials that increase the reflectance at low phase angles (Shkuratov and Helfenstein, 2001).

Additionally, a large fraction of the plume ice grains are ejected at well below speeds required to escape Enceladus (Hedman *et al.*, 2009; Ingersoll and Ewald, 2011; Postberg *et al.*, 2011; Schmidt *et al.*, 2008), thus they would fall back within the vicinity of the eruption sources and coat it with fresh bright materials. As a result, the plains between the Tiger Stripes are among the brightest regions on Enceladus (Porco *et al.*, 2006). Moreover, the largest grains can be found in the south polar region where continual resurfacing by the plume material is occurring and there is not enough time for surface weathering processes, e.g. micrometeorite bombardment, to break down the grains (Jaumann *et al.*, 2008).

2.3.3. Saturnian Magnetospheric Plasma

The Enceladus plume is a major source of water group ions observed in the Saturnian magnetospheric plasma (Tokar *et al.*, 2006). The magnetospheric plasma corotates with Saturn and travels at ~39 km/s near Enceladus, which is significantly faster than the orbital speed of Enceladus at ~12.6 km/s. The primary interaction between the plume and the plasma is via charge exchange in which a fast ion in the plasma picks up an electron from a slow neutral in the plume, resulting in a fast neutral and a slow ion (Tokar *et al.*, 2006). Then, this slow ion is caught up and accelerated by the rotating magnetic

fields. In this process, though the amounts of ions and neutrals remain about the same, momentum is effectively being transferred from the plasma to the neutrals. This is consistent with the deceleration and deflection in the plasma flow detected by CAPS (Tokar *et al.*, 2006) and the corresponding perturbations in the magnetic field frozen with the plasma flow measured by MAG (Dougherty *et al.*, 2006) near Enceladus. Other less dominant interaction processes between the plasma and the plume include electron impact ionization and ultraviolet photoionization (Tokar *et al.*, 2006).

The Enceladus plume also acts as a sink for electrons in the inner magnetosphere of Saturn, especially the low-energy electrons. High-energy electrons can penetrate the plume, i.e. the plume appears "transparent" to them, whereas low-energy electrons are absorbed by the gas molecules and ice grains in the plume. Such depletions in electron fluxes were detected near Enceladus by the Magnetospheric Imaging Instrument (MIMI) onboard Cassini (Jones *et al.*, 2006).

2.3.4. Large Neutral Torus around Saturn

A large torus of neutral water molecules and their dissociation products (O, OH and H) populate the inner magnetosphere of Saturn (Cassidy and Johnson, 2010; Esposito *et al.*, 2005; Johnson *et al.*, 1989, 2006). The OH component of the torus has been observed by HST to be too dense for plasma sputtering of the surfaces of icy moons and grains in that region to be the only production mechanism for the torus (Shemansky *et al.*, 1993). Consequently, the discovery of the Enceladus plume helped to resolve this conundrum. However, the plume does not directly produce the observed large neutral torus. Rather, the plume is responsible for a much narrower torus consisting primarily of water molecules (Johnson *et al.*, 2006). It is this narrower torus that interacts with the magnetospheric

plasma via charge exchange and reactive collisions to produce the neutrals that constitute the large neutral torus observed in the Saturn inner magnetosphere.

2.3.5. Liquid Water and the Possibility of Life

The discovery of the plume dominated by water (Waite *et al.*, 2006) raised the exciting possibility of finding liquid water on Enceladus (Pang *et al.*, 1984; Porco *et al.*, 2006; Showalter *et al.*, 1991). Liquid water, if found, together with the anomalous heat source detected in the south polar region (Spencer *et al.*, 2006) would provide a favorable environment for life on Enceladus (McKay *et al.*, 2008; Parkinson *et al.*, 2008). Organic compounds, such as methane (CH_4), propane (C_3H_8) and acetylene (C_2H_2), were detected in the plume by INMS (Matson *et al.*, 2007; Waite *et al.*, 2006, 2009).

2.4. CHARACTERISTICS OF THE PLUME

2.4.1. Composition

The Enceladus plume is composed of two phases: gas and tiny ice grains. Based on INMS data, the primary constituent of the gas component by far is H_2O, making up ~90%, while the second most abundant constituent is CO_2, making up ~3–5% (Waite *et al.*, 2006, 2009). The other constituents include ammonia (NH_3), various organic compounds (e.g. methane (CH_4), propane (C_3H_8) and acetylene (C_2H_2)) and possibly radiogenic argon (^{40}Ar) (Waite *et al.*, 2009). The detection of NH_3 and ^{40}Ar has implications on the existence of liquid water on Enceladus. Together with methanol and salts, NH_3 can lower the melting point of water to ~176 K whereas the significant amount of ^{40}Ar detected may indicate ancient water-rock interactions (Waite *et al.*, 2009). However, INMS found but could not identify a constituent with a mass of 28 amu, which could be nitrogen (N_2), carbon monoxide (CO) or ethylene (C_2H_4). With the assistance of UVIS, upper limits on the mixing ratios with H_2O for CO and N_2 were placed at 3% (Hansen *et al.*, 2008) and 0.5%

(Hansen *et al.*, 2011) respectively. Another indicator of liquid water is sodium (Na), though ground-based spectroscopy inferred mixing ratios with H_2O for atomic and molecular sodium that are well below those predicted by salty ocean models (Schneider *et al.*, 2009; Zolotov, 2007). Figure 2.4 shows the gas composition of the plume.

However, it is possible that the sodium is locked in the plume grains. A small fraction (~6%) of grains in the E ring, for which the plume is a major source, contain ~0.5–2% of sodium by mass (Postberg *et al.*, 2009). A more direct CDA measurement closer to the plume indicated that these salt-rich grains constitute a much larger fraction of the plume grains, ~70% or > 99% by mass due to their larger sizes (Postberg *et al.*, 2011). These salt-rich grains are postulated to form via liquid dispersion from a salty ocean underground and are naturally larger (Postberg *et al.*, 2009, 2011) than their salt-poor counterparts that are assumed to condense from the vapor phase (Postberg *et al.*, 2009, 2011; Schmidt *et al.*, 2008). Larger grains have been observed to have slower ejection speeds (Hedman *et al.*, 2009), thus the larger salty grains are less likely to escape Enceladus. This may explain the difference in salt content observed between the plume and E-ring grains.

Since a large fraction of plume grains are ejected at below escape speeds (Hedman *et al.*, 2009; Ingersoll and Ewald, 2011; Postberg *et al.*, 2011; Schmidt *et al.*, 2008), most of them fall back possibly near the eruption sources. As a result, the surface grain size distribution in the south polar region may provide a clue to the largest grains ejected. Grains with radii as large as ~100 μm have been detected by the Visual and Infrared Mapping Spectrometer (VIMS) in the south polar region (Jaumann *et al.*, 2008). In contrast, nanometer-sized grains have also been observed in the plume by CAPS (Jones *et al.*, 2009). With CDA detections of micron-sized grains in the plume (Postberg *et al.*, 2011; Spahn *et al.*, 2006b), the grain sizes in the plume span a wide range, from several nanometers to possibly a few hundred microns.

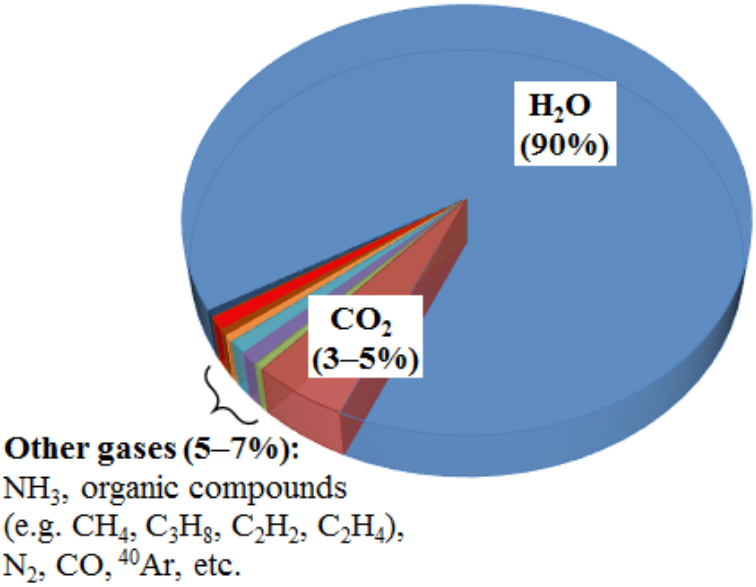

Figure 2.4. Gas composition of the plume.

2.4.2. Structure

Due to the weak gravity of Enceladus (with a surface gravity, $g_{Enc} \approx 0.113$ m/s^2), the plume extends out to several R_{Enc} over the south pole of Enceladus, as shown in Figures 2.2b and 2.5a. Observations indicate that the plume is made up of many discrete, collimated jets as well as a broad, more diffuse, distributed component (Hansen *et al.*, 2008, 2011; Porco *et al.*, 2014; Spitale and Porco, 2007; Postberg *et al.*, 2011). This is evident in the visible images of the plume taken by the Cassini Imaging Science Subsystem (ISS), as shown in Figures 2.2b, 2.5a and 2.5b, in which the grain component of the plume is visible due to the scattering of visible light by tiny ice grains.

As of September 2014, approximately 100 individual jets have been identified and their locations and orientations have been estimated (Porco *et al.*, 2014). Most of these jets lie along or near the Tiger Stripes and are oriented almost vertically, as shown in Figure 2.5c. Jetting activity is found to correlate with the thermal activity observed by CIRS and

VIMS, with several jets coinciding with a few individual hotspots (Porco *et al.*, 2014; Spitale and Porco, 2007). Porco *et al.* (2014) concluded that the hotspots are thermal footprints of individual jets. However, only a small fraction of the plume material (both gas and grains) originates from the jets. The majority of the plume material resides in the broad, more diffuse component, possibly arising from elongated fissures along the Tiger Stripes (Hansen *et al.*, 2011; Postberg *et al.*, 2011).

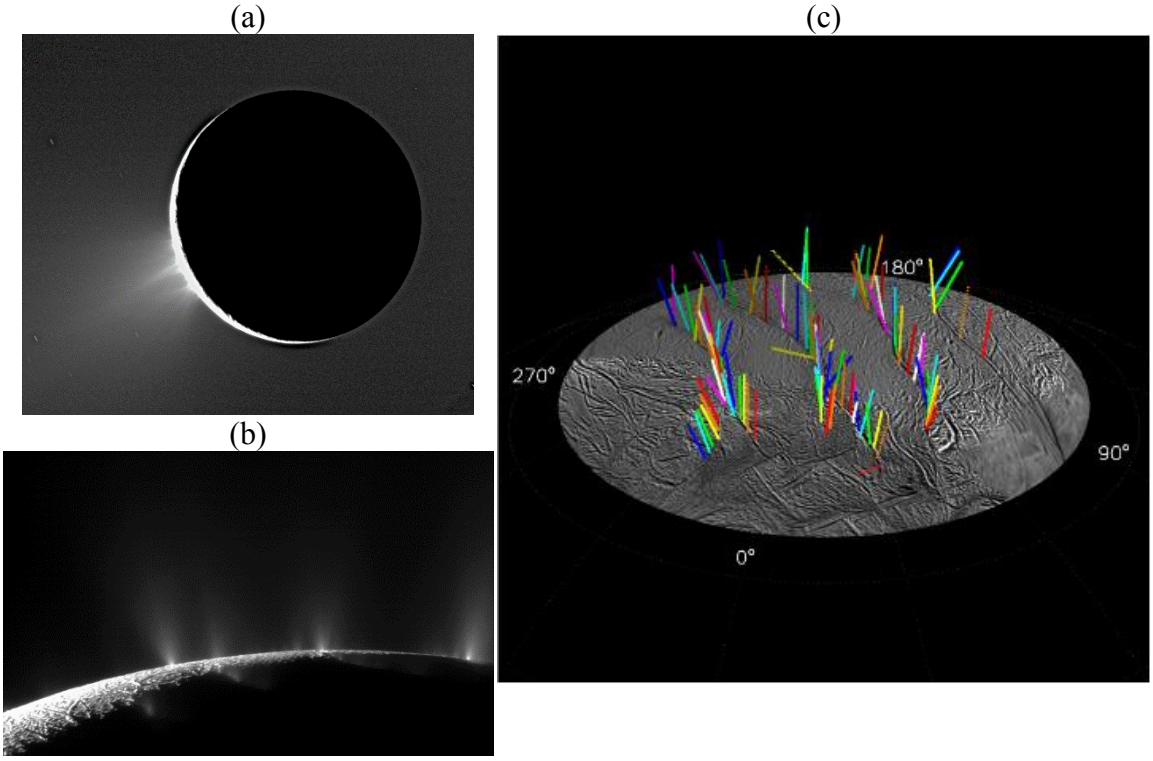

Figure 2.5. (a) Plume towering over the south polar region of Enceladus. Discrete structures can be seen in the plume. (*Image PIA07758, courtesy of NASA/JPL/SSI*). (b) Close-up view of the southern limb of Enceladus, revealing both jets and a more diffuse component emanating from along the Tiger Stripes. From left to right, the Tiger Stripes are Alexandria, Cairo, Baghdad, and Damascus. (*Image PIA11688, courtesy of NASA/JPL/SSI*). (c) Locations and jet orientations of 98 identified jets along or near the Tiger Stripes. From left to right, the Tiger Stripes are Damascus, Baghdad, Cairo and Alexandria. (*From Porco et al. (2014), courtesy of Carolyn Porco*).

In comparison to the gas in the broad diffuse component, the gas in the jets is not only denser but also faster. From UVIS observations, Mach numbers of 5–8 were inferred for the jets, leading to suggested possible gas speeds as high as 1–2 km/s (Hansen *et al.*, 2011). The supersonic nature of the jets is consistent with the jets originating from nozzle-like subsurface channels (Schmidt *et al.*, 2008). Moreover, CDA compositional measurements of the plume grains suggest a correlation between grain salinity and the nature of the grain source: smaller salt-poor grains come mostly from the jets while larger salt-rich grains are ejected mainly from slower distributed sources (Postberg *et al.*, 2011). Since the gas in the jets is denser and faster, the salt-poor grains are more likely to be launched to escape speeds. This is consistent with the salinity stratification of the plume grains observed, where the salt-poor grains are found in greater abundance away from Enceladus (Postberg *et al.*, 2011), as well as the difference in the fractions of salt-poor and salt-rich grains between the E ring and the plume (Postberg *et al.*, 2009, 2011).

2.4.3. Temporal Variability

Observations from multiple instruments onboard Cassini suggest that the plume may be varying with time. The plume contributes indirectly to the torus of water-dissociation products (O, OH and H) in the inner magnetosphere of Saturn (Johnson *et al.*, 2006) and also acts as a sink for electrons in the magnetospheric plasma (Jones *et al.*, 2006). UVIS observed variation in the torus population of O over a 2-month period (Esposito *et al.*, 2005) while MIMI measured changes in electron flux depletion rates occurring over shorter timescales, perhaps days or weeks, near Enceladus (Jones *et al.*, 2006). In addition, certain jets were observed in some ISS images but not in others, implying that they might have turned “on” and “off” between the images which were taken at different times (Porco *et al.*, 2014). Various plume modeling efforts also yielded plume H_2O content and

production rate that vary over timescales ranging from hours to possibly years (Dong *et al.*, 2011; Saur *et al.*, 2008; Smith *et al.*, 2010; Waite *et al.*, 2006). However, three UVIS stellar occultation observations of the plume between 2005 and 2010 inferred a relatively stable plume H_2O production rate of ~170–220 kg/s (Hansen *et al.*, 2006, 2008, 2011). It is possible that the temporal variability of the plume is periodic in nature and that UVIS might simply have observed the plume at around the same point in the cycle.

Such a periodic nature was detected when independent measurements of the plume brightness at the infrared and visible wavelengths by VIMS and ISS showed diurnal variation with the orbital position of Enceladus (Hedman *et al.*, 2013; Nimmo *et al.*, 2014), as shown in Figure 2.6. In both measurements, the plume appears to be brighter when Enceladus is near the farthest point from Saturn (apocenter) than when it is near the closest point (pericenter). Since the plume brightness is proportional to the amount of grains in the plume, venting activity may be more intense and thus more material is ejected when Enceladus is near the apocenter. However, it is unclear if the gas component of the plume also exhibits such a periodic nature.

The observed diurnal periodic nature of the plume variability is consistent with venting activity that is tidally controlled. Due to the slight eccentricity in the orbit of Enceladus around Saturn, the tidal stresses experienced at each surface point on Enceladus vary with orbital position. Consequently, the Tiger Stripes in the south polar region experience a progression of tensile and compressional stresses over the course of an orbit. Hurford *et al.* (2007) found that most of the Tiger Stripes are in tension, i.e. cracks are open, when Enceladus is near apocenter, implying higher activity and greater discharge of material. This agrees with VIMS and ISS observations. However, this simple tidally-modulated model is not sufficient to describe the entire situation (Nimmo *et al.*, 2014). An additional time delay is required to improve the match with observations. This delay may

be inherent in the ejection mechanism itself or caused by the viscoelastic behavior of the deforming ice shell. Alternatively, a better match could also be produced if Enceladus is experiencing physical libration, which changes the tidal stress patterns and thus the timing of the eruptions (Hurford *et al.*, 2009). Other possibilities exist. While the temporal variability of the plume seems to be tidally driven, the details of the process remain unclear.

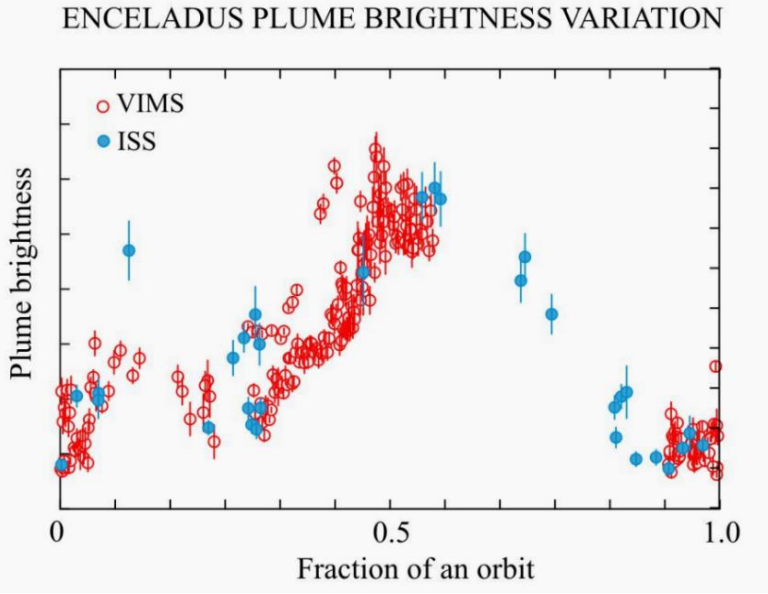

Figure 2.6. Variation in plume brightness with orbital position of Enceladus, based on images taken by VIMS and ISS in the infrared and visible spectrum. (*Image PIA17187, courtesy of NASA/JPL-Caltech/SSI*).

2.4.4. Production Rates of Water Vapor and Grains

Prior to the discovery of the plume, Richardson *et al.* (1998) and Jurac *et al.* (2002) estimated that H_2O source rates of ~42 kg/s and ~112 kg/s respectively are required to maintain the observed neutral densities around Saturn. A more recent estimate by Jurac and Richardson (2005) indicate that a higher H_2O source rate of ~300 kg/s is required. This more recent estimate is in closer agreement with the plume H_2O production rates estimated from observations and various plume models after the discovery of the plume. UVIS stellar

occultation observations inferred H_2O production rates of ~170–220 kg/s from the plume (Hansen *et al.*, 2006, 2008, 2011) while estimates from various modeling efforts range from ~100 kg/s to ~1000 kg/s (Burger *et al.*, 2007; Dong *et al.*, 2011; Saur *et al.*, 2008; Smith *et al.*, 2010; Tenishev *et al.*, 2010; Tian *et al*., 2007; Waite *et al.*, 2006).

Estimates of the grain production rate ranges from a few kg/s to hundreds of kg/s. Schmidt *et al.* (2008) estimated a production rate of ~5kg/s, with only ~10% escaping. This escape rate agrees with the estimated supply rate of ~1 kg/s required to maintain the E-ring (Juhasz and Horanyi, 2002). Ingersoll and Ewald (2011) inferred a much higher production rate of 51 ± 18 kg/s, with ~9% escaping. Spahn *et al.* (2006b) estimated a production rate of ~0.2 kg/s when assuming monodisperse grains of r_{grain} = 2 μm, though it may extend to several kg/s if a size distribution is assumed. Postberg *et al.* (2011) estimated a production rate of ~10 kg/s for r_{grain} > 0.2 μm when assuming a size distribution with a maximum r_{grain} of ~10 μm. Using plume brightness data derived from VIMS images, Hedman *et al.* (2009) estimated that the production rate for r_{grain} > 0.5 μm with ejection velocities between 80 and 160 m/s is between 2 and 200 kg/s.

2.4.5. Ice/Vapor Ratio

The mass ratio of ice grains to vapor in the plume provides an important constraint on the possible plume generation mechanisms. Any ice/vapor ratio larger than 0.1 or 0.2 would rule out any mechanism that requires a large fraction of the grains to be condensed from the vapor (Ingersoll and Pankine, 2010; Porco *et al.*, 2006; Schmidt *et al.*, 2008). Using column densities derived from UVIS and ISS data, Porco *et al.* (2006) inferred an ice/vapor ratio of ~0.4, though Kieffer *et al.* (2009) found errors in the calculations and calculated a lower ratio of ~0.2. They also suggested that ice/vapor ratio is likely to be < 0.1–0.2. Using the plume brightness data derived from ISS images taken at very high phase

angles, Ingersoll and Ewald (2011) estimated a higher ice/vapor ratio between 0.35 and 0.7. This ratio could be greater if a lot of the grains do not reach the altitudes where ISS had taken the images. In addition, the ice/vapor mass ratio in the plume is proportional to the mass flow rate ratio of ice grains to vapor coming out from the vents. With vapor and grain mass flow rates estimated to fall in the ranges of ~100–1000 kg/s and ~1–100 kg/s respectively (see Section 2.4.4), this would put the plume ice/vapor ratio from as small as 0.001 to as large as 1. Consequently, the plume ice/vapor ratio remains poorly constrained.

2.5. THERMAL EMISSION AND WARM SOUTH POLAR REGION

Elevated brightness temperatures were detected by CIRS in the south polar region, approaching ~85 K near the south pole (Spencer *et al.*, 2006). Based on CIRS data, the endogenic thermal emission from the south polar region was estimated to be 5.8 ± 1.9 GW (Spencer *et al.*, 2006). An improved estimate raised the thermal emission to 15.8 ± 3.1 GW (Howett *et al.*, 2011), but it was later revised back down to ~5 GW (Spencer *et al.*, 2013). Equilibrium tidal heating on Enceladus was estimated to produce ~1.1 GW (Meyer and Wisdom, 2007) while radiogenic heating was estimated to add ~0.32 GW (Porco *et al.*, 2006), thus the total heat output from these sources does not match observations. Several possibilities exist. Tidal dissipation may be enhanced by physical libration (Hurford *et al.*, 2009) or the presence of a localized or global subsurface ocean (Collins and Goodman, 2007; Nimmo *et al.*, 2007, 2014; Porco *et al.*, 2014; Roberts and Nimmo, 2008; Tobie *et al.*, 2008). Alternatively, the observed heat output may be an episodic release of the tidal heat generated from an epoch of high orbital eccentricity (Meyer and Wisdom, 2007). A fraction of the observed heat output may have also resulted from latent heat released by vapor condensing near the surface as it emerges from the cracks (Ingersoll and Pankine,

2010; Nimmo *et al.*, 2007; Porco *et al.*, 2014). However, it remains unclear how the observed heat output is generated on Enceladus.

As shown in Figure 2.7, the thermal emission is concentrated mostly along the Tiger Stripes, which are the warmest sites in the south polar region (Howett *et al.*, 2011; Porco *et al.*, 2006; Spencer *et al.*, 2006). High-resolution CIRS measurements detected temperatures as high as ~145 K along the Tiger Stripes (Spencer *et al.*, 2006). An independent VIMS measurement detected a hotspot on the Baghdad Sulcus with an even higher temperature of ~200 K (Goguen *et al.*, 2013).

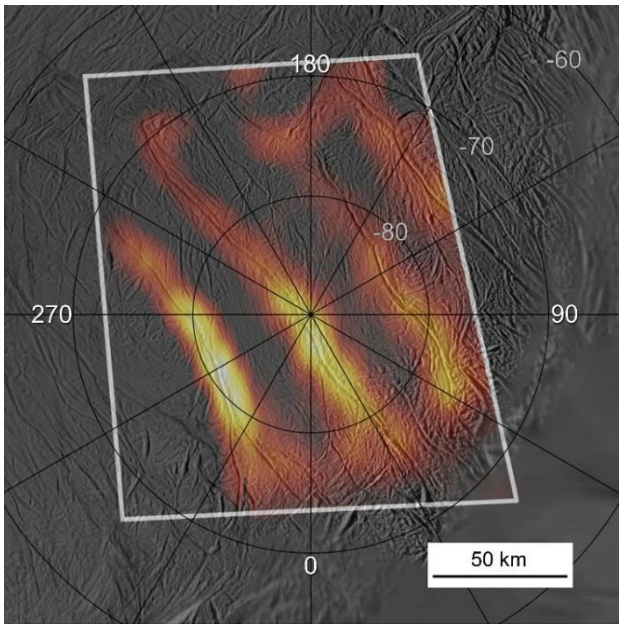

Figure 2.7. Spatial distribution of thermal emission from the south polar region of Enceladus, as measured by CIRS on 12 March 2008, showing the Tiger Stripes to be the most active regions. White box indicate region of CIRS observation. (*Image PIA10361, courtesy of NASA/JPL/Goddard Space Flight Center (GSFC)/Southwest Research Institute (SwRI)/SSI*).

2.6. PLUME GENERATION MECHANISMS

Since the plume has a major influence on the Saturnian system and its presence raises the possibility of finding liquid water on Enceladus, different hypotheses have been suggested as its generation mechanism. The plume generation mechanism must be able to account for the different aspects of the plume, e.g. composition, structure, amount of each phase present and temporal variability, as well as the warm temperatures and thermal emission observed in the south polar region in a consistent manner. Many hypotheses have been proposed, but only the most relevant ones are highlighted here.

2.6.1. "Cold Faithful" and "Frigid Faithful" Models

Two such hypotheses are the "Cold Faithful" (Porco *et al.*, 2006) and the "Frigid Faithful" (Kieffer *et al.*, 2006) models. In the Cold Faithful model, liquid water can exist as close as ~7 m from the surface. When a crack forms in the layer of ice and exposes the underlying liquid water to vacuum, it begins to boil violently. Bubbles of vapor form and travel up the crack, carrying along some liquid water that freezes upon expanding out of the crack. This results in the mixture of vapor and ice observed. However, this model presents several problems. First, percolation causes the bubbles to coalesce and rise up to the surface without carrying any liquid water along (Brilliantov *et al.*, 2008). Second, it cannot account for the methane detected in the plume (Waite *et al.*, 2006, 2009) because methane has low solubility in liquid water (Ingersoll and Ewald, 2011; Kieffer *et al.*, 2006). Third, the explosive boiling of salt water releases sodium atoms (Postberg *et al.*, 2011), which have not been detected (Schneider *et al.*, 2009).

The "Frigid Faithful" model postulates that a reservoir of clathrates or clathrates plus water ice is present under a thick layer of ice (Kieffer *et al.*, 2006). When fractures form in the ice due to tectonic activity, this reservoir is exposed to near-vacuum conditions, causing the clathrates to decompose, possibly explosively, and release noncondensable

gases such as nitrogen and methane. As these gases travel up the fractures, they entrain small ice grains (Laufer *et al.*, 2005), which then sublimate due to the pressure drop they encounter, producing a plume with the observed 10:1 molar ratio of water vapor to noncondensable gases (Waite *et al.*, 2006, 2009). Temporal variability of the plume is caused by fractures constantly being created by active tectonics and sealed by the rising vapor as it freezes. While this model could account for the noncondensable gases, it also has several shortcomings. First, sodium-rich grains have been detected in the plume (Postberg *et al.*, 2009, 2011), thus their sublimation would have released sodium, which has not been observed (Schneider *et al.*, 2009). Second, the cold temperatures (~140–170 K) of this model would not be able to produce vapor dense enough to support the measured grain fluxes in the plume (Brilliantov *et al.*, 2008; Schmidt *et al.*, 2008).

2.6.2. Possibility for Liquid Water

The existence of liquid water below the surface depends on how efficiently heat can be transported away from the source to the surface (Ingersoll and Pankine, 2010). Given the heat output observed from the south polar region, liquid water may exist within 40 m below the surface if thermal conduction through solid ice were the dominant mode of heat transfer (Spencer *et al.*, 2006). However, vapor carrying latent heat may provide a much more efficient mode of heat transfer (Nimmo *et al.*, 2007; Spencer *et al.*, 2006), thus liquid water may potentially exist several kilometers below the surface. Ingersoll and Pankine (2010) investigated two mechanisms of heat transfer by vapor: diffusion through an icy matrix and hydrodynamic flow in cracks. For vapor diffusion, the icy matrix must be rather porous, with porosity greater than ~0.1, and have grain sizes larger than ~1 cm to prevent melting at depth, i.e. the matrix is a rubble pile. For hydrodynamic flow, the cracks must be wider than ~0.1 m and the heat source must be in contact with the cracks to avoid

melting at depth. The temperature of the icy matrix or the crack walls has a strong effect on the ability of the vapor to transport heat as the partial pressure of the vapor equilibrates almost instantaneously to the saturation vapor pressure of the surrounding ice.

The grains have been observed to have slower ejection speeds than the gas. A large fraction of the grains are ejected at below escape speeds (≤ 240 m/s) (Hedman *et al.*, 2009; Ingersoll and Ewald, 2011; Postberg *et al.*, 2011; Schmidt *et al.*, 2008) while gas speeds of ~1–2 km/s have been inferred (Hansen *et al.*, 2011). Schmidt *et al.* (2008) proposed that the speed difference arises below the surface, where the grains are formed via condensation and transported by the vapor in narrow nozzle-like channels ~0.1–1 m in width. Wall collisions and changes in flow direction slow down the grains relative to the gas. As a result, a sufficiently dense vapor is required to produce the measured grain fluxes (Spahn *et al.* 2006b), implying temperatures > 260 K at the evaporation site and thus the existence of liquid water. Liquid water could possibly exist in equilibrium with ice and vapor (at its triple point) below the south polar region. The detection of propane (C_3H_8) and acetylene (C_2H_2) in the plume (Waite *et al.*, 2006, 2009) indicates catalytic reactions occurring in a very hot interior, with temperatures of 500–800 K (Matson *et al.*, 2007), further supporting the presence of liquid water. Moreover, the detection of silicon-rich nanometer-sized grains of a narrow size distribution, r_{grain} = 2–8 nm, indicates hydrothermal activity occurring at temperatures > 360 K in a subsurface ocean (Hsu *et al.*, 2015).

In addition, the shape of Enceladus is consistent with the subsurface presence of liquid water (Collins and Goodman, 2007). Enceladus is an ellipsoid with an asymmetry across the equator. It is slightly depressed at the south pole and bulges out at latitude 50°S (Porco *et al.*, 2006). The south polar depression may be caused by melting at the base of Enceladus' ice shell due to the anomalous heat flow observed at the south pole (Spencer *et al.*, 2006). As the ice melts, a localized sea is formed underneath the south polar region.

Measurements of the gravitational field of Enceladus appear to support this, with the localized ocean possibly located at depths of 30–40 km (Iess *et al.*, 2014).

2.6.3. Other Hypotheses Favoring Liquid Water

In the Cold Faithful model, the body of liquid water produces the observed vapor and ice grains directly. However, this may not necessarily be the case. Nimmo *et al.* (2007) argued that Enceladus' ice shell must be decoupled from its silicate core by a global ocean or a localized sea so that there is sufficient motion of the ice shell to produce enough shear heating to account for the anomalously large thermal emission and elevated temperatures observed at the south pole. In this model, tidal stresses cause lateral (strike-slip) motion of Enceladus' ice shell and generate shear heating along faults such as the Tiger Stripes (Nimmo and Gaidos, 2002; Roberts and Nimmo, 2008). About 10% of this heat is observed directly while the other 90% goes into sublimating ice along the faults. Only ~10% of this vapor escapes to form the plume while the remaining 90% recondenses on cold ice near the surface along the faults, producing additional heat and warm surface temperatures. A small fraction of the condensing vapor is entrained as ice grains. The periodic nature of tidal stresses, which vary over an orbital period, may give rise to periodic activity. This is consistent with the observed variation in plume brightness with the orbital position of Enceladus (Hedman *et al.*, 2013; Nimmo *et al.*, 2014). However, this model contains several problems. First, grains formed from recondensation of vapor sublimated from the ice shell could only produce salt-poor grains as the ice shell is salt-free (Zolotov, 2007), thus the observed salt-rich grains could not be accounted for (Postberg et al., 2009, 2011). Second, such a mechanism would produce kilometer-scale hotspots but the observed hotspots are only meters in scale (Porco *et al.*, 2014).

Postberg *et al.* (2009) attributed the source of the salt-rich grains to a deep salty ocean. The salinity of the ocean is derived from its interaction with Enceladus' rocky core over the years (Zolotov, 2007). According to this model, the liquid ocean exists with its vapor phase in a large cavernous chamber deep below the surface. The salt-rich grains are frozen droplets formed directly from the liquid via dispersion (Charvat and Abel, 2007) while the salt-poor grains are formed from condensation of the vapor rising to the surface via narrow channels (Brilliantov *et al.*, 2008; Schmidt *et al.*, 2008). This explains the lack of sodium observed in the vapor (Schneider *et al.*, 2009) as most of the sodium resides in the salt-rich grains. The inferred ice/vapor mass ratio of 0.35–0.7 supports the idea that the grains are formed directly from the liquid (Ingersoll and Ewald, 2011) as condensation could only produce ice/vapor ratios < 0.1 (Ingersoll and Pankine, 2010; Schmidt *et al.*, 2008). The noncondensable gases detected in the plume (Waite *et al.*, 2006, 2009) may be the products of chemical processes occurring in the ocean (Matson *et al.*, 2007), or clathrate decomposition at the water-ice boundary (Bouquet *et al.*, 2015). This deep salty ocean may be large, perhaps extending beyond the south polar region (Glein and Shock, 2010). A global ocean would be difficult to maintain by tidal dissipation alone (Roberts and Nimmo, 2008), thus a localized sea is more likely to exist (Collins and Goodman, 2007; Tobie *et al.*, 2008). However, a global ocean may be required to produce the amplitude of the 1:1 physical libration needed to match the observed variation in plume brightness (Nimmo *et al.*, 2014).

Porco *et al.* (2014) proposed a variation of the deep salty ocean model. As shown schematically in Figure 2.8, a localized salty sea exists under an ice shell with a thickness of ~30–40 km (Iess *et al.*, 2014) at the south pole. Unlike the model by Postberg *et al.* (2009), liquid water fills the entire subsurface chamber. Narrow cracks extend through the ice shell beneath the Tiger Stripes from the surface down to the subsurface sea, providing

pathways for material and heat to escape. These cracks are filled with salty water with a column height that is ~92% of the distance between the sea and the surface (Crawford and Stevenson, 1988; Ingersoll and Pankine, 2010). Consequently, the water level is only ~3–4 km from surface. From here, the salty water can reach the surface via a variety of processes, such as the rapid release of dissolved gases (Crawford and Stevenson, 1988; Matson *et al.*, 2012). Some salty water droplets are entrained and freeze upon experiencing a pressure drop while traveling up the crack, producing the salt-rich grains observed (Postberg *et al.*, 2009, 2011). Some of the rising vapor condenses on the crack walls near the surface, releasing latent heat and resulting in the small-scale thermal hotspots observed (Porco *et al.*, 2014). In this model, the eruption of material and the production of heat are governed by the normal component of the tidal stresses (perpendicular to the cracks). Normal stresses open and close the cracks over the course of the orbit (Hurford *et al.*, 2007), thus the plume activity is expected to vary in the same manner. This agrees with the observed variation in plume brightness with the orbital position of Enceladus (Hedman *et al.*, 2013; Nimmo *et al.*, 2014).

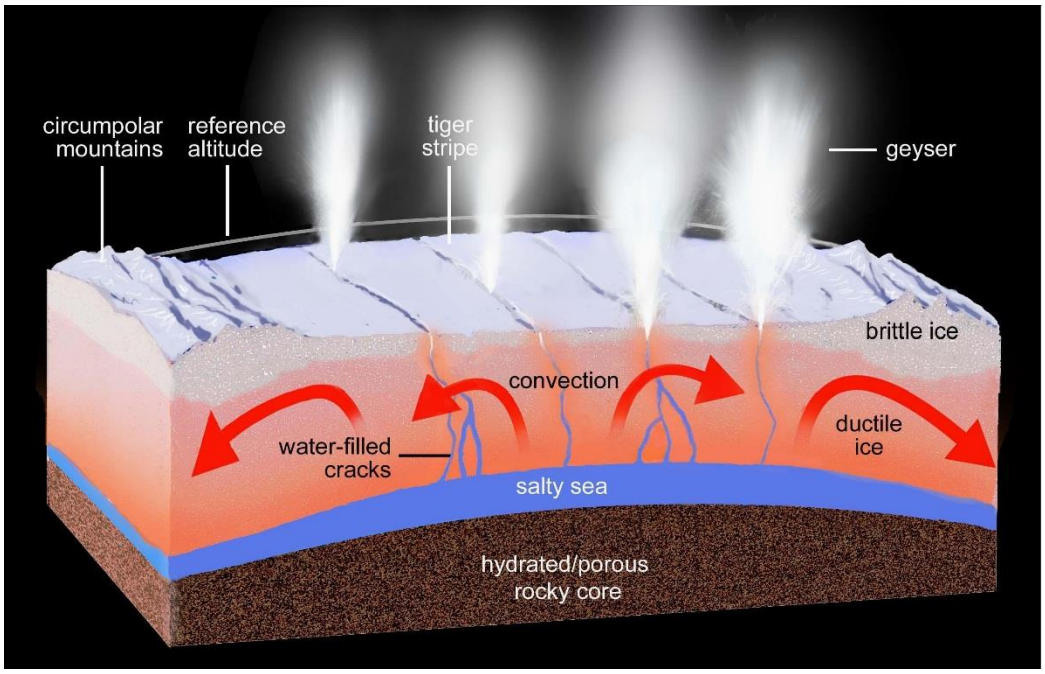

Figure 2.8. A schematic of the subsurface model proposed by Porco *et al.* (2014). A salty sea exists underneath a thick ice shell in the south polar region of Enceladus and is connected to the surface via narrow water-filled cracks through which material and heat can escape from the interior. (*Image PIA17190, courtesy of NASA/JPL-Caltech/SSI*).

2.7. Models of the Plume and Gas/Grain Environment near Enceladus

Substantial efforts have been made to model the plume and the H_2O and grain environment around Enceladus in order to understand their effects on the Saturnian system and the source conditions of the plume. Some of the relevant models are highlighted below.

2.7.1. Gas Component

Waite *et al.* (2006) tried to reproduce the asymmetry in the E2 INMS H_2O density data by simulating the plume using a cometary direct simulation Monte Carlo model with Enceladus' weak gravitational field added. The model included two sources: a south polar sublimation source and a global uniform surface source. Model parameters were varied in an attempt to match the INMS data. The poor fit between the simulation results and the

peak and egress portions of the INMS data could suggest a highly variable source rate, possibly fluctuating between 1×10^{26} and 3×10^{27} molecules/s (between 3 and 90 kg/s) on timescales shorter than an hour.

Tian *et al.* (2007) employed Monte Carlo simulations to model the E2 UVIS stellar occultation observations of the plume. They placed 17 identical point sources uniformly along the Tiger Stripes, from which H_2O molecules were ejected and traveled under gravity and collisions. Collision rates were first computed from a pre-determined spatial gas density distribution, which was then verified with simulation results for self-consistency. They inferred a surface density of ~10^{10}–10^{11} cm^{-3} and a surface normal velocity of 300–500 m/s. The high normal velocities imply venting from deep below the surface. They estimated a H_2O escape rate of ~4–6 $\times 10^{27}$ molecules/s (~120–180 kg/s) and a resurfacing rate as high as 3×10^{-4} cm/yr in the south polar region. This high resurfacing rate might explain bright plains between the Tiger Stripes (Porco *et al.*, 2006).

Burger *et al.* (2007) developed a Monte Carlo model of the H_2O source on Enceladus to investigate its nature and its effects on the Saturnian magnetospheric plasma. The modeled source has two components: a localized south polar source and a global sputtering source. Packets were ejected from the surface with specified velocity and spatial distributions and were tracked as they moved under gravity and evolved due to interactions with the magnetospheric plasma and solar ultraviolet radiation. A background torus was also included. Their model was unable to produce an entirely consistent fit to both the E2 INMS and UVIS data simultaneously due to various data and modeling limitations. They found that the south polar source is much stronger and produces ~10^{28} molecules/s (~300 kg/s), while the global source produces only ~8×10^{25} molecules/s (~2.4 kg/s). They also calculated a plasma mass loading rate of ~2–3 kg/s from the plume, which agrees with the rate estimated from magnetic field data (Dougherty *et al.*, 2006). However, they could not

reproduce the CAPS observation that the plasma was slowed down well upstream of Enceladus (Tokar *et al.*, 2006), implying the existence of another H_2O source.

Saur *et al.* (2008) analyzed the temporal variability of the plume using two analytical plume models constructed by fitting to the Cassini E0, E1 and E2 magnetic field data (Dougherty *et al.*, 2006). The first modeled the plume with only a single density distribution while the second accounted for the discrete nature of the plume by using the eight jets identified by Spitale and Porco (2007). Plume interactions with the Saturnian magnetospheric plasma and magnetic field were included. Their results were in good agreement with the E2 INMS and UVIS H_2O density measurements (Hansen *et al.*, 2006; Waite *et al.*, 2006) and indicated a highly variable plume, with its source rate and spatial distribution possibly varying on timescales of months or shorter. They inferred a total plume content of $\sim 7 \times 10^{32}$ molecules with a source rate of ~1600 kg/s for the E0 flyby and $\sim 9 \times 10^{31}$ molecules with a source rate of ~200 kg/s for both the E1 and E2 flybys.

Smith *et al.* (2010) constructed a Monte Carlo model of the plume to study its effects on the distribution of neutrals in Saturn's magnetosphere. In their model, H_2O molecules were ejected from the eight sources identified by Spitale and Porco (2007) and the populations of neutrals (H_2O, OH and O) in the magnetosphere were tracked. Other source and loss mechanisms for the neutrals were also incorporated, e.g. photolysis, electron impacts, charge exchange, absorption by Saturn's atmosphere, collisions with moons and ring particles, and escape from the Saturnian system. The parameters for the plume model were determined by fitting to E2, E3 and E5 INMS density data. Their best-fit results suggested plume sources with a bulk flow speed of ~720 m/s and ejection angles $\leq 30°$ from the southward normal direction. Moreover, they computed a plume source rate that could vary by at least a factor of four from $\sim 6.3 \times 10^{27}$ molecules/s (~190 kg/s) during

the E3 flyby to ~2.5 × 10^{28} molecules/s (~750 kg/s) during the E5 flyby, spanning a period of ~7 months. However, the timescale of variability may be shorter.

Tenishev *et al.* (2010) constructed a semi-analytical model of Enceladus' atmosphere with two sources: a plume source comprising the eight jet sources identified by Spitale and Porco (2007) and a global uniform source. The jet sources were modeled as point sources with gas injected according to a Maxwellian velocity distribution. The source parameters were determined by simultaneously fitting to the E2 UVIS and both the original and newly processed E3 and E5 INMS H_2O density data (Teolis *et al.*, 2010). The plume source was found to be dominant, and the plume and global source rates were estimated to be ~2.6–4.2 × 10^{28} molecules/s (~780–1260 kg/s) and ~3.6–4.7 × 10^{25} molecules/s (~1.1–1.4 kg/s) respectively. The improvement of their fits to the outbound portion of the *in-situ* data with greater distance from Enceladus suggested that additional weaker localized sources or some other atmospheric processes were important *near* Enceladus. Additionally, since a single model was used to simultaneously fit *in-situ* data from flybys made at different times, the different quality of the fit to each flyby data set might indicate long-term variability in the jet source rates or orientations.

Dong *et al.* (2011) modeled the H_2O density distribution around Enceladus by superimposing analytical distributions from three types of sources: a south polar plume source, a global expansion source and a uniform background source. The south polar plume source included multiple discrete jets from among those identified by Spitale and Porco (2007). Each jet was modeled as a point-like source with a radially flowing Maxwellian velocity distribution. Their results matched reasonably well with E3, E5 and E7 INMS and E2 UVIS H_2O density data and suggested temporal and spatial variability of the plume. Calculated flow velocities and source rates between the flybys were in the ranges of ~550–750 m/s and ~1.5–3.5 × 10^{28} molecules/s (~450–1000 kg/s) respectively, indicating

temporal variability over timescales of months (duration between flybys). They found intensity variations between different jets and also between different flybys.

2.7.2. Grain Component

Spahn *et al.* (2006b) modeled the grain distribution around Enceladus by simulating the trajectories of grains ejected from two types of sources on Enceladus: a localized south polar source and a global impactor-ejecta source. Their model was able to reproduce the temporal offset observed in the E2 CDA peak count rate with respect to closest approach. By fitting to the CDA data, they estimated a south polar source rate of $\sim 5 \times 10^{12}$ grains/s and a global impactor-ejecta source rate of no more than 10^{12} grains/s for $r_{grain} > 1.6$ μm. Moreover, they studied the effects of source locations and found that sources in the region around the Tiger Stripes could produce a grain distribution around Enceladus that is consistent with the temporal offset in the CDA peak rate.

Schmidt *et al.* (2008) simulated the grain component of the plume by launching grains into a cone of 25° half-angle about the surface normal from sources uniformly distributed in a circular region below latitude 80°S. The grains moved ballistically under the gravitational fields of Enceladus and Saturn and were removed once they were outside two Enceladus Hill radii ($R_H \approx 948$ km) or struck the moon again. The distributions of grain sizes and ejection speeds at the sources were determined from subsurface modeling. Grains were formed via condensation in variable-width channels through which water vapor escaped into vacuum from subsurface evaporation sites. The variation in channel width causes the vapor to expand and cool down, thus increasing supersaturation and enhancing condensation. By modeling nucleation and grain growth in the channel, they obtained the distribution of grain sizes at the outlet. Grain motion in the channel is governed by gas drag and wall collisions. Grains are accelerated by the vapor between wall collisions whose

frequency is determined by the crack width. A Poisson random process with an exponential distribution of flight times was used to model this. With this approach, the distribution of grain ejection speeds was calculated. Wall collisions and flow directional changes slow down the grains relative to the gas. To account for natural variations, they generated 5,000 different channel geometries and averaged over the resulting distributions of grain sizes and ejection speeds. In order to support the grain speeds inferred from the plume brightness profile, their results indicated that plausible channel widths of ~0.1–1 m would require temperatures > 260 K at the evaporation sites, suggesting the presence of liquid water. By fitting to E2 CDA data, they calculated a total grain production rate of ~5 kg/s venting from an area of ~200 m^2, with ~10% escaping. Grains with r_{grain} > 1 μm comprised over half the escaping mass. With a computed solid mass fraction of ~0.06, a H_2O production rate of ~100 kg/s was inferred.

To analyze how the plume replenished the E ring, Kempf *et al.* (2010) simulated the early stages of the trajectories of grains of various sizes (r_{grain} = 5 nm–50 μm) launched over a range of speeds (1–500 m/s) from the south polar region, including the eight sources identified by Spitale and Porco (2007). The ejection rates were determined from Schmidt *et al.* (2008). The grains were initially uncharged but subject to charging in the ambient plasma and by solar ultraviolet radiation (Horanyi, 1996). Both gravitational and Lorentz forces were included. They found that grains must be ejected at speeds ≥ 228 m/s to escape Enceladus into the E ring. This speed is greater than the three-body escape speed of the Saturn-Enceladus system of ~207 m/s. Their results indicated > 95% of the ejected grains could escape to resupply the E ring. However, these only represented ~10% of the ejected mass because most of the escaping grains were the smaller and lighter grains. They also found that the deposition rates of plume grains on Enceladus' surface dropped drastically

with distance away from the sources, ranging from 0.5 mm/year in the south polar region to ~10^{-5} mm/year at the equator.

Degruyter and Manga (2011) attempted to deduce the subsurface conditions from the surface grain size distributions on Enceladus derived from VIMS measurements (Jaumann *et al.*, 2008). They assumed that the surface grain size distributions were directly related to the eruption mechanism at the sources, allowing them to infer a gas temperature and a grain acceleration length below the surface. In their model, the grains are only affected by the gas below the surface and moved ballistically above. For a given grain size, the grain speed at the vent depended on the subsurface gas temperature and acceleration length. Two acceleration models were considered: the drag-limited model and the collision-limited model. In the drag-limited model, grains do not collide with the walls and their maximum speeds are governed by the length over which they are allowed to accelerate. In the collision-limited model, the distance between collisions governs the grain maximum speeds. By fitting to VIMS data, they obtained a relationship between the gas temperature and the acceleration length for each model. Their results agreed reasonably well with the VIMS data at 5–10 km from the sources but underestimated the grain sizes beyond 10 km. They also derived a relationship between the grain maximum height and the grain size. Comparisons of these results with other observations, including the E2 CDA (Spahn *et al.*, 2006b) and the November 2007 VIMS measurements (Hedman *et al.*, 2009), suggested that subsurface gas temperatures of 190–273 K were plausible.

Based on the calculations of Sremcevic *et al.* (2003), Postberg *et al.* (2011) developed two analytical models of the grain distribution around Enceladus to reproduce the E5 CDA measurements, which indicated an increase in the fraction of salt-rich grains and a simultaneous decrease in the fraction of salt-poor grains shortly before closest approach. The first model had the source as a broad emission along the Tiger Stripes while

the second model included the eight jets identified by Spitale and Porco (2007) with the broad emission. By fitting to CDA data, they attributed the observed compositional stratification of the plume to the difference in ejection speeds. Due to their different formation mechanisms (Postberg *et al.*, 2009), the salt-rich grains tend to be larger than the salt-poor grains. Consequently, the larger salt-rich grains are ejected at slower speeds. Additionally, they inferred that the slower, larger salt-rich grains are mainly ejected from the broad emission along the Tiger Stripes while the faster, smaller salt-poor grains come primarily from the collimated jets. Their results indicated that ~70% (> 99% by mass) of the ejected grains with $r_{grain} \geq 0.2$ μm were salt-rich. However, only ~6% of such grains were detected in the E-ring (Postberg *et al.*, 2008), implying that most of the salt-rich grains were ejected slower than the escape speed and fall back to Enceladus. This is consistent with the grain ejection speeds inferred from the 2007 VIMS measurements (Hedman *et al.*, 2009).

Ingersoll and Ewald (2011) extracted brightness data from images taken by the ISS wide angle (WAC) and narrow angle cameras (NAC) to estimate the total grain masses in the plume and the E-ring as well as the grain production rate from Enceladus. The images were taken at very high phase angles between 173° and 179°. Assuming several grain size distributions and grain shapes, they fitted their model to the WAC brightness data in a least-squares manner and found that the total grain mass in the plume is $(1.45 \pm 0.5) \times 10^5$ kg and the median grain radius is 3.1 ± 0.5 μm. In addition, they performed simulations using several grain velocity distributions and fitted the results to the spatially-resolved NAC brightness data and found that an exponential velocity distribution provided the best fit. From this, the grain mass production rate from Enceladus is estimated to be 51 ± 18 kg/s, with only ~4.6 kg/s escaping. However, they have not accounted for variations in grain size, shape and velocity distributions with altitude. For the E-ring, they estimated a total

grain mass of $(12 \pm 5.5) \times 10^8$ kg in the radial band of 206,500–296,500 km from the center of Saturn. With an estimated escaping mass rate of ~4.6 kg/s, this implied an average E-ring grain lifetime of ~8 years, which is less than half the pre-Cassini estimate of ~20 years by Juhasz and Horanyi (2002), who estimated a total E-ring mass of $\sim 6 \times 10^8$ kg. Remarkably, Ingersoll and Ewald (2011) found that the median E-ring grain radius is also 3.1 ± 0.9 μm. Moreover, their best-fit results indicated that small grains make up a larger fraction of the E ring than the plume and that the E-ring grains are more oblate. These differences could arise from observational errors or could be real. It might be that the grains escaping into the E-ring are different than those falling back or that the grains evolved upon entering the E-ring. An important implication from this work is the significant mass fraction of grains inferred in the plume, ~0.35–0.7 or possibly higher if a lot of the grains do not reach the altitudes where the ISS images were taken. This argues against grain formation via vapor condensation.

Chapter 3.

Method[2]

3.1. Overview

The Enceladus two-phase plume can be divided into several distinct dynamical regions. Below the vents, the gas is relatively dense and collisional, thus the motions of the gas and the grains are coupled. As the flow exits the vents and expands into vacuum, the gas density and thus the molecular collision frequency drop rapidly. The gas and the grains also start to decouple. Above a certain altitude, the gas and the grains have fully decoupled and move independently. At a higher altitude, the gas density has dropped sufficiently low that collisions have become very infrequent and the flow has become free-molecular. Beyond this, the gas molecules and the grains execute ballistic trajectories under the gravitational fields of Enceladus and Saturn and are subject to plasma processes, radiation and photochemistry, among others, over an extended period of time.

Due to their distinct natures, each region is treated separately in this plume model. Two subsurface models are considered: a simple analytical model and a more sophisticated computational model. Using the vent conditions derived from the subsurface models, the near-field region directly above the vents, where the flow transitions from collisional to free-molecular and the decoupling between the gas and the grains occurs, is simulated using the direct simulation Monte Carlo (DSMC) method. Once the flow has become free-molecular, a planetary-scale free-molecular model takes the output of the DSMC model and continues to propagate the plume into the far-field where Cassini *in-situ* data are available to provide constraints. A schematic of the plume model is shown in Figure 3.1.

[2]Parts of this chapter are published in Yeoh *et al.* (2015). All of the computations in this work were done by the author of this dissertation. The other authors provided useful ideas, suggestions and feedback, and also proofread and corrected the manuscript of the paper.

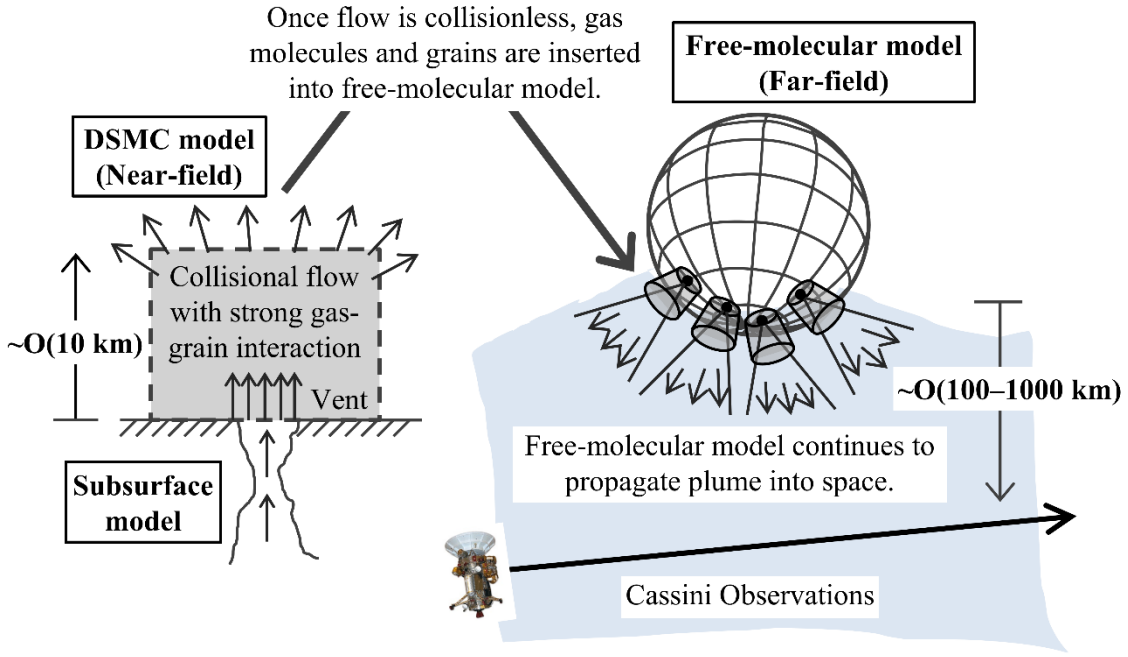

Figure 3.1. Schematic of plume model.

3.2. SUBSURFACE MODELS

To obtain the vent conditions for the DSMC model, two subsurface models are considered: a simple analytical model and a more sophisticated computational model. These models are based on the hypothesis proposed by Schmidt *et al.* (2008) where an underground reservoir of liquid water is connected to surface vents via narrow cracks of variable widths. Supersonic flow can be achieved as the gas expands through these cracks. This is supported by both modeling and observations: the thermal modeling of the observed IR radiation from the south polar region (Abramov and Spencer, 2009), the discovery of salt-rich E-ring and plume grains (Postberg *et al.*, 2009, 2011), the observation of non-vertical jets (Porco *et al.*, 2014; Spitale and Porco, 2007), the detection of highly collimated supersonic gas jets (Hansen *et al.*, 2008, 2011) and the observation of small-scale thermal hotspots (~10 m) rather than large-scale ones (~1 km) (Porco *et al.*, 2014). Furthermore, the observed variation in plume brightness with the orbital position of Enceladus suggests

that tidal stresses cause subsurface cracks to widen and narrow, thus varying the amount of plume material being ejected (Hedman *et al.*, 2013; Nimmo *et al.*, 2014).

3.2.1. Analytical Model

This simple model is an isentropic quasi-1D flow expanding through a converging-diverging (de Laval) nozzle with a circular cross-section from stagnation conditions taken to be the triple-point of water in the reservoir (Porco *et al.*, 2006; Schmidt *et al.*, 2008), as shown in Figure 3.2. This is similar to the flow in a rocket nozzle, which is also shown in Figure 3.2. The flow is subsonic (Mach number, $Ma < 1$) in the converging section, sonic ($Ma = 1$) at the throat, and becomes supersonic in the diverging section ($Ma > 1$). For such a flow, the solution is analytical and the flow conditions are completely governed by the channel geometry, i.e. the ratio of the local channel area to the throat area (Anderson, 2003). Consequently, the vent conditions are solely determined by the vent-to-throat area ratio. While the actual subsurface flow is possibly a mixture of gas and grains, it is modeled here as purely gas. This is reasonable as long as not too many grains are present to alter the gas flow significantly. In addition, only H_2O is considered as it makes up ~90% of the plume (Waite *et al.*, 2006, 2009).

Two vent-to-throat area ratios are considered, 4.8 and 36.6, resulting in vent Mach numbers, Ma_{vent}, of 3 and 5 respectively. The corresponding gas properties at the vent are listed in Table 3.1. There are several points to note here. The densities differ by an order of magnitude between the two vent conditions. However, they are many orders of magnitude lower than the air density (~1.2 kg/m^3) at standard atmospheric conditions on Earth. The pressures are also many orders of magnitude lower than the surface atmospheric pressure on Earth (~100 kPa), but are many orders of magnitude higher than the surface atmospheric pressure on Enceladus (~10^{-8}–10^{-5} Pa) (Waite *et al.*, 2006). Although Ma_{vent}

increases by nearly a factor of two, the speed increases only slightly. However, the temperature drops by about a factor of two, thus the increase in Ma_{vent} is mainly due to a decrease in temperature (and thus the speed of sound) rather than an increase in speed.

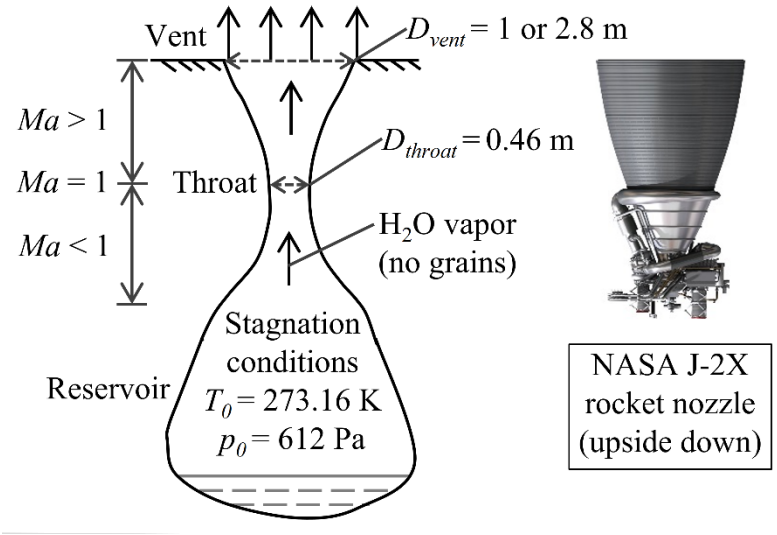

Figure 3.2. Model of the subsurface flow as an isentropic flow through converging-diverging nozzle (left). This is similar to a flow in a rocket nozzle (right). (*Image of rocket nozzle, courtesy of NASA*).

In comparison with other estimates, the Ma_{vent} considered are higher than the values of 1.4–1.8 obtained by Smith *et al.* (2010) and Dong *et al.* (2011) from fitting to INMS data. Earlier UVIS observations also inferred low Ma_{vent} of 1.3–1.7 (Hansen *et al.*, 2008). More recent UVIS observations, however, deduced very high Ma_{vent} of 5–8 (Hansen *et al.*, 2011), which are closer to the Ma_{vent} considered. The gas speeds at the vent are also higher than estimates of ~720 m/s by Smith *et al.* (2010), 570–730 m/s by Dong *et al.* (2011), 520–700 m/s by Tenishev *et al.* (2010), ~610 m/s by Hansen *et al.* (2008) and 300–500 m/s by Tian *et al.* (2007), though Hansen *et al.* (2011) estimated very high gas speeds of 1.6–2.6 km/s from UVIS observations.

Since the vent conditions depend only on the vent-to-throat area ratio in this model, any channel size would result in the same vent conditions as long as the area ratio is maintained and the channel is much larger than the mean free path, λ, of the flow (so that the continuum assumption remains valid). However, for convenience, a nominal channel size is chosen for each of the vent conditions. In this model, the channel size is characterized by two parameters: the throat diameter, D_{throat}, and the vent diameter, D_{vent}. Schmidt *et al.* (2008) inferred plausible channel widths of 0.1–1 m, thus D_{throat} is chosen to be ~0.46 m. This produces D_{vent} of ~1 m and ~2.8 m for Ma_{vent} = 3 and 5 respectively. These nominal channel dimensions are also listed in Table 3.1. The nominal vent mass flow rate, $\dot{m}_{vent}$, is ~0.2 kg/s for both vent conditions. Note that the nominal D_{vent} are smaller than the pixel size (~4 m) of the higher-resolution images of the surface of Enceladus (Porco *et al.,* 2006). Consequently, such vents could not be observed if they do exist.

Table 3.1. Vent conditions for gas component used in simulations.

Properties	Ma_{vent} **= 3**	Ma_{vent} **= 5**
Vent-to-throat Area Ratio	4.8	36.6
D_{throat} (m)	0.46	0.46
D_{vent} (m)	1	2.8
A_{vent} (m^2)	~0.8	~6.2
Density (kg/m^3)	3.1×10^{-4}	3.5×10^{-5}
Speed (m/s)	780	902
Temperature (K)	110	53
Pressure (Pa)	15.8	0.9
λ (m)	1.4×10^{-4}	1.2×10^{-3}
$\dot{m}_{vent}$ (kg/s)	0.2	0.2

This subsurface model contains several limitations. First, the Reynolds number of the modeled subsurface flow ranges from 10^4–10^6, thus turbulence effects may be important. Second, we have neglected various other subsurface physical processes, such as

grain condensation from the vapor phase, thermal interaction of the flow with the channel walls (including phase change) and viscous effects. Schmidt *et al.* (2008) and Ingersoll and Pankine (2010) have shown that grain condensation from the vapor phase is minimal and yields at most 5–6% of grains by mass fraction, though the latent heat released could raise the gas temperature at the vent to 200–250 K and thus reduce the supersaturation levels above the vents. Thermal interaction of the flow with the channel walls is important as the partial pressure of the vapor equilibrates almost instantaneously to the saturation vapor pressure of the channel walls (Ingersoll and Pankine, 2010). Third, the actual channel geometry is most likely complicated.

However, this model would be a good approximation if the channel width is comparable to or larger than its length. If the channel is significantly longer than its width, boundary layer (viscous) effects and the interaction (heat and mass exchange) between the channel walls and the flow might be important, thus violating the isentropic assumption.

3.2.2. Computational Model

The computational model is more complex and is an attempt to address the shortcomings of our simplistic analytical model. This modeling work is done by our collaborators (Li, Z., Dhariwal, R., and Levin, D.). The channel geometry under consideration is more complicated and contains an additional throat, as shown in Figure 3.3. The diameters of the first throat, $D_{throat,1}$, and the vent, D_{vent}, are 0.46 m and 2.8 m respectively, and have been chosen to match those of the converging-diverging nozzle which produces the Mach-5 vent conditions from our analytical model. The second throat is slightly larger than the first throat. The length of the channel, $L_{channel}$, is 45 m, thus the channel has a very high aspect ratio, $L_{channel}/D_{vent}$, of ~16. The wall temperature, T_{wall}, is set to 230 K throughout the entire channel.

As in the analytical model, the reservoir conditions are chosen to be the triple-point of water. The simulation domain extends from the first throat to somewhat beyond the vent so that the vacuum boundary conditions implemented along the edges of the domain do not affect the solution at the vent (see Appendices B and C). The first throat is assumed to be located very close to the reservoir, thus the flow can be assumed to expand isentropically from the reservoir to the first throat. The resulting sonic conditions at the first throat are used as the inlet conditions for the subsurface flow simulation. The inlet conditions for the gas and the grains are shown in Figure 3.3.

The equilibrium DSMC (eDSMC) method is used to simulate the flow in the channel. It is an extension of the DSMC method to high-pressure flows (Titov and Levin, 2007). In this method, collisions are stopped in a cell once the molecular velocity distribution in the cell has become Maxwellian since additional collisions would no longer change the velocity distribution but only redistribute the molecular velocities. Consequently, the eDSMC method is suitable for solving the continuum and highly collisional flow presumed within the subsurface channel. In addition, the cell and timestep size requirements for the eDSMC method are not as stringent. The cell size only needs to resolve length scales of the flow gradients while the timestep size has to be such that a particle does not cross multiple cells in a single timestep. The cell and timestep size requirements for DSMC are discussed later in Section 3.3.1.

The fluid used in the simulation is H_2O vapor seeded with grains at the inlet. Both gas and grains exchange momentum, mass and energy in a coupled manner. Gas molecules and grains interact with one another via two types of collisions: sticking and non-sticking. A sticking coefficient of 0.2 has been used. A sticking collision results in a loss of a molecule from the gas phase and the growth of the grain. All the momentum and energy of the molecule is transferred to the grain. Furthermore, latent heat is released into the

surrounding gas and is transferred entirely into the translational mode of the gas molecules, which is subsequently transferred to the internal modes via collisions. A non-sticking collision simply results in an exchange of momentum and energy and not mass. To model the effect of non-sticking collisions, a drag force exerted by the gas is first calculated and applied to the grains within a cell, and the grain velocities are appropriately updated. Then, the momentum change due to the drag is correspondingly removed from the gas phase to conserve momentum. The grains can also shrink due to evaporation, which is modeled using the unimolecular dissociation theory (UDT) (Borner *et al.*, 2013).

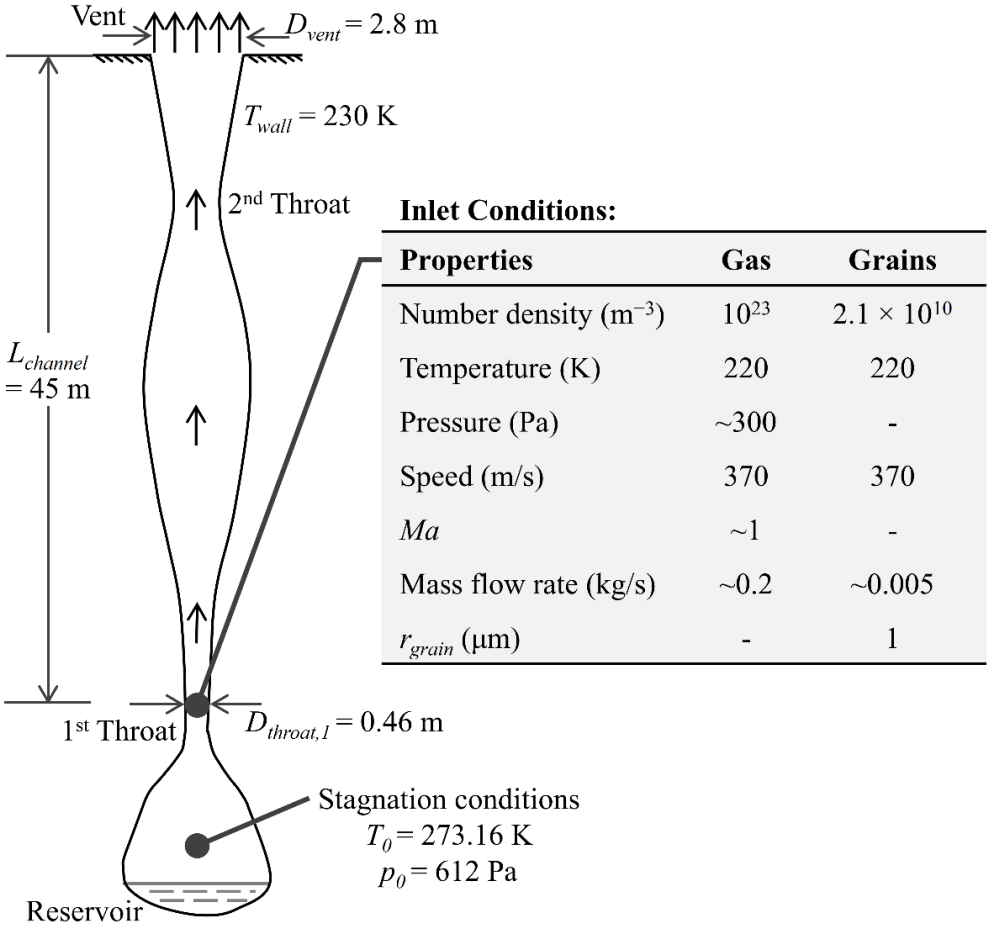

Inlet Conditions:

Properties	Gas	Grains
Number density (m^{-3})	10^{23}	2.1×10^{10}
Temperature (K)	220	220
Pressure (Pa)	~300	-
Speed (m/s)	370	370
Ma	~1	-
Mass flow rate (kg/s)	~0.2	~0.005
r_{grain} (μm)	-	1

Figure 3.3. Schematic of computational subsurface model. (*Adapted and reprinted with permission from Li et al.*)

The grains that collide with the channel walls experience a specular reflection while the gas molecules that collide with the channel walls can either stick or experience a diffuse reflection with full thermal accommodation at T_{wall}. The sticking coefficient of the wall has been set to 0.2. Gas molecules that stick to the wall are removed from the flow, resulting in a loss of material from the flow. Moreover, gas molecules are added to the flow via evaporation from the channel walls such that the pressure near the walls is maintained close to the H_2O equilibrium vapor pressure over ice, p_{vap}, at T_{wall}, which is ~9 Pa. This condition is implemented based on the work of Ingersoll and Pankine (2010). Collisions between grains are not modeled due to the dilute grain concentrations under consideration (see Appendix A).

3.3. DSMC MODEL

As the flow expands out of the vents into vacuum, it starts off collisional near the vents and only becomes free-molecular at higher altitudes. This near-field transition region is simulated using DSMC. The inputs for the DSMC simulations are obtained from the subsurface models described in Section 3.2.

3.3.1. DSMC Method

The DSMC method models gas flows stochastically using a representative set of computational particles that imitate the movements and collisions of real gas molecules (Bird, 1994). Each computational particle represents a very large number of real gas molecules (~10^{11}–10^{17} for these simulations), denoted as f_{num}. A DSMC domain is decomposed into cells in which particles move and collide. A fundamental assumption in DSMC is that the gas flow is dilute, thus gas molecules only spend a negligible fraction of time interacting with one another through collisions and spend the vast majority of time between collisions as if no other gas molecules are present. Consequently, the particle

movement and collision phases can be decoupled and executed in sequence. At each timestep, particles are first translated under the influence of any force field present (e.g. gravity). Then, particles within the same cells are collided in a probabilistic manner.

In DSMC, the timestep, Δt, should be much smaller than the local mean collision time, τ_{coll}. Since gradients can be smoothed out across a cell through the selection of collision partners spanning the cell, the cell size, Δx, should be smaller than the scale length of the macroscopic flow gradients in the direction in which the cell size is measured. In regions with large macroscopic gradients, Δx is typically chosen to be $\sim \frac{1}{3}\lambda$ (Bird, 1994, p. 216). Macroscopic flow properties (e.g. density, velocity and temperature) are computed by averaging over the appropriate molecular properties in each cell. Statistical noise in the computed macroscopic properties is inversely proportional to the square root of the number of independent computational particles in the cell and thus can be reduced by ensemble averaging, or time averaging in the case of a steady flow.

DSMC is commonly used to model rarefied gas flows where the continuum assumption fails, but it is physically accurate for all flow regimes. DSMC has been shown to satisfy the collision integral in the Boltzmann equation (Nanbu, 1986) and solve the Boltzmann equation itself (Wagner, 1992). However, it is computationally expensive for high-density flows (continuum regime). The different flow regimes are characterized by the local Knudsen number, Kn, which is defined as λ/L, where L is the scale length of the macroscopic flow property gradients (e.g. $L \triangleq \rho/|\nabla\rho|$ where ρ is the gas density). The versatility of DSMC makes it suitable for modeling the plume flow, which encompasses multiple flow regimes as it expands from the surface vents into space, from nearly continuum ($Kn << 1$) to free-molecular ($Kn >> 1$). Moreover, DSMC is capable of capturing the non-equilibrium effects present in such flows because it models the finite

energy transfer rate between different molecular internal energy modes (e.g. rotational and vibrational).

3.3.2. DSMC Implementation

Our DSMC code is developed from Bird's original DSMC procedure (Bird, 1994). Over the years, various modifications and improvements have been made to the code. However, only those relevant to this work will be highlighted here. The code has been used to simulate Io's volcanic plumes (McDoniel *et al.*, 2015; Zhang, 2004; Zhang *et al.*, 2003, 2004) and atmosphere (Moore, 2011; Moore *et al.*, 2009; Walker, 2012; Walker *et al.*, 2010, 2012); comet impacts on the moon (Prem *et al.*, 2014; Stewart, 2010; Stewart *et al.*, 2011); as well as rocket plume impingement on the lunar surface and the resulting dispersal of dust (Morris, 2012).

Between collisions, the computational particles travel along ballistic trajectories under the gravitational field of Enceladus. Our DSMC code accounts for the variation of gravity with altitude ($\propto 1/r^2$ where r is the distance from the center of Enceladus). The gravitational field of Enceladus is relatively weak, with a surface gravity, g_{Enc}, of ~0.113 m/s^2 (~1% of the surface gravity of Earth). The Coriolis and centrifugal forces associated with the motion of Enceladus around Saturn have been neglected in the DSMC model because they have a negligible effect over the timescales of the near-field simulations (~10 s). In comparison, the orbital period of Enceladus around Saturn is ~1.37 days (~33 hours).

The molecular model used is the variable hard sphere (VHS) model with parameters for H_2O molecules (Stewart, 2010). The rotational and vibrational energy states of the gas molecules are tracked, but the vibrational modes are hardly activated at the low temperatures considered ($\leq$ 230 K) as the lowest characteristic vibrational temperature for water vapor is ~2290 K (McGrath *et al.*, 2006). During collisions, energy exchanges occur

between the translational and the internal modes as well as among the internal modes. Energy from the internal modes could also be lost via radiation. However, as we shall see in Chapter 4, radiation has been neglected as the timescales associated with radiation are much longer than the mean time between collisions in the near-field. As collisions cease farther out, radiation becomes more important but its effects on the gas dynamics, which is the main focus of the work, should be minimal because the molecular internal energy can no longer be converted into the mean kinetic energy of the gas via collisions. Furthermore, our DSMC code is capable of handling grains entrained in the gas flow, which will be described in greater detail in Section 3.3.3.

The DSMC code uses a three-dimensional spherical geometry. A circular vent is assumed, thus the flow is axisymmetric and is simulated in a 1° wedge with the appropriate boundary conditions shown in Figure 3.4a. For the DSMC simulations that take input from the analytical subsurface model, the gas particles are inserted into the DSMC domain at the vent based on equilibrium distributions so as to produce the mean flow properties shown in Table 3.1. The gas mean velocity profile at the vent is assumed to be uniform as the subsurface flow *Re* is high (10^4–10^6) and therefore the boundary layer along the channel walls is thin. The grain particles are inserted at the vent at *discrete* sizes, speeds and temperatures, rather than distributions.

For the DSMC simulations that take input from the computational subsurface model, the gas and grain properties are first sampled along a row of cells below the vent. Based on these properties, gas and grain particles are then generated in a row of creation cells below the vent and are allowed to drift into the DSMC domain above. The molecular properties are sampled from equilibrium distributions. In particular, the molecular velocities are selected from a Maxwellian distribution based on the sampled cell properties. We find that the creation cells must be sufficiently deep in order to obtain the correct

molecular flux as well as to capture the fastest moving particles at the tail of the distribution. As a rule of thumb, the creation cell must have a minimum depth of:

$$d_{min} = \left[u_n + 2.5\left(\frac{k_b T}{m}\right)^{1/2}\right]\Delta t \tag{3.1}$$

where u_n is the component of the bulk gas velocity in the direction normal to the surface of the creation cell, k_b is the Boltzmann constant, T is the gas temperature, m is the molecular mass and Δt is the timestep size. All the grains in the same creation cell are simply assigned with properties sampled for that particular cell. As a result, the grains are inserted based on *distributions* of grain properties across the vent rather than at discrete values as we do for our simulations that take input from the analytical subsurface model. However, the grain sizes are still inserted at discrete values across the entire vent. As we shall see later in Chapter 6, this is reasonable because all the grains have nearly the same size.

Particles crossing a vacuum boundary do not return but are stored for calculations at a subsequent stage in a multi-stage calculation, which is described later in this section. Particles crossing a periodic boundary have their velocities appropriately rotated and are properly placed back into the domain so as to satisfy the symmetry condition in the azimuthal direction. Particles are reflected off a specular boundary at angles equal to their incidence angles. Particles striking a diffuse boundary equilibrate with the surface and come off with velocities drawn from a half-range Maxwellian distribution at the surface temperature. This is the boundary condition set for the bottom surface of the simulations that take input from the analytical subsurface model. The temperature of the bottom surface is set to 180 K (Spencer *et al.*, 2006). However, almost no particles hit the bottom surface, thus its boundary condition does not affect simulation results.

For the simulations that take input from the computational subsurface model, the bottom surface is set to sublimate based on the following piece-wise temperature distribution, in K:

$$T_{surf} = \begin{cases} 230\ , 1.4\ \text{m} \leq R < 2.8\ \text{m} \\ 230 \times \exp\left(-\dfrac{R-2.8}{L_T}\right), 2.8\ \text{m} \leq R < 13.4\ \text{m} \\ 80, R \geq 13.4\ \text{m} \end{cases} \tag{3.2}$$

where R is the horizontal distance from the centerline of the vent and L_T is the length scale over which the temperature drops, which is chosen to be 10 m (Abramov and Spencer, 2009). Note that 2.8 m is the diameter of the vent used. This temperature distribution is consistent with the observed small-scale hotspots (Porco *et al.*, 2014). The molecular flux from the sublimating surface is given by:

$$\varphi^{(n)} = \frac{p_{vap}(T_{surf})}{\sqrt{2\pi m k_b T_{surf}}} \tag{3.3}$$

where $p_{vap}(T_{surf})$ is the equilibrium vapor pressure of H_2O over ice, which is given by Wexler (1976) (see Section 4.4 for more details). The temperature distribution and the corresponding equilibrium vapor pressure are shown in Figure 3.4b. The equilibrium vapor pressure drops from ~9 Pa at T_{surf} = 230 K to negligible values within only a few vent diameters, thus sublimation is only important in the immediate vicinity of the vent. In addition, the sticking coefficient of the sublimating surface is set to 1, thus *all* the molecules that collide with the surface stick.

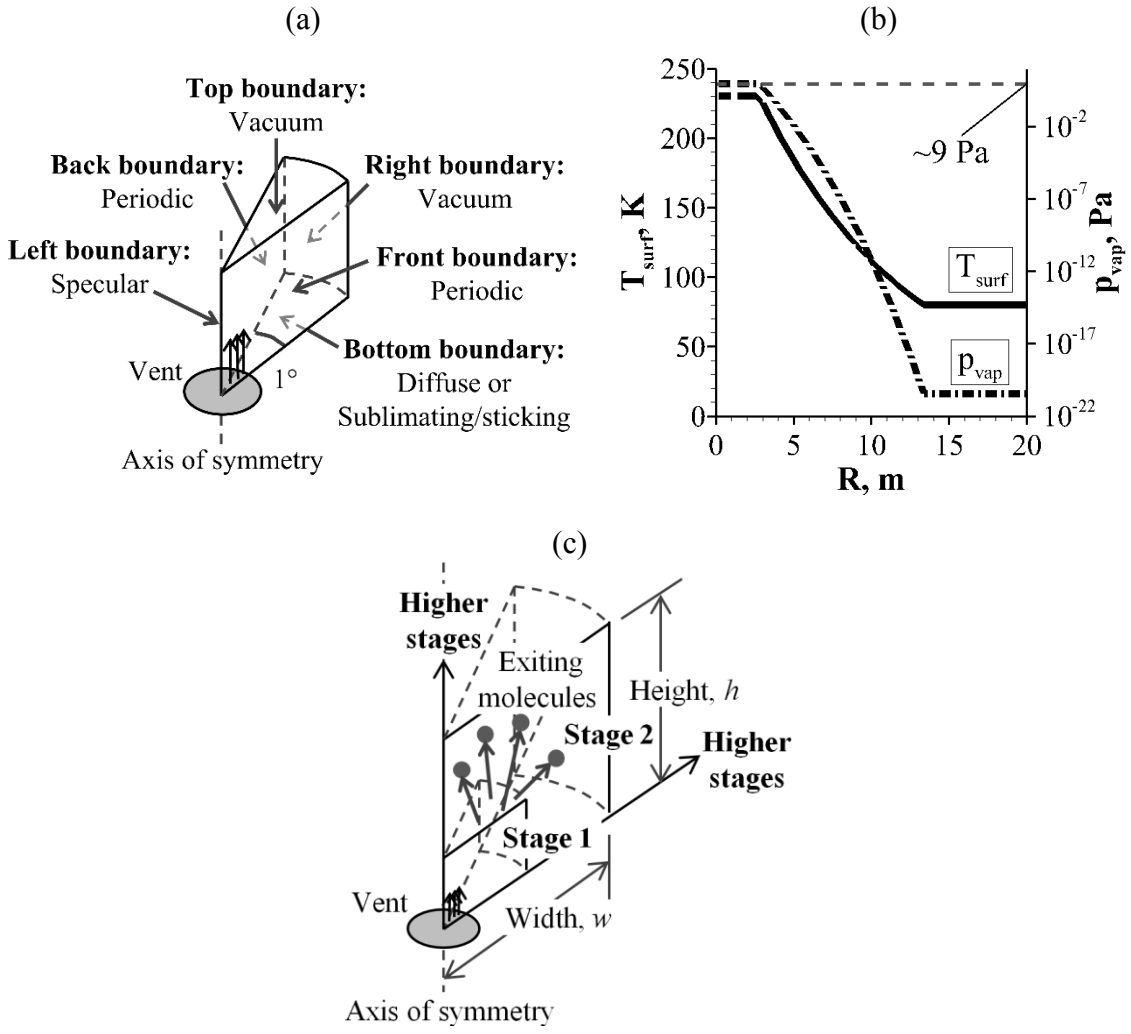

Figure 3.4. (a) Simulation domain with boundary conditions. (b) Distribution of surface temperature, T_{surf}, and the corresponding equilibrium vapor pressure of H_2O over ice, p_{vap}, used for sublimating boundary condition. Note the logarithmic scale used for p_{vap}. (c) Multi-stage calculation. Only the first two stages are shown, but the same procedure is repeated between each stage.

The plume flow passes through multiple flow regimes from the surface vent out to higher altitudes where it becomes free-molecular, thus λ and τ_{coll} vary over several orders of magnitude, as shown in Tables 3.2, 3.3 and 3.4. To resolve such large variations in length and timescales, the DSMC simulations are performed in several sequential stages, with the

finest spatial and temporal resolution nearest the vent and progressively coarser resolution farther out. The details for each stage are given in Tables 3.2, 3.3 and 3.4 and a schematic of the multi-stage calculation is shown in Figure 3.4c. First, a stage is run until steady state, after which the particles exiting the stage through the vacuum boundaries (top and right) are stored. The simulation is stopped after enough particles are collected. Then, the next stage is executed using the stored particles from the previous stage as input. This procedure is repeated until all stages are completed. This approach works because the flow is supersonic—and hence the downstream flow no longer significantly affects the upstream flow. More details on why this approach works can be found in Appendix B. Zhang *et al.* (2003) implemented a similar approach in modeling the volcanic plumes of Io.

The location of the vacuum interface between the first and second stages is important for the simulations that take input from the computational subsurface model because the flow is slightly subsonic at the vent (see Figure 6.3a). The interface must be placed far enough from the vent so that the flow has become sufficiently supersonic that the flow downstream of the interface no longer significantly affects the flow upstream (because the particles crossing a vacuum boundary do not return). Details on how the location of the interface is determined are discussed in Appendix C.

Table 3.2. Parameters for the multi-stage DSMC simulation of the near-field using the Mach-3 vent conditions from the analytical subsurface model.

Stage	**Domain size, w (m) × h (m)**	**Δx (m)**	**λ (m)**	**Δt (μs)**	**τ_{coll} (μs)**
1	2 × 1.024	5×10^{-4}	~1.4×10^{-4}	0.2	~0.4
2	10 × 5.12	4×10^{-3}	~5×10^{-4}	1	~1.5
3	50 × 25.6	0.02	~0.02	5	~140
4	500 × 256	0.2	~0.7	50	~8×10^{3}
5	2500 × 1280	1	~100	250	~1.4×10^{6}
6	10000 × 10240	8	~2×10^{3}	2×10^{3}	~5×10^{7}

Table 3.3. Parameters for the multi-stage DSMC simulation of the near-field using the Mach-5 vent conditions from the analytical subsurface model.

Stage	Domain size, w (m) × h (m)	Δx (m)	λ (m)	Δt (μs)	τ_{coll} (μs)
1	2 × 2	4×10^{-3}	$\sim 1.2 \times 10^{-3}$	1	~5
2	5 × 5	0.01	$\sim 1.2 \times 10^{-3}$	2.5	~5
3	10 × 10	0.02	$\sim 1.2 \times 10^{-3}$	5	~5
4	25 × 25	0.05	$\sim 5 \times 10^{-3}$	10	~30
5	100 × 100	0.2	~0.05	50	~360
6	500 × 500	1	~1	250	$\sim 1.4 \times 10^{4}$
7	2000 × 2000	4	~40	1×10^{3}	$\sim 7 \times 10^{5}$
8	10000 × 10000	20	~600	5×10^{3}	$\sim 1.6 \times 10^{7}$

Table 3.4. Parameters for the multi-stage DSMC simulation of the near-field using the vent conditions from the computational subsurface model.

Stage	Domain size, w (m) × h (m)	Δx (m)	λ (m)	Δt (μs)	τ_{coll} (μs)
1	5 × 5	0.02	$\sim 6.4 \times 10^{-4}$	1	~1.2
2	20 × 20	0.04	$\sim 6 \times 10^{-3}$	10	~15
3	50 × 50	0.1	~0.1	20	~300
4	200 × 200	0.4	~0.5	100	$\sim 3 \times 10^{3}$
5	1000 × 1000	2	~10	400	$\sim 8 \times 10^{4}$
6	5000 × 5000	10	~300	2×10^{3}	$\sim 3 \times 10^{6}$
7	20000 × 20000	40	$\sim 6 \times 10^{3}$	8×10^{3}	$\sim 7 \times 10^{7}$

The mean collision time, τ_{coll}, is given by $\lambda/\bar{c}$ where $\bar{c}$ is the mean molecular thermal speed. However, the root-mean-square (rms) molecular speed, c_{rms}, is used instead of $\bar{c}$ to estimate τ_{coll} because c_{rms} is readily available from the computed gas translational temperature (see definition in Section 4.2). This should be reasonable since c_{rms} and $\bar{c}$ are of the same order of magnitude. In Tables 3.2, 3.3 and 3.4, λ and τ_{coll} are computed at the location of highest density for that stage, which occurs on the axis of symmetry near the interface with the previous stage (or directly above the vent for the innermost stage). Therefore, they are the smallest for that stage. At the top of the domains, λ and τ_{coll} are

larger. For the outermost domains, $\lambda \sim$ O(10 km) and $\tau_{coll} \sim$ O(100 s) at the top of the domain at an altitude of 10 km. As shown in Tables 3.2, 3.3 and 3.4, Δt is smaller than τ_{coll} for all stages, thus the simulations are resolved in time. However, Δx exceeds λ for a few of the earlier stages, thus the simulations are not resolved in space at least within the densest regions of these stages. Consequently, a grid convergence study was performed and it was found that the solution does not change within the core region of the plume flow closest to the axis of symmetry where most of the phenomena being investigated are occurring. More details on this study can be found in Appendix D.

Each stage is run in parallel on multiple processors distributed along the width of the domain. More processors are placed near the axis of symmetry where the plume is denser and more collisional. The run time per stage ranges from one to ten hours. The first few stages (closest to the vent) take the longest times due to higher density and number of collisions. Since the domain is a wedge, the cells near the axis of symmetry are smaller and have fewer computational particles, leading to poor statistics. To mitigate this problem, a cell-based weighting factor for f_{num} is applied along the domain width to increase the number of particles in these cells (Zhang *et al.*, 2003). In this work, a linear weighting scheme is applied. The f_{num} is lowest for the cells nearest the axis of symmetry and increases linearly for the cells farther away from the axis of symmetry. However, the weighting scheme does not extend across the entire width of the domain. Beyond a certain distance from the axis of symmetry, the weighting scheme is deactivated as the cells have become large enough and thus there are enough particles in the cell that the weighting scheme is no longer needed. To obtain reasonable statistics, the instantaneous number of computational particles per cell is maintained > 10 throughout the domain (Bird, 1994) except near the centerline where the cells are smaller and the edges of the flow where the density drops to zero (transition to vacuum).

3.3.3. Two-way Coupling between Gas and Grains

The interaction between the gas and the grains is modeled using the two-way coupling method developed by Burt and Boyd (2004) for polyatomic gases. This method is modified from the one-way coupling method originally developed by Gallis *et al.* (2001) for monatomic gases. The method was implemented by Morris (2012) in the in-house DSMC code.

Only momentum and energy coupling are modeled between the gas and the grains. Mass coupling is not modeled, i.e. there is no evaporation or condensation, so the grains maintain a constant size. Additionally, no new grains are formed via condensation. Ingersoll and Pankine (2010) and Schmidt *et al.* (2008) showed that at most 5–6% of grains by mass fraction can be formed via condensation below the surface. This amount is expected to be even smaller above the surface due to lower gas densities and collision rates.

The main assumption of this method is that the flow around the grains is locally free-molecular, i.e. the grain Knudsen number, $Kn_{grain} \triangleq \lambda / r_{grain} >> 1$, where r_{grain} is the grain radius. For the simulations considered in this work, r_{grain} ~O(1 nm–1 μm) while $\lambda \geq$ 1 mm, thus $Kn_{grain} \geq 10^3$. Moreover, the temperature distribution within the grain is assumed to be uniform because the grains considered are very small (Morris, 2012). Furthermore, the grains are assumed to be spherical and their motions are limited to translation, i.e. grain rotation is neglected.

The gas molecules that collide with the grains could undergo either a specular reflection or a diffuse reflection with full thermal accommodation to the grain temperature. In the latter case, reflected molecules assume a half-range Maxwellian velocity distribution that is oriented in the outward normal direction at each point on the grain surface and has the grain velocity, $\boldsymbol{V}_{grain}$, and temperature, T_{grain}. The amounts of momentum and energy exchanged depend on the fractions of diffuse and specular reflections, denoted as γ and $1-\gamma$

respectively. A specular reflection only allows for the exchange of momentum and associated kinetic energy while a diffuse reflection permits the exchange of momentum as well as both kinetic and internal energy. All reflections are treated as diffuse in this work, i.e. $\gamma = 1$, as the grains are assumed to be rough and jagged on the molecular scale.

At each timestep, the rates of momentum and energy transfer to each grain are first computed from all computational gas molecules in the same cell. For $\gamma = 1$, the rates of momentum and energy transfer from *each* computational gas molecule are given by Equations (3.4) and (3.5) respectively (Burt and Boyd, 2004).

$$\boldsymbol{F_{gas\rightarrow grain}} = \frac{\pi r_{grain}^2 fnum_g}{\forall_{cell}} \left(m|\boldsymbol{u_r}| + \frac{1}{3}\sqrt{2\pi m k_b T_{grain}} \right) \boldsymbol{u_r} \tag{3.4}$$

$$\dot{Q}_{gas\rightarrow grain} = \frac{\pi r_{grain}^2 fnum_g |\boldsymbol{u_r}|}{\forall_{cell}} \left[\frac{1}{2} m|\boldsymbol{u_r}|^2 + e_{rot} - \left(2 + \frac{1}{2} N_{dof} \right) k_b T_{grain} \right] \tag{3.5}$$

where $fnum_g$ is the number of real gas molecules represented by each computational gas molecule, $\forall_{cell}$ is the volume of the DSMC cell, m is the mass of the gas molecule, k_b is the Boltzmann constant, $\boldsymbol{u_r}$ is the relative velocity between the gas molecule and the grain, e_{rot} is rotational energy of the gas molecule, and N_{dof} is the number of rotational degrees of freedom of the gas. However, the grain properties are not updated at this point. Then, gas molecule and grain pairs in the same cell are selected at random with each pair having a certain probability of collision using the standard DSMC procedure (Bird, 1994). For pairs that do result in a collision, only the velocities and internal energies of the gas molecules are updated based on diffuse reflection. Finally, the velocities and temperatures of the grains are updated based on the momentum and energy transfer rates computed at the beginning of the timestep as follows:

$$\frac{d\boldsymbol{V_{grain}}}{dt} = \frac{1}{m_{grain}} \sum_{i=1}^{N_{gas}} \boldsymbol{F_i} \tag{3.6}$$

$$\frac{dT_{grain}}{dt} = \frac{1}{m_{grain} c_{p,grain}} \sum_{i=1}^{N_{gas}} \dot{Q}_i \tag{3.7}$$

where m_{grain} are the grain velocity and mass respectively, N_{gas} is the number of computational gas molecules in the cell, $c_{p,grain}$ is the specific heat of the grain, and $\boldsymbol{F_i}$ and $\dot{Q}_i$ are given by Equations (3.4) and (3.5) respectively. A schematic of how the gas and the grains exchange momentum and energy is shown in Figure 3.5.

Since the transfer of momentum and energy is implemented in a probabilistic manner from the grains to the gas but in a deterministic manner from the gas to the grains, momentum and energy are not *exactly* conserved. However, the momentum and energy transferred from the grains to the gas approach those transferred from the gas to the grains after many collisions. Consequently, this method conserves momentum and energy in an *average* sense and is subject to random walk errors (Bird, 1994). However, these errors are relatively small and decrease with longer sampling periods (Burt and Boyd, 2004). With our steady-state problems, this issue is mitigated by time-averaging the results over longer periods. For more details on this method and its validation, refer to Gallis *et al.* (2001), Burt and Boyd (2004) and Morris (2012). This method has been used to simulate solid-propellant rocket plumes at high altitudes (Burt and Boyd, 2007) and the transport of dust from the lunar surface due to impinging rocket plumes from a lander (Morris, 2012).

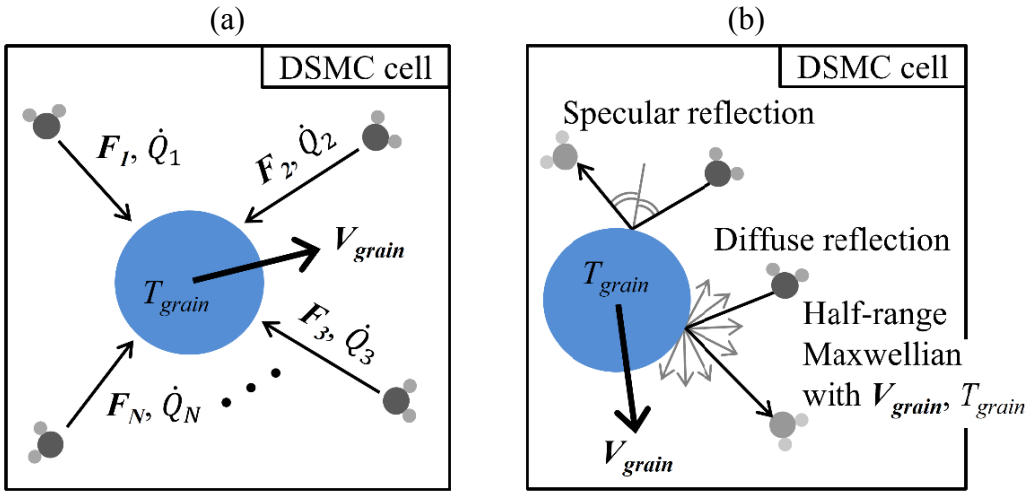

Figure 3.5. How momentum and energy are transferred: (a) from gas to grains and (b) from grains to gas.

3.3.4. Grain Simulations

Like a computational gas molecule, each computational grain represents a large number of real grains. This number, however, may be different from that used for the gas molecules and is usually smaller so that enough grains are present in the simulations for reasonable statistics. In these simulations, the grain-to-gas f_{num} ratios used are ~10^{-12}–10^{-10}. Grain flow properties (e.g. density, temperature and velocity) are obtained by averaging over each cell.

The grains are assumed to be made of ice, with a density, ρ_{grain}, of 920 kg/m^3 and a specific heat, $c_{p,grain}$, of 2.11 kJ/kg-K. In all the cases considered in this work (see Tables 5.1 and 5.2), the grain phase is determined to be dilute and thus collisions between grains are not important (see Appendix A) and the motion of grains is governed by fluid forces instead. Consequently, collisions between grains have been neglected.

Although grains have been neglected in the analytical subsurface model, they are included in the DSMC simulation of the flow above the surface. This calculation is self-

consistent provided that the grain/gas mass ratio is not so high that the subsurface gas flow would have been affected by the grains.

3.4. FREE-MOLECULAR MODEL

The axisymmetric DSMC simulations are performed in a 1° wedge (see Figure 3.4a) for a single jet oriented in the local surface normal (vertical) direction at the north pole. As the expanding flow becomes free-molecular at higher altitudes, the DSMC particles (gas molecules and grains) are sampled and inserted into the planetary-scale free-molecular model at the eight jet sources identified by Spitale and Porco (2007). Their locations and jet orientations are given in Table 3.5.

Table 3.5. Source locations and jet orientations by Spitale and Porco (2007).

Source	Tiger Stripe	Source Location		Jet Orientation	
		Lat.[a] (°)	Lon.[b] (° W)	Azimuth[c] (°)	Zenith[d] (°)
I	Baghdad	−81.5	32.8	(228.7)	9.7
II	Damascus	−79.4	315.5	(93.8)	6.8
III	Damascus	−81.3	292.8	83.2	30.2
IV	Alexandria	−72.9	148.7	(110)	3.7
V	Cairo	−78.6	72.3	(229.98)	6.0
VI	Baghdad	−87.1	231.4	(187.6)	10.2
VII	Baghdad	−74.6	29.8	352.5	20.8
VIII	Cairo	−82.1	115.5	(127.7)	6.8

[a]Latitudes (Lat.) are planetographic. Positive and negative values indicate north and south of the equator (latitude 0°) respectively.
[b]Longitudes (Lon.) increase toward the west. The 0° longitude passes through the sub-Saturnian point.
[c]Azimuths are measured clockwise from the local north. The values in parentheses are poorly determined.
[d]Zeniths are measured with respect to the local surface normal.

Prior to insertion, the positions and velocities of the particles are appropriately transformed through multiple coordinate rotations according to the location and jet orientation of the source at which the particles are inserted. Since the DSMC simulations are performed in a 1° wedge, the azimuthal insertion positions of the particles with respect to the local jet orientation are selected at random to produce a full 360° jet. The velocities of the particles are also converted accordingly. A schematic of the insertion procedure is shown in Figure 3.6. Details on the insertion procedure and its derivations can be found in Appendix E. This procedure of using the particles from a single vertical jet for the different non-vertical jets is acceptable due to the weak gravity of Enceladus ($g_{Enc} \approx 0.113$ m/s^2). Otherwise, the gravity of Enceladus would cause a significant near-field asymmetry in jets not oriented in the surface normal direction and each individual jet would have to be simulated in three dimensions right from the vent up.

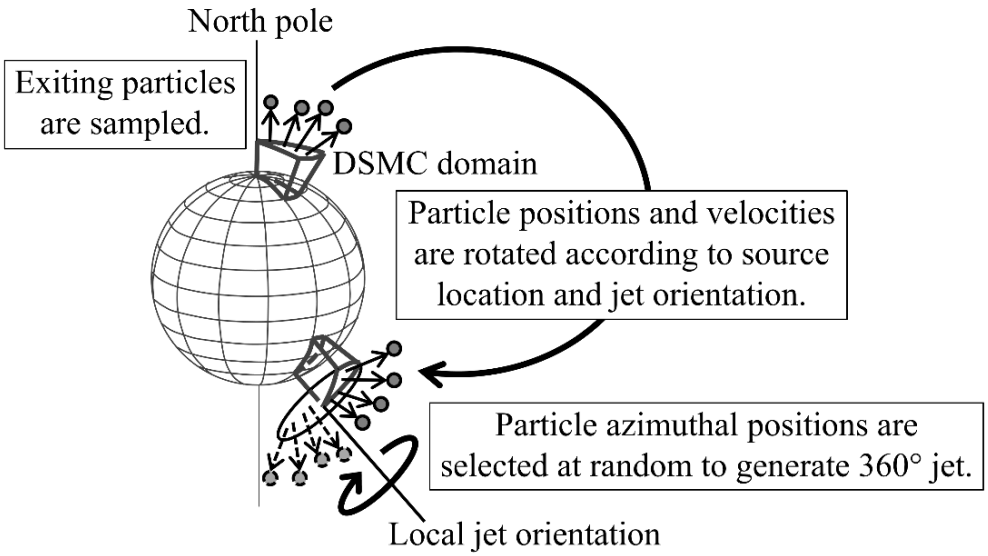

Figure 3.6. Insertion procedure of DSMC particles into free-molecular model.

In the DSMC simulations, the particle motions are computed with respect to the Enceladus-fixed frame and Coriolis and centrifugal forces have been neglected. This is

reasonable as the time it takes the flow to expand from the vents to where it becomes free-molecular is ~O(10 s) while the rotation and orbital periods of Enceladus (which are equal because Enceladus is tidally locked to Saturn) are ~O(10^5 s). Furthermore, only the gravitational field of Enceladus is included since the domains of the DSMC simulations are well within the Hill sphere of Enceladus ($R_H \approx 948$ km). However, these approximations are no longer valid for the free-molecular simulations. Consequently, the particles, upon insertion, move in a ballistic manner under the gravitational fields of Enceladus and Saturn (neglecting the J2 harmonic due to Saturn's oblateness), as well as Coriolis and centrifugal forces due to the rotation of Enceladus and its revolution around Saturn.

The equation of motion for a particle in the non-inertial Enceladus-fixed frame is:

$$\ddot{\boldsymbol{r}} = \boldsymbol{g_{Enc}} + \boldsymbol{g_S} - \boldsymbol{a_{Enc}} - 2(\boldsymbol{\omega_{Enc}} \times \dot{\boldsymbol{r}}) - \boldsymbol{\omega_{Enc}} \times (\boldsymbol{\omega_{Enc}} \times \boldsymbol{r}) \tag{3.8}$$

where $\boldsymbol{r}$ is the particle position vector. The superscript dot notation indicates differentiation with respect to time (i.e. rate of change). The first two terms on the right hand side, $\boldsymbol{g_{Enc}}$ and $\boldsymbol{g_S}$, are the variable gravitational accelerations due to Enceladus and Saturn respectively. This acceleration is proportional to the inverse of the square of the distance of the particle from the center of the parent body, with the proportionality constant, μ, given by the gravitational constant, G, times the mass of the parent body. For the simulations in this work, these values have been used: $\mu_{Enc} = 7.2077 \times 10^9$ m^3/s^2 and $\mu_S = 3.7975 \times 10^{16}$ m^3/s^2. The third term on the right hand side, $\boldsymbol{a_{Enc}}$, is the acceleration experienced by Enceladus as it revolves around Saturn. The last two terms on the right hand side are the Coriolis and centrifugal accelerations respectively, where, $\boldsymbol{\omega_{Enc}}$ is the rotational velocity of Enceladus. Since Enceladus is tidally locked to Saturn, its rotational period is equal to its orbital period of ~1.37 days (~1.184×10^5 s). Consequently, the rotational speed of Enceladus, $|\boldsymbol{\omega_{Enc}}|$, is ~$5.307 \times 10^{-5}$ rad/s (~0.73 rev/day).

The Enceladus-Saturn system used in the free-molecular model is shown in Figure 3.7a, where several approximations have been made:

(i) The orbital plane of Enceladus coincides with the equatorial plane of Saturn.

(ii) Enceladus executes a perfectly circular orbit.

(iii) The axis of rotation of Enceladus is perpendicular to its orbital plane.

These approximations reduce $\boldsymbol{a_{Enc}}$ to a centrifugal acceleration with a magnitude of $|\boldsymbol{\omega_{Enc}}|^2 d_{Enc\text{-}S}$ where $d_{Enc\text{-}S}$ is the distance between the centers of Enceladus and Saturn, which is taken to be 2.3802×10^8 m (~$3.95R_S$) in this work. The important parameters of the Enceladus-Saturn system used in the free-molecular model are summarized in Table 3.6.

Table 3.6. Parameters of Enceladus-Saturn system used in free-molecular model.

System Parameters	**Values**
Enceladus radius, R_{Enc}	2.521×10^5 m
Saturn radius, R_S	6.033×10^7 m
$G \times$ mass of Enceladus, μ_{Enc}	7.2077×10^9 m^3/s^2
G × mass of Saturn, μ_S	3.7975×10^{16} m^3/s^2
Enceladus orbital period	1.184×10^5 s
Enceladus orbital radius, $d_{Enc\text{-}S}$	2.3802×10^8 m

The positions and velocities of the particles are obtained by integrating Equation (3.8) using a 4th-order Runge-Kutta solver. The free-molecular model is capable of simulating the entire E ring, as shown in Figure 3.7b, although many important physical processes associated with the E ring have been ignored. However, the focus here is on modeling the gas and grain distributions in the immediate vicinity of Enceladus rather than on accurately modeling the entire E ring. Therefore, the physical processes already included should be sufficient. As in the DSMC model, each computational particle in the

free-molecular model represents a large number of real particles (~10^{20}–10^{25} for the simulations in this work).

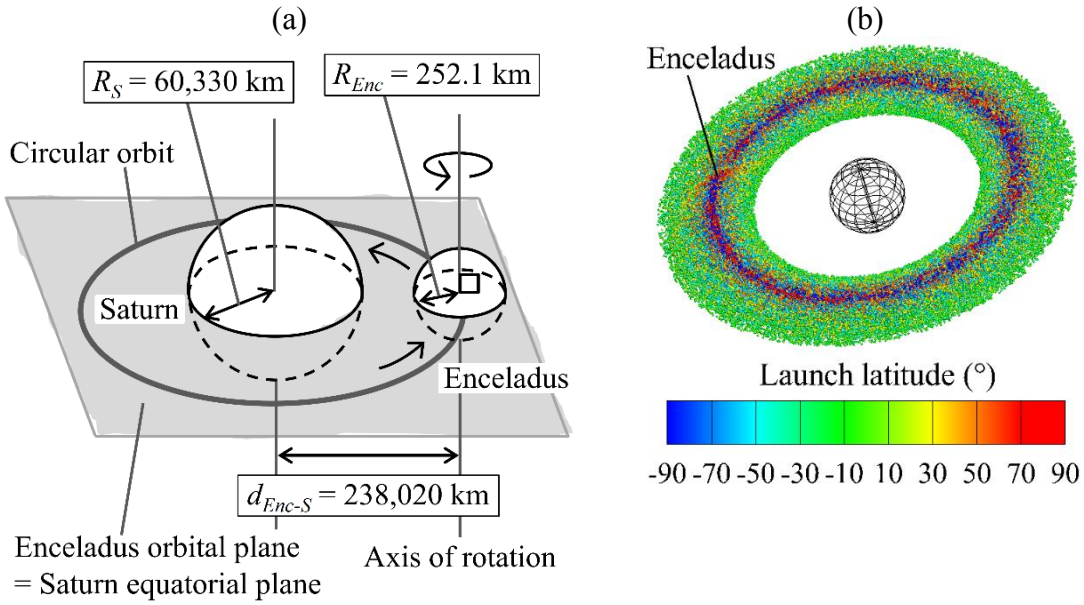

Figure 3.7. (a) Schematic of Enceladus-Saturn system used in the free-molecular model. (b) Simulated E ring formed from particles launched uniformly over the entire surface of Enceladus. Colors indicate the particle launch latitudes.

Various processes have been neglected in the free-molecular model. The chemistry associated with H_2O molecules, such as its ionization and dissociation, has not been modeled. The H_2O molecules are simply removed upon exiting the simulation domain. Grain interactions with the Saturnian magnetospheric plasma, e.g. grain charging and sputtering, have also been neglected. Grain charging is particularly important for the small nanometer-sized grains ($r_{grain} \leq 250$ nm) (Dong and Hill, 2014; Meier *et al.*, 2014; Mitchell *et al.*, 2015), thus the Lorentz force plays an important role in the spatial distributions of these grains. However, for this work, results are compared with CDA data for micron-sized grains ($r_{grain} \geq 1.6$ μm) for which the effects of grain charging should be minimal.

Moreover, solar radiation pressure and drag on the grains due to collisions with neutral and plasma particles have been ignored. These processes are necessary to properly model the E ring (Hedman *et al.*, 2012; Juhasz and Horanyi, 2002; Kempf *et al.*, 2010) but not so to model the grain distribution near Enceladus. Collisions between the grains are negligible due to the very low density of the E ring as inferred from its small optical depth (Juhasz *et al.*, 2007; Juhasz and Horanyi, 2002; Showalter *et al.*, 1991).

3.5. CONSTRAINING SIMULATION RESULTS USING CASSINI *IN-SITU* DATA

Once the entire plume is simulated from the surface vents out into the far-field (see Figure 3.1), Cassini *in-situ* data are used to constrain the results in order to infer certain properties and characteristics of the plume, e.g. gas and grain production rates and temporal variability, as well as to deduce the source conditions. In this section, the Cassini *in-situ* data used for constraint and how the simulation results are converted into the appropriate format are presented. Details on how the Cassini *in-situ* data are used to constrain the converted simulation results are described in Chapter 7.

3.5.1. *In-situ* Data Used for Constraint

Once the simulation reaches a steady state within the region of interest, we fit the simulation results to: (1) the INMS H_2O density distributions along the E2, E3, E5 and E7 trajectories and (2) the CDA grain density distribution for $r_{grain} \geq 1.6$ μm along the E2 trajectory. The data sets are shown in Figures 3.8–3.9. Only the error bars for the E3, E5 and E7 INMS data sets are provided and have been shown separately below each data set for clarity (see Figures 3.8c–d and Figure 3.9). Note the different x-axis on the E2 INMS data set: r_{flyby}/R_{Enc}, where r_{flyby} is the altitude of the spacecraft from the surface of Enceladus. The x-axis on the other data sets is the time from closest approach (CA). The sources of the data sets are provided in the captions of Figures 3.8–3.9.

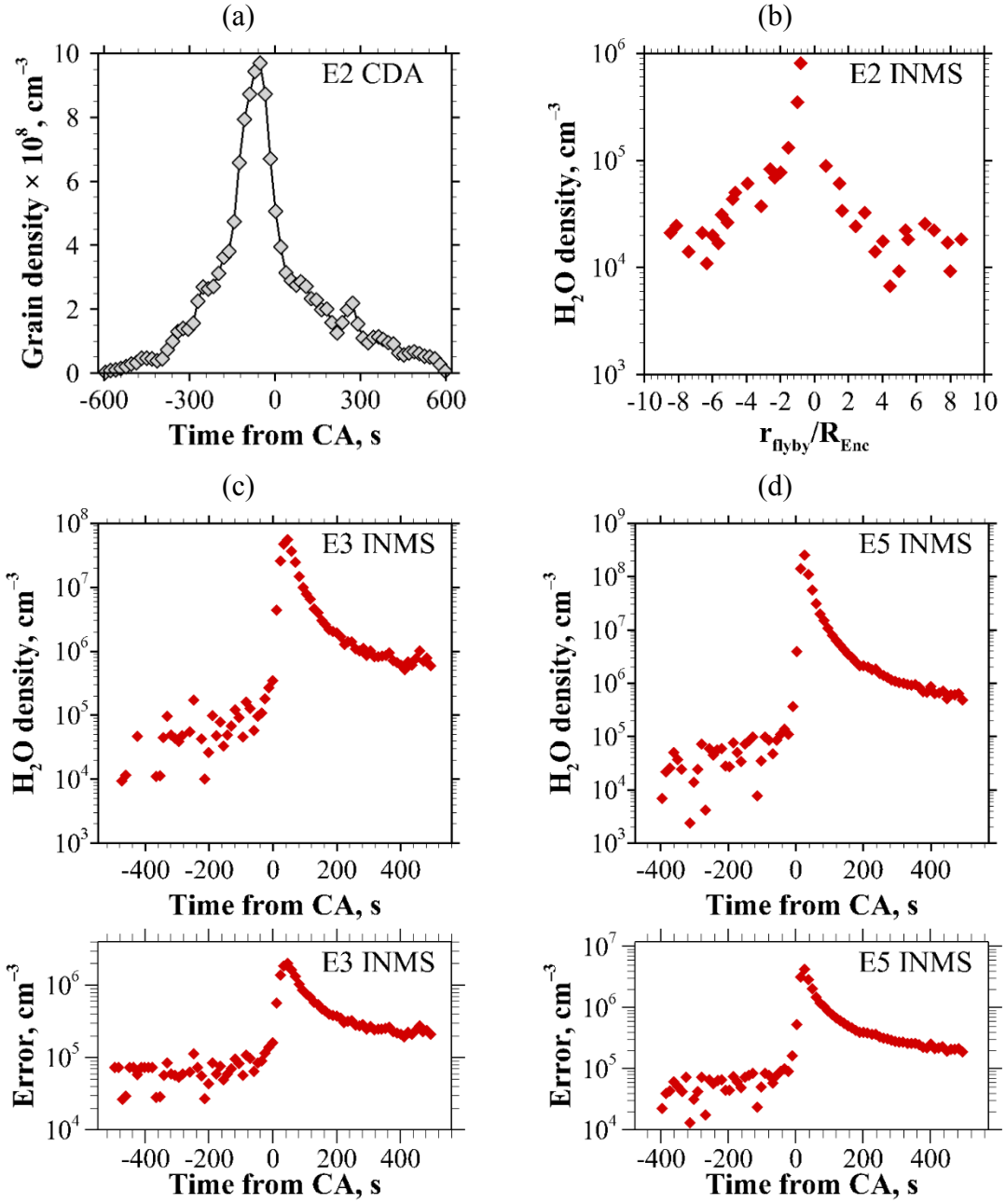

Figure 3.8. (a) E2 CDA grain density distribution for $r_{grain} \geq 1.6$ μm (Schmidt, J., personal communication, 2013). (b) E2 INMS H_2O density distribution (Smith *et al.*, 2010). (c) E3 and (d) E5 INMS H_2O density distributions and their error bars (Dong, Y., Teolis, B., personal communication, 2015). Note the linear scale on the y-axis in (a) and the logarithmic scales in (b)–(d).

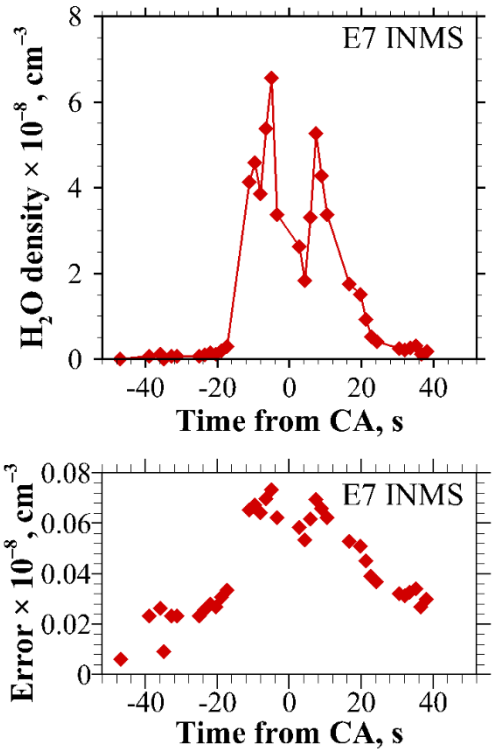

Figure 3.9 E7 INMS H_2O density distribution and its error bars (Dong, Y., Teolis, B., personal communication, 2015). Note the linear scale on the y-axis.

3.5.2. Sampling Density along Trajectory

To compute the density distribution along a trajectory, the simulation domain is first decomposed into cells to obtain a 3-D density field. Then, the density distribution along the trajectory is acquired by sampling the density of particles in the cells intersected by the trajectory. The Cassini trajectories are acquired from the NASA Navigation and Ancillary Information Facility (NAIF). Statistical noise in the computed densities is reduced by time-averaging and low-pass filtering.

The integration timestep used in all our free-molecular simulations is 1 s. With particle speeds not exceeding 1000 m/s, this should be adequate to resolve the particle

trajectories, especially when they are near Enceladus. For the E2, E3 and E5 trajectories, the sampling cell size used in each direction is ~31.5 km (~R_{Enc}/8). For the E7 trajectory where the sampling is done closer to Enceladus, a finer cell size is used, ~3.9 km (~R_{Enc}/64), in each direction. We vary the cell sizes by a factor of two to examine how the H_2O density distributions along the E5 and E7 trajectories for several jets would change. As shown in Figures 3.10a–b, they only change slightly, thus the cell sizes used should be adequate.

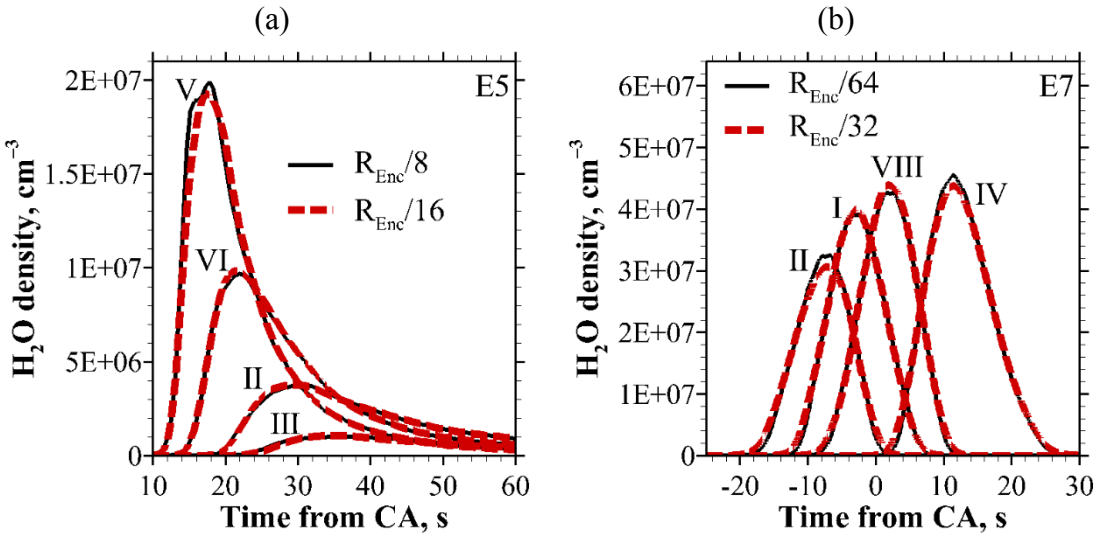

Figure 3.10. Comparisons of H_2O density distributions along two trajectories, (a) E5 and (b) E7, for several jets between two different sampling cell sizes. The x-axis is the time from closest approach (CA) (when the altitude of the spacecraft is minimum). Negative and positive values indicate before and after CA respectively. The jets have been set to equal strengths.

The gas molecules are removed once they exit the simulation domain, which is on the order of several Enceladus Hill Sphere radii, $R_H \approx 948$ km (~3.76R_{Enc}), in size. This is adequate as the gas molecules are quickly ionized and transported away by Saturn's magnetic field. For the grains, however, this is not enough. Ingersoll and Ewald (2011) discovered that as the grains cross the Saturn equatorial plane half an orbit after they are

ejected, they may experience a close encounter with Enceladus. If they do not collide with Enceladus, they travel north of the equatorial plane and form a cloud around Enceladus. From numerical simulations, Kempf *et al.* (2010) also determined that the most critical time for a grain is during its first ring-plane crossing after ejection, which determines whether it collides with Enceladus or survives the close encounter and goes on to populate the E ring. Therefore, the grains should be tracked for at least half an orbit after ejection.

In our simulations, we track the grains for more than 8 years (> 2000 orbital periods), which is estimated to be the average lifetime of an E-ring grain (Ingersoll and Ewald, 2011). Grains are removed either when they reach eight years old or when they collide with Enceladus. Therefore, our simulations should account for the jets, the cloud around Enceladus, and the E ring. Since the grains are tracked over their lifetimes, the entire E ring is simulated. A simple study on the simulated E-ring density profiles near Enceladus is presented in Appendix F. However, our simulations have neglected various processes (see Section 3.4), which may be important to the formation, evolution and dynamics of the E ring, thus our results may not capture all the phenomena observed in the actual E ring itself.

Chapter 4.

Gas-Only Flow Expansion into Vacuum[3]

As the flow expands from the vents into vacuum, various physical processes occur, e.g. the flow regime transition from continuum to free-molecular, the "freezing" of molecular internal modes and the energy transfer from the molecular thermal and internal modes into the directed mean motion of the gas. In this chapter, some of these physical processes are investigated for a *gas-only* flow expansion process in the absence of grains. The vent conditions are obtained from the analytical subsurface model (see Section 3.2.1). Only the Mach-5 vent conditions are considered here unless noted otherwise. However, the results should be qualitatively similar for the Mach-3 vent conditions. The effects of grains on the expansion process will be investigated later in Chapter 5.

4.1. MULTIPLE FLOW REGIMES

The local Knudsen number of the flow, Kn, (as defined in Section 3.3.1, where L is taken to be based on the gas density) is used to characterize the flow regimes. Figures 4.1a–b show that Kn varies by several orders of magnitude during expansion, from $\sim 10^{-3}$ (nearly continuum, highly collisional) near the vent to ≥ 10 (free-molecular) at an altitude of ~10 km for $D_{vent} = 2.8$ m. As we shall see later, the altitude at which the flow becomes free-molecular, Z_{FM}, depends on the vent size for a given set of vent conditions.

[3]Parts of this chapter are published in Yeoh *et al.* (2015). All of the computations in this work were done by the author of this dissertation. The other authors provided useful ideas, suggestions and feedback, and also proofread and corrected the manuscript of the paper.

During expansion, the gas number density, n, drops rapidly across expansion waves emanating from the edges of the vent, as shown in Figure 4.1c. An expansion wave is a Mach wave at the local Mach number, Ma, through which the flow expands (Anderson, 2003). Therefore, the first expansion wave is a Mach wave at the vent Mach number, Ma_{vent}. As shown in Figure 4.3a, n remains at the vent value, n_{vent} (~1.2×10^{21} molecules/m^3) along the centerline until the first expansion wave crosses the centerline at $Z \approx 2.25 D_{vent}$ (~6.3 m) and drops above this point before following an inverse-square law farther away, i.e. $n \propto (Z/D_{vent})^{-2}$ for $Z/D_{vent} >> 1$, where Z is the altitude above the vent. At $Z \approx 8.9 D_{vent}$ (25 m), n has dropped by nearly a factor of 40. Along the lateral edges of the flow, n drops smoothly to zero (vacuum) across the expansion waves. As a result, regions of free-molecular flow ($Kn >> 1$) occur along the edges of the flow at all altitudes, as shown in Figures 4.1a–b.

To determine how Z_{FM} varies with D_{vent} for a given set of vent conditions, we consider how Kn ($\triangleq \lambda|\nabla\rho|/\rho = \lambda|\nabla n|/n$) varies with Z along the *centerline* ($R = 0$). Since $n \propto (Z/D_{vent})^{-2}$ along the centerline for $Z/D_{vent} >> 1$, $\lambda \propto 1/n \propto (Z/D_{vent})^2$ and $|\nabla n| = |\partial n/\partial Z| \propto (1/D_{vent})(Z/D_{vent})^{-3}$ along the centerline ($\partial n/\partial R = 0$ at $R = 0$ by symmetry). Putting these together, we obtain $Kn \propto Z/D_{vent}^2$ and thus $Z_{FM} \propto D_{vent}^2 \propto \dot{m}_{vent}$ for a given set of vent conditions. Consequently, for a given set of vent conditions, a larger vent leads to the flow becoming free-molecular at a higher altitude. For the scaling to be valid, however, the physics of the system must not change significantly with size. The gravity of Enceladus is weak, thus its effects on the flow are negligible. Moreover, the Knudsen number at the vent, $Kn_{vent} \triangleq \lambda_{vent}/D_{vent}$ where λ_{vent} is the mean free path at the vent, must remain small, $\leq 10^{-3}$, so that the flow at the vent remains continuum. This should not be an issue when scaling to a larger vent while maintaining the vent conditions (λ_{vent} remains the same while D_{vent} increases). However, as the vent size increases, Z_{FM} may become large enough that

chemistry (e.g. ionization, dissociation and photolysis) and plasma effects become important and the scaling may no longer be valid.

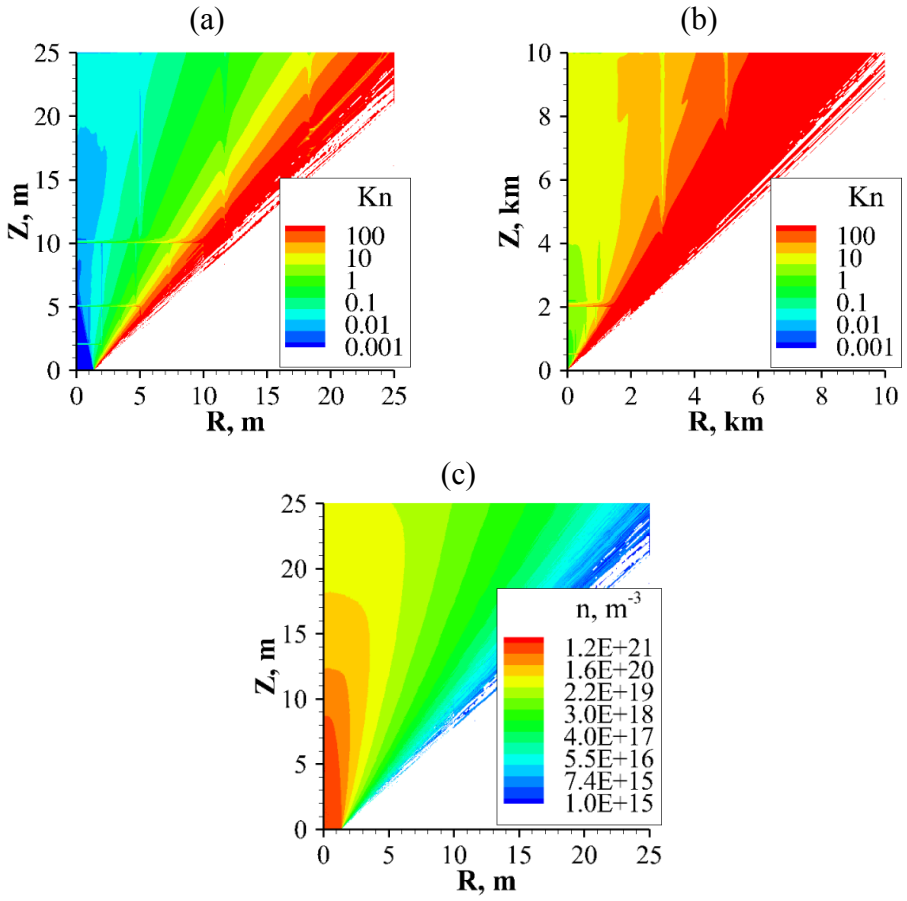

Figure 4.1. Contours of local Knudsen number, *Kn*, from (a) vent to 25 m and (b) vent to 10 km. Note the shift in axis scales from (a) to (b). (c) Contours of gas number density, *n*, from vent to 25 m. All contours are for $Ma_{vent} = 5$. In (a) and (b), the horizontal "lines" (e.g. at $Z = 5$ m, 10 m and 2 km) are not real but are numerical artifacts from computing $|\nabla\rho|$ across cells of different sizes along stage boundaries while the vertical "lines" are numerical artifacts from smoothing ρ across processor boundaries to reduce statistical noise when computing $|\nabla\rho|$.

4.2. ENERGY TRANSFER BETWEEN DIFFERENT MOLECULAR MODES

As the flow expands, the random kinetic (thermal) energy and the rotational energy of the gas molecules are converted into the directed mean kinetic energy of the flow through collisions. There is negligible vibrational excitation at these low temperatures, ≤ 50 K. Consequently, the gas translational temperature, T_{tr}, and rotational temperature, T_{rot} (measures of the molecular thermal and rotational energy respectively) drop as the bulk gas speed increases, as shown in Figures 4.2a–e. The gas translational and rotational temperatures are defined as: $T_{tr} \triangleq \left(m\overline{c'^2}\right)/(3k_b)$ and $T_{rot} \triangleq (2\overline{e_{rot}})/\left(k_b N_{dof}\right)$, where m is the mass of an H_2O molecule, c' is the thermal or peculiar molecular speed, k_b is the Boltzmann constant, e_{rot} is the molecular rotational energy and N_{dof} is the number of rotational degrees of freedom (3 for H_2O molecules). The superscript bar indicates averaging over the gas molecules.

This conversion of energy is also evident in Figure 4.2f showing contours of *Ma*, which is defined as the ratio of the bulk gas speed to the local speed of sound and thus provides a measure of the directed mean kinetic energy of the gas to the random thermal energy of the gas molecules. As the flow expands, *Ma* increases rapidly from ~5 to ~10 within ~8.9D_{vent} (25 m) of the vent. This is mainly due to the rapid drop in T_{tr} from 53 K at the vent down to ~15 K at $Z = 8.9D_{vent}$ (see Figure 4.2a) rather than the increase in bulk gas speed, which only goes from ~900 m/s at the vent to ~980 m/s at $Z = 8.9D_{vent}$ (see Figure 4.2e).

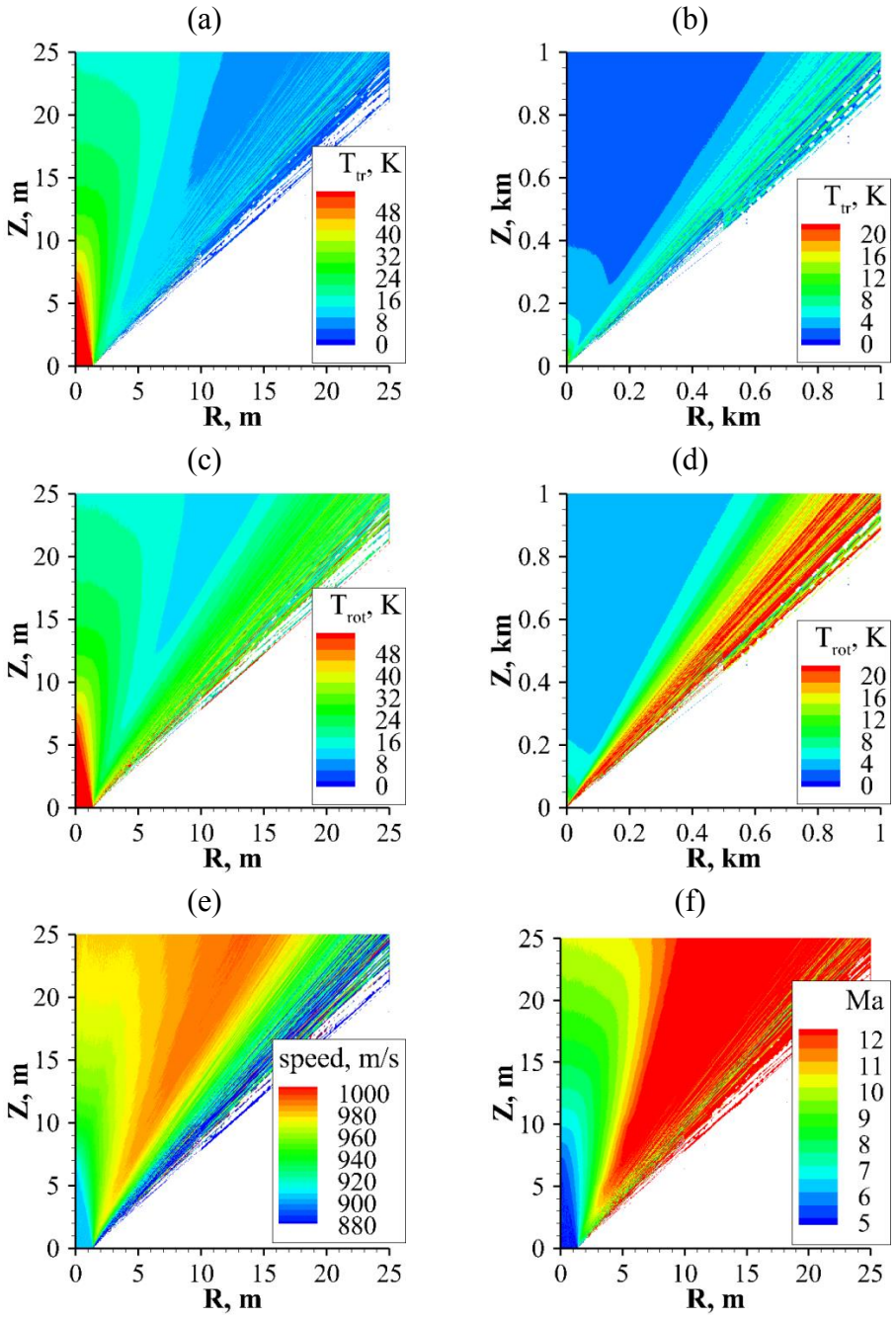

Figure 4.2. Contours of gas translational temperature, T_{tr}, from: (a) vent to 25 m and (b) vent to 1 km. Contours of gas rotational temperature, T_{rot}, from: (c) vent to 25 m and (d) vent to 1 km. Note the shifts in axis and temperature scales from (a) to (b) and from (c) to (d). (e) Contours of gas speed from vent to 25 m. (f) Contours of Mach number, Ma, from vent to 25 m. All contours are for $Ma_{vent} = 5$.

Rotational cooling by microwave emission is too slow to be significant near the vent. The timescales associated with pure rotational emission are much longer (1–100 s) (Crovisier, 1984) than the mean time between collisions (~10 μs) near the vent. Consequently, given enough collisions to convert all the molecular thermal and rotational energy into the directed mean kinetic energy of the gas, the gas reaches the ultimate speed of adiabatic expansion, $V_{ult} \triangleq [(2\gamma R_{H2O} T_0)/(\gamma - 1)]^{1/2} \approx 1005$ m/s, where γ is the specific heat ratio (4/3 when only the translational and rotational modes are excited and vibrational modes are frozen), R_{H2O} is the gas constant for H_2O (~462 J/kg-K) and T_0 is the stagnation temperature at the source (273.16 K for the triple point of H_2O). For supersonic vent conditions, the rotational mode freezes above a certain altitude but the gas speed is very nearly V_{ult} since the amount of energy trapped in the rotational mode is small. Most of the gas escapes into space since V_{ult} is significantly greater than the escape speed of Enceladus, $V_{esc} \triangleq (2GM_{\mathrm{Enc}}/R_{\mathrm{Enc}})^{1/2} \approx 240$ m/s, where G is the universal gravitational constant, and M_{Enc} and R_{Enc} are the mass and radius of Enceladus respectively.

Gas speeds of 1.6–2.6 km/s have been inferred from UVIS observations (Hansen *et al.*, 2011). Such speeds far exceed V_{ult} for a source temperature of 273.16 K, as calculated above. This ultimate speed is the maximum speed that the gas could possibly achieve under adiabatic conditions. One possibility is that the source temperature is higher than 273.16 K. Ultimate speeds of 1.6–2.6 km/s imply a source temperature in excess of 700 K. Matson *et al.* (2007) pointed out that the detection of certain organic compounds, e.g. propane and acetylene (Waite *et al.*, 2006, 2009), might indicate catalytic reactions occurring at subsurface temperatures of 500–800 K. However, this would mean that all three phases of water do not exist near equilibrium in the reservoir. We cannot imagine such a scenario happening, though we cannot rule it out.

Alternatively, the presence of a lighter gas, e.g. H_2, in a gas mixture with water vapor, could raise V_{ult}. For example, a H_2 mass fraction of ~23%, possibly from clathrate decomposition (Lunine and Stevenson, 1985; Kieffer *et al.*, 2006) or hydrothermal activity (Hsu *et al.*, 2015; Matson *et al.*, 2012; Monnin *et al.*, 2014), could raise V_{ult} to ~1.6 km/s for a source temperature of 273.16 K (see Appendix G). Another possibility is that subsurface heat transfer from the channel walls to the gas could increase the energy of the gas, allowing it to achieve greater speeds. In modeling the subsurface flow, Ingersoll and Pankine (2010) found that heat can go from the channel walls to the gas when the heat source is distributed along the channel walls. Other possibilities exist. Therefore, the question of how the gas could achieve such high speeds remains open.

4.3. NON-EQUILIBRIUM EFFECTS

The degree of non-equilibrium in the flow is shown in the contours of the mode temperatures. Equilibrium occurs when the temperatures of the different molecular energy modes are equal (Vincenti and Kruger, 1967). This is achieved through collisions, which allows energy to be exchanged between the different modes. Figures 4.2a–b show T_{tr} in the immediate vicinity of the vent (a) and up to an altitude of 1 km (~$360D_{vent}$) (b). Figures 4.2c–d show T_{rot} in the same spatial regions and on the same temperature scale. Comparing Figures 4.2a and 4.2c, we see that the flow is in equilibrium ($T_{tr} \approx T_{rot}$) close to the vent in the core region along the centerline. At higher altitudes, T_{tr} and T_{rot} start to deviate, as shown in Figures 4.2b and 4.2d. Along the lateral edges, T_{tr} and T_{rot} are different at all altitudes. These trends reflect the contours of Kn shown in Figures 4.1a–b (a larger Kn indicates a greater degree of non-equilibrium).

Figure 4.3b shows that both T_{tr} and T_{rot} remain at the vent value, $T_{vent} = 53$ K, along the centerline until the first expansion wave crosses the centerline at $Z \approx 2.25D_{vent}$ (~6.3 m)

and follow an inverse-power law above that, i.e. T_{tr}, $T_{rot} \propto (Z/D_{vent})^{-0.8}$, before deviating at $Z \approx 20D_{vent}$ (~56 m) and approaching different asymptotic values: $T_{tr} \approx 0.015T_{vent}$ and $T_{rot} \approx 0.055T_{vent}$. An energy mode is said to have "frozen" when its temperature reaches an asymptotic value. The energy remains trapped in that mode because there are not enough collisions for energy exchange to occur (in the absence of other energy transfer mechanisms, e.g. radiation). The rotational mode freezes first because it requires more collisions to equilibrate (5–10 for rotation but only 1–2 for translation). Despite the lower collision rates at higher altitudes, the translational mode can still equilibrate, i.e. the molecular velocity distributions are close to a locally shifted Maxwellian, whose width is characterized by T_{tr}, which continues to drop until the gas flow goes free-molecular. However, the rotational mode no longer equilibrates and freezes at the asymptotic value.

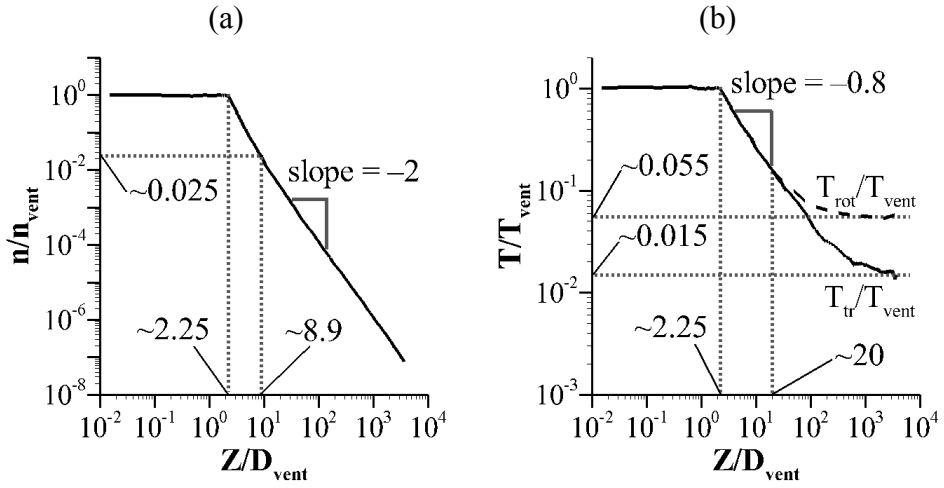

Figure 4.3. Centerline distributions of: (a) gas number density, n, (b) gas translational temperature, T_{tr}, and rotational temperature, T_{rot}, normalized by vent values. These are for $Ma_{vent} = 5$. Note the logarithmic axes.

4.4. SUPERSATURATION LEVELS AND COLLISION RATES ABOVE VENT

Figures 4.4a–b show that the supersaturation ratio, p/p_{vap}, is extremely high near the vent for both Ma_{vent} = 3 and 5, where p and p_{vap} are the local gas pressure and equilibrium vapor pressure over ice respectively. Thus conditions would appear to be very favorable for condensation. At the vent, the supersaturation ratio is $\sim 10^{13}$ for $Ma_{vent} = 3$ and $\sim 10^{40}$ for Ma_{vent} = 5 respectively. The pressure, p, is calculated as nk_bT_{tr} while p_{vap} is obtained from a relationship derived by Wexler (1976), which is described later in this section.

The collision rate must also be sufficiently high for condensation and grain growth to actually occur. Figures 4.4c–d shows that the collision rate per unit volume, ζ, drops by several orders of magnitude from the vent value, ζ_{vent}, within only $\sim 8.9 D_{vent}$ of the vent for both $Ma_{vent} = 3$ and 5 ($\zeta_{vent} \approx 1.3 \times 10^{28}$ s^{-1} m^{-3} for $Ma_{vent} = 3$ and $\zeta_{vent} \approx 1.2 \times 10^{26}$ s^{-1} m^{-3} for $Ma_{vent} = 5$). Consequently, any of the condensation and grain growth must occur within several D_{vent} of the vent. We calculate ζ using Equation 6.15b from Vincenti and Kruger (1967) for like molecules. Note that in calculating both p and ζ, equilibrium conditions have been assumed. This is reasonable because the calculations are performed for the region near the vent where the flow is nearly in equilibrium (see Section 4.3).

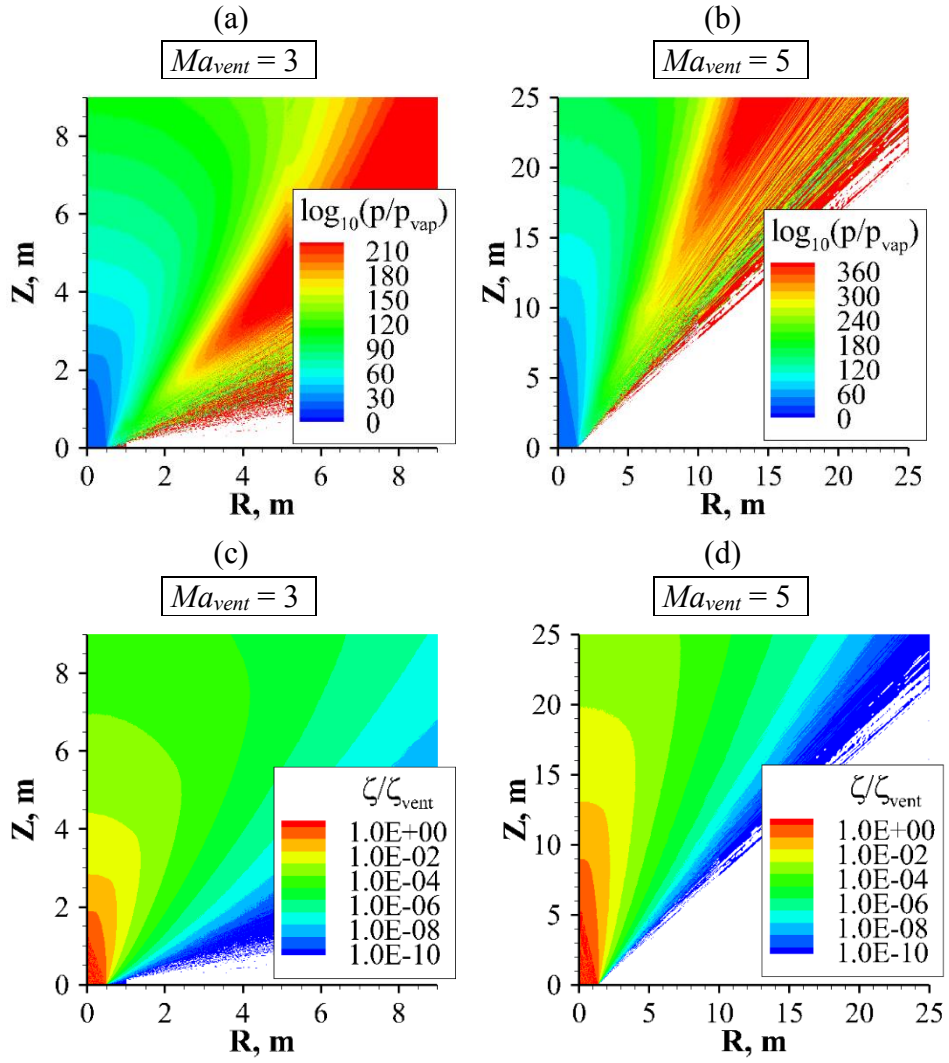

Figure 4.4. Contours of $\log_{10}(p/p_{vap})$ from vent to $8.9D_{vent}$ for: (a) $Ma_{vent} = 3$ and (b) $Ma_{vent} = 5$. Contours of collision rate per unit volume, ζ, normalized by vent value, ζ_{vent}, from vent to $8.9D_{vent}$ for: (c) $Ma_{vent} = 3$ and (d) $Ma_{vent} = 5$. Note the different color bars in (a) and (b). Also note the different axis scales between $Ma_{vent} = 3$ and $Ma_{vent} = 5$ due to the different D_{vent} used: 1 m for $Ma_{vent} = 3$ and 2.8 m for $Ma_{vent} = 5$ (see Table 3.1).

Wexler (1976) derived p_{vap} as a function of temperature, T, for the intended temperature range from ~173 K (−100 °C) to 273.16 K (triple point). This relationship is given by Equation (4.1). However, it has been extrapolated down to $T \leq 110$ K for these calculations because no experimental data for p_{vap} are available for these low temperatures. Since the derivation is based on thermodynamics rather than simply a curve fit, this should be reasonable. Plots of p_{vap} vs. $1/T$ over the intended range and a wider range going down to 20 K are shown in Figures 4.5a–b respectively.

$$\ln\left(\frac{p_{vap}}{p_t}\right) = K_0\left(\frac{1}{T} - \frac{1}{T_t}\right) + K_2(T - T_t) + K_3(T^2 - T_t^2) + K_4(T^3 - T_t^3) + K_5\ln\left(\frac{T}{T_t}\right) \tag{4.1}$$

where $K_0 = -5865.37$ K, $K_2 = 1.375 \times 10^{-2}\,\mathrm{K}^{-1}$, $K_3 = -3.403 \times 10^{-5}\,\mathrm{K}^{-2}$, $K_4 = 2.697 \times 10^{-8}\,\mathrm{K}^{-3}$, $K_5 = 0.692$, $p_t = 611.657$ Pa (pressure at triple point) and $T_t = 273.16$ K (temperature at triple point).

While p_{vap} has been derived for hexagonal ice (the most stable form of ice), it is possible that metastable forms of ice may have been produced at such low temperatures. For $T < 200$ K, deposition from the vapor phase produces cubic ice first, which transforms into hexagonal ice over minutes to days (Hobbs, 1974). Cubic ice is estimated to have p_{vap} ~3–11% higher than hexagonal ice at $T = 200$ K (Murphy and Koop, 2005). Consequently, the supersaturation levels calculated using Equation (4.1) may be slightly higher than the actual values, though the supersaturation levels should remain very high.

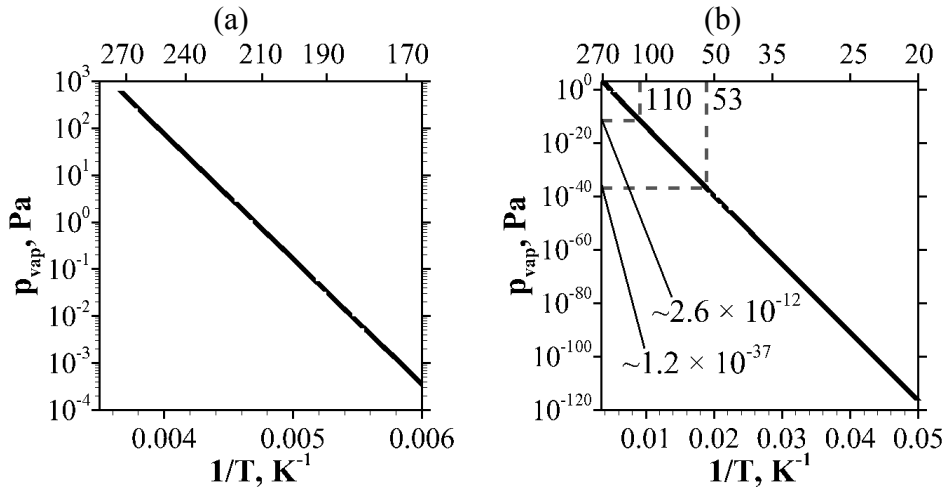

Figure 4.5. Equilibrium vapor pressure over ice, p_{vap}, as a function of temperature, T, based on the relationship derived by Wexler (1976) over (a) the range of validity and (b) a larger range (extrapolated down to 20 K). Note the logarithmic scale on the y-axis.

4.5. CONDENSATION GRAIN GROWTH

Since the expanding flow is highly supersaturated just above the vents, we consider heterogeneous nucleation and analytically estimate the *maximum* possible increment in grain radius due to condensation above the vents, $\Delta r_{grain} = r_f - r_0$, where r_f and r_0 are the final and initial grain radii respectively. This maximum growth is derived along the *centerline* where the gas density remains high until the first expansion wave emanating from the edges of the vent crosses the centerline. Calculations are made based on the gas properties obtained from the gas-only DSMC simulations.

4.5.1. Derivation

Consider a grain starting at the center of the vent with initial radius r_0. As it travels up with the gas, the surrounding gas phase condenses on it due to the high supersaturation levels. Here, we derive an equation to estimate Δr_{grain}. The assumptions made are:

1) All molecules colliding with the grain stick (sticking coefficient equals to 1).

2) Molecules do not escape the grain (no evaporation).
3) Gas is in equilibrium (Maxwellian velocity distribution).
4) Grain moves with gas (i.e., $u_{grain} = u_{gas}$).
5) Grain is spherical.
6) Condensation does not affect the gas (no depletion of gas phase or latent heat released).

Assumption 3 is reasonable as most of the grain growth occurs within several D_{vent} of the vent where conditions are near equilibrium. Assumption 4 results in minimal error if the grain starts off small ($r_0 \leq 10$ nm) and is therefore well entrained with the gas flow. Once the grain has grown large enough and a significant velocity difference develops, the grain is already at an altitude where the growth rate has become negligible. Assumption 6 is made because the gas properties used in the calculations are obtained from simulations that do not account for condensation. This assumption is reasonable as long as not too much condensation is occurring, thus the amount of gas phase depleted and latent heat released is negligible and the gas phase is not affected significantly.

First, we normalize the altitude Z with D_{vent} and recast the centerline gas properties, $n_{gas}(Z)$, $T_{gas}(Z)$ and $u_{gas}(Z)$, in terms of the normalized altitude Z^*:

$$Z^* = Z/D_{vent}$$

$$n_{gas}(Z^*) = n_{gas}(Z)$$

$$T_{gas}(Z^*) = T_{gas}(Z)$$

$$u_{gas}(Z^*) = u_{gas}(Z)$$

where n_{gas}, T_{gas} and u_{gas} are the number density, temperature and the speed of the gas respectively.

The rate of grain mass accumulation is given by the product of the molecular number flux to the grain surface, the mass of a molecule, and the grain surface area:

$$\frac{dm_{grain}}{dt} = \frac{d}{dt}\left(\frac{4}{3}\pi r_{grain}^3 \rho_{ice}\right) = \frac{n_{gas}(Z)\bar{c}(Z)}{4} m\, 4\pi r_{grain}^2$$

$$\frac{dr_{grain}}{dt} = \frac{n_{gas}(Z)\bar{c}(Z)}{4\rho_{ice}} m = \frac{n_{gas}(Z^*)\bar{c}(Z^*)}{4\rho_{ice}} m \tag{4.2}$$

where m_{grain} and r_{grain} are the mass and radius of the grain respectively, ρ_{ice} is the density of ice (~920 kg/m^3), m is the mass of an H_2O molecule, and $\bar{c}(Z)$is the mean molecular speed given by:

$$\bar{c}(Z) = \sqrt{\frac{8k_b T_{gas}(Z)}{\pi m}} = \bar{c}(Z^*) = \sqrt{\frac{8k_b T_{gas}(Z^*)}{\pi m}}$$

where k_b is the Boltzmann constant.

By Assumption 4, the equation of motion of the grain is given by:

$$\frac{dZ}{dt} = u_{grain}(Z) = u_{gas}(Z)$$

$$D_{vent}\frac{dZ^*}{dt} = u_{gas}(Z^*)$$

$$dt = D_{vent}\frac{dZ^*}{u_{gas}(Z^*)} \tag{4.3}$$

Substituting Equation (4.3) into Equation (4.2) and integrating from the vent into the far-field, we get:

$$\frac{u_{gas}(Z^*)}{D_{vent}}\frac{dr_{grain}}{dZ^*} = \frac{n_{gas}(Z^*)\bar{c}(Z^*)}{4\rho_{ice}} m$$

$$\frac{dr_{grain}}{D_{vent}} = \frac{m}{4\rho_{ice}}\frac{n_{gas}(Z^*)\bar{c}(Z^*)}{u_{gas}(Z^*)} dZ^*$$

$$\frac{\Delta r_{grain}}{D_{vent}} = \frac{r_f - r_0}{D_{vent}} = \frac{m}{4\rho_{ice}}\int_0^\infty \frac{n_{gas}(Z^*)\bar{c}(Z^*)}{u_{gas}(Z^*)} dZ^* \tag{4.4}$$

The gas properties on the right hand side are only functions of Ma_{vent}. Consequently, Δr_{grain} is only a function of the vent size, D_{vent}, and Ma_{vent} but not the initial grain size, r_0.

4.5.2. Results

Now, we quantitatively examine the implications from our derivation above for Ma_{vent} = 3 and 5. Figure 4.6a shows how a grain starting at the vent with a negligible size ($r_0 \approx 0$) grows due to condensation as a function of altitude above the vent. For both Ma_{vent}, ~60% growth occurs below where the first expansion wave crosses the centerline (at $Z \approx 1.36D_{vent}$ for Ma_{vent} = 3 and at $Z \approx 2.25D_{vent}$ for Ma_{vent} = 5) and ~95% growth occurs below $Z = 6D_{vent}$. Growth has effectively ceased above $Z = 10D_{vent}$ due to the rapid drop in collision rates (see Figures 4.4c–d).

From Equation (4.4), we see that Δr_{grain} is a linear function of D_{vent} for a given Ma_{vent}, i.e. $\Delta r_{grain}/D_{vent} = f(Ma_{vent})$. For a given Ma_{vent}, the altitude at which the first expansion wave crosses the centerline and the density drops from the vent value is proportional to D_{vent}. As a result, a larger vent leads to a greater growth because the grain travels a longer distance and spends more time in a region of higher density and collision rates. Figure 4.6b shows Δr_{grain} as a linear function of D_{vent} for Ma_{vent} = 3 and 5 on a log-log scale (a linear function is also a straight line on a log-log scale with a slope of one).

As shown in Figure 4.6b, vents with $D_{vent} \geq 20$ m for Ma_{vent} = 3 and $D_{vent} \geq 180$ m for Ma_{vent} = 5 would be required to produce the grains detected by CDA ($r_{grain} \geq 1.6$ μm) via condensation if the grains emerge from the vent with $r_0 \approx 0$. In comparison, Goguen *et al.* (2013) inferred a crack width of ~9 m from VIMS observations. If this is the typical vent size found on Enceladus, condensation alone could not account for the grains detected by CDA as a vent with D_{vent} = 9 m could only produce $\Delta r_{grain} \approx 710$ nm for Ma_{vent} = 3 and $\Delta r_{grain} \approx 80$ nm for Ma_{vent} = 5. Another mechanism must have also been responsible, perhaps occurring below the surface so that the grains start out at the vent already fairly large, i.e. $r_0 \approx 1$ μm. One possibility is liquid dispersion from an underground reservoir, which was proposed by Postberg *et al.* (2009) as the formation mechanism for the micron-

sized salt-rich grains detected. For a given vent size, a larger Δr_{grain} is possible with a lower Ma_{vent} due to higher densities and collision rates, though the observed degree of collimation of the gas jets suggests higher Ma_{vent} of 5–8 (Hansen *et al.*, 2011). However, Figure 4.6b shows that condensation above the vents in the plume could easily account for the nanometer-sized grains detected by CAPS (Jones *et al.*, 2009) as these can be generated within very short distances above moderately sized vents.

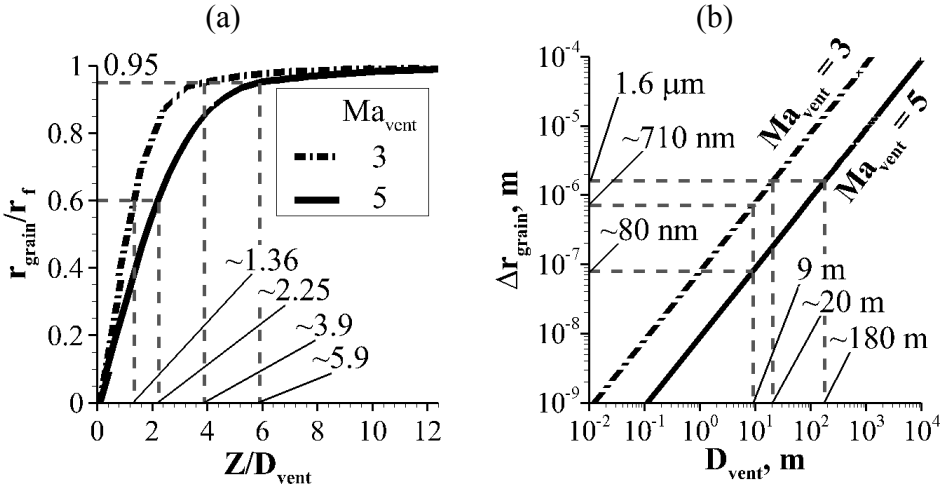

Figure 4.6. (a) Condensation growth of grain radius, r_{grain}, as a function of altitude, Z, above the vent. The grain starts at the vent with a negligible initial size, $r_0 \approx 0$. (b) Maximum possible increment in grain radius due to condensation, Δr_{grain}, as a function of vent diameter, D_{vent}. Note the logarithmic scales on both axes.

Above, we have derived the maximum condensation growth occurring above the vent along the *centerline*. In light of the salt-rich plume grains detected (Postberg *et al.*, 2009, 2011), we have also extended the condensation model derived in Section 4.5.1 to the *entire* vent and examined the resulting distributions of Δr_{grain}, r_f and final grain salt mass fractions, β_f, for an axisymmetric case (i.e. properties depend on R only). The derivations and results can be found in Appendix H.

Our calculations have neglected condensation below the surface, which may raise the vent temperature to 200–250 K due to the latent heat released (Schmidt *et al.*, 2008) and significantly reduce the supersaturation levels above the vents (due to the exponential dependence of p_{vap} on temperature). This would make condensation less likely to occur above the vents. To estimate the effect of vent temperature on the supersaturation levels above the vents, we compute the supersaturation ratio *at the vent* by assuming the same properties in Table 3.1 but only changing the temperature to 200–250 K. In doing so, we find that the supersaturation ratio at the vent drops by many orders of magnitude from $>10^{10}$ (see Section 4.4) to $\sim 10^2$ for both $Ma_{vent} = 3$ and 5. However, this is only a rough estimate. The computational subsurface model (see Section 3.2.2), which includes condensation, will be used to more accurately examine the effects of subsurface condensation on the flow above the vents in Chapter 6.

4.6. EFFECTS OF COLLISIONS NEAR VENT ON MOLECULAR VELOCITIES FAR AWAY

In the previous sections, we investigated the gas-only expansion process into vacuum on a macroscopic level and determined that collisions play an integral role. They are required for maintaining equilibrium, for driving the flow to the maximum speed possible, and for condensation grain growth to occur. Here, we explore the expansion process on a microscopic level by examining the effects of collisions near the vent on the distribution of molecular velocities far from the vent as the flow becomes free-molecular. To do so, we sample the gas molecules at higher altitudes as the flow becomes free-molecular and examine their 2-D velocity distributions.

To construct the 2-D velocity distributions, the molecular velocities, $\boldsymbol{V_{mol}}$, are first decomposed into three mutually orthogonal components, as shown in Figure 4.7. The normal component, V_n, points in the local surface normal direction; the tangential

component, V_t, is tangential to the surface and points away from the axis of symmetry; and the azimuthal component, V_{az}, completes the orthogonal set. Note that this velocity decomposition is local in nature and changes with position. Then, any two velocity components to be examined (e.g. V_n and V_t) are sorted into 2-D grids consisting of bins 10 m/s by 10 m/s in size. The velocity distribution is normalized to unity when integrated from $-\infty$ to ∞ for both components.

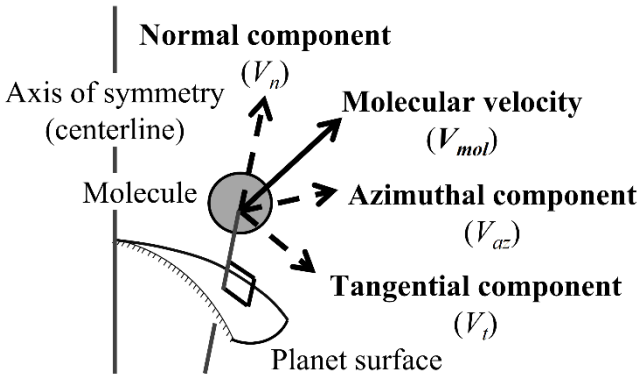

Figure 4.7. Decomposition of molecular velocity, $\boldsymbol{V_{mol}}$.

Before we examine the velocity distributions of the gas molecules at higher altitudes as the flow becomes free-molecular, we first examine their velocity distributions as they emerge from the vent, as shown in Figures 4.8a–b. They are consistent with the velocity distributions of gas molecules fluxing across a surface in a high-*Ma* flow in equilibrium. As shown in Figure 4.8a, the peak of the velocity distribution is located at (V_n, V_t) ≈ (900, 0), which is expected since bulk gas flow at the vent only has a surface normal component of ~900 m/s (see Table 3.1). This is also evident in Figure 4.8b, where the peak of the velocity distribution is located at (V_{az}, V_t) ≈ (0, 0).

The effects of collisions at the vent are characterized by the Knudsen number at the vent, Kn_{vent} (as defined in Section 4.1). The velocity distributions of gas molecules at Z = 10 km (for D_{vent} = 2.8 m) are shown in Figures 4.10a–e for Kn_{vent} ranging from ~10^{-4} (very collisional at the vent) to ∞ (collisionless at the vent). Except for the case of $Kn_{vent} \rightarrow \infty$ where collisions are turned off, we vary Kn_{vent} by changing the density but retaining the other properties for Ma_{vent} = 5 (see Table 3.1). The corresponding range of vent mass flow rate, $\dot{m}_{vent}$, is from ~10^{-4} kg/s to ~1 kg/s. We denote the Mach-5 vent conditions given in Table 3.1 ($Kn_{vent} \approx 10^{-3}$, $\dot{m}_{vent} \approx 0.2$ kg/s) as the nominal case.

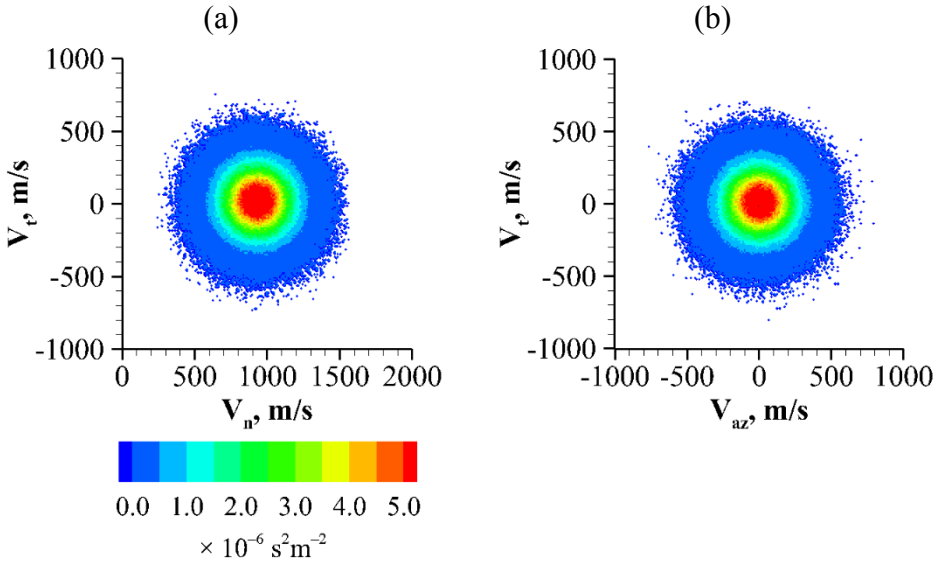

Figure 4.8. Velocity distributions of gas molecules *at the vent* for Ma_{vent} = 5.

Figure 4.9a shows that $|V_{az}| \leq 50$ m/s while $|V_t| \leq 800$ m/s at Z = 10 km for the nominal case. Since $|V_n| \geq |V_t|$ at Z = 10 km (see Figure 4.10d), $|V_{az}| << |V_n|$ or $|V_t|$ for most of the gas molecules at this altitude and we only examine V_n and V_t. Consequently, the molecular velocities are effectively 2-D at Z = 10 km and can therefore be approximated using their projections onto the normal-tangential plane, $\boldsymbol{V}_{proj}$, as shown in Figure 4.9b. For

all Kn_{vent} considered, the flow has become free-molecular at Z = 10 km, but the altitude at which the flow *first* becomes free-molecular varies with Kn_{vent}. We compare the velocity distributions obtained at the same 10-km altitude due to the local nature of the velocity decomposition.

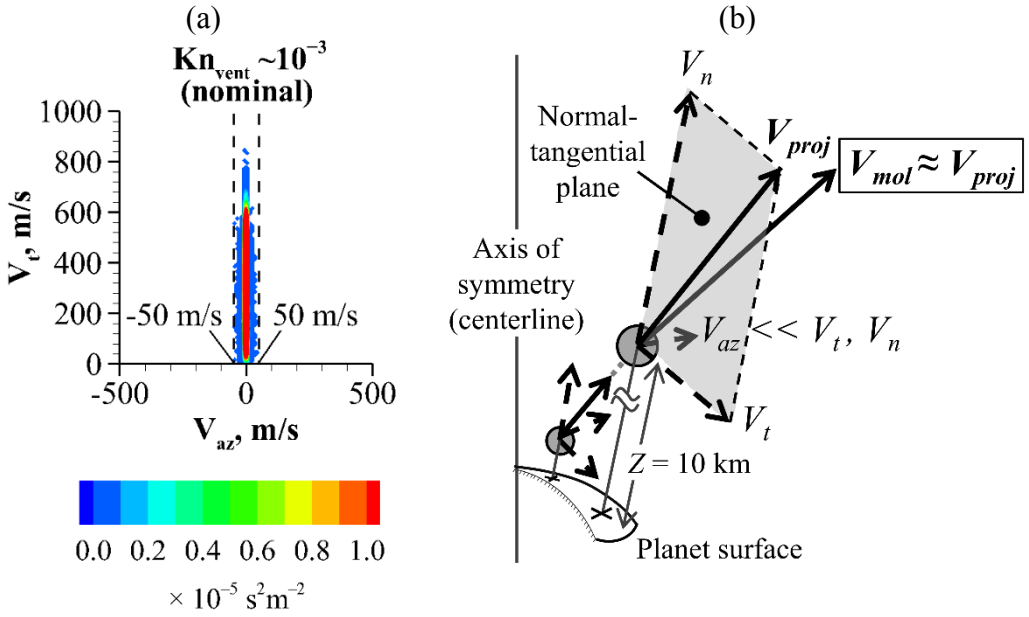

Figure 4.9. (a) Velocity distribution of gas molecules at an altitude of 10 km for the nominal case, showing that $|V_{az}| << |V_t|$ for most of the gas molecules. (b) Approximation of the molecular velocity, $\boldsymbol{V_{mol}}$, using the velocity projection onto the normal-tangential plane, $\boldsymbol{V_{proj}}$, when $V_{az} << V_t$, V_n at an altitude of 10 km.

As shown in Figures 4.10a–e, collisions at the vent have a strong effect on the distribution of molecular velocities as the flow becomes free-molecular. As Kn_{vent} decreases (i.e. vent flow becoming more collisional), the spread of molecular velocities (thermal spread) shrinks and the molecular speeds, which are approximated by the distance from the origin (because V_{az} is small), approach the ultimate speed, V_{ult} (as defined in Section 4.2). This is because a more collisional flow at the vent (smaller Kn_{vent}) can convert

a larger fraction of the molecular thermal and internal energy into the directed mean kinetic energy of the gas before the flow becomes free-molecular. Once Kn_{vent} is sufficiently small ($\leq 10^{-3}$), the flow is collisional enough to convert nearly all molecular thermal and internal energy into directed mean kinetic energy and any further decrease in Kn_{vent} only changes the velocity distribution slightly, as shown in Figures 4.10d–e.

However, there is a larger spread of velocities near the top part of the distribution even when Kn_{vent} is very small, as shown in Figures 4.10d–e. Figure 4.10f explains this phenomenon by color-coding the velocity samples used to construct the velocity distribution for the nominal case. The color-coding shows the initial radial position, r_{init}, of the molecules in the vent. There is a clear correlation of velocity with initial position. As shown in Figure 4.10f, the top part of the distribution consists of molecules originating from near the edges of the vent where the flow is always close to free-molecular. As a result, these molecules preserve their initial thermal spread of velocities.

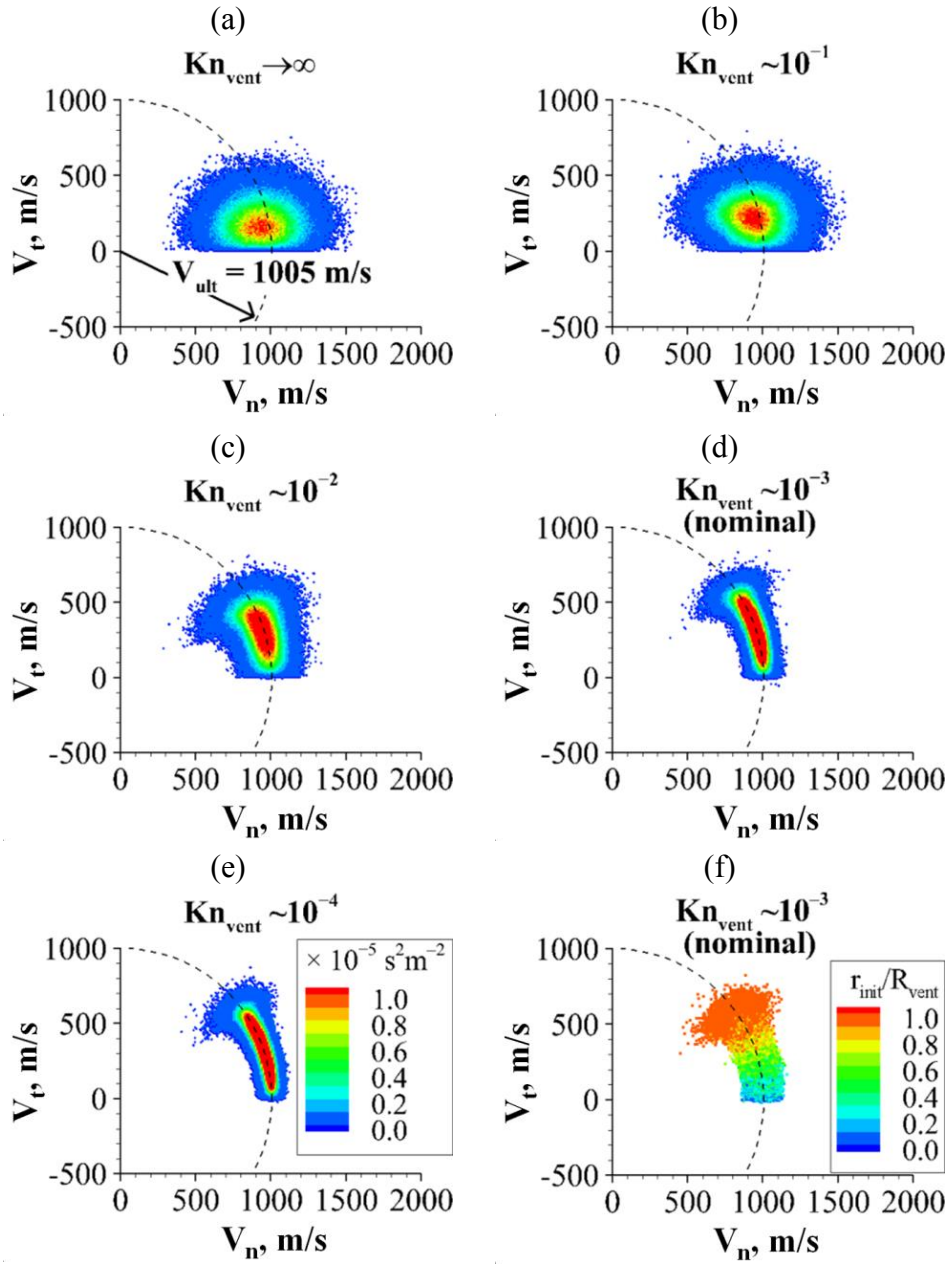

Figure 4.10. (a)–(e) Velocity distributions of gas molecules at an altitude of 10 km for a range of Kn_{vent}. A circle centered at the origin with a radius equal to the ultimate speed, V_{ult}, is plotted for comparison. (f) Velocity distribution of gas molecules at an altitude of 10 km for the nominal case colored by the initial radial positions of the molecules in the vent, r_{init}. (R_{vent} is vent radius.)

As shown in Figures 4.10a–e, nearly all the molecules have $V_t \geq 0$ and are therefore moving either in the local normal direction or away from the axis of symmetry. In our model, only collisions and gravity can change the molecule velocity (Coriolis and centrifugal forces are negligible in the near-field). Collisions reorient the velocity, thus a molecule moving away from the axis of symmetry ($V_t > 0$) can reverse its direction because of a collision and move towards the axis of symmetry ($V_t < 0$). Gravity acts in the local normal (radial) direction and does not affect V_t. Once collisions cease, V_t only changes with molecular position because the velocity decomposition is local. There are three possible scenarios after a molecule experiences its last collision, as shown in Figure 4.11. If the last collision a molecule experiences makes $V_t < 0$ (Trajectory 1 in Figure 4.11), it remains so until it crosses a radial plane through the axis of symmetry and normal to the projection of the velocity vector, as shown in Figure 4.11; thereafter, $V_t > 0$. A molecule with $V_t = 0$ after its last collision continues to travel in the normal direction (Trajectory 2 in Figure 4.11). A molecule with $V_t > 0$ after its last collision simply retains it (Trajectory 3 in Figure 4.11).

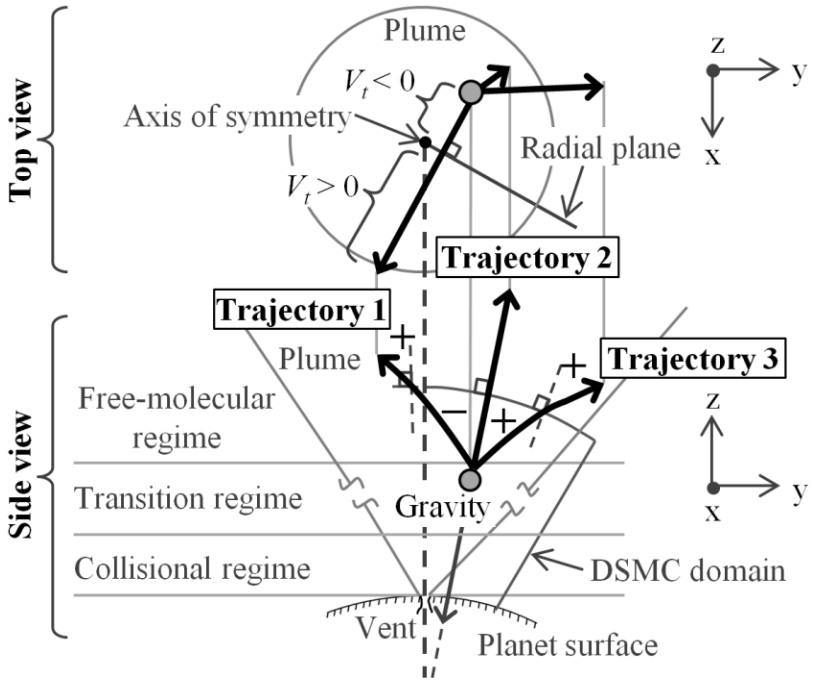

Figure 4.11. Top and side views of three possible trajectories of a molecule after its last collision. Trajectories 1, 2 and 3 represent a molecule with negative, zero and positive tangential velocity components, V_t, respectively, immediately after its last collision.

4.7. SUMMARY

In this chapter, we studied the important physical processes associated with the *gas-only* expansion flow from the vents into vacuum. We presented only the Mach-5 vent conditions (see Table 3.1) in most of the cases, though results from the Mach-3 vent conditions should be qualitatively similar. Below is a summary of the important results gained from the study.

As the flow expands from the vents into vacuum, it passes through multiple regimes, from nearly continuum (very collisional) close to the vents to free-molecular at higher altitudes. For a given set of vent conditions, the altitude at which this transition occurs, Z_{FM}, increases with vent diameter, D_{vent}, i.e. $Z_{FM} \propto D_{vent}^2 \propto \dot{m}_{vent}$ (vent mass flow rate). For meter-sized D_{vent}, the transition occurs at an altitude of a few kilometers. In

comparison, Cassini has so far sampled the plume at altitudes ≥ 25 km. In addition, the flow along the edges of the plume is free-molecular at *all* altitudes.

Collisions play an integral role in the expansion process. They are required for maintaining the flow in equilibrium and for converting the thermal and internal energy of the gas molecules into the directed mean kinetic energy of the gas flow. Consequently, the Mach number, *Ma*, which provides a measure of the directed mean kinetic energy of the gas flow to the thermal energy of the gas molecules, increases rapidly in the first few D_{vent} during expansion. However, this is mainly due to the rapid drop in gas temperature (thermal energy) rather than the increase in bulk gas speed.

Since collisions cease as the flow expands into vacuum, the collision rate of the flow *at the vent* is important. If the flow is sufficiently collisional at the vent, the expansion process would essentially be adiabatic and the flow would be driven to the ultimate speed, V_{ult}, which is the maximum speed possible. This ultimate speed depends on the source temperature, T_0. For T_0 = 273.16 K (triple-point temperature of water), $V_{ult} \approx$ 1005 m/s. This is significantly higher than the two-body escape speed of Enceladus, $V_{esc} \approx$ 240 m/s. Consequently, most of the water vapor would escape Enceladus. However, this V_{ult} is much lower than the speeds of 1.6–2.6 km/s inferred from UVIS observations (Hansen *et al.*, 2011). Ultimate speeds of 1.6–2.6 km/s imply a source temperature in excess of 700 K, which seems unlikely. Alternatively, a mixture of water vapor and a lighter gas, e.g. H_2, has a higher V_{ult} than purely water vapor for the same T_0. A H_2 mass fraction of ~23%, possibly from clathrate decomposition (Lunine and Stevenson, 1985; Kieffer *et al.*, 2006) or hydrothermal activity (Hsu *et al.*, 2015; Matson *et al.*, 2012; Monnin *et al.*, 2014), could raise V_{ult} to ~1.6 km/s for T_0 = 273.16 K. Other possibilities exist.

The expansion flow is highly supersaturated just as it emerges from the vents, thus condensation is very likely. However, condensation is mostly confined to several D_{vent}

above the vents as collision rates drop rapidly with altitude. We analytically derived the maximum condensation growth that could occur above the vents, Δr_{grain}, via heterogeneous nucleation and found that $\Delta r_{grain} \propto D_{vent}$ for a given vent Mach number, Ma_{vent}. For Ma_{vent} = 3 and 5, fairly large vents, $D_{vent} \geq 20$ m, are required to produce the grains detected by CDA ($r_{grain} \geq 1.6$ μm) if the grains start at the vent with a negligible initial size, $r_0 \approx 0$. If the crack width of ~9 m inferred by VIMS (Goguen *et al.*, 2013) is a typical vent size on Enceladus, mechanisms other than condensation above the vents must also be responsible for these grains. Perhaps, these mechanisms are occurring below the surface. Postberg *et al.* (2009) proposed that the micron-sized grains are formed via liquid dispersion from a subsurface reservoir. Larger growth is possible with lower Ma_{vent}, though more recent UVIS observations have inferred even higher Ma_{vent} of 5–8 (Hansen *et al.*, 2011) than those considered. However, condensation above the vents could easily account for the nanometer-sized grains detected by CAPS (Jones *et al.*, 2009).

Chapter 5.

Two-Phase Flow Expansion into Vacuum[4]

In Chapter 4, we analyzed the important physical processes associated with the flow expansion into vacuum in the *absence* of grains. In this chapter, we consider the *presence* of grains and examine how they affect the expansion process. We also investigate several phenomena related to the interaction between the gas and the grains during expansion, such as the decoupling of grain motion from gas motion and the spreading and acceleration of grains by the expanding gas. We only model the exchange of momentum and energy between the gas and the grains but not the exchange of mass (no phase change).

A parametric study is performed involving three parameters: (i) grain radius/size, r_{grain}, (ii) vent mass flow rate ratio, φ ($\triangleq \dot{m}_{grain}/\dot{m}_{gas}$), and (iii) vent velocity ratio, α ($\triangleq V_{grain}/V_{gas}$). The vent mass flow rate ratio is proportional to the *total* mass ratio of ice grains to vapor in the plume (Crowe *et al.*, 2012) while the vent velocity ratio measures the effects of an initial velocity difference between the gas and the grains at the vent. These parameters are varied one at a time to study their effects independently. For this study, we only consider the Mach-5 vent conditions from the analytical subsurface model (see Table 3.1) for the gas component. However, the results for the Mach-3 vent conditions should be qualitatively similar.

[4]Parts of this chapter are published in Yeoh *et al.* (2015). All of the computations in this work were done by the author of this dissertation. The other authors provided useful ideas, suggestions and feedback, and also proofread and corrected the manuscript of the paper.

5.1. EFFECTS OF GRAINS ON FLOW EXPANSION PROCESS

In this section, we investigate how several gas macroscopic properties are altered by the presence of grains for the cases and parameter values listed in Table 5.1. In all these cases, the bulk gas and grain velocities at the vent are in the vertical direction. Moreover, the grains exit the vent at the same temperature as the gas ($T_{grain} = T_{gas} = 53$ K).

Table 5.1. Cases considered in parametric study.

Case	Grain radius, r_{grain} (μm)	Vent mass flow rate ratio, φ	Vent velocity ratio, α
1	0.005 (5 nm)	0.1	1.0
2	0.005 (5 nm)	1.0	1.0
3	0.5	0.1	1.0
4	0.5	1.0	1.0
5	0.5	1.0	0.5
6	0.005 (5 nm)	10.0	1.0
7	0.5	10.0	1.0

We choose $r_{grain} = 5$ nm and 0.5 μm so as to capture the smaller and the larger grains in the broad distribution of plume grain sizes inferred, which ranges from several nanometers to a few microns (Jones *et al.*, 2009; Postberg *et al.*, 2011; Spahn *et al.*, 2006b). If the surface grain size distribution in the south polar region also reflects the plume grain sizes, very large grains, $r_{grain} \approx 100$ μm, may have also been ejected (Jaumann *et al.*, 2008). A broad range of plume ice/vapor mass ratios have also been reported, from as small as 0.001 to as large as 1 (Hedman *et al.*, 2009; Ingersoll and Ewald, 2011; Kieffer *et al.*, 2009; Porco *et al.*, 2006; Schmidt *et al.*, 2008). As a result, we consider φ ranging from 0.1 to 10.

Schmidt *et al.* (2008) suggested that wall collisions and directional changes in the gas flow within irregular subsurface channels can slow down the grains relative to the gas and cause them to exit the vents slower. The effects are greater on the larger grains, thus they tend to have slower ejection velocities. This is consistent with several observations

(Hedman *et al.*, 2009; Ingersoll and Ewald, 2011; Postberg *et al.*, 2011). Consequently, nanometer-sized grains most likely exit the vents at or near the gas speeds while micron-sized grains exit slower. Therefore, we only examine the effects of a vent velocity difference for r_{grain} = 0.5 μm. Furthermore, we analyze the effects qualitatively and thus only consider α = 0.5, i.e. the grains exit the vent at half the gas speed.

5.1.1. Effects of Vent Mass Flow Rate Ratio and Grain Size

First we examine how the grains affect the gas flow in the cases of φ = 0.1 and 1.0 for r_{grain} = 5 nm and 0.5 μm in the *absence* of an initial velocity difference between the gas and the grains (α = 1.0). Comparing Figures 5.1a−f from Cases 1 and 3 with Figures 4.1c (n), 4.2a (T_{tr}) and 4.2e (speed) from the gas-only case, we find that the grains *barely* affect the gas flow when φ = 0.1 regardless of the grain size. The gas number density (n) contours are nearly identical. Near the centerline where the grains are concentrated (the black line marks the boundary of the grain jet), the gas translational temperature (T_{tr}) is slightly higher and the gas speed is slightly slower due to the presence of grains. The effects are more pronounced for the 5-nm grains. Consequently, there is minimal exchange of momentum and energy between the gas and the grains. The coupling is effectively one-way, from the gas to the grains.

As indicated by the black lines in Figures 5.1a, 5.1c and 5.1e, the 5-nm grains are more strongly affected by the gas flow as they spread with the gas (the grain jet widens at the top) and are accelerated to the gas speeds (as we shall see later in Section 5.2). In contrast, as shown in Figures 5.1b, 5.1d and 5.1f, the 0.5-μm grains hardly spread (the grain jet is straight) and retain the speeds they had at the vent (as we shall see later in Section 5.2). Their larger mass (by a factor of 10^6 relative to the 5-nm grains), and consequent inertia, make their motions harder to change by the gas flow.

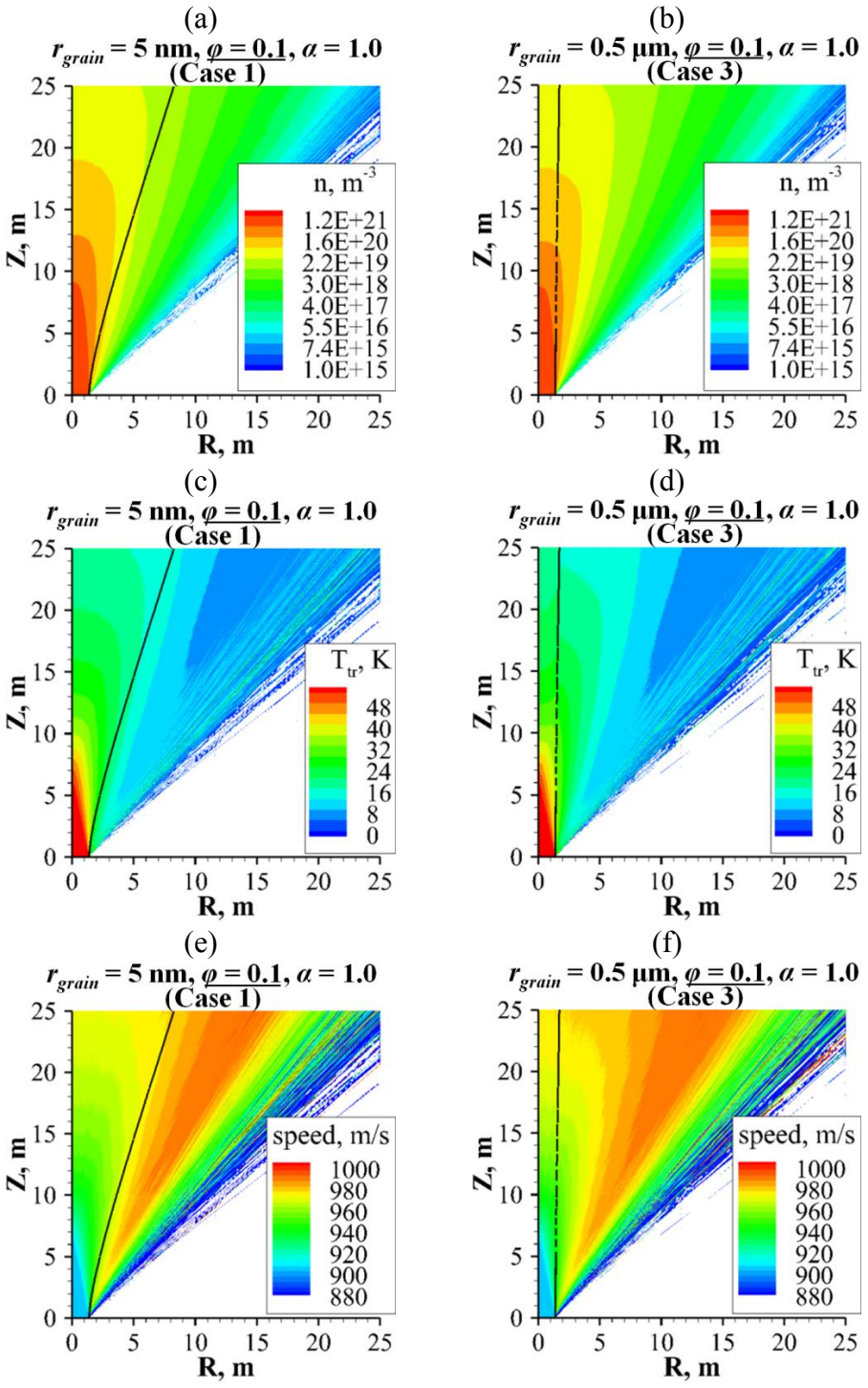

Figure 5.1. Contours of gas number density (n), translational temperature (T_{tr}) and speed for Cases 1 (left column) and 3 (right column). Both cases are for φ = 0.1 and α = 1.0. Solid black line indicates boundary of grain jet.

Comparing Figures 5.2a−f from Cases 2 and 4 with Figures 4.1c (n), 4.2a (T_{tr}) and 4.2e (speed) from the gas-only case, we find that the effects of the grains become more significant when φ = 1.0. Near the centerline where the grains are concentrated, the gas number density and translational temperature are noticeably higher, and the gas speed is noticeably slower. A higher φ results in more grains in the gas flow, leading to a greater exchange of momentum and energy between the gas and the grains. The coupling is no longer one-way but two-way. As in Cases 1 and 3 (φ = 0.1), the 5-nm grains are more strongly affected by the gas flow and spread out while the 0.5-μm grains are hardly affected and thus remain in a tight beam near the centerline.

Moreover, the more numerous grains form a thicker column over the vent and trap the gas in the column, as evidenced by the higher gas densities near the centerline. As a result, the gas can no longer expand freely into vacuum but is constrained by the column of grains. As the gas expands within the column, some escapes through the sides and continues to expand freely into vacuum. This is more evident for the 0.5-μm grains, as shown in Figure 5.2b, where density contours can be seen to emanate from the sides of the grain jet. The trapping of gas by the grains becomes even more evident for higher φ (as we shall see later in Section 5.1.3).

For both φ, the 5-nm grains have a greater and more widespread effect on the gas flow than the 0.5-μm grains. Even with φ = 1.0, the effects of the 0.5-μm grains are minimal and largely confined to near the centerline where the grains are concentrated. For equal φ, there are significantly more 5-nm grains than 0.5-μm grains (by a factor of 10^6) in the gas flow. Additionally, the 5-nm grains track the gas flow better. These factors combine to distribute the 5-nm grains more widely throughout the flow, causing a more widespread effect. Furthermore, for equal φ, both the total surface and cross-sectional areas of the grains in the gas flow are inversely proportional to r_{grain}. As a result, the 5-nm grains have

a larger total surface area (by a factor of 100 relative to the 0.5-μm grains), which leads to a higher overall rate of heat transfer, and a larger total cross-sectional area, which results in a larger overall drag on the gas flow.

Since the grains are mostly concentrated near the centerline, we also investigate the centerline distributions of the gas properties. Figures 5.3a–f show the centerline distributions of n, T_{tr} and speed for Cases 1–4 compared to those for the gas-only case from $Z/D_{vent} = 0$ (vent) to $Z/D_{vent} \approx 3600$ (10 km). As shown in Figures 5.3a, 5.3c and 5.3e, the centerline distributions of all three properties for Cases 1 and 3 ($\varphi = 0.1$) are nearly identical to those for the gas-only case, except that of T_{tr} for Case 3 where T_{tr} remains higher at the higher altitudes. This may be because the 0.5-μm grains remain concentrated in a tight beam near the centerline and thus enhance the heat transfer between the gas and the grains. As shown in Figure 5.3e, the gas flows in Cases 1 and 3 accelerate to ultimate speeds slightly slower than the gas flow in the gas-only case along the centerline.

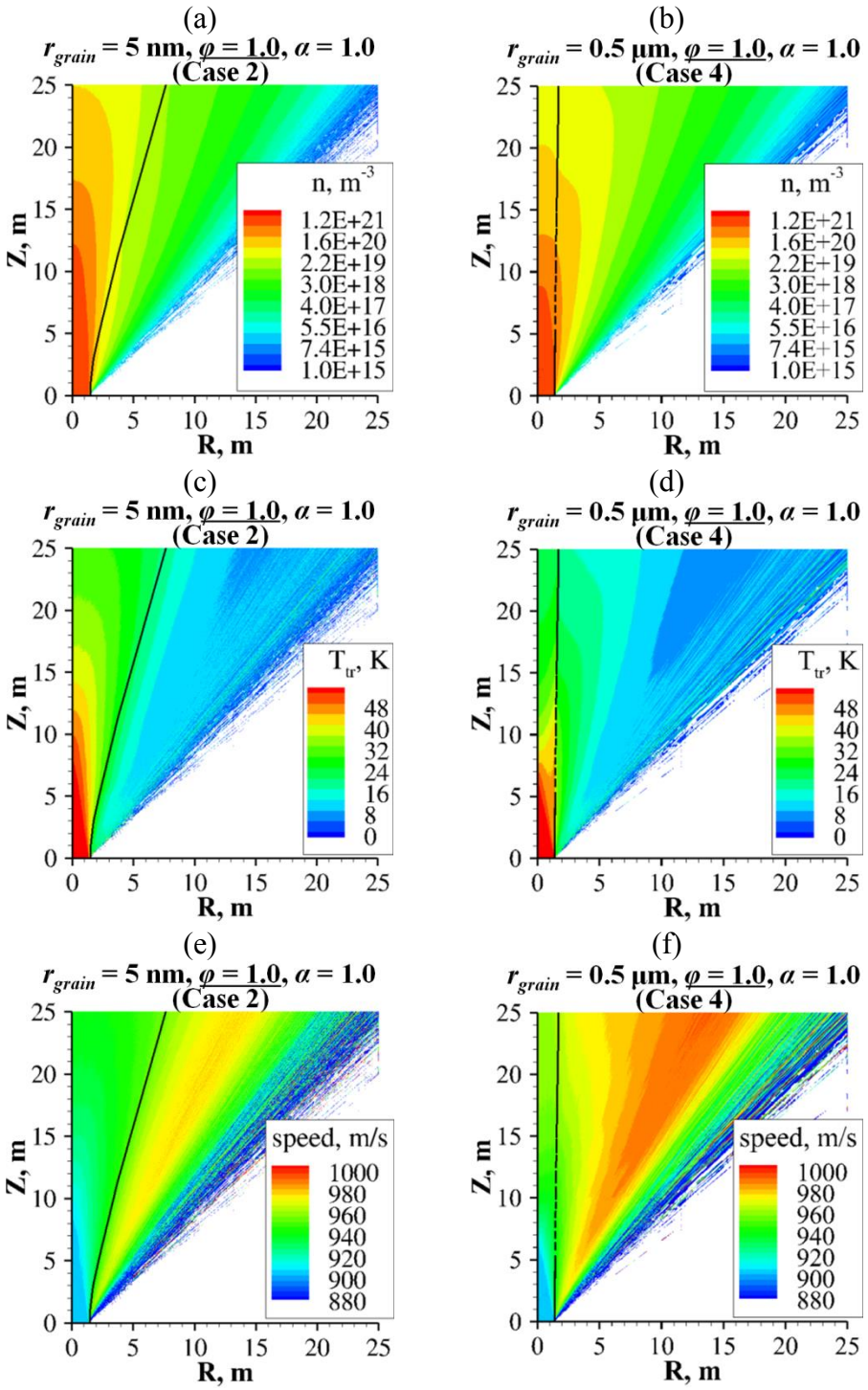

Figure 5.2. Contours of gas number density (n), translational temperature (T_{tr}) and speed for Cases 2 (left column) and 4 (right column). Both cases are for φ = 1.0 and α = 1.0. Solid black line indicates boundary of grain jet.

As shown in Figures 5.3b, 5.3d and 5.3f, the effects of grains on the gas flow along the centerline are greater for Cases 2 and 4 (φ = 1.0). This is especially evident in the centerline distributions of T_{tr} and speed where the gas flows in Cases 2 and 4 remain hotter at higher altitudes and achieve noticeably slower ultimate speeds than the gas flow in the gas-only case along the centerline. Consequently, the effects of grains on the gas flow along the centerline increase with φ, which is consistent with the results obtained from the analyses of the gas macroscopic properties in the vicinity of the vent.

While the effects of grains on the gas flow increase with φ, their effects should not be too significant for plausible $\varphi \leq 1.0$ in the *absence* of an initial velocity difference between the gas and the grains ($\alpha \approx 1.0$). The gas flow may be slightly hotter ($\leq$ 5 K higher) at higher altitudes and may reach slower ultimate speeds ($\leq$ 20 m/s slower). Later in Sections 5.1.2 and 5.1.3, we examine how the grains affect the gas flow in the *presence* of an initial velocity difference between the gas and the grains as well as under very high mass loading conditions (φ = 10.0) respectively.

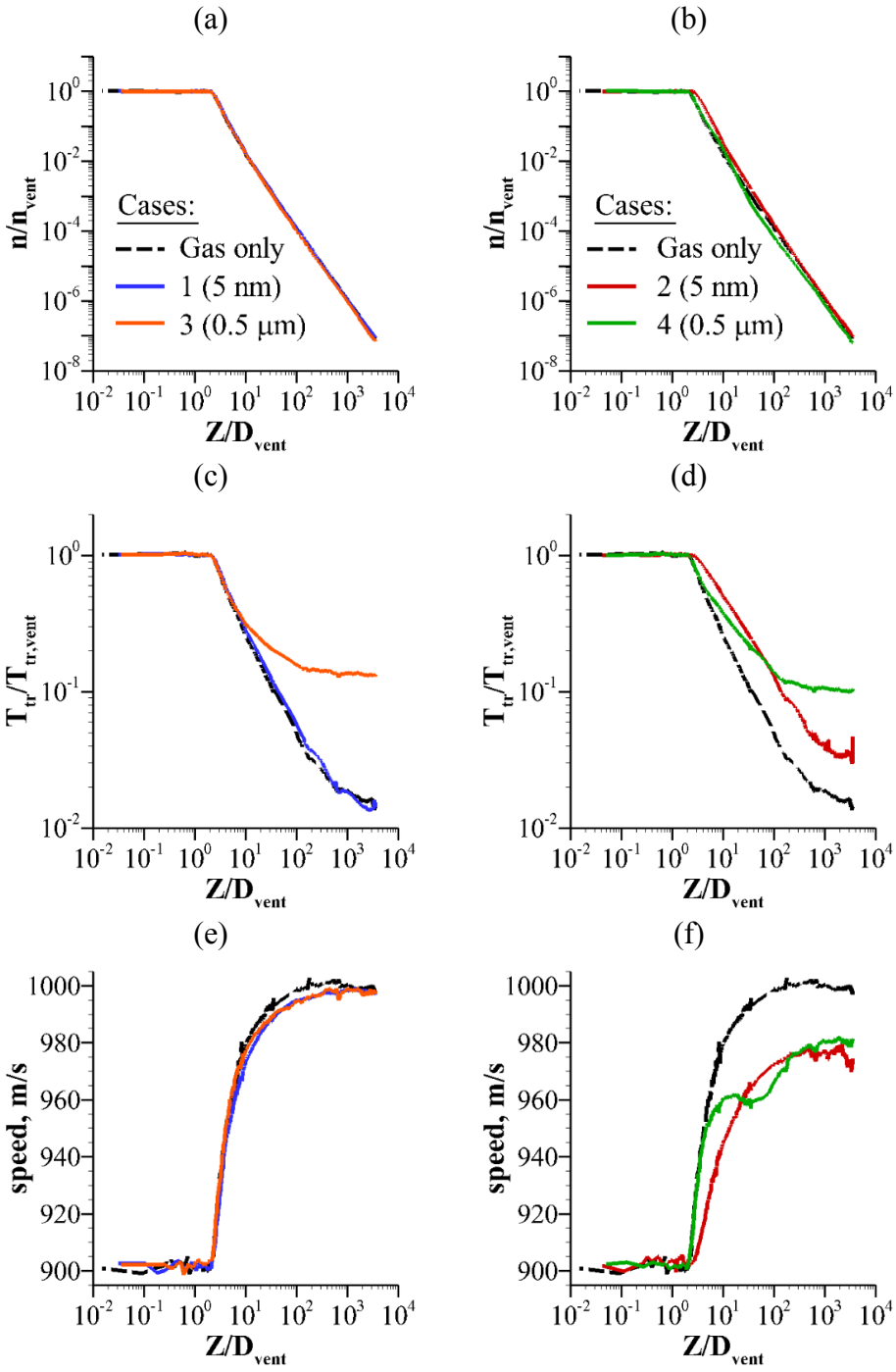

Figure 5.3. Centerline distributions of gas properties for Cases 1–4 in comparison to those for the gas-only case. Cases 1 and 3 (left column) are for $\varphi = 0.1$ and Cases 2 and 4 (right column) are for $\varphi = 1.0$. For these cases, gas and grains exit the vent at the same speed ($\alpha = 1.0$).

5.1.2. Effects of Vent Velocity Ratio

Here we investigate how the grains affect the gas flow in the *presence* of an initial velocity difference between the gas and the grains at the vent ($\alpha < 1.0$) for $r_{grain} = 0.5$ μm. We consider the case of $\alpha = 0.5$, i.e. the grains exit the vent at half the gas speed, and $\varphi = 1.0$. Comparing Figures 5.4a−c from Case 5 with Figures 4.1c (n), 4.2a (T_{tr}) and 4.2e (speed) from the gas-only case, we find that the gas flow is significantly affected by the grains.

The gas number density (n) contours are similar to those in Case 4 ($\alpha = 1.0$) (see Figures 5.2b and 5.4a), except that contours of the same value do not extend as high up but are more spread out laterally in Case 5. The gas translational temperature (T_{tr}) remains high (> 50 K) near the centerline where the grains are concentrated up to at least $Z = 25$ m. The major difference lies in the gas speed near the centerline. As shown in Figures 4.2e and 5.4c, the gas flow accelerates near the centerline in the gas-only case but decelerates in Case 5. As shown in Figure 5.2f, the gas flow also accelerates near the centerline in Case 4. Note the different speed scale used in Figure 5.4c to better capture the deceleration. The gas flow decelerates as it transfers momentum to the slower grains to accelerate them, as we shall see later in Section 5.5.

Consequently, there is a significant exchange of momentum and energy between the gas and the grains when $\alpha = 0.5$. Two factors enhance the exchange of momentum and energy in comparison to Case 4 ($\alpha = 1.0$). First, the slower grains lead to a higher drag due to a larger velocity difference. Second, there is a greater concentration of grains near the centerline. With the grain velocity halved, the grain number density, n_{grain}, is doubled to maintain the same grain mass flow rate out of the vent, since $\varphi \propto \alpha(n_{grain}/n)$. The greater exchange of momentum also causes the 0.5-μm grains to spread more as the grain jet widens at the top in Case 5. In contrast, the 0.5-μm grains are hardly affected by the gas

flow in Case 4 and stay in a narrow beam. Later in Section 5.4, we see that the grain spreading increases with velocity difference between the gas and the grains at the vent (decreasing α). Moreover, these factors cause the grains to pose a greater obstruction to the gas flow as it exits the vent and push the gas out more in the lateral direction, which may explain why contours of the same gas density are lower but broader in Case 5 as compared to Case 4 (see Figures 5.2b and 5.4a). Later in Section 5.4, we see that the gas jet broadens as the velocity difference between the gas and the grains increases at the vent (α decreases).

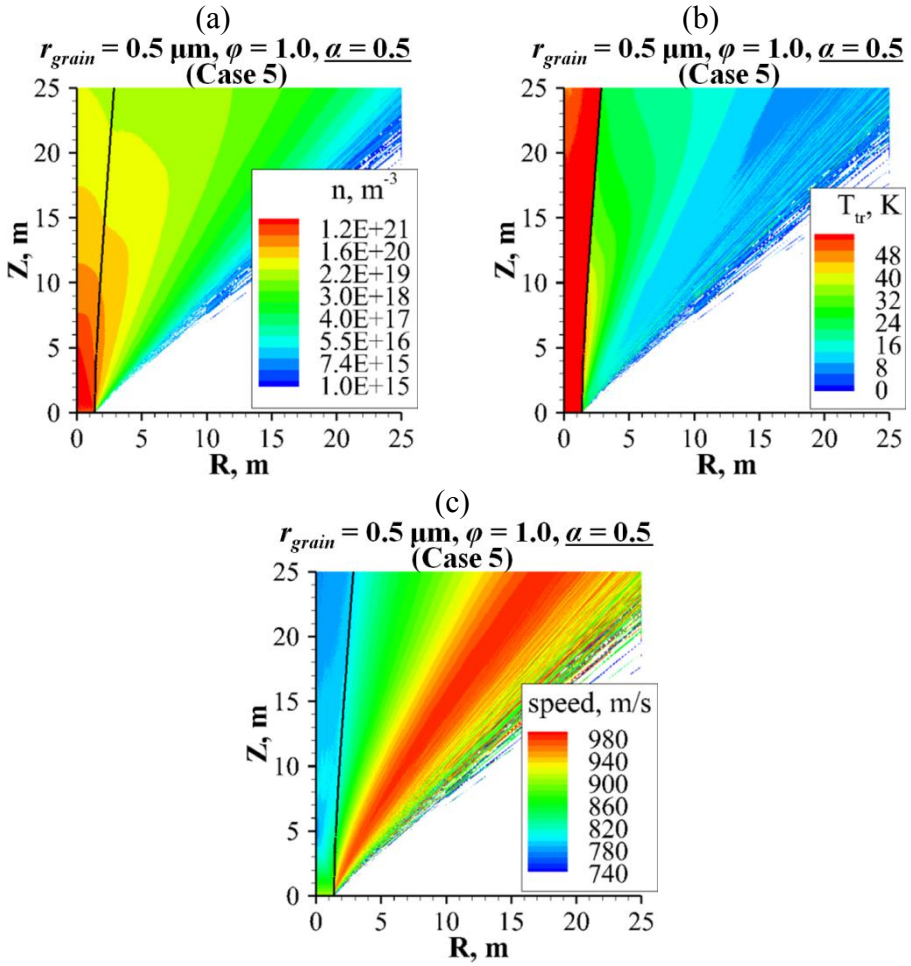

Figure 5.4. Contours of gas number density (n), translational temperature (T_{tr}) and speed for Case 5. In this case, 0.5-µm grains exit the vent at *half* the gas speed (α = 0.5). Solid black line indicates boundary of grain jet.

Next we examine the centerline distributions of n, T_{tr} and gas speed for Case 5 compared to those for the gas-only case from $Z/D_{vent} = 0$ (vent) to $Z/D_{vent} \approx 3600$ (10 km), as shown in Figures 5.5a–c. The centerline n drops slightly below that for the gas-only case for $Z/D_{vent} \geq 10$ (~30 m). This is consistent with the gas being pushed out more to the sides by the denser column of slower grains just as the gas emerges from the vent. Moreover, the centerline T_{tr} is more than twice that for the gas-only case near the vent and drops to ~30 K farther up and then remains constant up to at least $Z = 10$ km while the centerline T_{tr} continues to drop for the gas-only case. The gas speed drops with altitude along the centerline as the gas flow transfers its momentum to the slower grains to accelerate them.

While the effects of grains on the gas flow are significant when $\alpha = 0.5$, their effects should decrease as α increases (compare with results from Case 4). A larger α, i.e. a smaller velocity difference between the gas and the grains at the vent, leads to a lower drag and a less dense column of grains. Furthermore, we have only examined $r_{grain} = 0.5$ μm but we expect $r_{grain} = 5$ nm to have a greater effect for the same α and φ for the same reasons given in Section 5.1.1.

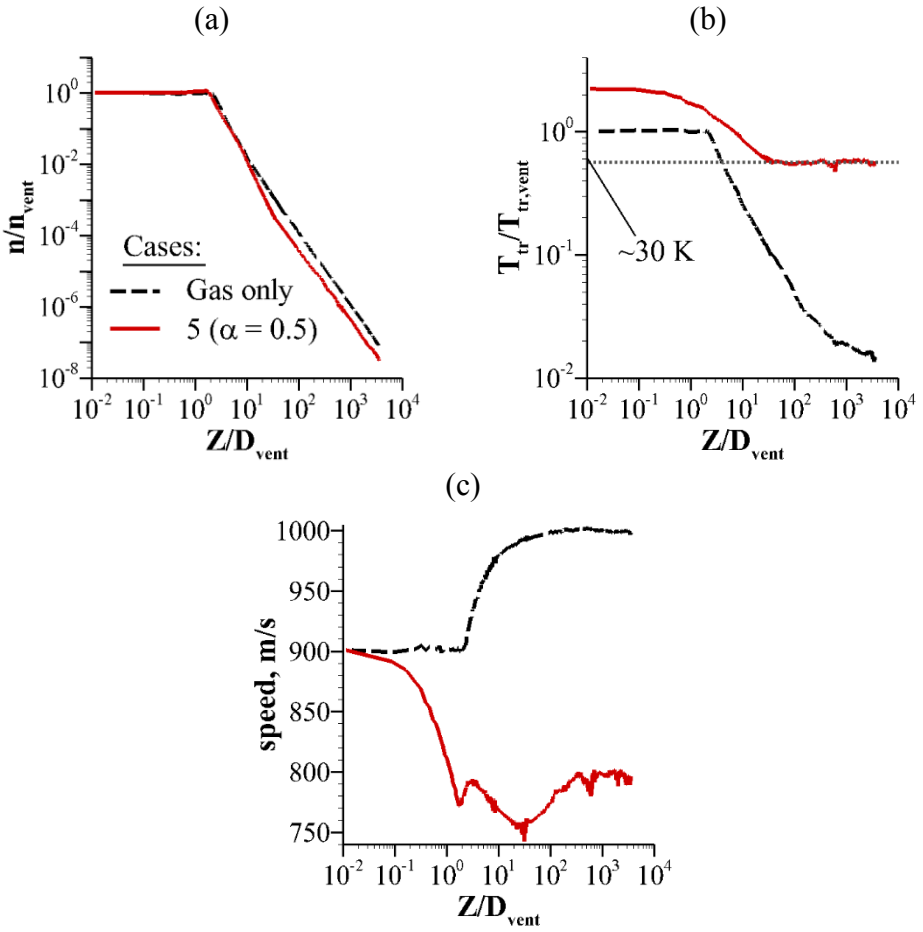

Figure 5.5. Centerline distributions of gas properties for Case 5 in comparison to those for the gas-only case. Case 5 is for r_{grain} = 0.5 μm and φ = 1.0.

5.1.3. Very High Mass Loading Conditions

Here we examine how the grains affect the gas flow under very high mass loading conditions (φ = 10.0) for r_{grain} = 5 nm and 0.5 μm in the *absence* of an initial velocity difference between the gas and the grains (α = 1.0). Comparing Figures 5.6a–f from Cases 6 and 7 with Figures 4.1c (n), 4.2a (T_{tr}) and 4.2e (speed) from the gas-only case, we find that the gas flow is very significantly altered by the grains. This follows the trend observed in Section 5.1.1: the effects of grains on the gas flow increase with φ. There is significant exchange of momentum and energy between the gas and the grains and thus a strong two-

way coupling. Near the centerline where the grains are concentrated, the gas number density (n) and translational temperature (T_{tr}) are much higher, especially for Case 6 with the 5-nm grains, while the gas speeds are much slower.

In addition, the trapping of the gas in the grain column is more evident in these cases as the grain column is much denser and is therefore capable of trapping more gas. As a result, n is much higher near the centerline. This also enhances the interaction between the gas and the grains near the centerline, resulting in a much higher T_{tr} and much slower gas speeds there.

The 5-nm grains are better at trapping the gas than the 0.5-μm grains as n is higher in Case 6 than in Case 7 near the centerline. Moreover, this can be seen from the values of the contours emanating from the sides of the grain column as the gas escapes from the column; the contour values are lower for Case 6 since less gas is escaping. This is because the 5-nm grains have a larger total cross-sectional area (by a factor of 100) than the 0.5-μm grains for equal φ. As a result, the 5-nm grains form a more effective seal to prevent the gas from escaping from the central plume.

As we shall see later in Section 5.4, the trapping of gas within a thick column of grains when $\varphi = 10.0$ does not actually lead to a narrower gas jet in the far-field. On the contrary, the gas jets are broader (see Figure 5.13b). The precise mechanism responsible for this is not clear due to the complex gas-grain interactions occurring under such high mass loading conditions.

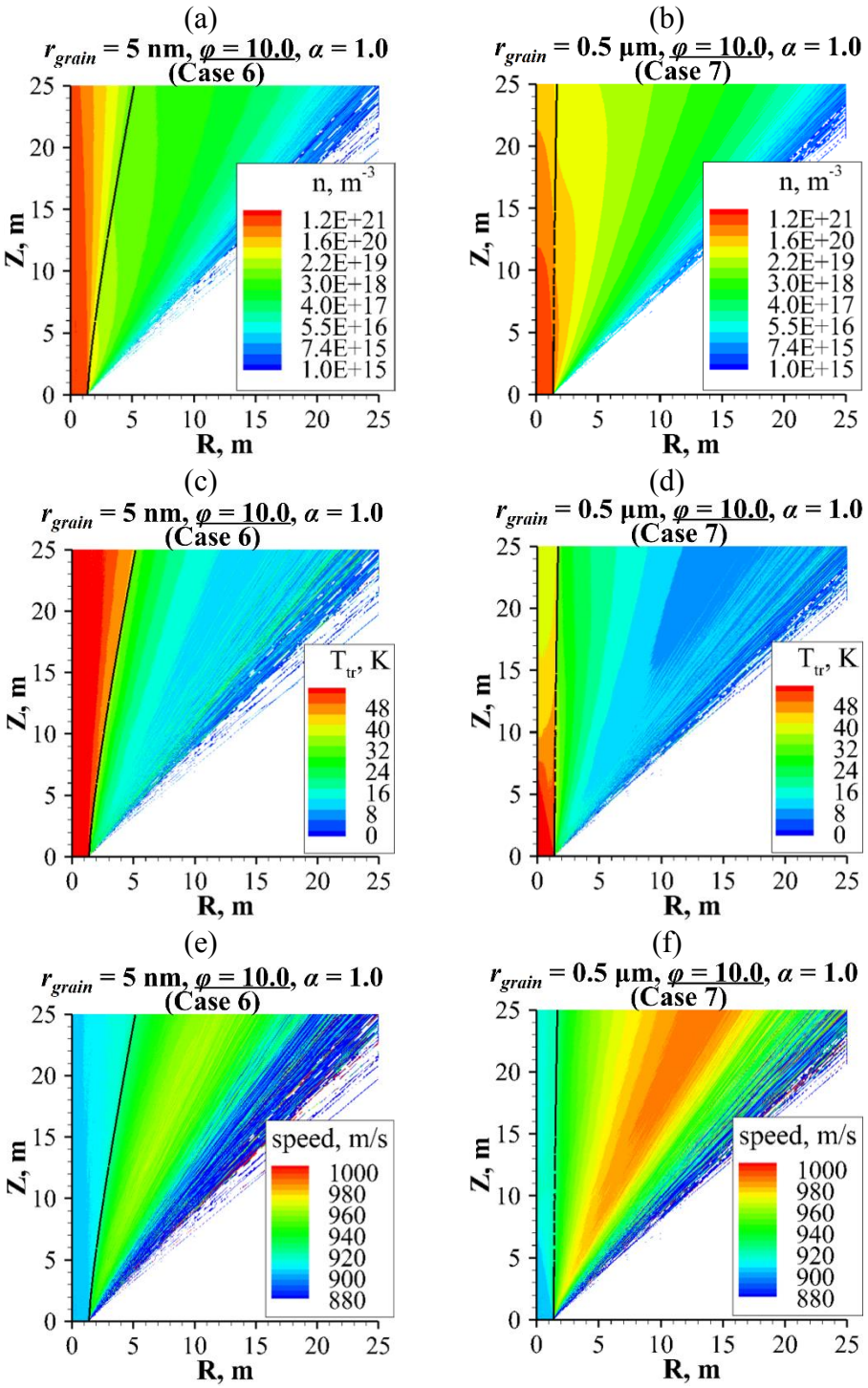

Figure 5.6. Contours of gas number density (n), translational temperature (T_{tr}) and speed for Cases 6 (left column) and 7 (right column). Both cases are for φ = 10.0 and α = 1.0. Solid black line indicates boundary of grain jet.

Next we examine the centerline distributions of n, T_{tr} and gas speed for Cases 6 and 7 compared to those for the gas-only case from $Z/D_{vent} = 0$ (vent) to $Z/D_{vent} \approx 3600$ (10 km), as shown in Figures 5.7a–c. Due to the greater trapping of the gas within the denser grain columns, n along the centerline remains higher out to higher altitudes for Cases 6 and 7 than for the gas-only case. However, n drops below that of the gas-only case at $Z \approx 25D_{vent}$ (~70 m) for Case 7 with the 0.5-μm grains. The reason for this is unclear due to the complex interaction between the gas and the grains. The centerline n also shows that the 5-nm grains are better at trapping the gas as n remains higher out to $Z \approx 1000D_{vent}$ (~2.8 km) for Case 6. The centerline T_{tr} for Cases 6 and 7 are higher than those for Cases 2 and 4 for $\varphi = 1.0$ (see Figure 5.3d) while the centerline gas speeds for Cases 6 and 7 are slower than those for Cases 2 and 4 (see Figure 5.3f) due to the greater exchange of momentum and energy between the gas and the grains.

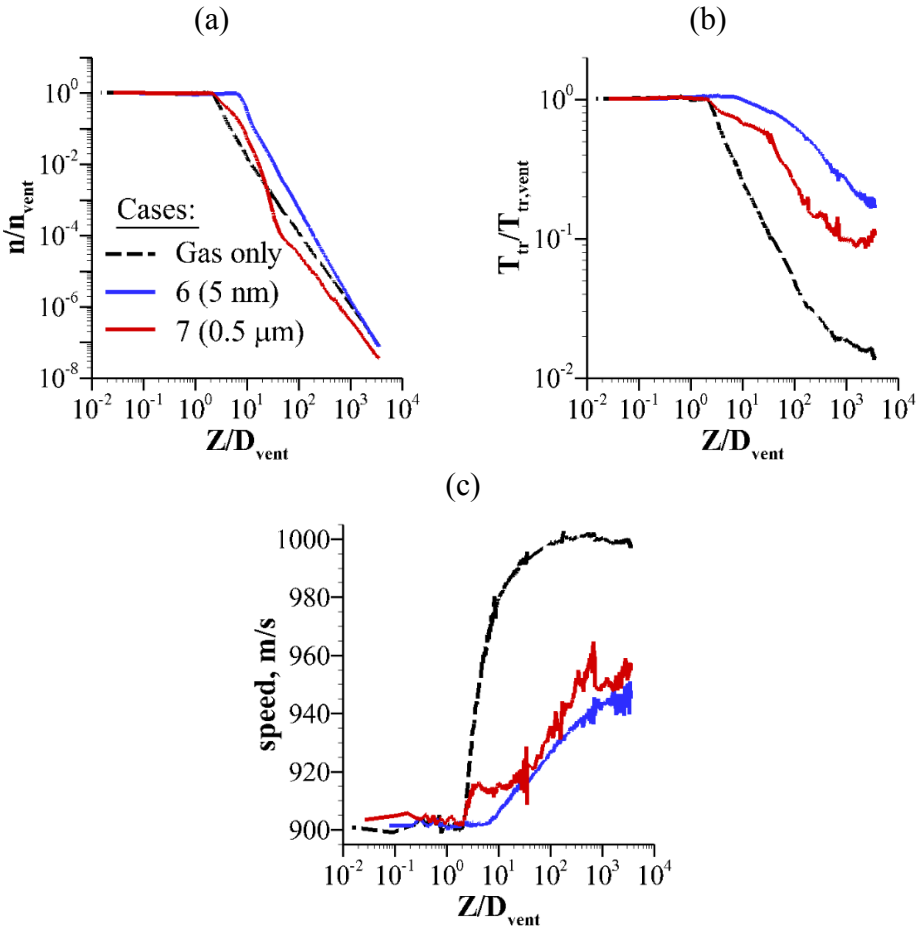

Figure 5.7. Centerline distributions of gas properties for Cases 6 and 7 in comparison to those for the gas-only case. Cases 6 and 7 are for $\varphi = 10.0$ and $\alpha = 1.0$.

5.2. Effects of Gas-Grain Interaction on Molecular and Grain Velocities far from Vent

In this section, we investigate how the interaction between the gas and the grains affects their velocity distributions far from the vent at $Z = 10$ km where the gas component has become free-molecular for the same cases as in Section 5.1 (see Table 5.1). The velocity distributions of the gas molecules (color) and the grains (black in translucent gray boxes) for the different cases are shown in Figures 5.8a–e and 5.9a–b. For comparison, the velocity distribution of the gas molecules, in the absence of grains, is shown in Figure

4.10d (nominal case). The molecular and grain velocities are decomposed as shown in Figure 4.7, and the velocity distributions are constructed in the same way as those in Section 4.6.

The effects the grains have on the distribution of molecular velocities far from the vent are consistent with those observed on the gas flow near the vent in Section 5.1. Comparing Figures 5.8a and 5.8c with Figure 4.10d, we find that the molecular velocities are hardly affected by the grains regardless of grain size when $\varphi = 0.1$ (Cases 1 and 3) in the absence of an initial velocity difference ($\alpha = 1.0$). Comparing Figures 5.8b and 5.8d with Figure 4.10d, we find that the 5-nm grains significantly change the velocity distribution of gas molecules while the 0.5-μm grains still only have a minimal effect when $\varphi = 1.0$ (Cases 2 and 4) in the absence of an initial velocity difference ($\alpha = 1.0$). Consequently, the 5-nm grains also have a stronger effect than the 0.5-μm grains on the molecular velocities. The effects of the grains on the molecular velocities become greater for even higher φ, as we shall see later in this section.

Comparing Figure 5.8e with Figure 4.10d, we find that the grains strongly affect the molecular velocities when the grains exit the vent at half the gas speed ($\alpha = 0.5$) for $\varphi = 1.0$. The 0.5-μm grains, as we have seen in Section 5.1.2, only spread out slightly and are confined to near the centerline. As a result, the lower portion of the velocity distribution, which consists of gas molecules originating from near the centerline at the vent (see Figure 4.10f), is most significantly affected. The lower portion of the distribution is "pulled" towards the origin because the gas near the centerline is being slowed down as it transfers momentum to the slower grains. This is consistent with Figure 5.4c where the gas flow is decelerated near the centerline.

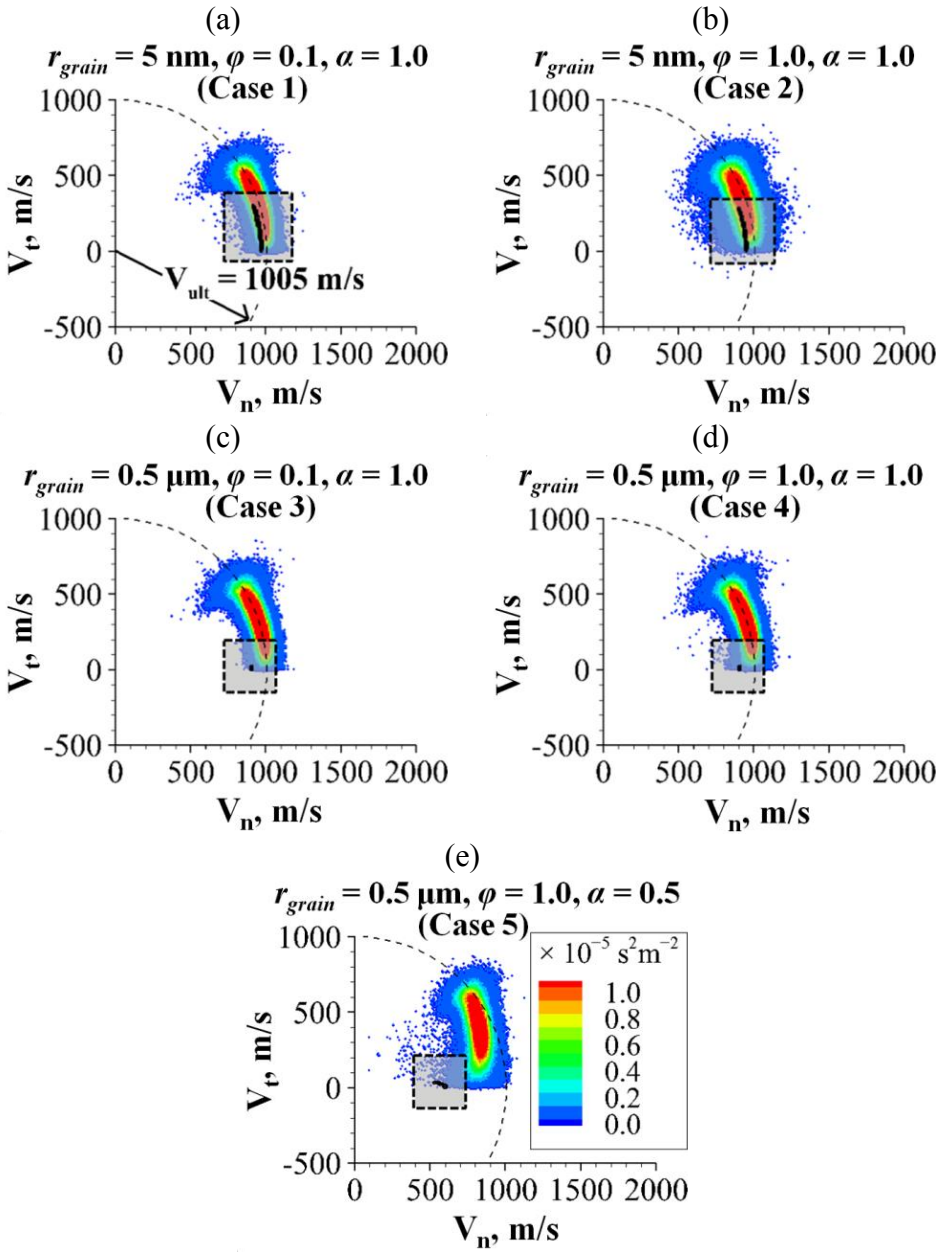

Figure 5.8. Distributions of molecular (color) and grain (black in translucent gray boxes) velocities at Z = 10 km for Cases 1–5. A circle centered at the origin with a radius equal to the ultimate speed, V_{ult}, is plotted for comparison.

As shown in Figures 5.8a–b, the velocities of the 5-nm grains spread out with the molecular velocities into a circular arc and are accelerated to near the ultimate speed, V_{ult} (see definition in Section 4.2). In contrast, the 0.5-μm grains, due to their larger mass and inertia, are hardly affected by the gas and thus maintain their velocities at the vent (~900 m/s), as shown in Figures 5.8c–d. Even with a larger drag due to a velocity difference (α = 0.5), the velocities of the 0.5-μm grains still do not spread out much, as shown in Figure 5.8e. The grains near the centerline, which experience the largest drag, are accelerated from 450 m/s to ~600 m/s, which is not even close to V_{ult}.

Next, we examine the cases with very high mass loading (φ = 10.0). Comparing Figures 5.9a–b with Figure 4.10d, we find that the molecular velocities are significantly affected by the grains. Consistent with previous results, the 5-nm grains have a stronger and more widespread effect. As shown in Figure 5.9a, the entire velocity distribution of the gas molecules is altered. In contrast, the 0.5-μm grains only affect the lower portion of the velocity distribution. The top portion is essentially unchanged. The lower portion consists of gas molecules originating from near the centerline in the vent (see Figure 4.10f), where the 0.5-μm grains are concentrated (see Figures 5.6b, d and f).

Moreover, the velocities of the 5-nm grains for the case of φ = 10.0 do not spread out as much and are not accelerated as close to the ultimate speed, V_{ult}, as in the cases of φ = 0.1 and 1.0 (compare Figure 5.9a with Figures 5.8a–b). As shown in Figures 5.6a, c and e, the gas flow is significantly affected by the grains. In turn, this affects the gas-to-grain momentum transfer to spread and accelerate the grains.

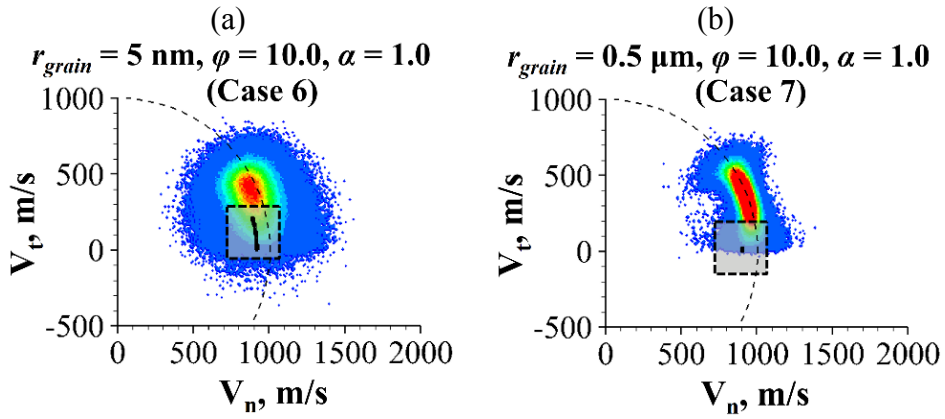

Figure 5.9. Distributions of molecular (color) and grain (black in translucent gray boxes) velocities at Z = 10 km for Cases 6 and 7 (φ = 10.0). A circle centered at the origin with a radius equal to the ultimate speed, V_{ult}, is plotted for comparison.

5.3. GRAIN DECOUPLING HEIGHTS

As the gas expands and its density drops rapidly (see Figures 4.1c and 4.3a), it loses the ability to affect the grain motions. Beyond a certain height above the vent, the grains are decoupled from the gas flow, i.e. the grain motions are no longer affected by the gas flow. In this section, we determine this decoupling height, $h_{decoupl}$, for the cases in Table 5.1 and three additional cases in Table 5.2. These additional cases are for r_{grain} = 0.5 µm and φ = 1.0 and explore the effects of a velocity difference between the gas and the grains at the vent (α < 1.0).

Table 5.2. Additional cases considered in parametric study.

Grain radius, r_{grain} (µm)	Vent mass flow rate ratio, φ	Vent velocity ratio, α
0.5	1.0	0.4
0.5	1.0	0.3
0.5	1.0	0.11

To determine $h_{decoupl}$, we consider the Stokes number, $St_V \triangleq \tau_V/\tau_F$ (Crowe *et al.*, 2012), where τ_V is the grain momentum response or acceleration timescale and τ_F is the characteristic flow timescale. The momentum response or acceleration timescale, τ_V, indicates how fast the grain is accelerated by the gas to the gas velocity and is given by:

$$\tau_V = \frac{16\rho_{grain} r_{grain}^2}{3\mu C_D Re_{rel}} \tag{5.1}$$

where ρ_{grain} is the grain density (= 920 kg/m^3 for ice grains), μ is the gas dynamic viscosity, C_D is the drag coefficient, and Re_{rel} is the relative Reynolds number, defined as $(\rho|V_{gas}-V_{grain}|2r_{grain})/\mu$ where ρ is the gas density and $|V_{gas}-V_{grain}|$ is the relative speed between the grain and the gas. In a constant freestream (i.e. V_{gas} = constant), a grain starting from rest would take the time τ_V to reach ~$0.63V_{gas}$. Since $Kn_{grain} >> 1$ for all the cases considered (see Section 3.3.3), the flow is free-molecular around the grain and C_D is given by the free-molecular drag coefficient (Equation 7.71 of Bird (1994)).

For the free expansion into vacuum, we define the characteristic flow timescale, $\tau_F \triangleq L/V_{grad}$, where L is the gradient length scale based on the gas density (i.e. $L \triangleq \rho/|\nabla\rho|$) and V_{grad} is the magnitude of the gas velocity component along the direction of $\nabla\rho$, i.e. $V_{grad} \triangleq |\boldsymbol{V}_{\boldsymbol{grad}}| = |\boldsymbol{V}_{\boldsymbol{gas}} \bullet \nabla\rho|/|\nabla\rho|$, as shown in Figure 5.10a. Therefore, τ_F provides a measure of how rapidly the gas density changes along the gas streamlines.

When $St_V << 1$, the grains have plenty of time to respond to changes in the gas velocity and track the gas flow well ($V_{grain} \approx V_{gas}$). On the contrary, when $St_V >> 1$, the grains have virtually no time to respond to changes in the gas velocity and move independently of the gas flow, i.e. the grains are decoupled from the gas flow. We set the decoupling criterion to be $St_V \geq 10$. Figures 5.10b–c show the contours of St_V for Cases 1 (5 nm) and 3 (0.5 μm) respectively, superimposed on their grain jets. Both cases are for φ = 0.1 and α = 1.0. As shown in Figures 5.10b–c, St_V increases with Z for both cases and the

5-nm grains decouple from the gas flow much higher up than the 0.5-μm grains. Moreover, the contour of $St_V = 10$ is curved downwards, thus the grains decouple at lower altitudes towards the edges of the jets. Consequently, we select $h_{decoupl}$ to be the maximum height that the contour of $St_V = 10$ reaches (at $R = 0$), as marked in Figures 5.10b–c.

As shown in Figure 5.10c, St_V remains nearly constant ~O(0.1–1) in the region below the first expansion wave (where the gas properties are constant) before increasing rapidly above it. As the gas density drops rapidly across the expansion waves emanating from the edges of the vent (see Figure 4.1c), the grains quickly decouple from the gas flow. The first expansion wave crosses the centerline at $Z \approx 6.3$ m (~$2.25D_{vent}$). Slightly farther up at $Z \approx 6.5$ m (~$2.3D_{vent}$), St_V has reached 10. Within only several more D_{vent} at $Z \approx 18$ m (~$6.4D_{vent}$), St_V has increased to ~100.

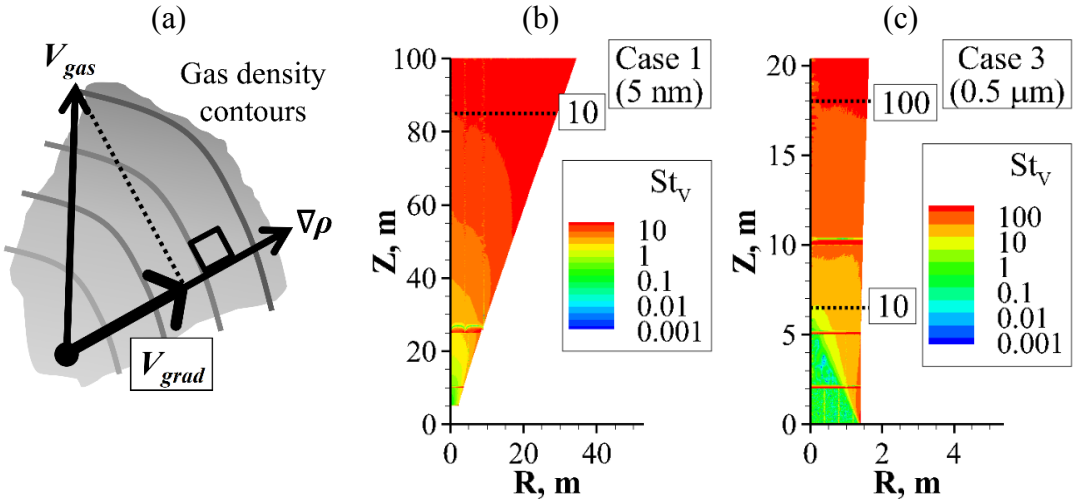

Figure 5.10. (a) Definition of $\boldsymbol{V_{grad}}$. Contours of Stokes number, St_V, for (b) Case 1 and (c) Case 3. Note the different spatial and color scales in (b) and (c). The "lines" appearing in (b) and (c) (e.g. at $Z = 25$ m in (b) and at $Z = 2$ m, 5 m and 10 m in (c)) are not real but are numerical artifacts from computing $\nabla\rho$ (to obtain τ_F) across cells of different sizes between the stages.

We notice two trends for $h_{decoupl}$ in Figure 5.11. First, $h_{decoupl}$ increases with φ ($\triangleq \dot{m}_{grain}/\dot{m}_{gas}$) in the absence of an initial velocity difference ($\alpha \triangleq V_{grain}/V_{gas} = 1.0$) regardless of the grain size, especially from $\varphi = 1.0$ to 10.0. Second, $h_{decoupl}$ increases with α (smaller velocity difference) when $\varphi = 1.0$ for $r_{grain} = 0.5$ μm. The mechanisms responsible for these trends are unclear due to the complex interactions between the gas and the grains when φ is high or α is low (see Section 5.1). Based on this decoupling criterion, nanometer-sized grains decouple at a height of $10–100D_{vent}$ while micron-sized grains decouple much closer to the vent within only several D_{vent} ($< 10D_{vent}$).

The results above are obtained from DSMC simulations for $Ma_{vent} = 5$. Since only the gas-only case has been simulated for $Ma_{vent} = 3$, its results are used to estimate $h_{decoupl}$ for $r_{grain} = 5$ nm and 0.5 μm for $Ma_{vent} = 3$. This should correspond to cases with low φ ($\leq$ 0.1) and large α (~1.0) as the gas flow is hardly affected by the grains in these cases (see Section 5.1). Comparing the Mach-3 estimates with the Mach-5 simulation results for $\varphi =$ 0.1 and $\alpha = 1.0$ (see Figure 5.11), we find that $h_{decoupl}/D_{vent}$ is nearly equal for the 0.5-μm grains (~2.6 for $Ma_{vent} = 3$ and ~2.3 for $Ma_{vent} = 5$). In contrast, $h_{decoupl}/D_{vent}$ is ~46 for $Ma_{vent} = 3$ and ~30 for $Ma_{vent} = 5$ for the 5-nm grains, but remains on the same order of magnitude. It is unclear if these trends would hold for higher φ or smaller α due to the complex gas-grain interactions occurring under such conditions (see Section 5.1). Simulations are required to determine this. Nonetheless, we expect $h_{decoupl}/D_{vent}$ to be about the same order of magnitude for both Ma_{vent}.

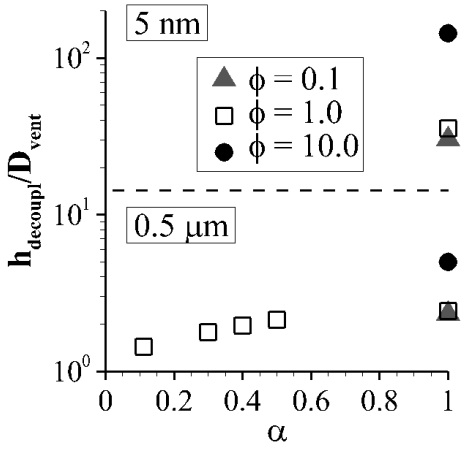

Figure 5.11. Grain decoupling height, $h_{decoupl}$, normalized by vent diameter, D_{vent}, as a function of vent mass flow rate ratio, φ, and velocity ratio, α. Note the logarithmic scale on the y-axis.

5.4. SPREADING ANGLES OF GRAIN AND GAS JETS

In this section, we determine the spreading angles of the grain and gas jets for the same cases as in Section 5.3 (see Tables 5.1 and 5.2). The spreading angle of the jet, δ, is characterized by the full-width-half-maximum (FWHM) of its number density (n) profile across its width at Z = 10 km, as shown in Figure 5.12a, i.e. $\delta = 2\tan^{-1}(0.5 \times \text{FWHM}/10$ km), where FWHM is measured in km. Note that this way of characterizing the jet width is different from that used in Section 5.1 to determine the grain jet boundaries, which are defined by the location where the grain number density drops to zero (as opposed to half the maximum).

Figures 5.12b–d show the density profiles across *half* the width of the grain (b, c) and gas (d) jets at Z = 10 km for several cases. These profiles have been smoothed to reduce statistical noise. The profiles for the other cases are similar and thus are not shown here. The gas density profiles do not drop as sharply as the grain density profiles towards the edges of the jets. In most cases, the maximum occurs at the center (R = 0), except the gas

density profile for Case 5 (α = 0.5) (see Figure 5.12d) where the maximum occurs near R = 3 km. This is because the slower grains push the gas out to the sides, leaving the central plume with less gas (see Section 5.1.2). The gas density profiles for the other cases with slower grains (α < 1.0) also exhibit a similar shape. The dips near the center in the grain density profiles in Figures 5.12b–c are not real but are due to a lack of computational particles in the smaller cells near the centerline of our wedge-shaped simulation domain (see Figure 3.4a).

Furthermore, the gas profiles for Cases 2 and 3 are not too different from that for the gas-only case, which agrees with the result from Section 5.1.1 that the effects of grains on the gas flow remain minimal for $\varphi \leq 1.0$ when $\alpha \approx 1.0$. In addition, the trapping of gas by the grain column when φ is sufficiently high (> 1.0), as inferred in Sections 5.1.1 and 5.1.3, is evident in the gas profile for Case 6 (φ = 10.0) in Figure 5.12d where there is a "bump" near the centerline. The half width of this bump is ~2 km, which is consistent with the half width of the grain column (see Figure 5.12b).

As shown in Figure 5.13a, the 0.5-μm grain jet barely spreads out ($\delta_{grain} \approx 2^{\circ}$) in the absence of an initial velocity difference (α = 1.0) regardless of φ. The 0.5-μm grains are hardly turned by the gas flow due to their large inertia and move essentially straight up. When α < 1, the 0.5-μm grain jet spreads more as α decreases (increasing velocity difference). A larger velocity difference leads to a higher drag on the grains and thus a greater spreading. However, even with $\alpha \approx 0.11$, the 0.5-μm grain jet still barely spreads, $\delta_{grain} \approx 12^{\circ}$. We expect even smaller δ_{grain} for larger grains due to their larger inertias. This is much smaller than the ~30º for the jets and ~70º for the distributed sources along the Tiger Stripes inferred by Postberg *et al.* (2011) from fitting to the E5 CDA data and the ~50º obtained by Ingersoll and Ewald (2011) from fitting to the brightness data derived from ISS images taken at high phase angles. Consequently, velocity difference at the vents

alone cannot account for the large spreading angles inferred. Other mechanisms must also be responsible.

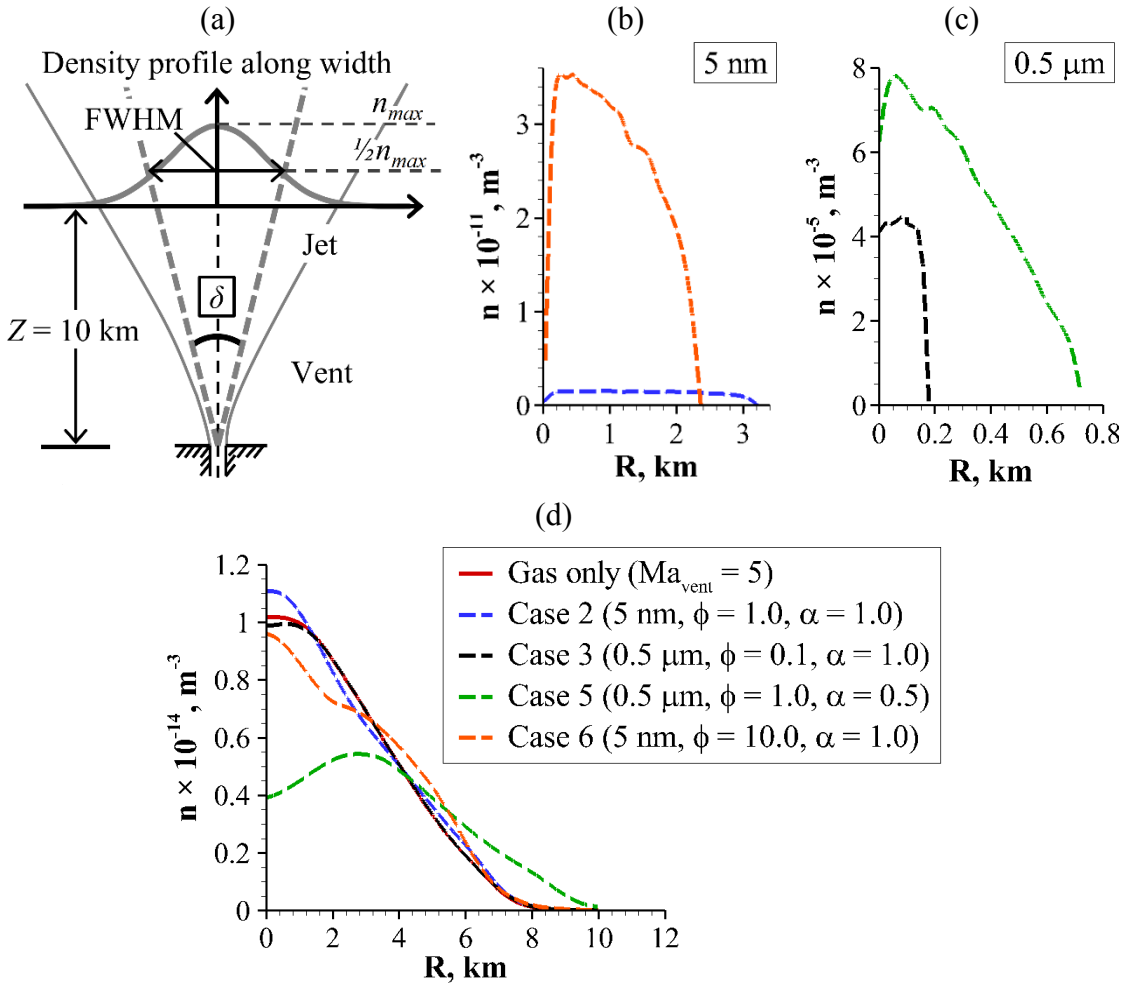

Figure 5.12. (a) Jet spreading angle, δ, measured using FWHM at Z = 10 km. Half-width density profiles of the *grain* jets for: (b) r_{grain} = 5 nm (Cases 2 and 6) and (c) 0.5 μm (Cases 3 and 5). (d) Half-width density profiles of the *gas* jets for Cases 2, 3, 5 and 6. The density profile for the Mach-5 gas-only case is also included for comparison. Note the different scales on the axes of (b)–(d).

As shown in Figure 5.13a, the 5-nm grains spread out more significantly than the 0.5-μm grains. Unlike the 0.5-μm grains, the spreading angle of the 5-nm grain jet varies with φ in the absence of an initial velocity difference (α = 1.0). The 5-nm grain jet is narrower for larger φ (more grains in the flow), with δ_{grain} dropping slightly from φ = 0.1 to 1.0 but falling significantly from φ = 1.0 to 10.0. When φ = 10.0, the gas flow is significantly affected by the grains, which in turn affects the ability of the gas flow to transfer momentum to the grains to spread them (see Section 5.1.3).

Figure 5.13b shows that in the absence of an initial velocity difference (α = 1.0), the spreading angle of the gas jet, δ_{gas}, deviates more from that of the gas-only case ($\delta_{gas} \approx$ 43º) as φ increases, regardless of the grain size. This is consistent with our results in Section 5.1.1: the grains have a greater effect on the gas flow as φ increases. For the cases with 0.5-μm grains, φ = 1.0 and $\alpha < 1$, we find that the gas jet spreads more as α decreases (increasing velocity difference). This is consistent with our results in Section 5.1.2: with a smaller α, the grains pose a greater obstruction to the gas flow exiting the vent and push it out more in the lateral direction, resulting in a broader gas jet.

The results above are obtained from DSMC simulations for Ma_{vent} = 5. For Ma_{vent} = 3, the grain jets should spread more due to higher gas densities (greater drag). The difference in δ_{grain} between the different Ma_{vent}, however, should decrease as r_{grain} increases because the larger grains have a larger inertia (less affected by the gas flow) and decouple at a lower height (shorter distance over which the grains are affected by the gas flow). Consequently, we expect δ_{grain} to differ only slightly for the 0.5-μm grains and more for the 5-nm grains between the different Ma_{vent}. The *gas-only* jet for Ma_{vent} = 3 has $\delta_{gas} \approx$ 56º, thus we expect the gas jets for the cases with grains to also be broader for Ma_{vent} = 3.

From fitting to INMS and UVIS data, Smith *et al.* (2010) and Tenishev *et al.* (2010) obtained $\delta_{gas} \approx$ 60º and 50º–80º respectively. These estimates agree with δ_{gas} for Ma_{vent} = 3

but are larger than δ_{gas} for Ma_{vent} = 5. Consequently, their estimates suggest low Mach numbers (< 5), which are consistent with the inferred Mach numbers of 1.3–1.7 from earlier UVIS observations (Hansen *et al.*, 2008). However, more recent UVIS observations inferred higher Mach numbers of 5–8 (Hansen *et al.*, 2011).

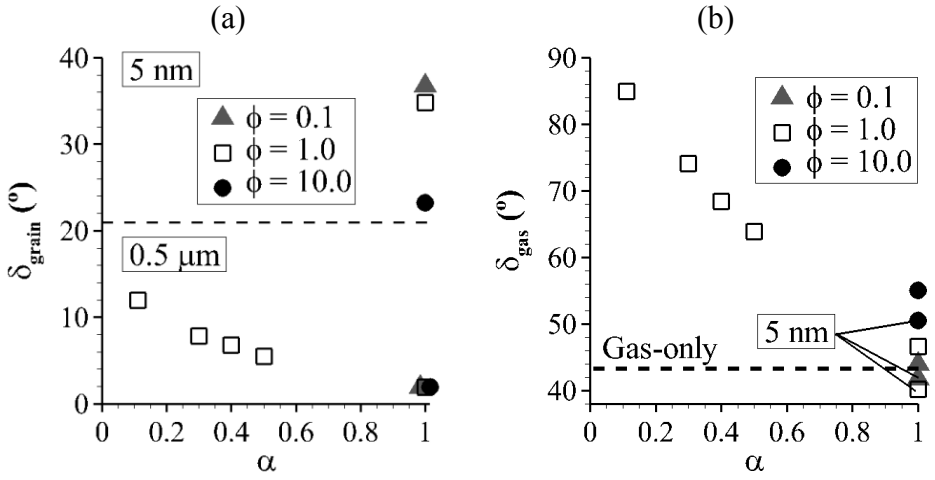

Figure 5.13. (a) Grain jet spreading angle, δ_{grain}, as a function of vent mass flow rate ratio, φ, and velocity ratio, α. (b) Gas jet spreading angle, δ_{gas}, as a function of φ and α. Cases with 5-nm grains are labeled; others are cases with 0.5-μm grains. The dashed black line indicates δ_{gas} for the Mach-5 gas-only case for comparison.

5.5. GRAIN ACCELERATION

In this section, we investigate the maximum speeds, V_{max}, achieved by the grains due to acceleration by the gas for the same cases as in Sections 5.3 and 5.4 (see Tables 5.1 and 5.2). For a given Ma_{vent}, the maximum speeds achieved by the grains depend on D_{vent}. A larger vent allows the grains to be accelerated over a longer distance and thus achieve a greater V_{max}. However, V_{max} is limited by the speed achieved by the gas when the flow becomes free-molecular, which in this case is nearly the ultimate speed, $V_{ult} \approx 1005$ m/s.

Figure 5.14a shows the ranges of V_{max} for the different cases considered for the nominal D_{vent} = 2.8 m ($\dot{m}_{vent} \approx 0.2$ kg/s) for $Ma_{vent} = 5$. As shown schematically in Figure 5.14b, the grains along the centerline are accelerated to the highest V_{max} (marked by the upper symbol in Figure 5.14a). The grains are progressively accelerated to lower V_{max} farther away from the centerline due to the more rapid decrease in gas density with altitude away from the centerline. Along the edges, the grains are accelerated to the lowest V_{max} (marked by the lower symbol in Figure 5.14a).

As shown in Figure 5.14a, in all the cases considered, all the grains are accelerated to V_{max} greater than the two-body escape speed of Enceladus, $V_{esc} \approx 240$ m/s, even when the grains exit the vent much slower than the gas ($\alpha \approx 0.11$). Saturn's gravity has been neglected when calculating V_{esc}. Kempf *et al.* (2010) included Saturn's gravity in their calculations and determined that the ejection speeds must be at least 228 m/s for the grains to truly escape Enceladus into the E ring and not collide with Enceladus within its first orbit after ejection. Consequently, all the grains escape Enceladus into the E ring for all our cases. This contradicts other results. Schmidt *et al.* (2008) and Ingersoll and Ewald (2011) determined that only ~10% of the grain mass exiting the vents escape Enceladus. Moreover, VIMS observations indicate that larger grains have progressively slower ejection speeds (Hedman *et al.*, 2009). In addition, the observed stratification of plume grains by salt content suggests that most of the grains are larger and have very slow ejection speeds (Postberg *et al.*, 2011). However, we have only considered two grain sizes, r_{grain} = 5 nm and 0.5 μm, for several discrete ejection velocities ≥ 100 m/s. Larger or initially slower grains would not be accelerated to such high speeds for this nominal vent size. Later in this section, we will examine this further and estimate the largest grains that can be accelerated to V_{esc} as a function of D_{vent}.

The results above are obtained from DSMC simulations for $Ma_{vent} = 5$. For $Ma_{vent} = 3$, the gas speed at the vent is slightly slower but the gas density is nearly an order of magnitude higher (see Table 3.1), thus we expect the effects of gas density to be greater. As a result, we expect the grains to be accelerated to greater speeds for $Ma_{vent} = 3$ for the same initial speeds at the vent. However, as mentioned earlier, the highest speed the grains can attain is also limited by $V_{ult} \approx 1005$ m/s for $Ma_{vent} = 3$ since the same stagnation/reservoir conditions have been used (see Section 3.2.1).

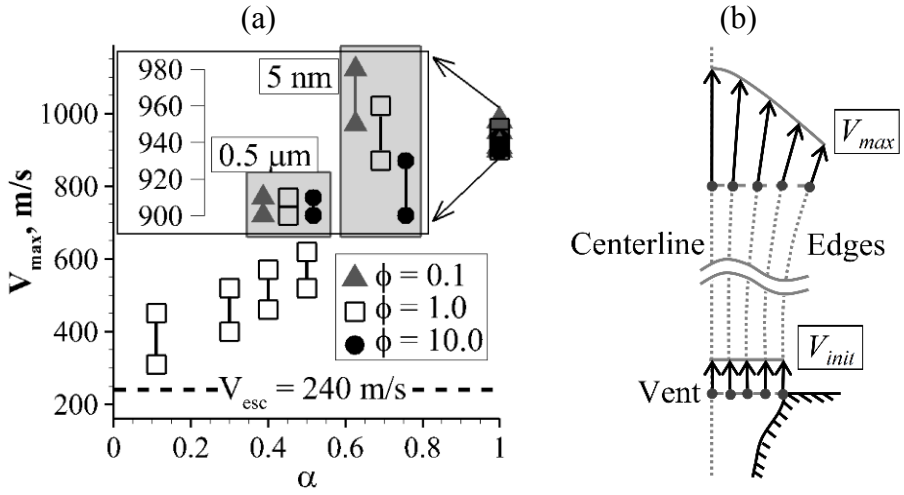

Figure 5.14. (a) Ranges of maximum grain speeds, V_{max}, as a function of vent mass flow rate ratio, φ, and velocity ratio, α, for $D_{vent} = 2.8$ m ($\dot{m}_{vent} \approx 0.2$ kg/s) and $Ma_{vent} = 5$ (gas speed at the vent is ~900 m/s). The inset shows cases for $\alpha = 1.0$ magnified and separated for clarity. All cases are for $r_{grain} = 0.5$ μm unless labeled otherwise. For each α, the upper and lower symbols indicate the upper and lower bounds respectively. (b) Schematic of how V_{max} varies from the centerline to the edges.

Next, we estimate the largest grain radius, r_{max}, that can be accelerated to V_{esc} (~240 m/s) as a function of D_{vent}. This largest grain radius occurs at the *centerline* where the gas density is the highest and the acceleration length is the longest. Grains with $r_{grain} \leq r_{max}$ are accelerated to $V_{max} \geq V_{esc}$ while grains with $r_{grain} > r_{max}$ are accelerated to $V_{max} < V_{esc}$. A

larger vent leads to a longer acceleration length and thus allows larger grains to be accelerated to V_{esc}. Moreover, r_{max} depends on Ma_{vent}.

Figure 5.15 shows r_{max} as a function of D_{vent} for Ma_{vent} = 3 and 5. We calculate r_{max} using the centerline gas properties from gas-only simulations, thus our calculations are valid for cases with low grain/gas mass ratios ($\varphi \leq 0.1$) since the gas is affected by the grains when φ is high (see Sections 5.1.1 and 5.1.3). Moreover, the grains start from rest at the vent, i.e. $V_{init} = 0$. Consequently, larger grains could be accelerated to V_{esc} if $V_{init} > 0$, and the estimated values of r_{max} are simply the *lower* bound.

As shown in Figure 5.15, for Ma_{vent} = 5 and D_{vent} = 2.8 m, r_{max} is ~8 μm, thus our nominal D_{vent} for Ma_{vent} = 5 can easily launch grains detectable by CDA ($r_{grain} \geq 1.6$ μm) to escape speeds. The Mach-3 vent conditions can accelerate larger grains to escape speeds for the same D_{vent} due to higher gas densities (see Table 3.1). For Ma_{vent} = 3 and D_{vent} = 2.8 m ($\dot{m}_{vent} \approx 1.5$ kg/s), r_{max} is ~40 μm. In fact, a small D_{vent} ~O(0.1 m) is sufficient to accelerate grains detectable by CDA to escape speeds for either Ma_{vent}.

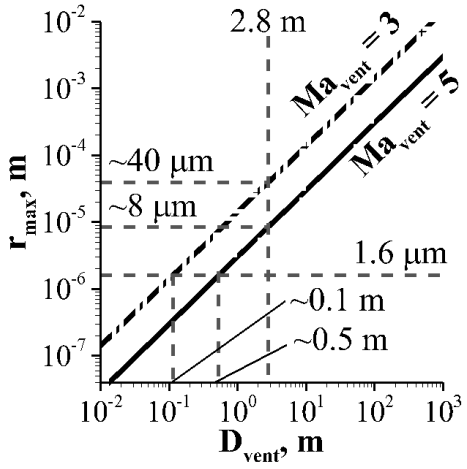

Figure 5.15. Largest grain radius, r_{max}, that can be accelerated to V_{esc} (~240 m/s) along the centerline for Ma_{vent} = 3 and 5 for V_{init} = 0 (starting from rest at the vent).

5.6. SUMMARY

In this chapter, we examined how the grains affect the expansion flow from the vents into vacuum and investigated several phenomena related to the gas-grain interaction during expansion, such as the decoupling of grain motion from gas motion and the spreading and acceleration of grains by the expanding gas flow. A parametric study was conducted, involving grain radius/size, r_{grain}, vent mass flow rate ratio, φ ($\triangleq \dot{m}_{grain}/\dot{m}_{gas}$), and vent velocity ratio, α ($\triangleq V_{grain}/V_{gas}$). The vent mass flow rate ratio is proportional to the *total* ice/vapor mass ratio of the plume (Crowe *et al.*, 2012) while the vent velocity ratio measures the effects of a velocity difference between the gas and the grains at the vent. We only modeled the exchange of momentum and energy between the gas and the grains but not the exchange of mass (no phase change). Moreover, we mostly considered the Mach-5 vent conditions, though the results from the Mach-3 vent conditions should be qualitatively similar. Below is a summary of the important results obtained from the study.

The effects of grains on the gas flow increase as φ increases or as α decreases (vent velocity difference increases) due to the greater exchange of momentum and energy between the gas and the grains. The gas temperatures are higher and the gas speeds are slower due to interaction with the grains. If φ is sufficiently high (> 1), the grains form a dense column that traps the gas flow, thus constraining its expansion and preventing it from expanding freely into vacuum as it would in the absence of grains. Moreover, if α is sufficiently low (≤ 0.5), the gas flow can be decelerated by the grains as its momentum is transferred to the slow grains to accelerate them. Furthermore, grains exiting the vent slower than the gas flow obstruct the gas flow and push it out to the sides, leading to a broader gas jet. The slower the grains are relative to the gas flow (smaller α), the broader the gas jet.

Smaller grains have a greater and more widespread effect on the gas flow for the same φ and α. For the same total mass, smaller grains are more numerous (the number of grains is inversely proportional to r_{grain}^3). Moreover, smaller grains track the gas flow better due to their lower inertia. Due to these factors, smaller grains are more widely distributed throughout the flow and thus affect a larger portion of the gas flow. For the same total mass, the total surface and cross-sectional areas of the grains are inversely proportional to r_{grain}. As a result, smaller grains also have larger total surface and cross-sectional areas, leading to a higher overall heat transfer rate and a higher drag on the gas flow respectively. For the same total mass, smaller grains are also more effective at trapping gas as their larger total cross-sectional area results in a tighter seal.

For $\varphi \leq 0.1$, the grains barely affect the gas flow regardless of r_{grain} and α. In fact, for $\varphi \leq 1.0$, the effects of the grains on the gas flow remain minimal unless a large velocity difference exists between the gas and the grains at the vent ($\alpha \leq 0.5$). For $\varphi > 1.0$, the effects of the grains on the gas flow are no longer negligible regardless of r_{grain} and α. Figure 5.16 illustrates the effects of the 5-nm and 0.5-μm grains on the gas flow. Note that these plots are only *qualitative* in nature and not quantitative.

So far, the inferred plume ice/vapor mass ratios have been ≤ 1.0 (Hedman *et al.*, 2009; Ingersoll and Ewald, 2011; Kieffer *et al.*, 2009; Porco *et al.*, 2006; Schmidt *et al.*, 2008), thus plausible φ are also probably ≤ 1.0 (φ may vary between the individual jets). Since the larger grains possibly exit the vents slower than the gas flow (Hedman *et al.*, 2009; Ingersoll and Ewald, 2011; Postberg *et al.*, 2011; Schmidt *et al.*, 2008), their effects on the gas flow are enhanced. However, the inferred ice/vapor mass ratios are for a size distribution, thus the larger grains account for a smaller fraction of the total grain mass. The effects of a velocity difference between the gas and the larger grains at the vent are

thus mitigated. As a result, we do not expect the ice grains to significantly affect the gas component of the Enceladus plume.

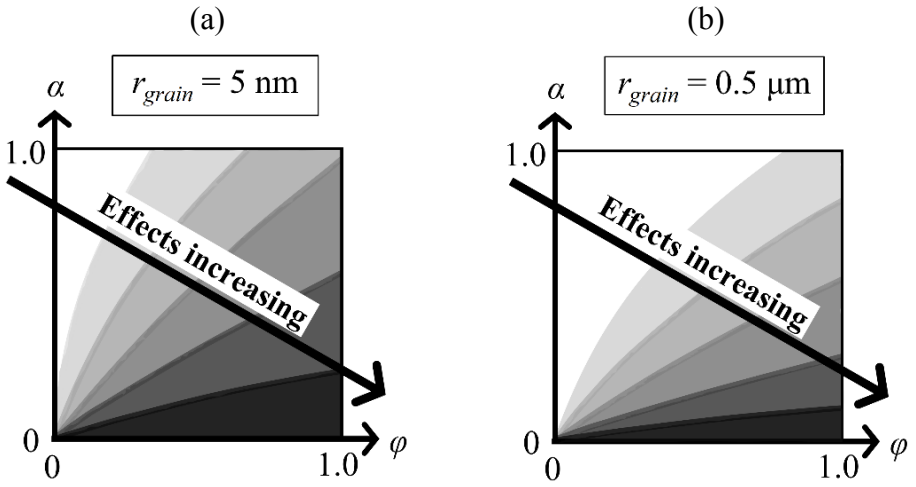

Figure 5.16. Qualitative plots showing the effects of grains on the gas as a function of grain radius (r_{grain}), vent mass flow rate ratio (φ), and vent velocity ratio (α).

Smaller grains are more strongly affected by the gas flow. Nanometer-sized grains decouple from the gas flow at altitudes of 10–100D_{vent} above the vents and spread out with the gas flow, whereas micron-sized grains decouple lower, at < 10D_{vent}, and remain in collimated beams. The spreading angle of the grain jet increases as α decreases (vent velocity difference increases), but remains small (≤ 12°) for r_{grain} = 0.5 μm even with small $\alpha \leq 0.5$. Larger grains would spread even less. Consequently, the large spreading angles ≥ 30° inferred (Ingersoll and Ewald, 2011; Postberg *et al.*, 2011) cannot be caused by a vent velocity difference alone. Micron-sized grains may have emerged from the vents already with a large spreading angle due to vent geometry or processes occurring below the surface. Spreading above the vents caused by collisions between grains should be minimal for plausible $\varphi \leq 1.0$ (see Appendix A).

In addition, nanometer-sized grains are accelerated close to gas speeds while micron-sized grains tend to retain their initial speeds at the vent due to their larger inertia. Consequently, the speeds of the smaller grains provide a better constraint on the gas speeds while the ejection (initial) speeds of the larger grains can be better constrained by measurements. In all the cases considered, *all* the grains are accelerated to escape speeds (> 240 m/s), even when the grains start much slower than the gas flow at the vent ($\alpha \leq 0.5$). This contradicts other results and observations, which indicate that a large fraction of the grains are ejected at below escape speeds (Hedman *et al.*, 2009; Ingersoll and Ewald, 2011; Postberg *et al.*, 2011; Schmidt *et al.*, 2008). However, we have only considered two grain sizes, r_{grain} = 5 nm and 0.5 μm, ejected at several discrete velocities ≥ 100 m/s. Larger or initially slower grains would not be accelerated to escape speeds. The largest r_{grain} that can be accelerated by the gas flow from rest to escape speeds is proportional to D_{vent}. Small vents, D_{vent} ~O(0.1 m), are enough to launch grains with r_{grain} = 1.6 μm (CDA threshold) from rest to escape speeds for our Mach-3 and Mach-5 vent conditions.

Chapter 6.

Results from Computational Subsurface Model

In this chapter, we examine the results obtained from the computational subsurface model (see Section 3.2.2). The subsurface flow simulations and results were generated by our collaborators (Li, Z., Dhariwal, R., and Levin, D.). Their results are discussed here because they directly feed into our DSMC simulations above the surface and provide the needed context. First, we investigate the flowfield in the subsurface channel. Then, using the conditions produced at the vent, we continue to propagate the flow into the far-field until it becomes free-molecular. We also study this resulting collisional near-field directly above the vent.

6.1. SUBSURFACE FLOWFIELD

The subsurface flow is dominated by evaporation from the channel walls and not the flow at the inlet. As shown in Figure 6.1a, the gas pressure, p, is high at the inlet, ~300 Pa (see Figure 3.3 for inlet conditions), but quickly drops to ~10–11 Pa, which is close to the H_2O equilibrium vapor pressure ($p_{vap} \approx 9$ Pa) over ice at the wall temperature, T_{wall} = 230 K. It remains so throughout most of the channel before dropping further near the vent as the flow accelerates out of the vent. As shown in Figure 6.1b, the gas number density, n, is also nearly uniform throughout most of the channel at ~3–3.5 × 10^{21} m^{-3}, which is close to the value of 2.8 × 10^{21} m^{-3} corresponding to p_{vap} at T_{wall}. However, as shown in Figure 6.1c, the gas translational temperature, T_{tr}, is not constant throughout the channel. It is ~230 K near the walls as the vapor has just evaporated from the walls. Near the centerline, T_{tr} is higher due to interaction with the grains.

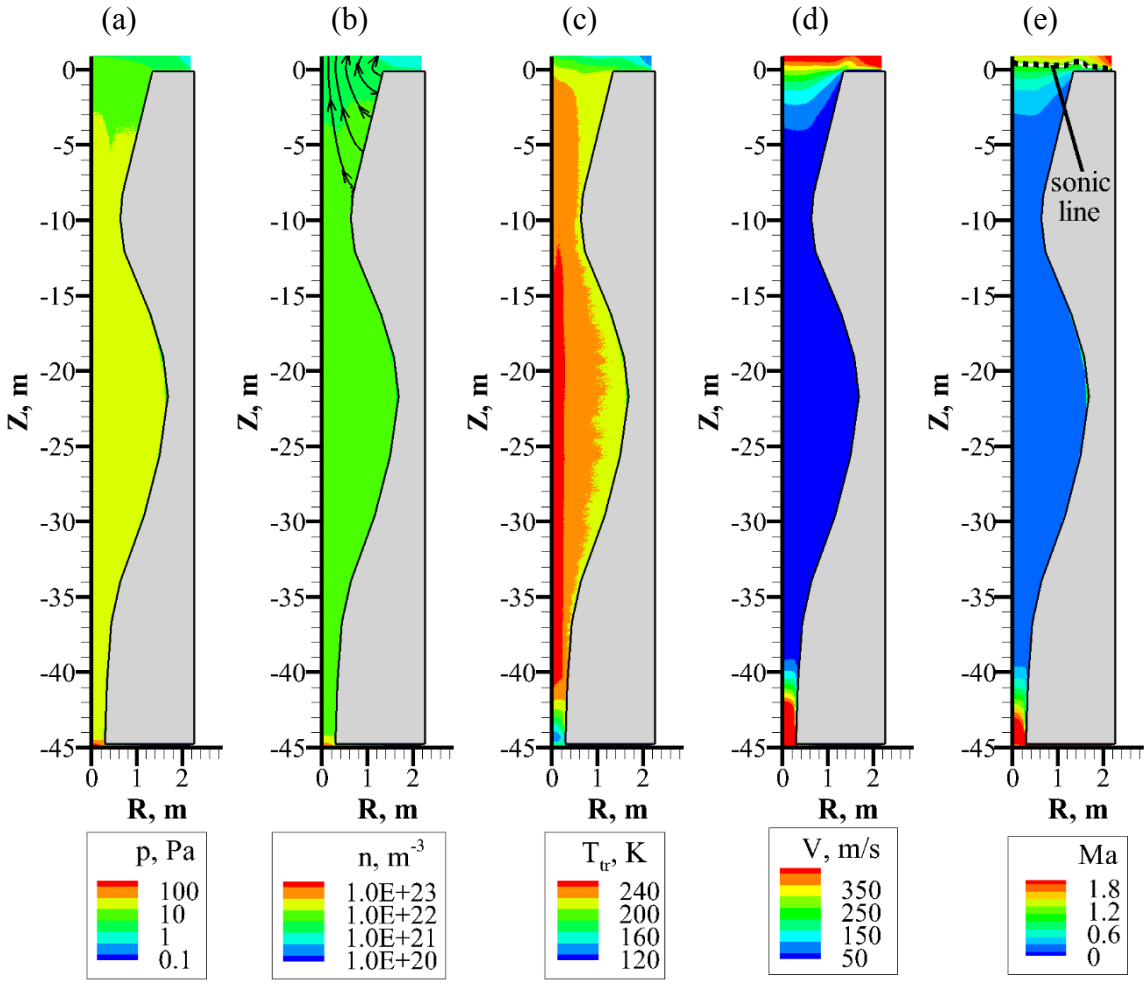

Figure 6.1. Contours of *gas* properties for the subsurface flow: (a) pressure, p, (b) number density, n, (c) translational temperature, T_{tr}, (d) vertical velocity component, V, and (e) Mach number, Ma. The surface is located at $Z = 0$. Note that the x- and y-axis have been plotted on different spatial scales for clarity. (*Adapted and reprinted with permission from Li et al.*)

As shown in Figure 6.1d (V is the vertical velocity component), the gas flow enters the channel at the inlet at ~370 m/s but slows down rapidly (probably through a shock or a set of shocks) to < 50 m/s and remains slow throughout most of the channel before experiencing a rapid acceleration right before it exits the vent. This is consistent with the contours of Mach number, Ma, shown in in Figure 6.1e where the flow is mostly subsonic

throughout the channel before accelerating to nearly sonic speeds as it exits the vent. As we shall see later, the flow is still slightly subsonic at the vent but reaches sonic conditions almost immediately after it exits, as indicated by the sonic line in Figure 6.1e.

Next, we examine the grains. As shown in Figure 6.2a, the grains are barely affected by the gas flow and remain mostly in a tight beam. For the most part, they also do not collide with the channel walls. This is due to the channel geometry chosen. If the channel were not as straight but had more twists and turns, the grains would have scattered off the walls and their motion would have been more complicated. Moreover, as shown in Figure 6.2b, the grains barely grow, starting with an initial size of 1 μm at the inlet, and grow at most to ~1.03 μm. As shown in Figure 6.2c, the grains start at ~370 m/s at the inlet but are slightly decelerated as they move through the much slower gas resulting from evaporation from the channel walls.

The streamlines in Figure 6.1b indicate that most of the gas flow at the *vent* actually originates from the channel walls very near the vent. Since only a negligible amount of vapor condenses on the grains in the channel, most of the gas flow from the inlet must have condensed on the channel walls and never makes it out of the vent. As a result, the gas flow emerging from the vent does not tell us much about the inlet conditions near the source but more about the subsurface wall conditions, particularly those close to the vent. On the other hand, there is hardly any exchange of mass and momentum between the gas and the grains in the channel, thus the grains mostly retain their properties at the source. Consequently, the grains emerging from the vent inform us about the source conditions.

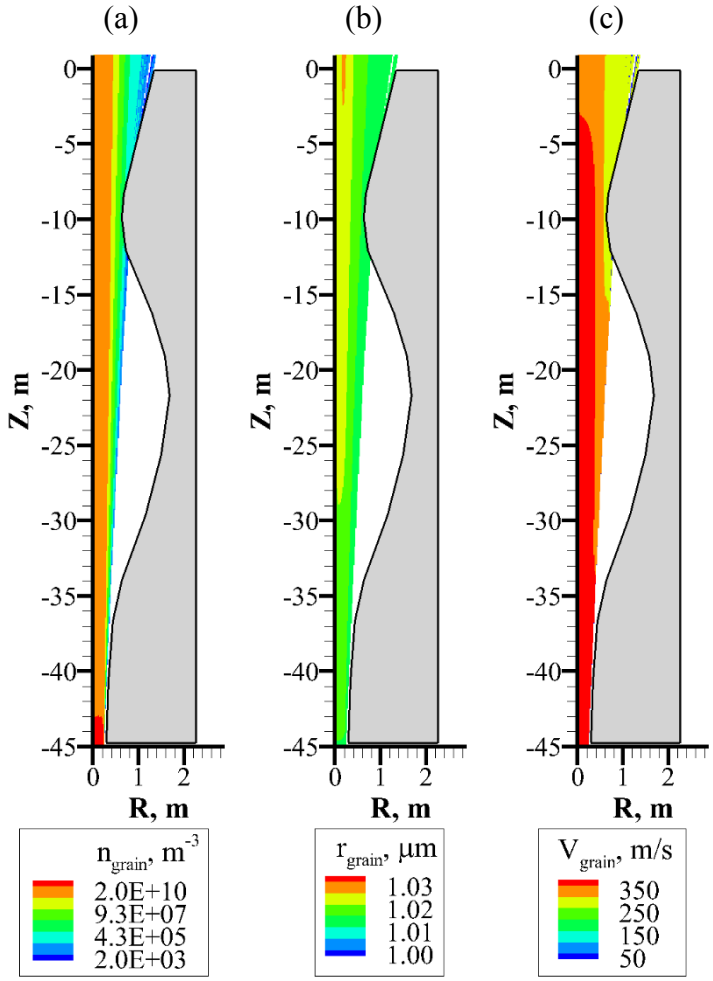

Figure 6.2. Contours of *grain* properties for the subsurface flow: (a) number density, n_{grain}, (b) radius, r_{grain}, and (c) vertical velocity component, V_{grain}. The surface is located at $Z = 0$. Note that the x- and y-axis have been plotted on different spatial scales for clarity. (*Adapted and reprinted with permission from Li et al.*)

Whether the gas flow emerging from the vent is dominated by evaporation from the channel walls or by the inlet flow depends on two factors: (1) the ratio of the channel length to its width, and (2) the ratio of the inlet pressure to the wall equilibrium vapor pressure. If the inlet pressure is much higher than the wall equilibrium vapor pressure, the inlet flow would condense on the walls and thus be less likely to make it out of the vent. If the channel is long and narrow, there is a greater distance over which evaporation from the walls could occur and the inlet flow could condense. The case considered above has very large ratios of channel length to width (> 16, based on vent diameter) and inlet pressure to equilibrium vapor pressure at the walls (> 30), thus we would expect the flow at the vent to be dominated by evaporation from the walls.

6.2. COLLISIONAL NEAR-FIELD ABOVE THE VENT

Figures 6.3a–b show the distributions of various gas and grain properties across the vent from the computational subsurface model (U and T_{rot} are the horizontal velocity component and the gas rotational temperature respectively, and T_{grain} is the grain temperature). As shown in Figure 6.3a, the flow is slightly subsonic at the vent, $Ma \approx 0.8$. The mass flow rate of gas out of the vent is ~0.1 kg/s, which is less than ~0.2 kg/s at the inlet (see Figure 3.3 for inlet conditions), because most of the inlet flow condenses on the channel walls and never makes it out. As expected, the mass flow rate of grains is ~0.005 kg/s at both the inlet and the vent because the grains hardly grow in the channel. In addition, the grains actually exit the vent, on the average, faster than the gas because the gas exiting the vent mostly originates from the walls close to the vent and has only begun to expand as it reaches the vent. The vent mass flow rate ratio, φ, is ~0.05 while the vent velocity ratio, α, which varies across the vent, is on the average ~1.1–1.2 (see definitions of φ and α in Chapter 5).

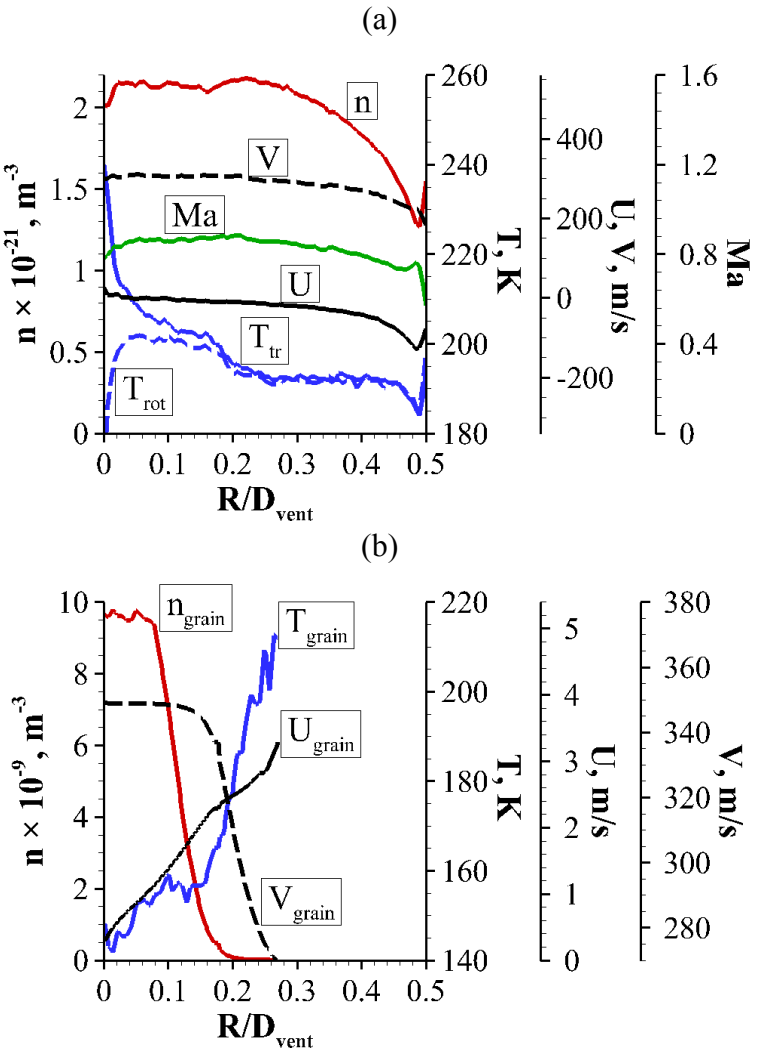

Figure 6.3. Properties across the vent from the computational subsurface model: (a) gas and (b) grains.

While n remains mostly uniform throughout the subsurface channel (see Figure 6.1b), it drops rapidly above the vent as the flow expands freely into vacuum. As shown in Figure 6.4a, n drops by about two orders of magnitude from ~10^{21} m^{-3} to ~10^{19} m^{-3} within just the first 25 m (~$8.9D_{vent}$) and has dropped by nearly eight orders of magnitude to ~10^{13} m^{-3} at $Z = 20$ km (~$7140D_{ven}$), as shown in Figure 6.4b. In the flow expanding from the Mach-5 vent conditions (see Chapter 4), the first expansion wave does not cross the centerline until $Z \approx 6.3$ m (~$2.25D_{vent}$) before the gas properties start to drop. Here, the first expansion wave crosses the centerline only a very short distance above the vent (as indicated by the sonic line in Figure 6.1e) and thus n drops almost immediately after the flow emerges from the vent.

As shown in Figures 6.4c–d, the local Knudsen number of the flow, Kn, (see definition in Section 3.3.1), varies by several orders of magnitude from ~10^{-3} near the vent to > 10 at $Z = 20$ km. Consequently, as with the Mach-5 vent conditions (see Figures 4.1a–b), the expansion flow passes through multiple regimes, from nearly continuum and highly collisional near the vent to free-molecular at higher altitudes.

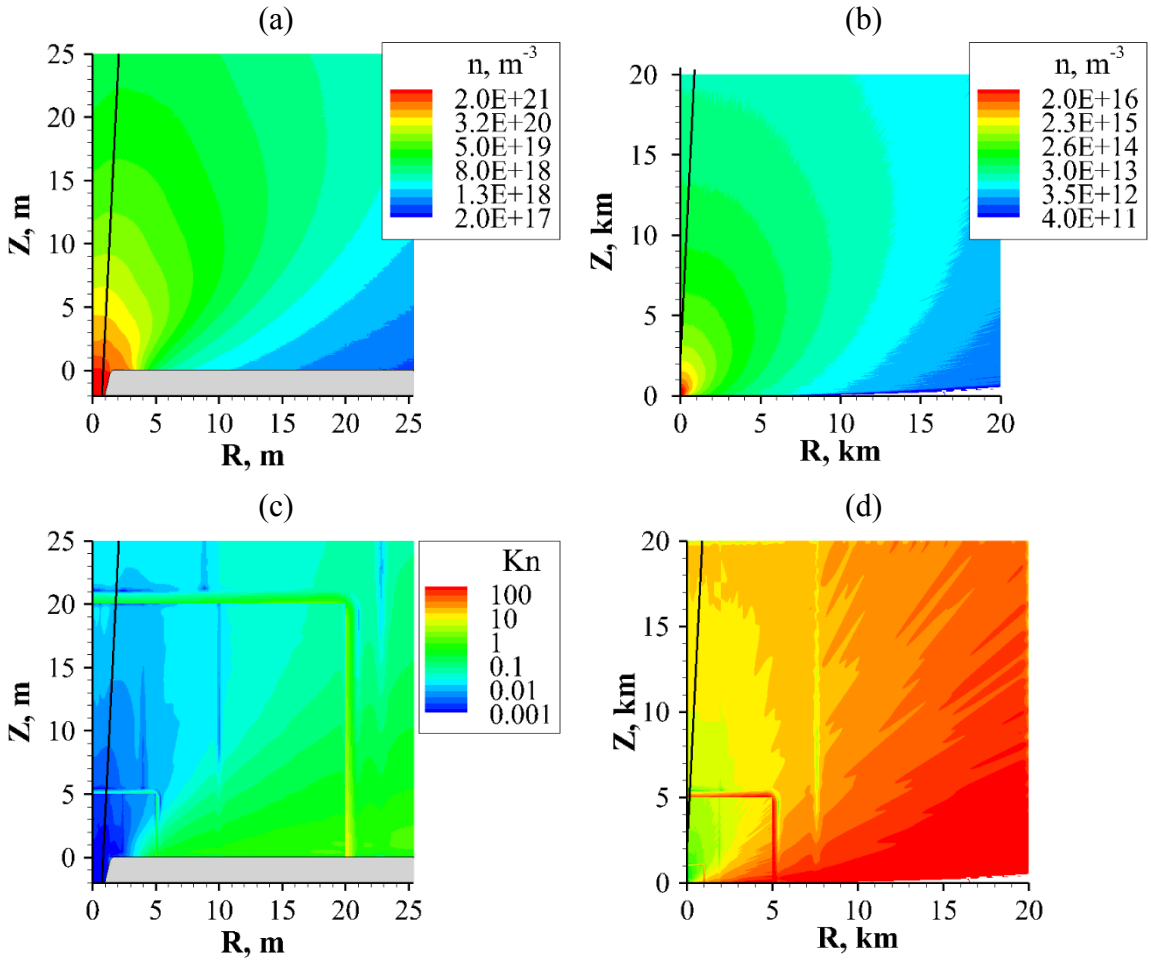

Figure 6.4. Contours of gas number density, n, from (a) vent to 25 m and (b) vent to 20 km. Note the different color bars in (a) and (b). Contours of local Knudsen number, Kn, from (c) vent to 25 m and (d) vent to 20 km. Both (c) and (d) share the same color bar. Note the shift in axis scales from (a) to (b) and from (c) to (d). In (c) and (d), the horizontal and vertical "lines" (e.g. at Z = 5 m, 20 m and 5 km and at R = 20 m, 5 km and ~8 km) are numerical artifacts either from computing $|\nabla\rho|$ across cells of different sizes along stage boundaries or from smoothing ρ across processor boundaries to reduce statistical noise when computing $|\nabla\rho|$. The black lines mark the boundary of the grain jet.

Figures 6.5a–b show T_{tr} in the immediate vicinity of the vent (a) and up to an altitude of 20 km (~7140D_{vent}) (b). Figures 6.5c–d show T_{rot} in the same spatial regions and on the same temperature scale. As shown in Figures 6.5a and 6.5c, the flow is in equilibrium ($T_{tr} \approx T_{rot}$) close to the vent in the core region near the centerline. Away from the centerline near the surface where sublimation is occurring, $T_{tr} \neq T_{rot}$. At higher altitudes, the flow is also not in equilibrium, as shown in Figures 6.5b and 6.5d. The translational mode requires fewer collisions to equilibrate and thus T_{tr} continues to drop with altitude while T_{rot} remains constant or "frozen" beyond a certain altitude because there are not enough collisions for the rotational mode to equilibrate. These trends are consistent with the contours of *Kn* shown in Figures 6.4c–d where *Kn* is small close to the vent in the core region near the centerline and is larger away from the centerline near the surface and at higher altitudes.

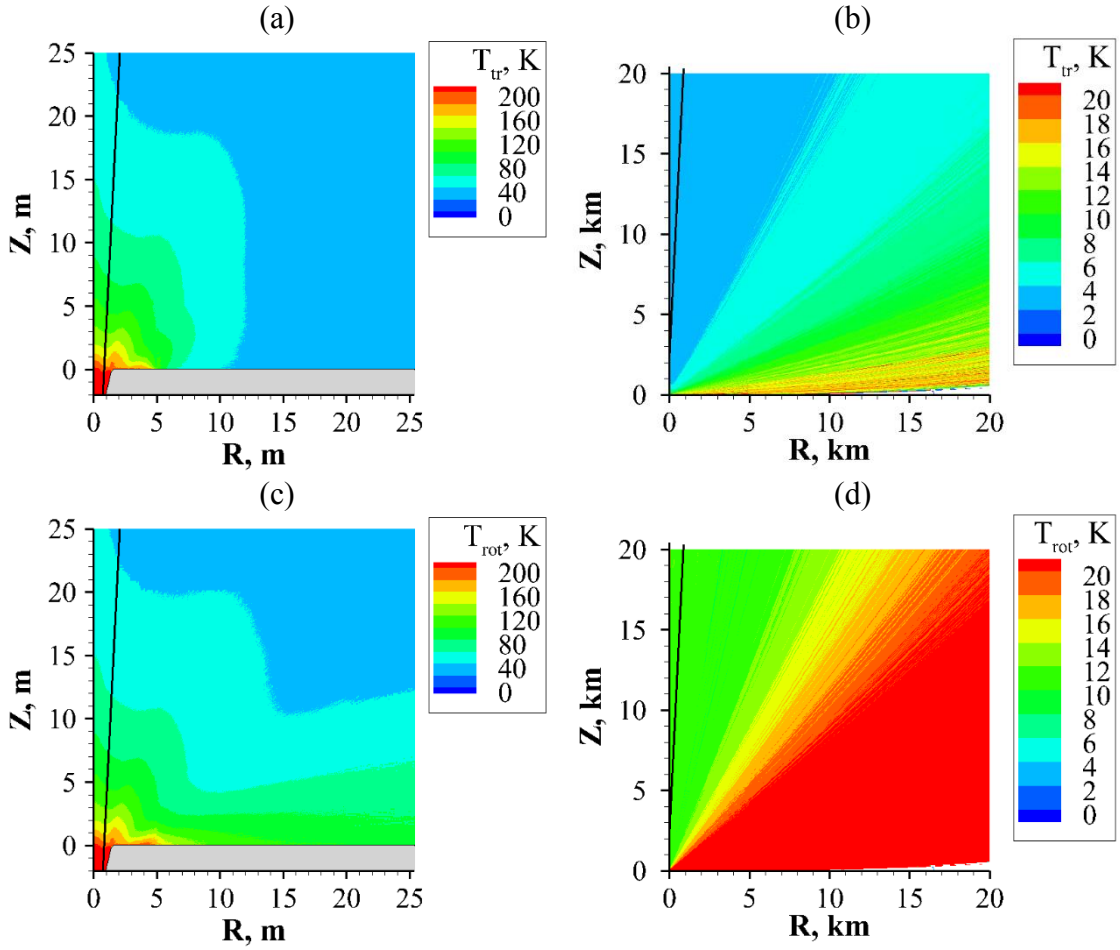

Figure 6.5. Contours of gas translational temperature, T_{tr}, from: (a) vent to 25 m and (b) vent to 20 km. Contours of gas rotational temperature, T_{rot}, from: (c) vent to 25 m and (d) vent to 20 km. Note the shifts in axis and temperature scales from (a) to (b) and from (c) to (d). The black lines mark the boundary of the grain jet.

As shown in Figure 6.6a, the gas accelerates very rapidly from ~300 m/s to ~800 m/s within just the first 25 m (~8.9D_{vent}). The magnitude of acceleration is much greater in this case than in the Mach-5 case (see Figure 4.2e) where the gas only accelerates from ~900 m/s to ~980 m/s. This is because the gas has done most of its expansion below the vent in the Mach-5 case and only has a bit more to expand above before reaching the ultimate speed, $V_{ult} \approx 1005$ m/s. In contrast, the gas has barely expanded in this case as it reaches the vent since most of the gas at the vent originates from the channel walls very near the vent (see Figure 6.1b). As a result, the gas still has to undergo significant expansion above the vent before reaching V_{ult}.

In this case, $V_{ult} \neq 1005$ m/s, which is calculated based on a stagnation temperature, T_0, of 273.16 K in the reservoir (see Figure 3.3). Instead, the more appropriate T_0 is T_{wall}, which is 230 K, because most of the gas is evaporated from the channel walls. This results in $V_{ult} \approx 920$ m/s. As shown in Figure 6.6b, the maximum speed achieved by the gas is ~890 m/s (near the centerline), thus the flow at the vent is not collisional enough to convert *all* the molecular thermal and rotational energy into the directed mean kinetic energy of the gas. This conversion of energy is captured in the contours of Mach number, *Ma*, shown in Figure 6.6c where *Ma* increases as the gas expands (bulk gas speed increases and T_{tr} drops). Moreover, the flow at the edges reach slower maximum speeds, as shown in Figure 6.6b, due to the lower collision rates there. This is reflected in Figures 6.4c–d where *Kn* is larger at the edges. The same sonic line in Figure 6.1e is also indicated in Figure 6.6c.

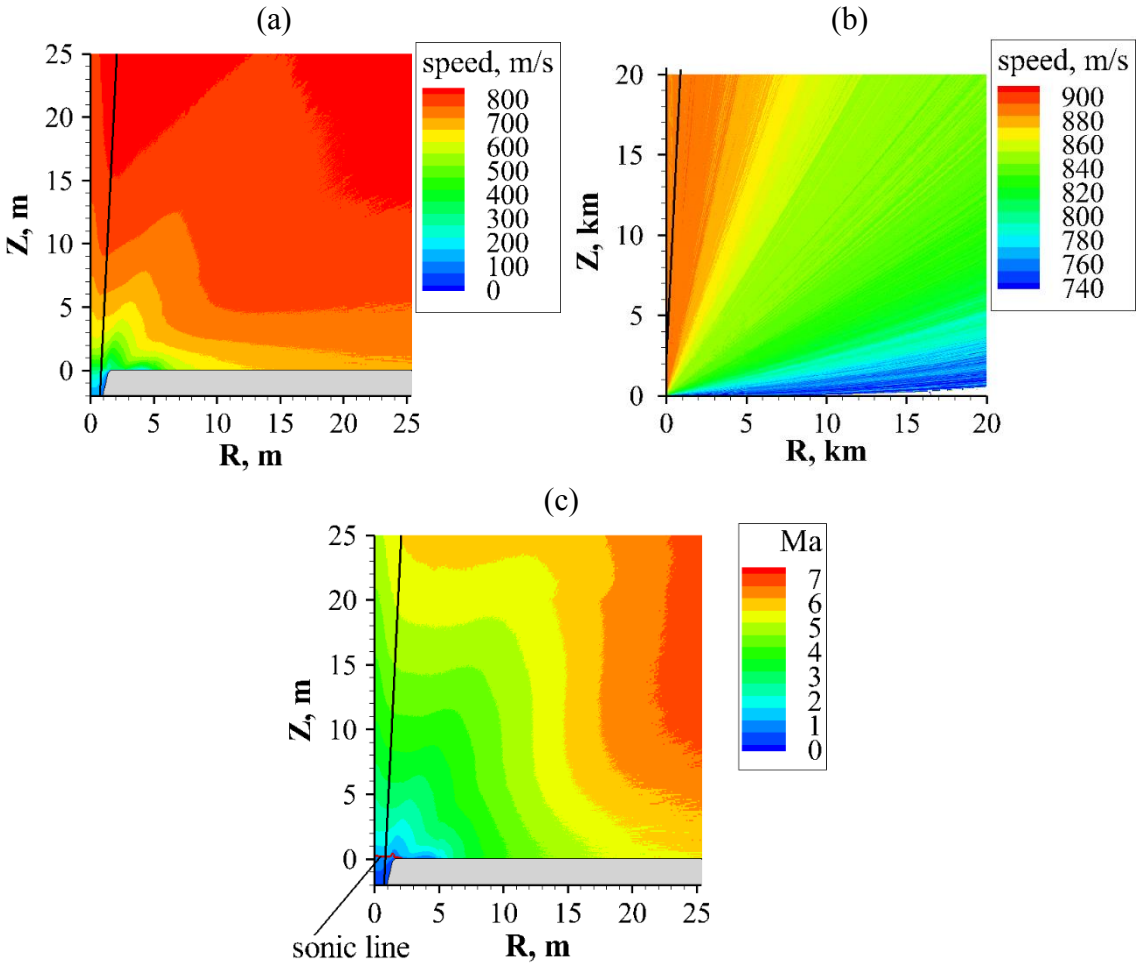

Figure 6.6. Contours of gas speed from: (a) vent to 25 m and (b) vent to 20 km. Note the shifts in axis and speed scales from (a) to (b). (c) Contours of Mach number, *Ma*, from vent to 25 m. The black lines mark the boundary of the grain jet.

As shown in Figure 6.4a, there is a dip in the contours of n near the centerline where the grains are concentrated (within the black line delineating the boundary of the grain jet). This dip is caused by the grains. Though the relative speed between the gas and the grains is only ~50 m/s at the vent, it increases quickly with altitude, as shown in Figure 6.7a, because the gas accelerates rapidly (see Figure 6.6a) while the grains are hardly affected by the gas and retain the speeds they had at the vent. Moreover, the local mass concentration of grains relative to gas increases with altitude, as shown in Figure 6.7b, where contours of $\psi \triangleq (n_{grain} \times m_{grain})/(n \times m)$ have been plotted. As the flow emerges from the vent, the gas expands and spreads out while the grains remain in a collimated beam. As a result, a smaller and smaller amount of gas remains in the grain column as the altitude increases, thus increasing ψ. Both these factors enhance the effects of the grains on the gas with altitude (see Sections 5.1.1 and 5.1.2), producing the dip in n near the centerline. As the altitude increases, however, the collision rate between the gas and the grains also drops, thus decreasing the interaction between the two. Consequently, we would expect the dip to disappear at higher altitudes, which is observed in Figure 6.4b.

As shown in Figure 6.7a, the relative speed between the gas and the grains is a minimum at the vent. While the grains move at essentially a constant speed (see Figure 6.2c), the gas accelerates rapidly from being much slower than the grains to being much faster over the distance of several vent diameters above and below the vent, as shown in Figures 6.1d and 6.6a.

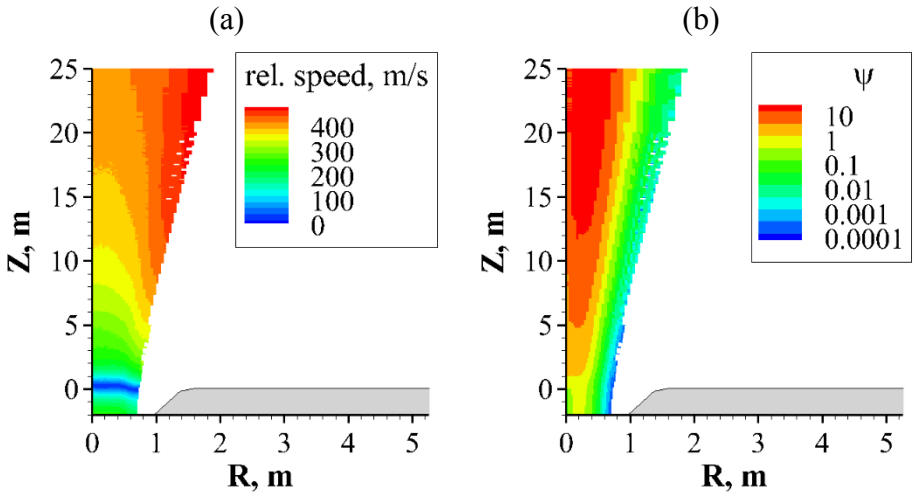

Figure 6.7. Contours of: (a) relative speed between the gas and the grains and (b) local mass concentration of grains relative to gas, ψ. Note that the x- and y-axis have been plotted on different spatial scales for clarity.

The spreading angles of the gas and the grain jets are ~62° and ~2° respectively, based on the full-width-half-maximum (FWHM) of the density profiles across the width of the jets at Z = 10 km (see Section 5.4). The spreading angles remain approximately the same even when the FWHM at Z = 20 km is used. The gas jet is broader than both the Mach-3 and Mach-5 jets, which have spreading angles of ~56° and ~43° respectively (see Section 5.4). The spreading angle of the grain jet is consistent with those of the 0.5-μm grain jets examined in Chapter 5 (see Figure 5.13a) when the grains exit the vent as fast as the gas (α = 1.0). The grain jet is narrow because the grains are hardly affected by the expanding gas flow. The grains are also hardly accelerated by the gas, going from ~350 m/s at the vent (see Figure 6.3b) to ~400 m/s at Z = 20 km.

6.3. SUMMARY

In this chapter, we examined the results from the computational subsurface model. In particular, we investigated the flowfield in the subsurface channel as well as the resulting collisional near-field directly above the vent.

The flow in the channel is dominated by evaporation from the walls and not the inlet flow. The gas pressure and density are mostly uniform throughout the channel at values corresponding to the H_2O equilibrium vapor pressure at the wall temperature of ~230 K. The gas temperature is ~230 K near the walls due to evaporation but is higher near the centerline due to interaction with the grains. The gas flow is mostly slow and subsonic throughout the channel, except near the vent where it accelerates rapidly to nearly sonic speeds. The flow remains slightly subsonic at the vent, with a Mach number of ~0.8, but reaches sonic conditions shortly after it exits.

The grains barely grow in the channel, starting at ~1 μm and growing at most to ~1.03 μm, and remain mostly collimated. They also hardly collide with the walls due to the straight channel geometry chosen. The grains are slightly decelerated by the much slower gas evaporating from the walls and exit the vent, on the average, faster than the gas.

Most of the gas emerging from the vent originates from the channel walls near the vent. Most of the inlet flow condenses on the walls and never makes it out. This is consistent with the gas mass flow rates of ~0.2 kg/s and ~0.1 kg/s at the inlet and the vent respectively. Since the grains hardly exchange momentum or mass with the gas, they retain their properties at the source. As a result, the gas and grains emerging from the vent provide clues to the subsurface wall conditions near the vent and the source conditions respectively. Whether the flow in the channel is dominated by evaporation from the walls or by the inlet flow would depend on the ratios of the channel length to its width and the inlet pressure to the wall equilibrium vapor pressure.

The collisional near-field flow above the vent exhibits similar trends to that of the Mach-5 vent conditions from the analytical subsurface model. The density drops rapidly with altitude, though it drops almost immediately above the vent in this case while it stays constant and does not drop until the several vent diameters above the vent in the Mach-5 case. The flow also passes through multiple regimes from nearly continuum close to the vent to free-molecular at higher altitudes and is in equilibrium near the vent but not at higher altitudes. A non-equilibrium region also exists near the surface where sublimation is occurring.

The gas experiences a greater acceleration above the vent in this case than in the Mach-5 case because the gas has only begun to expand in this case whereas the gas has mostly expanded in the Mach-5 case as it reaches the vent. However, the gas does not quite reach the maximum speed possible, which in this case is ~920 m/s and not ~1005 m/s. This is because most of the gas is evaporated from the walls, thus its stagnation temperature is the wall temperature at 230 K instead of the reservoir temperature at 273.16 K. Since the gas does not quite reach the maximum speed possible, the flow at the vent is not collisional enough to convert all its molecular thermal and internal energy into mean kinetic energy before the flow becomes free-molecular.

The relative speed between the gas and the grains and the local mass concentration of grains relative to gas are small near the vent, but increase with altitude. This enhances the interaction between the gas and the grains, producing a dip in the gas density near the centerline. However, this dip disappears at higher altitudes as collision rates drop.

The resulting gas jet is broader than the Mach-3 and Mach-5 jets, with a spreading angle of ~62°, while the resulting grain jet is narrow, with a spreading angle of ~2°. In addition, the grains are hardly accelerated by the gas, going from ~350 m/s at the vent to ~400 m/s at 20 km.

Chapter 7.

Constraining Far-field to Cassini *In-Situ* Data

Now that we have analyzed the collisional near-field of the plume within several kilometers above the surface vents, we examine the free-molecular far-field of the plume which extends out to several Enceladus radii ($R_{Enc} \approx 252.1$ km) and constrain it using Cassini *in-situ* data. In particular, we constrain the gas component of our simulation results to the E2, E3, E5 and E7 INMS H_2O density distributions (see Figures 3.8b–d and Figure 3.9) and the grain component to the E2 CDA grain density distribution for $r_{grain} \geq 1.6$ μm (see Figure 3.8a). By constraining our simulation results using Cassini data, we attempt to estimate the H_2O and grain production rates from the plume and deduce certain conditions at the vent (e.g. Mach number).

7.1. FITTING TO INMS DATA

We fit our simulated H_2O density distributions (see Section 3.5.2) to the INMS H_2O density distributions by minimizing the quantity χ^2 under the constraint that the free parameters to be fitted cannot be negative (because source strengths cannot be negative). The quantity χ^2 is defined as:

$$\chi^2 = \sum_{i=1}^{N_{data}} \left(\frac{n_{total}(x_i) - n_i}{\sigma_i} \right)^2 \tag{7.1}$$

where N_{data} is the number of data points, n_{total} is the density distribution from our model (see Equation (7.2)), n_i is the INMS density distribution, x is the independent variable, and σ_i is the error bar associated with each data point. In essence, this fitting procedure is a weighted least-squares fitting method where each data point is weighted by the reciprocal of its estimated error. As a result, data points with larger errors have smaller weights. Error

bars have not been provided for the E2 INMS data set, thus we simply weight each data point equally by setting $\sigma_i = 1$ for all data points in our fits to this data set.

Three types of sources are considered in our fits: (i) plume, (ii) global, and (iii) background. Since the density distributions are sampled at altitudes ≥ 100 km above the surface where the flow has become free-molecular (see Sections 4.1 and 6.2), the total density distribution, n_{total}, is the sum of the contributions from all the sources:

$$n_{total} = n_{plume} + n_{glb} + n_{bg} \tag{7.2}$$

where n_{plume}, n_{glb} and n_{bg} are the contributions from the plume, global and background sources respectively. The plume contribution is obtained via simulation, as described in Sections 3.3 and 3.4, whereas the global and background contributions are modeled analytically.

7.1.1. Plume Source

In this chapter, the plume source is modeled using the eight jet sources identified by Spitale and Porco (2007). However, more than 98 jets have recently been identified (Porco *et al.*, 2014) and should be incorporated in a future work. Some preliminary work and analysis on this can be found in Appendix I. The density distribution along the spacecraft trajectory from the plume source is the sum of the contributions from the individual jets along the trajectory:

$$n_{plume} = \sum_{j=1}^{8} w_{Jet,j} n_{Jet,j} \tag{7.3}$$

where $w_{Jet,j}$ is the scaling factor for Jet j such that the strength of Jet j, $s_{Jet,j}$, (in kg/s) is $w_{Jet,j}$ s_{ref} and $n_{Jet,j}$ is the density distribution along the spacecraft trajectory from Jet j with strength s_{ref} = 0.2 kg/s. The scaling factors for the individual jets, $w_{Jet,j}$, are the free

parameters to be fitted. Physically, $w_{Jet,j}$ corresponds to the vent area in units of the nominal vent area which produces s_{ref} = 0.2 kg/s for a given set of vent conditions. The nominal vent areas are ~0.8 m^2 and ~6.2 m^2 for the Mach-3 and Mach-5 vent conditions respectively (see Table 3.1).

7.1.2. Global Source

The global source is modeled as a uniform spherical outflow under negligible gravity and its density distribution along the spacecraft trajectory is given analytically by:

$$n_{glb} = \frac{s_{glb}}{4\pi r^2 vm} \tag{7.4}$$

where s_{glb} is the strength of the global source (in kg/s), r is the distance from the center of Enceladus, v is the most probable speed of H_2O molecules sputtered from an icy surface, experimentally determined to be 770 m/s (Burger *et al.*, 2007; Johnson, 1990), and m is the mass of an H_2O molecule (~2.99×10^{-26} kg). The strength of the global source, s_{glb}, is the free parameter to be fitted.

The low surface temperatures on Enceladus, except for the anomalously warm south polar region detected by CIRS (Spencer *et al.*, 2006), rule out sublimation of surface ice and leave energetic surface sputtering as a possible mechanism for the global source (Burger *et al.*, 2007). However, the existence of a global source is yet to be confirmed. Waite *et al.* (2006) included a global source in their fit to the E2 INMS data but Smith *et al.* (2010) found it to be unnecessary to fit the E2, E3 and E5 INMS data. Dong *et al.* (2011) and Tenishev *et al.* (2010) also considered a global source in their models.

We validate this analytical model via simulation by launching particles uniformly from the surface of Enceladus with a surface normal velocity of 770 m/s. The analytical and simulated density fields agree well, thus the effects of gravitational, Coriolis and

centrifugal forces on the density field of the global source are negligible, at least, within our regions of interest.

7.1.3. Background Source

The background source originates from the narrow neutral H_2O torus around Saturn formed from H_2O molecules ejected from the south polar region of Enceladus (Johnson *et al.*, 2006). Since our regions of interest are much smaller than the length scales of the neutral torus (Cassidy and Johnson, 2010; Johnson *et al.*, 2006), we assume a constant value for the background source. This constant value, n_{bg}, is the free parameter to be fitted.

Table 7.1. Free parameters to be fitted for each source.

Source	Parameter
Plume	$w_{Jet,j}$ for j = 1 through 8
Global	s_{glb}
Background	n_{bg}

7.1.4. Assessing Quality of Fit

We employ two methods to *quantitatively* evaluate the quality of our fits to the data sets. In the first method, we assume that the measurement errors, σ_i, are normally distributed. Suppose we repeat the measurements many times and fit to every measurement by minimizing χ^2 (as defined by Equation (7.1)), we would find that the minimizing values of χ^2 follow the chi-square probability distribution for v degrees of freedom (pages 221 and 660 of Press *et al.* (1992)) for our model that is linear in the free parameters to be fitted (see Equations (7.2), (7.3) and (7.4)). The number of degrees of freedom, v, is the number of data points minus the number of free parameters.

Then, we can assess the quality of the fit by calculating the probability of finding $\chi^2(\nu) \geq \chi^2_{fit}$ by chance. This probability can easily be computed from available computer programs or looked up in tables. If this probability is very small, the "quality" of the fit is poor because the value of χ^2_{fit} obtained is likely to be a random occurrence rather than because the model was a good one, or the fit parameters explained the observations. However, a small probability could also mean that the model is right but the measurement errors are actually larger than those provided. Moreover, it is possible that the measurement errors are not normally distributed, though errors arising from this assumption are usually minimal (Press *et al.*, 1992).

In the second method, we calculate the coefficient of determination, R^2, which is defined as (page 111 of Mack (1967)):

$$R^2 = \frac{\sum_i^{N_{data}} (n_{total}(x_i) - \bar{n})^2}{\sum_i^{N_{data}} (n_i - \bar{n})^2} \tag{7.5}$$

where $\bar{n}$ is the mean of the data values. The numerator is called the "explained variation" because it is the variation of the model while the denominator is called the total variation. Consequently, R^2 measures the amount of total variation that is accounted for by the model and thus indicates a better fit if its value is closer to 1.

7.2. RESULTS OF FITS TO INMS DATA

Here we present the results of fits to the E2, E3, E5 and E7 INMS H_2O density distributions for the Mach-3 and Mach-5 vent conditions from the analytical subsurface model (see Table 3.1) and the vent conditions from the computational subsurface model (see Figure 6.3). While the plume flow is two-phase, we consider *gas-only* jets for the Mach-3 and Mach-5 vent conditions as we do not expect the grains to have a significant effect on the gas component at the inferred ice/vapor mass ratios of 0.01–1.0 (Hedman *et al.*, 2009; Ingersoll and Ewald, 2011; Porco *et al.*, 2006; Schmidt *et al.*, 2008) (see Section 5.1.1). Larger grains might exit the vents slower than the gas (Hedman *et al.*, 2009; Ingersoll and Ewald, 2011; Postberg *et al.*, 2011; Schmidt *et al.*, 2008), thus enhancing their effects on the gas (see Section 5.1.2). However, the inferred ice/vapor mass ratios are for a distribution of sizes, thus the larger grains would account for only a fraction of the inferred ice/vapor mass ratio. Consequently, the velocity difference at the vents for the larger grains should only have a small effect on the gas.

7.2.1. E2 INMS Data

The E2 trajectory takes Cassini from the south side to the north side of Enceladus, with a distance at closest approach (CA) of ~168 km. It misses the densest regions of the plume and only passes through its edges, thus it is most likely that the E2 INMS data provide a poor constraint for the plume, which we have modeled using eight discrete jets. This is consistent with our simulations where the E2 trajectory either misses most of the jets completely or only passes through their edges depending on the vent conditions. We only consider the Mach-3 and Mach-5 vent conditions for the fits to the E2 INMS data. For the Mach-5 vent conditions, only Jets II and III register a signal along the E2 trajectory. The other jets are missed entirely. For the Mach-3 vent conditions, the signals of Jets II

and III are more than five times stronger than the others as the E2 trajectory only passes through the edges of these other jets.

Table 7.2 lists the results from our fits to the E2 INMS data. As shown in Figures 7.1a–b, regardless of the vent conditions, the jets-only fit could only account for the inbound portion (before CA) of the INMS data, which corresponds to when Cassini is located over the south pole of Enceladus. Consequently, the outbound portion of the INMS data possibly originates from sources other than the eight jets used, e.g. unmodeled jets, a global sputtered atmosphere and/or the background neutral torus.

Table 7.2. Results of fits to E2 INMS data.

Fit		$s_{Jet,j}$ **(kg/s)**[a]		$s_{Jet,tot}$	s_{glb}	n_{bg}
		II	**IV**[b]	**(kg/s)**	**(kg/s)**	**(cm^{-3})**
Jets only (j-only)	Mach-3	3.0	0.1	3.1		
	Mach-5	3.0	-	3.0		
Jets + Global + Background (j+g+b)	Mach-3	0	0	0	19.6	0
	Mach-5	0	-	0	19.6	0
Jets + Background (j+b)	Mach-3	0.9	0	0.9		7.6×10^4
	Mach-5	0	-	0		8.4×10^4

[a]Only jets contributing to the best-fit solutions are shown. The others are either not detected or not contributing.
[b]For the Mach-5 vent conditions, Jet IV is not detected along the E2 trajectory in our simulation.

Since the jets alone could not account for the outbound portion of the INMS data, we include the global and background sources into the fit. When these sources are included, the jet contributions vanish from the fit for both vent conditions. This further supports the idea that the E2 INMS data provide a poor constraint for the plume. The background source also does not contribute. The best-fit solution involves only the global source and thus does not depend on the vent conditions. The best-fit global source strength (see Table 7.2) is

higher than estimates by Burger *et al.* (2007) of ~2.4 kg/s, Tenishev *et al.* (2010) of 1.1–1.4 kg/s and Waite *et al.* (2006) of ~3.6 kg/s. Dong *et al.* (2011) estimated a global surface density of ~5.7×10^5 cm^{-3}, which translates to a source strength of ~11 kg/s if a surface velocity of 770 m/s is assumed (as we did in Section 7.1.2). As shown in Figures 7.1a–b, the simulated density profiles of this fit (identical for both vent conditions) are symmetric about CA and capture the gradual rise and fall of the inbound and outbound portions of the INMS profile respectively. However, the simulated profiles are higher in the outbound portion.

We also fit to the INMS data using only the jets and the background source, without the global source. In this case, the jet contributions vanish for the Mach-5 vent conditions and are diminished for the Mach-3 vent conditions in comparison to the jets-only fits (see Table 7.2). The best-fit background source strengths are higher than estimates by Burger *et al.* (2007) and Dong *et al.* (2011) of ~1.6×10^4 cm^{-3} but remains within the neutral torus peak densities determined by Smith *et al.* (2010) of 10^4–10^5 cm^{-3}. As shown in Figures 7.1a–b, the simulated density profiles of this fit do not match the shape of the INMS data for either vent conditions. This is because we have modeled the background source as a constant. A better background model may improve the match.

The best-fit total plume (jet) strengths, $s_{Jet,tot}$, (see Table 7.2) are orders of magnitude smaller than estimates by Saur *et al.* (2008) of ~200 kg/s, Hansen *et al.* (2006, 2008, 2011) of 170–220 kg/s, Burger *et al.* (2007) of ~300 kg/s, and Tian *et al.* (2007) of 120–180 kg/s, but are closer to estimates by Smith *et al.* (2010) of ~12 kg/s and Waite *et al.* (2006) of ~5 kg/s. Waite *et al.* (2006), however, indicated that the source strength may vary by over an order of magnitude on timescales of less than an hour. Tenishev *et al.* (2010), by simultaneously fitting to the E3 and E5 INMS data and the E2 UVIS data, also obtained total plume strengths much higher than ours, at 780–1250 kg/s. As discussed

above, however, our simulations and fits suggest that the E2 INMS data provide a poor constraint for the plume, which is consistent with the geometry of the trajectory. As a result, we will not make any inferences about the plume based on our fits to the E2 INMS data.

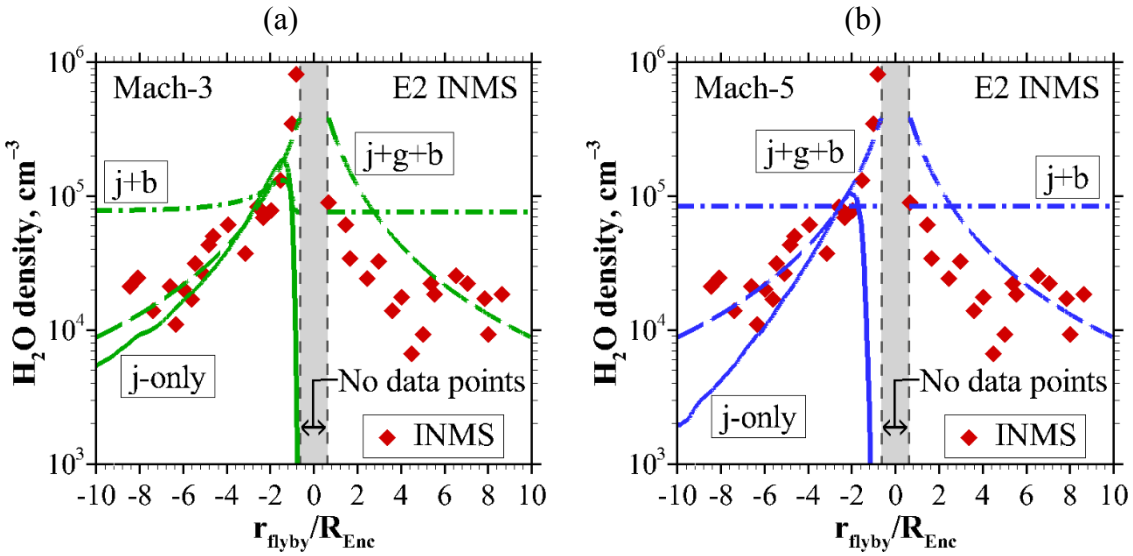

Figure 7.1. Simulated H_2O density profiles of fits (see Table 7.2) in comparison with the E2 INMS density profile for the (a) Mach-3 and (b) Mach-5 vent conditions. On the x-axis is the altitude of Cassini from surface of Enceladus, r_{flyby}, normalized by Enceladus radius, R_{Enc} (~252.1 km). Negative and positive values denote before and after closest approach (CA) respectively. Note the logarithmic scales on the y-axis. The shaded region contains no data points because the distance at CA for E2 is ~168 km (~0.7R_{Enc}).

7.2.2. E3, E5 and E7 INMS Data

The E3 and E5 trajectories take Cassini from the north side to the south side of Enceladus, with distances at closest approach (CA) of ~50 km and ~25 km respectively, and pass directly over the south polar region of Enceladus in the outbound portion (after CA). Consequently, the plume signal dominates the outbound portions of the E3 and E5 INMS data. The E7 trajectory takes Cassini horizontally over the south polar region of Enceladus, with a distance at CA of ~100 km. As a result, the E7 INMS data are mostly dominated by the plume signal and resolve the fine structures within the plume, e.g. the individual jets, and thus should provide the best constraint for the plume among the INMS data sets under consideration.

We include the jets, the global and the background sources in our fits to the E3 and E5 INMS data but only include the jets in our fits to the E7 INMS data. As we shall see later, the best-fit jet strengths for our fits to all three data sets are for the most part insensitive to the global and background source strengths. The best-fit source strengths for the fits to the E3, E5 and E7 INMS data are listed in Tables 7.3, 7.4 and 7.5 respectively and the corresponding H_2O density profiles are shown in Figures 7.2a, 7.2b and 7.2c respectively for our three different vent conditions. We have used "Comp" to denote the vent conditions from the computational subsurface model. Note that Jet VII is not detected along the E5 and E7 trajectories for $Ma_{vent} = 5$ in our simulations and thus its strength cannot be constrained for $Ma_{vent} = 5$ using the INMS data from these trajectories.

Table 7.3. Results of fits to E3 INMS data using jets, global and background sources.

	$s_{Jet,j}$ (kg/s)								$s_{Jet,tot}$ (kg/s)	s_{glb} (kg/s)	n_{bg} (cm^{-3})
	I	**II**	**III**	**IV**	**V**	**VI**	**VII**	**VIII**			
Mach-3	0	343.8	0	37.2	0	0	548.8	0	929.7	12.3	5.1×10^3
Mach-5	0	0	1096.3	16.3	9.3	0	0	58.8	1180.5	12.9	5.2×10^3
Comp	0	685.0	0	0	0	0	0	0	685.0	9.4	8.1×10^3

Table 7.4. Results of fits to E5 INMS data using jets, global and background sources.

	$s_{Jet,j}$ (kg/s)								$s_{Jet,tot}$ (kg/s)	s_{glb} (kg/s)	n_{bg} (cm^{-3})
	I	**II**	**III**	**IV**	**V**	**VI**	**VII**	**VIII**			
Mach-3	23.1	0	841.3	0	0	0	0	0	1354.4	14.8	1.6×10^4
Mach-5	0	0	685.2	451.7	0	164.2	-	0	1301.0	14.9	1.5×10^4
Comp	0	88.8	1910.1	0	0	0	0	0	1998.9	14.8	1.4×10^4

Table 7.5. Results of fits to E7 INMS data using only jets.

	$s_{Jet,j}$ (kg/s)								$s_{Jet,tot}$ (kg/s)
	I	**II**	**III**	**IV**	**V**	**VI**	**VII**	**VIII**	
Mach-3	139.3	130.4	0	148.8	0	0	0	0	418.4
Mach-5	0	195.3	0	111.9	0	0	-	63.9	371.0
Comp	303.8	0	0	132.5	0	0	0	0	436.3

For the E3 and E5 INMS data sets, the best-fit solutions for the global and background source strengths only vary slightly with the vent conditions chosen for the jets. This gives us confidence that the fitting method is reasonable because the global and background sources should not be affected by the vent conditions of the jets. However, the best-fit solution for the jets is very sensitive to the vent conditions of the jets for all three INMS data sets. Different vent conditions result in different sets of jets in the best-fit solutions. The main difference among the jets produced by the different vent conditions is the jet spreading angle, δ_{gas}. The Mach-5 vent conditions produce the narrowest jet, with $\delta_{gas} \approx 43°$, while the vent conditions from the computational subsurface model where the flow is barely sonic at the vent produce the broadest jet, with $\delta_{gas} \approx 62°$. The Mach-3 vent conditions produces a jet with $\delta_{gas} \approx 56°$. This is consistent with the number of jets detected along each trajectory. All the jets register a signal along all three trajectories for the Mach-3 vent conditions and the vent conditions from the computational subsurface model while Jet VII is missed along the E5 and E7 trajectories for the Mach-5 vent conditions because the narrower Mach-5 jets are less likely to be intersected.

While the best-fit solution for the jets to each INMS data set varies with the vent conditions chosen, we notice that Jet III is present in the best-fit solutions to the E5 INMS data set (see Table 7.4) and Jet IV in the best-fit solutions to the E7 INMS data set for all three vent conditions (see Table 7.5). However, the best-fit strength of Jet III varies with the vent conditions by more than a factor of 2. The best-fit strength of Jet IV does not vary as much, changing by only ~25%. It is also worth noting that the total jet strength only varies by ~16% among the vent conditions in the best-fit solutions to the E7 INMS data (see Table 7.5).

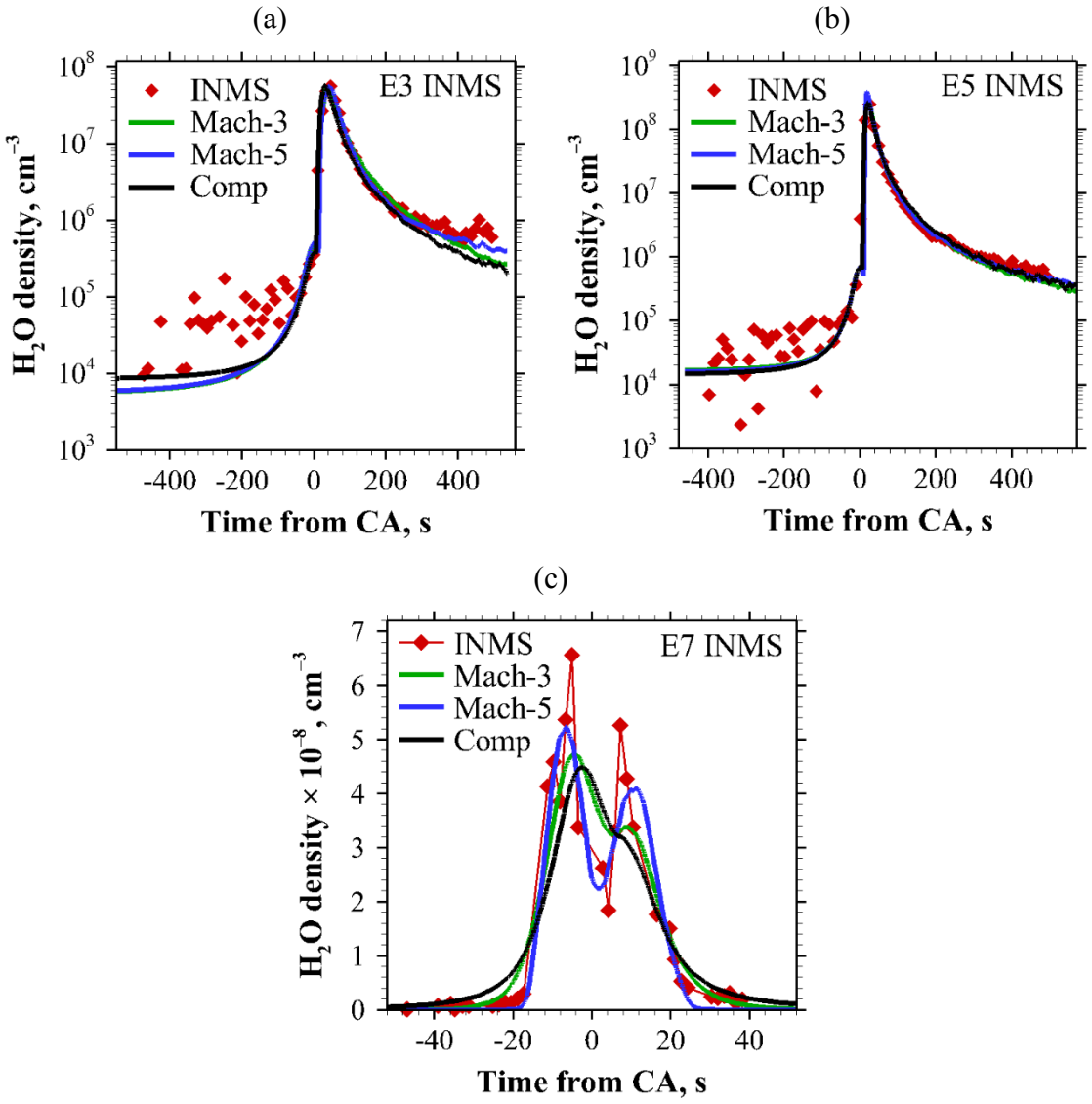

Figure 7.2. Simulated H_2O density profiles of fits (see Tables 7.3, 7.4 and 7.5) in comparison with the INMS density profile for: (a) E3, (b) E5 and (c) E7. On the x-axis is the time from closest approach (CA). Negative and positive values denote before and after CA respectively. Note the logarithmic scales on the y-axis in (a) and (b) and the linear scale in (c).

We also examine the sensitivity of our best-fit jet strengths to the global and background source strengths. For the E3 and E5 INMS data, we perform two other fits for each set of vent conditions: (1) we fit only the jets to the data without the global and the background sources, and (2) we fit the jets to the data with the global and source strengths set to *twice* their best-fit strengths listed in Tables 7.3 and 7.4. For the E7 INMS data, we perform one other fit for each set of vent conditions: we fit the jets to the data with the global and background source strengths set to 100 kg/s and 10^6 cm^{-3} respectively. We find that most of the jet strengths vary by ≤ 30% from the best-fit strengths, with the few exceptions listed in Table 7.6. Therefore, most of the best-fit jet strengths obtained are *not* very sensitive to the global and background source strengths. The total jet strengths are even less sensitive, varying by ≤ 12%.

Table 7.6. Most sensitive jets to the global and background source strengths.

	Vent Conditions	**Jet**	**Variation in $s_{Jet,j}$**
E3	Mach-3	III	0–94 kg/s
	Mach-5	V	9–23 kg/s
E7	Comp	III	0–130 kg/s

With the best-fit solutions for the jets varying significantly among the vent conditions for all three INMS data sets, we attempt to determine which vent conditions provide the "best" fit and thus are the most plausible by analyzing the quality of our fits to the data. We quantify the quality of the fits using the χ^2 and R^2 values obtained for each fit (see Section 7.1), which are listed in Table 7.7 along with the numbers of degrees of freedom, ν, and the probabilities $p\left(\chi^2(\nu) \geq \chi^2_{fit}\right)$ of finding $\chi^2(\nu) \geq \chi^2_{fit}$. As discussed in Section 7.1, a larger probability and R^2 value indicate a better fit. For all three INMS data sets, both the probabilities and the R^2 values of the fits indicate that the Mach-5 jets

provide the best fits and thus the Mach-5 vent conditions appear to be the most plausible among the three vent conditions considered.

The probabilities for the fits to the E7 INMS data for all three vent conditions are exceedingly small, with the Mach-5 vent conditions providing the highest probability and the vent conditions from the computational subsurface model providing the lowest. This is consistent with the simulated H_2O density profiles of the fits to the E7 INMS data shown in Figure 7.2c where all three profiles fail to capture the two largest peaks of the INMS density profiles at around −5 s and 5 s. However, the Mach-5 jets seem to do the best job in matching not only the peak magnitudes but also the peak widths. As shown in Figures 7.2a–b, the simulated H_2O density profiles for all three vent conditions capture the peaks of the E3 and E5 INMS density profiles but drop off more rapidly in the outbound portions > 200 s. This is more evident in the profiles of the fits to the E3 INMS data. Dong *et al.* (2011) also found this in their work and explained that this may be due to higher background densities in the outbound portions of these trajectories.

Table 7.7. The χ^2 and R^2 values and the probabilities of finding $\chi^2(\nu) \geq \chi^2_{fit}$ for the different fits to the E3, E5 and E7 INMS data.

	Vent Conditions	$\boldsymbol{\chi^2_{fit}}$	$\boldsymbol{R^2}$	$\boldsymbol{\nu}$	$\boldsymbol{p(\chi^2(\nu) \geq \chi^2_{fit})}$
E3	Mach-3	144	0.98	75	~0
	Mach-5	93	0.99	75	0.08
	Comp	448.3	0.88	75	~0
E5	Mach-3	66.7	~1	67	0.49
	Mach-5	58.7	~1	67	0.76
	Comp	151.6	0.99	67	~0
E7	Mach-3	4886.3	0.89	36	~0
	Mach-5	2871.4	0.93	36	~0
	Comp	8625.4	0.82	36	~0

A summary of the best-fit total jet, global and background source strengths is provided in Table 7.8. Smith *et al.* (2010) estimated a total plume strength of ~190 kg/s for E3 and ~750 kg/s for E5 while Dong *et al.* (2011) estimated a total plume strength of ~500 kg/s for E3 and ~1000 kg/s for E5. Our best-fit total plume (jet) strengths are higher than their estimates but remain on the same order of magnitudes. As in their estimates, we also find a higher total plume strength for E5 than for E3. For E7, our best-fit total plume strengths agree very well with the estimate of ~500 kg/s by Dong *et al.* (2011). Tenishev *et al.* (2010) simultaneously fitted to E3 INMS, E5 INMS and E2 UVIS data and obtained a total plume strength of 780–1250 kg/s. Hansen *et al.* (2006, 2008, 2011) inferred lower plume strengths of 170–220 kg/s from various UVIS data collected at different times. Various other estimates, derived from different flybys, lie in the range of 100–1000 kg/s (Burger *et al.*, 2007; Saur *et al.*, 2008; Tian *et al.*, 2007).

Our best-fit global source strengths are higher than the estimates by Burger *et al.* (2007) of ~2.4 kg/s, Tenishev *et al.* (2010) of 1.1–1.4 kg/s and Waite *et al.* (2006) of ~3.6 kg/s. However, our estimates agree well with the global surface densities of $7.2–7.4 \times 10^5$ cm^{-3} computed by Dong *et al.* (2011), which translates to source strengths of 13–14 kg/s if a surface velocity of 770 m/s is assumed (as we did in Section 7.1.2). Burger *et al.* (2007) and Dong *et al.* (2011) estimated background densities of $1.6–3.3 \times 10^4$ cm^{-3} and Smith *et al.* (2010) determined neutral torus peak densities of $10^4–10^5$ cm^{-3}. Our best-fit background source strengths are slightly lower than their estimates for E3 but are within their estimates for E5. In general, our estimates for the source strengths agree with other estimates.

Table 7.8. Total jet, global and background source strengths from best-fit solutions.

	$s_{Jet,tot}$ (kg/s)	s_{glb} (kg/s)	n_{bg} (cm^{-3})
E3	700–1200	9–13	5–8 × 10^3
E5	1300–2000	~15	~1.5 × 10^4
E7	370–440	-	-

7.3. FITTING TO CDA DATA

Three components make up the grain density field around Enceladus (see Section 3.5.2): the jets, the surrounding cloud, and the E ring. In our simulations, all three components originate from the eight jets located in the south polar region of Enceladus. Therefore, for each jet, the three components are related and cannot be treated independently when fitting to the CDA data. In principle, we could treat the components from one jet to be independent of those from another jet, and fit the weighted sum of the contributions from all jets to the CDA data as we do in fitting to the INMS data (see Section 7.1) to determine the strengths of each individual jet. However, it is infeasible to do so because the E2 trajectory completely misses either all or most of the simulated grain jets depending on the case considered due to their narrow spreading angles.

Instead, we simply set all eight jets to have *equal* strengths. To determine the total grain mass production rate, $\dot{M}_{grain}$, from Enceladus (sum from all jets), we scale the mass of the simulated E ring based on estimates derived from observations. This procedure is described in greater detail below in Section 7.4.

No global source of grains has been included, though it may result from an impactor-ejecta mechanism (Krivov *et al.*, 2003; Kruger *et al.*, 1999; Sremcevic *et al.*, 2003) as hypervelocity particles, e.g. E-ring grains and interplanetary dust particles (Spahn *et al.*, 2006a), collide with the surface of Enceladus and sputter off materials. However, such ejecta clouds have so far not been clearly observed around Saturnian satellites and

should only have a negligible contribution to the CDA measurements, if any (Kempf *et al.*, 2010; Spahn *et al.*, 2006b).

7.4. RESULTS OF FITS TO CDA DATA

Here we present the results of our fits to the E2 CDA grain density distribution for $r_{grain} \geq 1.6$ μm. Note that the CDA data are for grains with a distribution of sizes while our simulations are for monodisperse grains at two sizes: $r_{grain} = 5$ nm and 0.5 μm (see Tables 5.1 and 5.2). Both sizes are below the CDA threshold.

However, the only size-dependent force acting on the grains in our near-field DSMC simulations is the drag exerted by the gas (gravity is not size-dependent). Since the larger micron-sized grains are hardly affected by the gas due to their high inertia and low decoupling heights ($< 10D_{vent}$) (see Chapter 5), their near-field motions do not depend as much on their sizes as on their initial velocities at the vents, V_{init}. Consequently, we pick a grain size, $r_{grain} = 5$ μm (> 1.6 μm), which is about the inferred median r_{grain} of (3.1 ± 0.5) μm (Ingersoll and Ewald, 2011), and use the DSMC results from our simulations with r_{grain} = 0.5 μm to approximate the near-field motions of the 5-μm grains for the *same* V_{init}.

Recall that our simulations are performed in multiple stages (see Section 3.3.2). First, the near-field is simulated using DSMC. Then, the DSMC particle positions and velocities are sampled once the flow becomes free-molecular and appropriately input into the free-molecular model which continues to propagate the plume into the far-field (see Section 3.4). We approximate the near-field motions of the 5-μm grains by using the sampled positions of the 0.5-μm grains but appropriately scaling their sampled velocities, if necessary, prior to input into the free-molecular model. The velocity scaling will be described later in this section.

We consider two grain velocities at the vent: V_{init} = 900 m/s (fast grains) and 100 m/s (slow grains). Since the DSMC simulations are for Ma_{vent} = 5 with a vent gas velocity of ~900 m/s (see Table 3.1), these cases correspond to vent velocity ratios, α ($\triangleq V_{grain}/V_{gas}$), of 1.0 and ~0.11 respectively. The vent parameters of the DSMC simulations used to approximate the near-field motions of the 5-μm grains are listed in Table 7.9. The gas drag exerted on the grains is greater when the velocity difference between the gas and the grains at the vent is larger, i.e. α is smaller (see Section 5.1.2). Therefore, we do not need to rescale the velocities for α = 1.0 and simply use both the positions and velocities of the 0.5-μm grains from the DSMC simulation with α = 1.0 (see Table 7.9) for the 5-μm grains. This is reasonable because the larger micron-sized grains are essentially moving at V_{init} throughout the near-field in a narrow collimated beam when $\alpha \approx 1.0$ (see Sections 5.2, 5.4 and 5.5).

For $\alpha \approx 0.11$, we use the positions of the 0.5-μm grains but rescale their velocities from the DSMC simulation with $\alpha \approx 0.11$ (see Table 7.9) for the 5-μm grains. To determine the appropriate scaling, we first analytically calculate the maximum velocity a 5-μm grain would achieve along the *centerline* due to gas drag for V_{init} = 100 m/s. Then, we determine the scaling by comparing this maximum centerline velocity to that of the 0.5-μm grains from the DSMC simulation. The maximum centerline velocity achieved by a 5-μm grain is calculated to be ~300 m/s, compared to ~450 m/s for the 0.5-μm grains from the DSMC simulation. Therefore, we rescale the velocities of the 0.5-μm grains by 2/3 (=300/450) to approximate those for the 5-μm grains. We apply the same scaling to all the velocities of the 0.5-μm grains, including those off the centerline, although the scaling has been derived based on the grain motion along the centerline.

We have only considered the Mach-5 vent conditions (see Table 3.1) for the gas component in our DSMC simulations. The Mach-3 vent conditions would result in greater grain spreading and acceleration (see Sections 5.4 and 5.5) for a given r_{grain} and V_{init}.

However, we do not expect the results to vary significantly from those of the Mach-5 vent conditions for the micron-sized grains because they are hardly affected by the gas anyway.

Table 7.9. Parameters of the DSMC simulations used to approximate the near-field motions of 5-μm grains.

Grain radius, r_{grain} (μm)	**Vent mass flow rate ratio, φ**	**Vent Velocity ratio, α**	**Initial velocity at vent, V_{init} (m/s)**
0.5	1.0	1.0	900
0.5	1.0	0.11	100

In our free-molecular grain simulations, we simulate the entire E ring (see Section 3.5.2). Since the total mass of the E ring is proportional to the total grain mass production rate (sum from all jets), $\dot{M}_{grain}$, from Enceladus, we estimate $\dot{M}_{grain}$ by scaling the total mass of our simulated E ring to be equal to the inferred value of $(12 \pm 5.5) \times 10^8$ kg derived from observations (Ingersoll and Ewald, 2011). The inferred value has been calculated for the E-ring radial band of 3.5–5R_S (Saturn radius, $R_S \approx 60{,}330$ km), from the center of Saturn. This is slightly larger than the horizontal (radial) extent of our simulated E ring (see Figure F.1b in Appendix F).

From this scaling and using a grain lifetime of 8 years (see Section 3.5.2), we estimate $\dot{M}_{grain}$ to be (4.7 ± 2.2) kg/s. The error bars are propagated from those of the inferred E-ring mass. A pre-Cassini estimate by Juhasz and Horanyi (2002) put the total E-ring mass at ~6×10^8 kg for the radial band of 3.5–4.5R_s, which would halve our estimate from ~4.7 kg/s to ~2.4 kg/s.

To determine the total rate of escaping grain mass, $\dot{M}_{esc}$, we count the number of grains with speeds exceeding V_{esc} (~240 m/s). Based on this criterion, all the grains escape for V_{init} = 900 m/s while ~92% of the grains escape for V_{init} = 100 m/s. If, instead, we count the number of grains with speeds exceeding 228 m/s, which is the minimum speed a grain

must have to escape Enceladus into the E ring (Kempf *et al.*, 2010), the result remains the same for V_{init} = 900 m/s but the fraction increases slightly to ~97% for V_{init} = 100 m/s. Nonetheless, regardless of V_{init} or the criterion used, the vast majority of our grains escape Enceladus. As a result, $\dot{M}_{esc} \approx \dot{M}_{grain}$ for both our cases.

Our estimate of $\dot{M}_{grain}$ is close to that of ~5 kg/s by Schmidt *et al.* (2008), although they estimated only ~10% escape. However, our estimate is an order of magnitude lower than that by Ingersoll and Ewald (2011), who inferred a $\dot{M}_{grain}$ of (51 ± 18) kg/s, with ~4.6 kg/s escaping. Note that these estimates are for a distribution of grain sizes and ejection velocities whereas ours is based on monodisperse grains of r_{grain} = 5 μm ejected from the vents at single velocities. Spahn *et al.* (2006b) estimated a $\dot{M}_{grain}$ of ~0.2 kg/s when assuming monodisperse grains of r_{grain} = 2 μm, but it may extend to several kg/s if a size distribution is assumed. Postberg *et al.* (2011) estimated a $\dot{M}_{grain}$ of ~10 kg/s for $r_{grain} > 0.2$ μm when assuming a size distribution with a maximum r_{grain} of ~10 μm. Juhasz and Horanyi (2002) determined that a supply rate of ~1 kg/s is required to maintain the E ring. If we assume distributions of grain sizes and ejection velocities in our simulations, our estimate of $\dot{M}_{grain}$ might change. Since larger or slower grains are less likely to escape Enceladus, our fraction of escaping mass might decrease and thus our estimate of $\dot{M}_{esc}$ might vary too. This should be considered in future modeling work (see Section 8.2).

Figure 7.3 shows the E2 simulated grain density profiles for r_{grain} = 5 μm resulting from our estimate of $\dot{M}_{grain} \approx (4.7 \pm 2.2)$ kg/s for V_{init} = 900 m/s (α = 1.0) and 100 m/s ($\alpha \approx$ 0.11) in comparison with the E2 CDA profile for $r_{grain} \geq 1.6$ μm. For V_{init} = 100 m/s, the upper and lower density profiles are also plotted based on the upper and lower bounds on our estimate of $\dot{M}_{grain}$. For V_{init} = 900 m/s, only the density profile for $\dot{M}_{grain}$ of 4.7 kg/s is plotted.

As shown in Figure 7.3, the simulated density profile for V_{init} = 900 m/s (α = 1.0) is flat and does not exhibit a prominent peak like the CDA profile does. The CDA peak is possibly a signal from a jet or perhaps multiple jets. However, our simulated grain jets for α = 1.0 are narrow collimated beams with spreading angles, δ_{grain}, of only a few degrees (see Figure 5.13a). Consequently, the E2 trajectory completely misses all the simulated jets when V_{init} = 900 m/s and only picks up the other components, notably the grain cloud around Enceladus and the E ring.

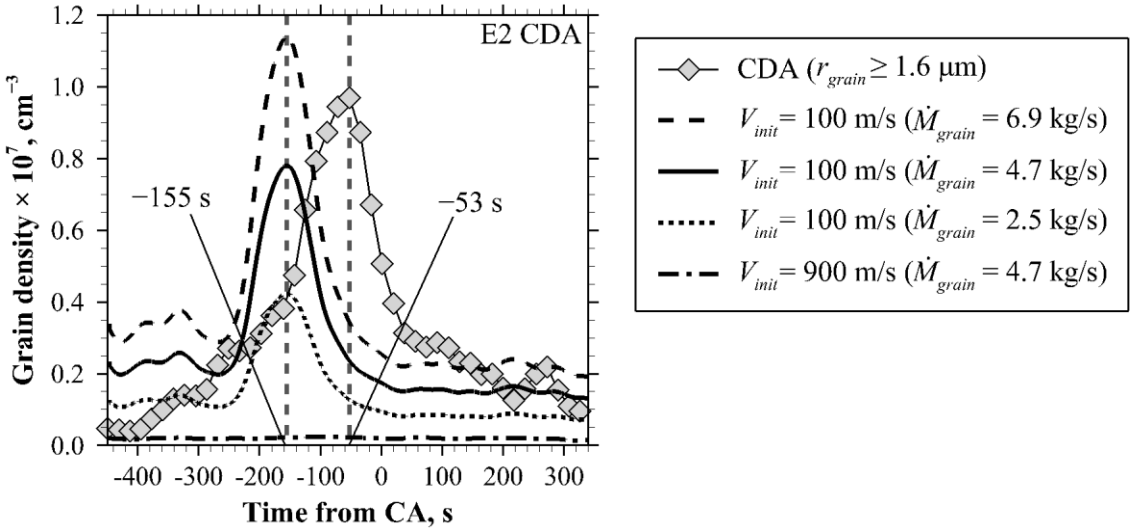

Figure 7.3. E2 simulated grain density profiles (r_{grain} = 5 μm) for V_{init} = 900 m/s (α = 1.0) and 100 m/s ($\alpha \approx 0.11$) in comparison with the CDA grain density profile ($r_{grain} \geq 1.6$ μm). On the x-axis is time from closest approach (CA). Negative and positive values denote before and after CA respectively. Note the linear scale on the y-axis.

The simulated density profile for V_{init} = 100 m/s ($\alpha \approx 0.11$), however, more closely matches the CDA profile. For this case, our simulated grain jets are broader, with $\delta_{grain} \sim$ O(10º) (see Figure 5.13a), and are therefore more likely to be detected. As a result, the E2 trajectory no longer misses all the jets but passes through Jet III located on the Damascus

Sulcus, resulting in a prominent peak at around −155 s in the simulated density profile. Kempf *et al.* (2010) obtained similar results. In their simulations, only Jet III (which they denoted D2) was detected along the E2 trajectory based on the original jet orientations given by Spitale and Porco (2007). However, they found that the CDA peak is too broad to be produced by Jet III alone, thus they reoriented Jet II (which they denoted D1) to improve the match with the CDA data. As shown in Figure 7.3, the width of our peak due to Jet III alone is comparable to the width of the CDA peak.

However, our peak timing is off by ~100 s from the CDA peak timing. We explore one possible cause for this discrepancy. We find that the peak timing is closer to the CDA peak timing when V_{init} is slower, as shown in Figure 7.4a, which compares the E2 simulated grain density profiles for V_{init} = 100 m/s and 400 m/s (new case). The peak for V_{init} = 100 m/s is ~15 s closer than the peak for V_{init} = 400 m/s. This is because a slower V_{init} results in the grains being accelerated to slower speeds, thus they spend more time near Enceladus. As a result, the gravity of Enceladus acts on them longer and curves their trajectories more, as shown in Figure 7.4b. Nonetheless, this change in peak timing by ~15 s due to a factor of 4 decrease in V_{init} appears too small to suggest that a slower V_{init} caused the difference in peak timing. Other possibilities exist. Reorienting Jet III may resolve the discrepancy since there are uncertainties in the jet orientations given by Spitale and Porco (2007). Furthermore, it may be due to unmodeled jets, with over 98 jets having been recently identified (Porco *et al.*, 2014). These possibilities remain to be explored.

Additionally, as shown in Figure 7.3, the background density (away from the peak) of our simulated grain density profiles for either V_{init} does not fall as far as that of the CDA does towards the edges. In fact, it remains approximately constant. The background density for V_{init} = 900 m/s is lower than that for V_{init} = 100 m/s for the same $\dot{M}_{grain}$. This is because the faster grains reach greater distances above and below the Saturn equatorial plane.

Consequently, the grains for V_{init} = 900 m/s are more spread out than those for V_{init} = 100 m/s, resulting in a lower background density. This is evident in the vertical extent of the simulated E ring for these cases as the E ring produced from V_{init} = 900 m/s has a larger vertical extent but a lower density than the E ring produced from V_{init} = 100 m/s (see Figure F.1a in Appendix F). Remarkably, the magnitude and the shape of the simulated grain density profile for V_{init} = 100 m/s match those of the CDA profile very well, as shown in Figure 7.3, though we have not used the CDA profile for fitting at all—we scale the total mass in our simulated E ring based on the estimate derived from observations (Ingersoll and Ewald, 2011).

Based on our fits to the INMS data, which result in total H_2O production rates of hundreds to thousands of kg/s (see Table 7.8), our estimate of $\dot{M}_{grain}$ suggests that the mass flow rate ratio out of the vents, φ ($\triangleq \dot{m}_{grain}/\dot{m}_{gas}$), is small (< 0.1). This is consistent with our assumption that the gas is barely affected by the grains when we use *gas-only* jets to fit to the INMS data (see Section 7.2).

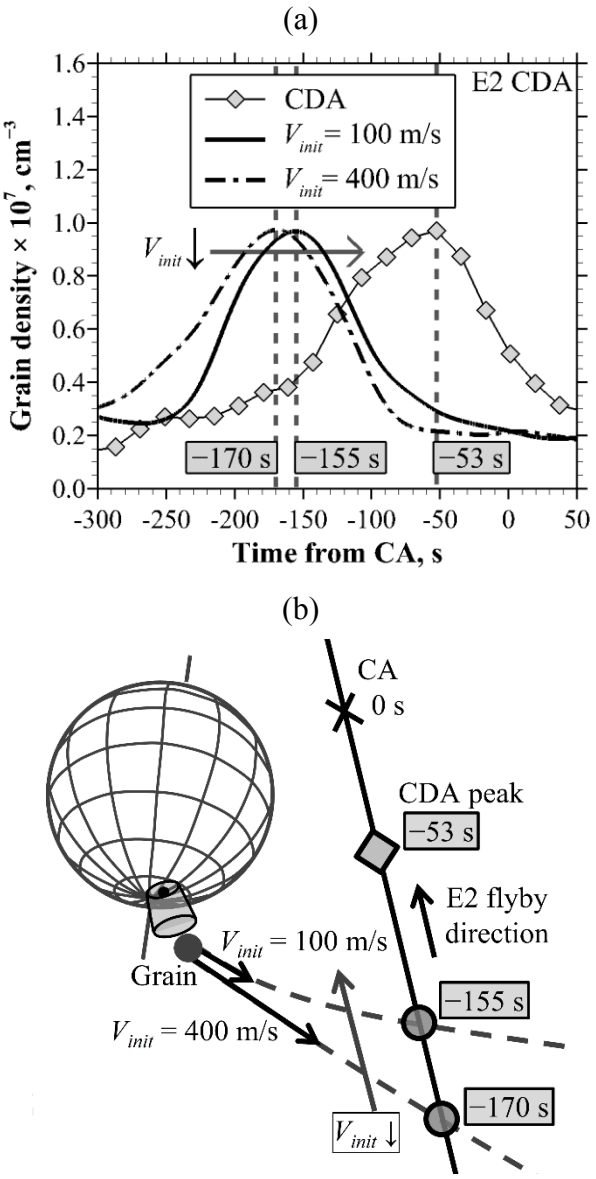

Figure 7.4. (a) Comparison of the peak timings of the simulated density profiles for initial grain velocities at vent, V_{init} = 100 m/s and 400 m/s, with the CDA peak timing. The peak magnitudes of the simulated profiles have been scaled to match the CDA peak magnitude for clarity. Note the linear scale on the y-axis. (b) The gravity of Enceladus curves trajectories of slower grains more, leading to a peak timing closer to the CDA peak timing.

7.5. SUMMARY

In this chapter, we constrain the free-molecular far-field of our simulated plume which extends out to several Enceladus radii over the south polar region by fitting the gas and grain components to the INMS H_2O density distributions along the E2, E3, E5 and E7 trajectories and the CDA grain density distribution for $r_{grain} \geq 1.6$ μm along the E2 trajectory respectively. Through fitting, we attempt to estimate the H_2O and grain production rates from the plume and deduce certain conditions at the vent.

We consider three types of sources in our fits to the INMS data: a plume source, a global source and a background source. Our plume source consists of the eight jets determined by Spitale and Porco (2007). Three vent conditions are examined: the Mach-3 and Mach-5 vent conditions from the analytical subsurface model and the vent conditions from the computational subsurface model. The global source is modeled as a uniform spherical outflow while the background source is modeled as a constant. This is adequate since the length scale of the background source is much larger than our regions of interest. Furthermore, our focus lies on the plume source.

Our simulations and fits suggest that the E2 INMS data provide a poor constraint for the plume. This is consistent with the geometry of the trajectory, which misses the densest regions of the plume and only passes through its periphery. Consequently, we cannot make any inferences about the plume source based on our fits to this data set. In contrast, the E3, E5 and E7 trajectories take Cassini through the densest regions of the plume, particularly E7, and thus provide better constraints for the plume. This is consistent with our results that indicate that the best-fit solutions for the jets are mostly insensitive to the global and background source strengths. However, they are very sensitive to the vent conditions. The major difference among the three vent conditions is the spreading angle of the jet produced. The Mach-5 vent conditions produce the narrowest jet while the vent

conditions from the computational model produce the broadest jet. The width of a jet affects its density distribution along a particular trajectory because a narrower jet is less likely to be intersected by the trajectory.

By assessing the quality of our fits, we find that the Mach-5 vent conditions provide the best fits for all three trajectories and are therefore the most plausible. However, the best-fit E7 simulated density profile from using the Mach-5 jets has slightly broader peaks than the INMS peaks and fails to capture their magnitudes. This suggests even higher Mach numbers at the vent. Our best-fit estimates for the total plume strengths of a few hundred to a few thousand kg/s, the global source strengths of ~10–15 kg/s, and the background source strengths of $\sim 10^4$ cm^{-3} agree with other estimates.

We only consider the plume source in our fits to the CDA data and examine monodisperse grains of $r_{grain} = 5$ μm at two ejection velocities: 100 m/s and 900 m/s. Three components result from the plume source: the jets, the cloud surrounding Enceladus and the E ring. In order to capture all three components, we simulate the entire E ring. Then we scale the mass of the simulated E ring based on observed values to estimate the total grain production rate from the plume. By doing so, we obtain a total grain production rate of several kg/s, which is within the range of other estimates. However, almost all the grains escape Enceladus while the other estimates found that the vast majority of grains return and do not escape (Hedman *et al.*, 2009; Ingersoll and Ewald, 2011; Postberg *et al.*, 2011; Schmidt *et al.*, 2008).

For the grains ejected at 900 m/s, the simulated density profile is flat and fails to capture the peak of the CDA profile. This is because the E2 trajectory completely misses the narrow beams of fast grains. For the grains ejected at 100 m/s, however, the simulated density profile captures the magnitude and width of the peak of the CDA profile well

though its timing is off by ~100 s. A slightly better agreement on the peak timing is obtained with slower ejection velocities.

Our estimates of the H_2O and grain production rates from plume suggest ice/vapor mass ratios of < 0.1 in the plume. The ice/vapor mass ratio in the plume can potentially tell us how the grains are formed. A large mass ratio (> 0.1) would rule out condensation from the vapor phase (Ingersoll and Ewald, 2011; Schmidt *et al.*, 2008). Our low mass ratio suggests that condensation remains a possibility. Nonetheless, we have only considered monodisperse grains ejected at several discrete velocities as opposed to distributions of grain sizes and ejection velocities. Moreover, more than 98 jets have recently been identified (Porco *et al.*, 2014). We have also not included distributed sources along the Tiger Stripes, which Postberg et al. (2011) found is important in fitting to the E5 CDA data. As a result, the limitations of our plume model, particularly the grain component, makes it hard for us to constrain the ice/vapor mass ratios in the plume.

Chapter 8.

Conclusions

8.1. SUMMARY

The Enceladus south polar plume plays an important role in shaping the Saturnian system and provides a valuable window into the interior of Enceladus, particularly as to whether liquid water exists below the surface. Consequently, this work is focused on understanding the physics and source conditions of the plume. The plume can be divided into three distinct regions: a subsurface region connecting a reservoir to the surface, a collisional near-field just above the surface and a free-molecular far-field. In this work, a hybrid model of the plume, which treats each region separately, is constructed. Two subsurface models are considered: an analytical model and a more complex computational model. The analytical model is simply an isentropic gas-only flow through a converging-diverging nozzle while the computational model involves a more complicated geometry and includes various physics, e.g. grain condensation and wall interactions, which are neglected in the analytical model. Using the resulting vent conditions from these models, the plume is propagated from the surface vents out to several Enceladus radii using the direct simulation Monte Carlo (DSMC) method in the collisional near-field and a planetary-scale free-molecular model in the free-molecular far-field.

This model is then used to study the important physical processes associated with the expansion of the plume flow from the vents into vacuum, first in the absence of grains (only gas) and then in the presence of grains. In the latter study, various phenomena related to the gas-grain interaction during expansion, including the decoupling, lateral spreading and acceleration of the grains by the gas flow, are examined via a parametric study involving the grain radius radius/size and the grain-to-gas ratios of mass flow rates and

velocities at the vent. The subsurface flow resulting from the more complex computational subsurface model is also briefly investigated. Finally, the free-molecular far-field from the plume model is constrained using Cassini *in-situ* data to estimate the H_2O and grain production rates from the plume as well as infer certain conditions at the vent. A global source, which is modeled as a uniform spherical outflow, and a background source arising from the neutral torus around Saturn, which is modeled as a constant, are also included for the gas component when constraining the plume far-field using Cassini data.

In the study of the gas-only flow expansion process, Mach-3 and Mach-5 vent conditions resulting from the analytical subsurface model are considered, but most of the results are derived from the Mach-5 vent conditions. The Mach-3 vent conditions should produce qualitatively similar results. As the flow expands from the vents into vacuum, it passes through multiple regimes, from nearly continuum (very collisional) near the vents to free-molecular at higher altitudes. The altitude at which this transition occurs depends on the vent size for a given set of vent conditions. Moreover, collisions are important in the expansion process for maintaining equilibrium conditions, converting the molecular thermal and internal energy into the directed mean kinetic energy of the gas flow, and ensuring that the process is adiabatic. Since collisions cease as the flow expands, the flow must therefore be sufficiently collisional *at the vent* to drive the gas flow to the maximum speed possible, which depends on the source temperature. A source temperature of 273.16 K (H_2O triple-point temperature) produces a maximum speed of ~1005 m/s. The presence of an additional lighter species, e.g. H_2, could increase the maximum speed for the same source temperature. In addition, the flow is highly supersaturated just as it emerges from the vent. Consequently, condensation is very likely but is mostly confined to the first few vent diameters as collision rates drop rapidly. The maximum condensation growth via heterogeneous nucleation is derived and is found to be proportional to the vent size.

Assuming a negligible initial grain size, the micron-sized grains (≥ 1.6 μm in radius) detected by CDA would require vent diameters ~O(10–100 m), which could be easily observed. However, much smaller vents ~O(0.1–1 m) are enough to produce the nanometer-sized grains detected by CAPS.

In the study of the flow expansion process with grains, most of the results are again derived from the Mach-5 vent conditions because the Mach-3 vent conditions should produce qualitatively similar results. The effects of grains on the gas flow increase as the vent mass flow rate ratio increases or the vent velocity ratio decreases due to the greater exchange of momentum and energy between the gas and the grains. If the mass flow rate ratio is sufficiently high (> 1), the grains form a dense column which traps the gas flow and prevents it from expanding freely into vacuum. If the velocity ratio is sufficiently low (≤ 0.5), the expanding gas flow can actually be decelerated as its momentum is transferred to the slower grains to accelerate them. Furthermore, the slower grains can obstruct the gas flow and push it out to the sides, leading to a broader gas jet. For the same mass flow rate and velocity ratios, smaller grains have a greater and more widespread effect on the gas flow due to their greater quantity, lower inertia, and larger total surface and cross-sectional areas which result in a higher overall heat transfer rate and a larger drag on the gas flow. Smaller grains are also better at trapping gas within the grain column. For plausible mass flow rate ratios ≤ 1.0, however, the effects of grains on the gas flow should be minimal unless the velocity ratio is low (≤ 0.5).

Smaller grains are more strongly affected by the gas flow. Nanometer-sized grains decouple from the gas flow at altitudes of ~10–100 vent diameters and spread out with the gas flow while micron-sized grains decouple lower at < 10 vent diameters and remain in collimated beams. While the spreading angle of the grain jet increases as velocity ratio decreases due to greater drag, it remains small, ≤ 12°, for the micron-sized grains even at

small velocity ratios (≤ 0.5). Observations have inferred spreading angles ≥ 30°, suggesting that other mechanisms may be responsible for the spreading. For plausible mass flow rate ratios ≤ 1, the grain concentration is too dilute for grain-grain collisions to cause any significant spreading. Additionally, nanometer-sized grains are accelerated close to gas speeds whereas micron-sized grains tend to retain their initial speeds at the vent. As a result, the speeds of the smaller grains provide a better constraint for the gas speeds while the ejection (initial) speeds of the larger grains can be better constrained from measurements. In all the cases considered, however, all the grains are accelerated to escape speeds (> 240 m/s) even when they start much slower than the gas flow at the vent (at a velocity ratio of ~0.11). This contradicts other results and observations, which indicate that most of the grains are actually ejected at below escape speeds. Nonetheless, only two grain radii, 5 nm and 0.5 μm, and ejection velocities ≥ 100 m/s have been considered. Larger or slower grains would not be accelerated to escape speeds. The largest grains that can be accelerated from rest to escape speeds by the gas flow is proportional to the vent size. Small vents ~O(0.1 m) are enough to launch the micron-sized CDA grains (≥ 1.6 μm in radius) from rest to escape speeds for our Mach-3 and Mach-5 vent conditions.

In the study of the flow expansion process resulting from the vent conditions derived from the computational subsurface model, it is found that the collisional near-field directly above the vent is similar to that of the Mach-5 vent conditions from the analytical subsurface model. The flow passes through multiple regimes, from nearly continuum near the vent to free-molecular at higher altitudes, and is in equilibrium near the vent but not at higher altitudes. A non-equilibrium region also exists near the sublimating surface. The major differences in the near-field between the two cases are: (1) the gas density begins to drop almost immediately above the vent in this case while it does so higher up in the Mach-5 case, and (2) the gas experiences a greater acceleration above the vent in this case because

it has only begun to expand as it reaches the vent while it has done most of its expansion below the vent in the Mach-5 case. However, the gas does not accelerate to the maximum speed possible, which in this case is ~920 m/s, thus the flow at the vent is not collisional enough to convert all its molecular thermal and internal energy into mean kinetic energy.

The relative speed between the gas and the grains and the local mass concentration of grains relative to gas are small near the vent, but increase with altitude. This enhances the interaction between the gas and the grains, producing a dip in the gas density near the centerline. However, this dip disappears at higher altitudes as collision rates drop. The resulting gas jet is broader than the Mach-3 and Mach-5 jets and the resulting grain jet is narrow, spreading by only ~2°. Additionally, the grains are only accelerated by the gas from ~350 m/s at the vent to ~400 m/s at an altitude of 20 km.

The plume far-field is constrained using the E2, E3, E5 and E7 INMS H_2O density distributions and the E2 CDA grain density distribution for grains with radii $\geq$ 1.6 μm. In particular, the gas component is fitted to the INMS data in a weighted least-squares manner. The E2 INMS data are found to provide a poor constraint for the plume, which is consistent with the geometry of the spacecraft trajectory. The E3, E5 and E7 INMS data are dominated by the plume signal (especially E7) and offer better constraints. Accordingly, the best-fit solutions for the plume to these data sets are mostly insensitive to the global and background source strengths. They are, however, very sensitive to the vent conditions used. Three vent conditions are considered: the Mach-3 and Mach-5 vent conditions from the analytical subsurface model and the vent conditions from the computational subsurface model. The main difference among the vent conditions is the spreading angle of the gas jet produced. By assessing the quality of the fits from the different vent conditions, the Mach-5 vent conditions, which produce the narrowest jet, provide the best fits and are therefore the most plausible. Nonetheless, the best-fit simulated density distribution to the E7 INMS

data for the Mach-5 vent conditions has slightly broader peaks than the INMS data and fails to capture the peak magnitudes, implying even higher Mach numbers at the vent.

For the grain component, two ejection velocities, 100 m/s and 900 m/s, are considered for monodisperse grains of 5 μm. The entire E ring is simulated and its total mass is scaled to match estimates from observations to estimate the grain production rate from the plume. For the grains ejected at 900 m/s, the resulting grain density distribution is flat and does not capture the CDA peak as the spacecraft trajectory completely misses all the narrow grain jets. For the grains ejected at 100 m/s, the resulting grain density distribution captures both the width and magnitude of the CDA peak but not its timing. Slower ejection velocities result in slightly better agreement on the timing.

The H_2O and grain production rates from the plume are estimated to be ~O(100–1000 kg/s) and < 10 kg/s respectively, which are in agreement with other estimates. This suggests low ice/vapor mass ratios of < 0.1 in the plume, which has implications for the formation mechanism of the grains. A high ice/vapor mass ratio (> 0.1) would rule out condensation from the vapor phase, but our low ratio suggests that condensation remains a possibility. However, our plume model, especially the grain component, contains many limitations, thus making it hard to constrain the ice/vapor mass ratios in the plume. Some improvements on the plume model are suggested below.

8.2. FUTURE CONSIDERATIONS

In this work, the plume model consists of only the eight jets identified by Spitale and Porco (2007). While these jets have been shown to be able to capture the shapes and magnitudes of the Cassini data quite well, particularly the INMS H_2O density distributions, they do not represent the reality as more than 98 jets have recently been identified (Porco *et al.*, 2014). Some preliminary work and analysis on this have been done and can be found

in Appendix I. Furthermore, the plume model does not account for the distributed sources along the Tiger Stripes, which Postberg *et al.* (2011) found to be important in fitting to the CDA data along the E5 trajectory. Consequently, any future modeling work might consider incorporating the new jets and the distributed sources along the Tiger Stripes.

So far, only cases with single grain sizes and discrete ejection velocities have been considered. Moreover, a large fraction (> 90%), if not all, of the grains in these cases escape Enceladus and do not return. This contradicts various observations which indicate that a large fraction of the grains are ejected at well below escape speeds (Hedman *et al.*, 2009; Ingersoll and Ewald, 2011; Postberg *et al.*, 2011; Schmidt *et al.*, 2008) and would return to coat the surface with fresh materials. Additionally, the spreading mechanism studied, the velocity difference between the gas and the grains at the vent, could not reproduce the inferred spreading angles of ≥ 30° for the micron-sized grains (Ingersoll and Ewald, 2011; Postberg *et al.*, 2011). Therefore, different vent conditions (e.g. distributions of grain sizes and ejection velocities) or configurations (e.g. subsurface conditions and/or channel geometries), which could reproduce the observations, could be investigated. In addition, grain charging could be modeled, especially for the smaller nanometer-sized grains, as the Lorentz force has been found to strongly affect their motions (Dong and Hill, 2014; Meier *et al.*, 2014; Mitchell *et al.*, 2015).

All the suggestions above would add more free parameters to the plume model. As a result, more data would be required to constrain the model. To this end, Cassini data from newer trajectories (e.g. E14, E17 and E18) or existing data from other instruments (e.g. UVIS) could be used. The UVIS instrument provides line-of-sight H_2O column densities obtained from stellar occultation measurements. Some of the UVIS data sets that could be used as constraint could be found in Hansen *et al.* (2006, 2008, 2011). Surface grain size distributions in the south polar region, such as those found in Jaumann *et al.* (2008), could

also serve as a constraint because most of the plume grains fall back onto the surface. With such data, the distribution of grain deposition rates over the surface of Enceladus could also be estimated, similar to the analysis performed by Kempf *et al.* (2010).

In addition to needing more data, a greater number of free parameters would mean that a more systematic approach to the sensitivity analysis of the parameters is necessary because an exhaustive approach would be intractable. Consequently, a Bayesian analysis may be the next step in modeling to assess the significance of each parameter (Prudencio and Cheung, 2012; Strand, 2012).

In this work, the sharp peaks in the E7 INMS data are attributed to a high Mach number at the vent. However, it is possible that those peaks could have resulted from interaction between jets in the collisional near-field. Jets emerging from vents in close proximity may interact and produce shock interaction regions (Prisbell *et al.*, 2011). The gas density rises abruptly across the shocks, resulting in high-density regions. The sharp peaks may be signatures of these regions in the far-field. A study of this phenomenon would shed some light on this possibility. Since the flow becomes free-molecular at higher altitudes, the maximum distance between the vents that could still result in a shock interaction region should be computed.

As this work has shown, the grains form a thick column, which inhibits the free expansion of the gas flow into vacuum when the grain concentration is sufficiently high, leading to several interesting phenomena. Therefore, a study of the gas expansion through such a grain column would be helpful in gaining a greater understanding of the physical processes that could be occurring in the plume. A similar study of high-speed gas flows loaded with grains has been conducted experimentally in the past (Anilkumar, 1989).

Appendices

Appendix A.

Effects of Collisions between Grains

To determine the regime of the grain phase, we examine the magnitude of the grain volume fraction, Γ_{grain}, which is defined as:

$$\Gamma_{grain} \triangleq n_{grain} \forall_{grain} \tag{A.1}$$

where n_{grain} is the number density of grains and $\forall_{grain}$ is the volume of a grain ($\frac{4}{3}\pi r_{grain}^3$ for spherical grains). The grain phase is said to be dilute when $\Gamma_{\text{grain}} < 0.001$ and dense when $\Gamma_{\text{grain}} > 0.001$ (Crowe *et al.*, 2012). In the dilute regime, the motion of grains is governed by fluid forces. The dense regime can further be divided into collision-dominated and contact-dominated regimes. In the collision-dominated regime ($0.001 < \Gamma_{\text{grain}} < 0.1$), the motion of grains is governed by collisions between grains. The time of contact is much shorter than the time between collisions. On the other hand, the grains are in constant contact in the contact-dominated regime ($\Gamma_{\text{grain}} > 0.1$) and the motion of grains is governed by contact forces.

As shown in Table A.1, Γ_{grain} is very small, ranging from 10^{-9} to 10^{-7}, for all the cases considered in this work. As a result, the grain phase is dilute for all the cases considered and thus collisions between grains can be neglected. Note that the calculations have been performed based on properties at the vent. Farther from the vent, n_{grain} drops as the grain jet spreads, especially for cases with $r_{grain} = 5$ nm or $\alpha < 1.0$ where the grains are turned more by the gas flow (see Chapter 5). Consequently, Γ_{grain} would be even smaller.

Table A.1. Grain number density, n_{grain}, and volume fraction, Γ_{grain}, for all the cases considered in this work.

Case	r_{grain} **(μm)**	φ	α	n_{grain}, **m^{-3}**	Γ_{grain}
1	0.005 (5 nm)	0.1	1.0	7.5×10^{15}	3.9×10^{-9}
2	0.005 (5 nm)	1.0	1.0	7.5×10^{16}	3.9×10^{-8}
3	0.5	0.1	1.0	7.5×10^{9}	3.9×10^{-9}
4	0.5	1.0	1.0	7.5×10^{10}	3.9×10^{-8}
5	0.5	1.0	0.5	1.5×10^{11}	7.8×10^{-8}
6	0.005 (5 nm)	10.0	1.0	7.5×10^{17}	3.9×10^{-7}
7	0.5	10.0	1.0	7.5×10^{11}	3.9×10^{-7}
-	0.5	1.0	0.4	1.9×10^{11}	9.8×10^{-8}
-	0.5	1.0	0.3	2.5×10^{11}	1.3×10^{-7}
-	0.5	1.0	0.11	6.7×10^{11}	3.5×10^{-7}

As a side note, n_{grain} at the vent can be written in terms of φ, α and the gas number density, n, at the vent (~1.2×10^{21} m^{-3}):

$$n_{grain} = \left(\frac{\varphi}{\alpha}\right)\left(\frac{m}{m_{grain}}\right)n \tag{A.2}$$

where m and m_{grain} are the masses of an H_2O molecule and a grain respectively.

Appendix B.

Supersonic Boundary Conditions for Multi-Stage DSMC Calculations

As the flow expands from the vent into vacuum, it passes through multiple regimes, from collisional to free-molecular, and therefore spans a wide range of length and timescales (see Tables 3.2, 3.3 and 3.4). As a result, we simulated the expansion flow in multiple stages (see Section 3.3.2 for details on the implementation). This approach works only if the flow downstream of the interface between the stages does not significantly affect the flow upstream, i.e. only a small fraction of molecules are traveling upstream back into the lower stage. Several mechanisms can cause this. In our simulations, the main mechanism is collisions as a molecule could be scattered backwards after a collision. Consequently, this would be more of a problem in the near-field where the flow is collisional. As the flow expands into the far-field, collisions cease and this problem becomes less severe.

Let us consider the molecules in a cell immediately downstream of the interface, as shown in Figure B.1a. The surface outward normal unit vector of the interface is $\hat{\boldsymbol{n}}$**.** We have selected a cell along the top interface, but this also applies to the right interface (where downstream is to the right of the interface). In the limit of a very collisional flow, the gas is in equilibrium and its molecular velocities follow the Maxwellian distribution, which is given by:

$$f_M(C_i) = \left(\frac{m}{2\pi k_b T}\right)^{\frac{3}{2}} \exp\left\{-\frac{m}{2k_b T}[(C_1 - V_1)^2 + (C_2 - V_2)^2 + (C_3 - V_3)^2]\right\} \qquad \text{(B.1)}$$

where C_i and V_i are the different components of the molecular and bulk gas velocities respectively, m is the molecular mass, k_b is the Boltzmann constant, and T is the gas temperature. Integrating Equation (B.1) over all molecular velocities with a negative

outward normal component, i.e. $\boldsymbol{C}\bullet\hat{\boldsymbol{n}} = C_n < 0$, we obtain the fraction of molecules traveling upstream across the interface back into the lower stage, ξ_b:

$$\xi_b = \iiint_{C_n<0} f_M(C_i)\, dC_1 dC_2 dC_3$$

$$\xi_b = \frac{1}{2}\mathrm{erfc}\left(\frac{|\boldsymbol{V_n}|}{\sqrt{\frac{2k_bT}{m}}}\right) = \frac{1}{2}\mathrm{erfc}\left(\sqrt{\frac{\gamma}{2}}Ma_n\right) \tag{B.2}$$

where erfc() is the complementary error function, $|\boldsymbol{V_n}|$ is the magnitude of the bulk gas velocity component in the outward normal direction (see Figure B.1a), γ is the ratio of specific heats of the gas (4/3 for H_2O at our low temperatures) and Ma_n is the Mach number in the outward normal direction, i.e. $|\boldsymbol{V_n}|/a$ where a is the local speed of sound. As shown in Figure B.1b, ξ_b decreases rapidly as Ma_n increases. At $Ma_n = 0.5$, $\xi_b \approx 28\%$ and drops to ~12% at $Ma_n = 1$ and ~1% at $Ma_n = 2$. Consequently, the staging approach is more valid as the flow becomes more supersonic in the outward normal direction at the interface.

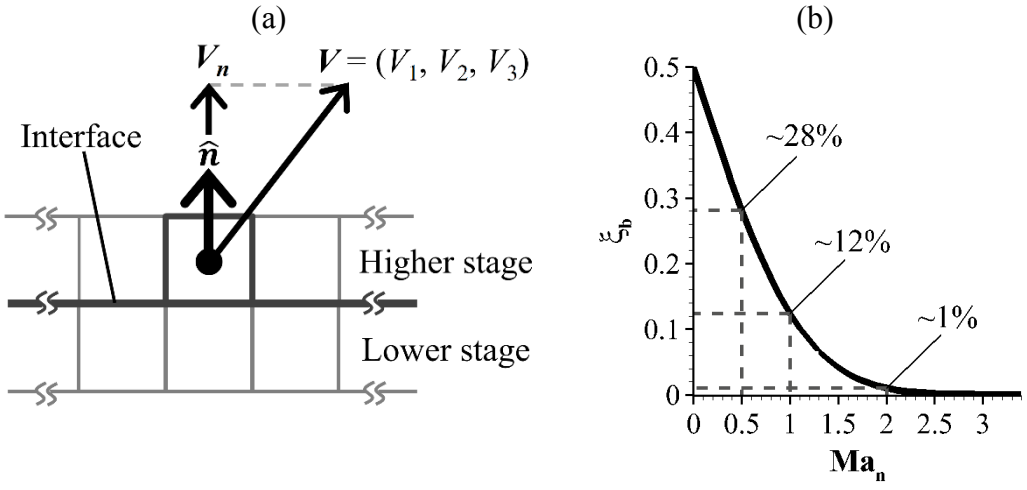

Figure B.1. (a) Cell immediately downstream of the interface. (b) Fraction of molecules traveling across the interface back into the lower stage, ξ_b, as a function of the outward normal Mach number at the interface, Ma_n.

Now, we examine if this condition is satisfied in our simulations. Let us denote the outward normal Mach numbers at the top and right interfaces as $Ma_{n,1}$ and $Ma_{n,2}$ respectively. Figures B.2a–f show contours of $Ma_{n,1}$ (top row) and $Ma_{n,2}$ (bottom row) in the first stage (directly above the vent where the flow is most collisional) for our Mach-3 and Mach-5 vent conditions and the case using input from the computational subsurface model. Note the different color and spatial scales of these figures. As shown in Figures B.2a–c, $Ma_{n,1}$ is larger than 2 across the *top* interface for all three cases. As shown in Figures B.2d–e, $Ma_{n,2}$ is also larger than 2 across the *right* interface for the Mach-3 and Mach-5 vent conditions. However, the flow along the edges of the jet is free-molecular and thus is highly non-equilibrium (see Figures 4.1a–b). As shown in Figure B.2f, $Ma_{n,2}$ is larger than 2 across the *right* interface for the case using input from the computational subsurface model except very close to the surface ($Z = 0$) where $Ma_{n,2} \approx 1$ due to sublimation from the surface.

However, a supersonic flow can be artificially produced across the interface due to the vacuum boundary condition (see Section 3.3.2), thus we must be careful in the placement of the interface. This is not so much of a problem for our Mach-3 and Mach-5 vent conditions because the flow is already supersonic at the vent. However, this is an issue for the case using input from the computational subsurface model where the flow is slightly subsonic at the vent. To determine if the interface is placed at the right location, we performed several runs with the location of the interface moved farther away from the vent in each run. The location of the interface is determined once the flowfield no longer changes. This procedure is illustrated in Appendix C.

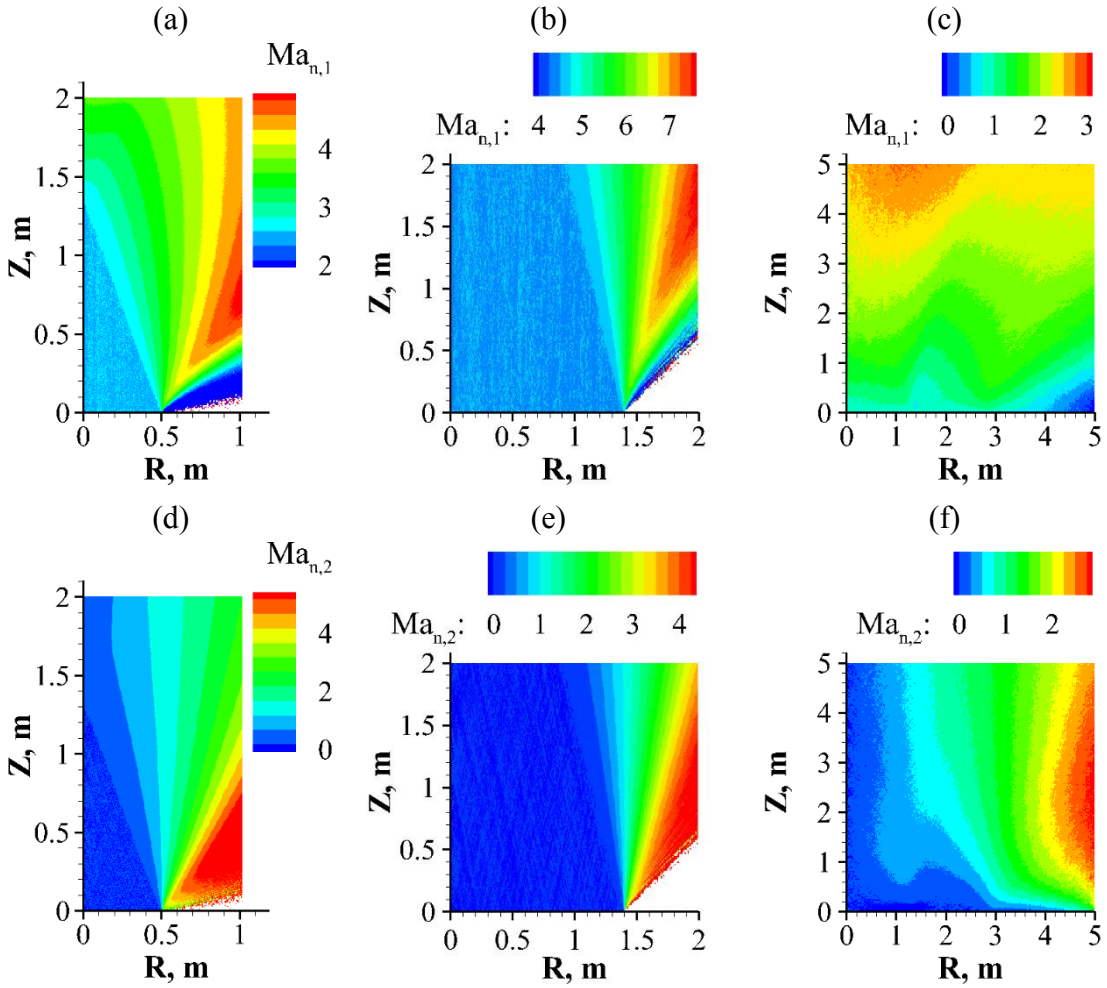

Figure B.2. Contours of outward normal Mach numbers at the top interface, $Ma_{n,1}$, and at the right interface, $Ma_{n,2}$, for the Mach-3 and Mach-5 vent conditions (first and second columns respectively) and the case using input from the computational subsurface model (third column). Note the different color and spatial scales for each figure.

Appendix C.

Placement of Vacuum Interface between Stages

In the multi-stage DSMC calculations, the interfaces between the stages are treated as vacuum boundaries and particles crossing these interfaces do not return but are stored for calculations at the subsequent stage (see Section 3.3.2). Consequently, it is important that the interfaces are placed at locations where the flow has become sufficiently supersonic in the direction normal to the interfaces so that the downstream flow no longer significantly affects the upstream flow (see Appendix B). This is not so much of a problem for the Mach-3 and Mach-5 vent conditions where the flow is already sufficiently supersonic at the vent but more of a problem for the simulation that takes input from the computational subsurface model where the flow is slightly subsonic at the vent (see Figure 6.3a). Moreover, a supersonic flow can be *artificially* produced normal to a vacuum boundary. Therefore, in order to determine if the interface has indeed been placed at the right location, the interface is progressively moved farther from the vent until the flowfield no longer changes.

This procedure is done to determine the size of the *innermost* domain of the simulation that takes input from the computational subsurface model (see Section 3.2.2). Figures C.1a–i show the contours of gas number density, n, translational temperature, T_{tr}, and rotational temperature, T_{rot}, (see definitions of T_{tr} and T_{rot} in Section 4.2) for three innermost domains with different sizes: 3 m × 3 m, 5 m × 5 m and 5.5 m × 5.5 m. The gas property contours in the overlapping region no longer change between the 5 m × 5 m domain and the 5.5 m × 5.5 m domain, thus a 5 m × 5 m innermost domain (see Table 3.4) puts the interface far enough from the vent.

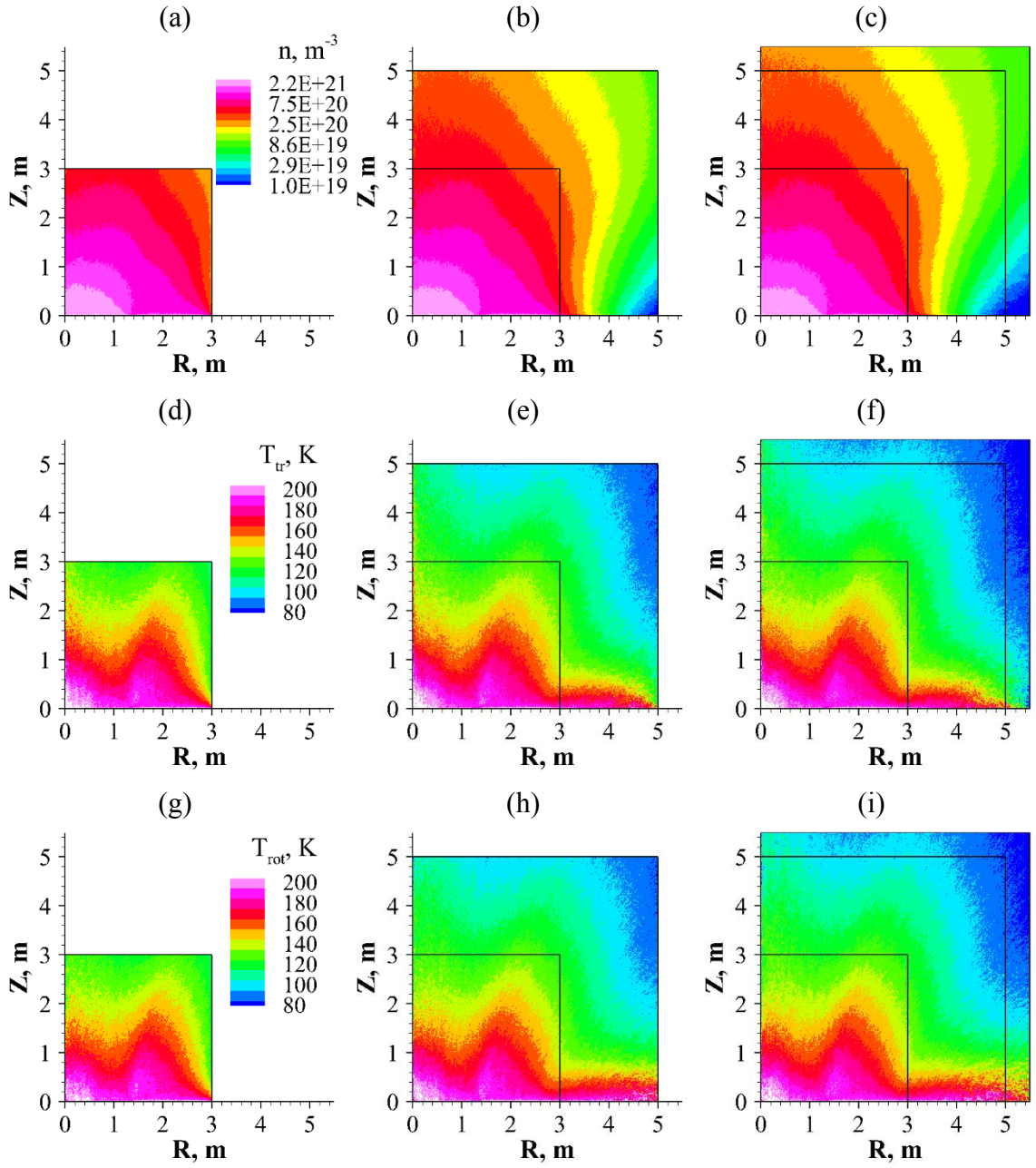

Figure C.1. Contours of gas number density (n), translational temperature (T_{tr}) and rotational temperature (T_{rot}) for domains with sizes: 3 m × 3 m (first column), 5 m × 5 m (second column) and 5.5 m × 5.5 m (third column). Each row (property) shares the same color bar. In the larger domains, the boundaries of the smaller domains have been drawn to aid with comparison.

This is consistent with the contours of outward normal Mach numbers at the top and right interfaces, denoted as $Ma_{n,1}$ and $Ma_{n,2}$ respectively, which are shown in Figures C.2a–f. In Appendix B, we have shown that less than 1% of the particles crossing the interface would return into the inner domain when the Mach number normal to the interface is greater than 2 (see Figure B.1b). Consequently, for the 5 m × 5 m domain, the flow is sufficiently supersonic normal to both the top interface, where $Ma_{n,1} \geq 2.4$ along the entire interface (see Figure C.2b), and the right interface, where $Ma_{n,2} \geq 2$ along most of the interface except near the surface (see Figure C.2e). Also note in Figure C.2d that a supersonic flow is artificially produced normal to the right interface of the 3 m × 3 m domain as this supersonic flow does not exist in the larger domains (see Figures C.2e–f).

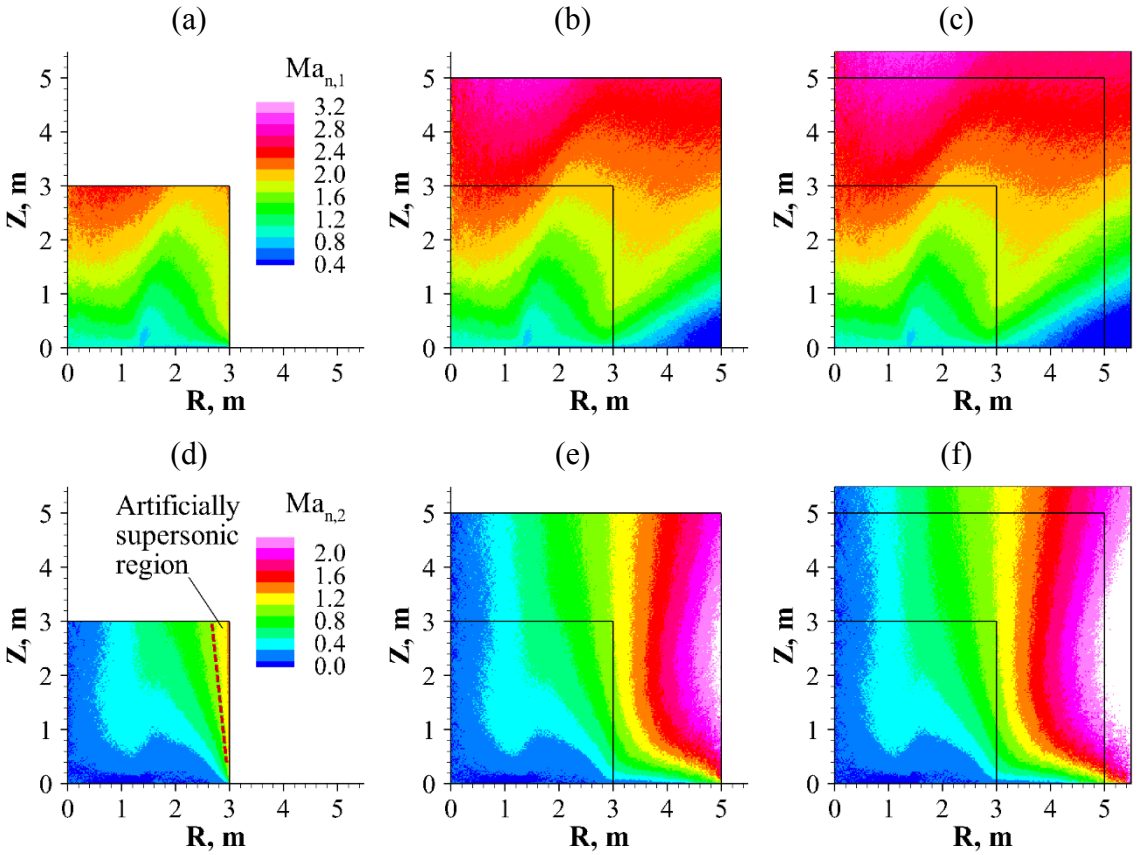

Figure C.2. Contours of outward normal Mach numbers at the top interface ($Ma_{n,1}$) and the right interface ($Ma_{n,2}$). Each row shares the same color bar. In the larger domains, the boundaries of the smaller domains have been drawn to aid with comparison.

Appendix D.

Grid Convergence Study

D.1. Vent Conditions from Analytical Subsurface Model

DSMC requires that the grid size, Δx, and the timestep, Δt, be smaller than the local mean free path, λ, and the local mean collision time, τ_{coll}, respectively (Bird 1994). As shown in Tables 3.2 and 3.3, the first few stages of the DSMC calculations for both the Mach-3 and Mach-5 vent conditions are resolved in timestep but not in grid size everywhere in the simulation domain of that stage (since λ given in Tables 3.2 and 3.3) is the minimum within the domain of that stage).

Collision rates away from the vent fall quickly due to the rapid drop in gas density (see Figures 4.4c–d). Moreover, most of the interactions between the gas and the grains, e.g. condensation grain growth (see Section 4.4) and the decoupling of the larger micron-sized grains (see Section 5.3), are confined to the region directly above the vent. Therefore, the grid convergence study performed is focused on the region within several vent diameters above the vent. Only the Mach-5 vent conditions (see Table 3.1) are considered because most of the results are based on these vent conditions.

The vent diameter, D_{vent}, chosen for the study is 2.8 m. The simulation domain is a 1° wedge with a height, h, of 10.08 m (~$3.6D_{vent}$) and a width, w, of 5.04 m (~$1.8D_{vent}$) directly above the vent (see Figure 3.4a for the shape of the domain). The timestep and grid size are chosen to be 0.4 μs ($<< \tau_{coll}$) and 1.2 mm (~λ) respectively. In addition, a particle traveling at ~900 m/s (the mean gas speed at the vent) would take ~3–4 timesteps to traverse a cell. The number of computational particles per cell is maintained at 5–50 except along the edges of the flow where the gas density drops to zero across expansion waves. The simulation is run in parallel on 960 processors distributed along the domain width.

First, a qualitative analysis is performed by comparing the contours of several macroscopic gas properties between the coarse case (as given in Tables 3.2 and 3.3) and fine case (as described above). Note that the fine case is run in a single stage while the coarse case is run in three stages. As shown in Figures D.1a and D.1d, the contours of gas number density, n, are almost identical between the two cases. In contrast, the contours of gas translational temperature, T_{tr} (see definition in Section 4.2), exhibit slightly more variations, as shown in Figures D.1b and D.1e. In particular, the red region, which corresponds to $T_{tr} \geq 52$ K, extends slightly higher for the fine case. As shown in Figures D.1c and D.1f, this is also observed in the contours of the gas rotational temperature, T_{rot} (see definition in Section 4.2). In addition, there are large differences in T_{rot} towards the edges of the flow ($R \geq 2$ m) as T_{rot} drops to lower values for the coarse case.

Next, a quantitative analysis is performed by comparing the profiles of these gas properties across half the width of the jet between the coarse and the fine cases at three different altitudes: $Z = 1.4$ m ($0.5D_{vent}$), 4.5 m ($\sim 1.6D_{vent}$) and 9.5 m ($\sim 3.4D_{vent}$). As shown in Figures D.2a, D.2c and D.2e, the profiles of n exhibit only slight differences between the cases at all three altitudes, which is in agreement with the results from the qualitative analysis. As shown in Figures D.2b, D.2d and D.2f, the computed profiles of T_{tr} in both cases are very similar at all three altitudes, with relatively small differences towards the edges of the flow ($R \geq 2$ m). The profiles of T_{rot} also shown in Figures D.2b, D.2d and D.2f exhibit greater differences between the cases. As in the profiles of T_{tr}, the differences are mostly confined towards the edges. The profiles of T_{tr} and T_{rot} in the core region of the flow ($R < 2$ m), however, are essentially identical between the cases at all three altitudes. The statistical noise has been reduced in the profiles of T_{tr} and T_{rot} via low-pass filtering.

At all three altitudes, T_{rot} is higher towards the edges of the flow for the fine case. Two possibilities could have caused this. First, the cells in the coarse case may be too large

towards the edges, resulting in too many collisions and too much rotational energy being converted into kinetic energy. Alternatively, it may be that there are not enough particles per cell towards the edges of the flow in the fine case, thus there are not enough collisions to convert rotational energy into kinetic energy.

However, this will not be investigated further in this work because of the excellent agreement in the computed gas properties between the coarse and the fine cases in the core region of the flow ($R < 2$ m) where most of the phenomena being investigated are occurring. Even if T_{rot} is incorrect towards the edges of the flow, it should not affect the fits of the simulated data to the *in-situ* data in this work as the fits involve only the density, which shows excellent agreement between the two cases everywhere. However, the plume emission signature, which is not studied in this work, may be affected. We estimate ~30% of the mass has a computed difference in $T_{rot} > 1$ K between the two cases.

In an expansion flow into the vacuum, the density drops to zero across expansion waves along the edges and the flow becomes free-molecular beyond a certain distance from the centerline ($R = 0$), as shown in Figures 4.1a–b where the local Knudsen numbers, Kn, are very large along the edges of the flow at all altitudes. Consequently, a non-equilibrium region exists along the edges of the flow, as shown in Figures 4.2a–d (where $T_{tr} \neq T_{rot}$). In a DSMC simulation of an expansion flow into vacuum, there will always be a dearth of particles near the edges of the flow. When the number of particles per cell drops below 2, collisions cannot occur and the different molecular energy modes cannot equilibrate. Therefore, it would be best if the number of particles per cell is maintained at ≥ 2 out to at least where non-equilibrium starts to occur in the physical flow to avoid an artificially larger non-equilibrium region along the edges of the simulated flow due to having insufficient particles in each cell.

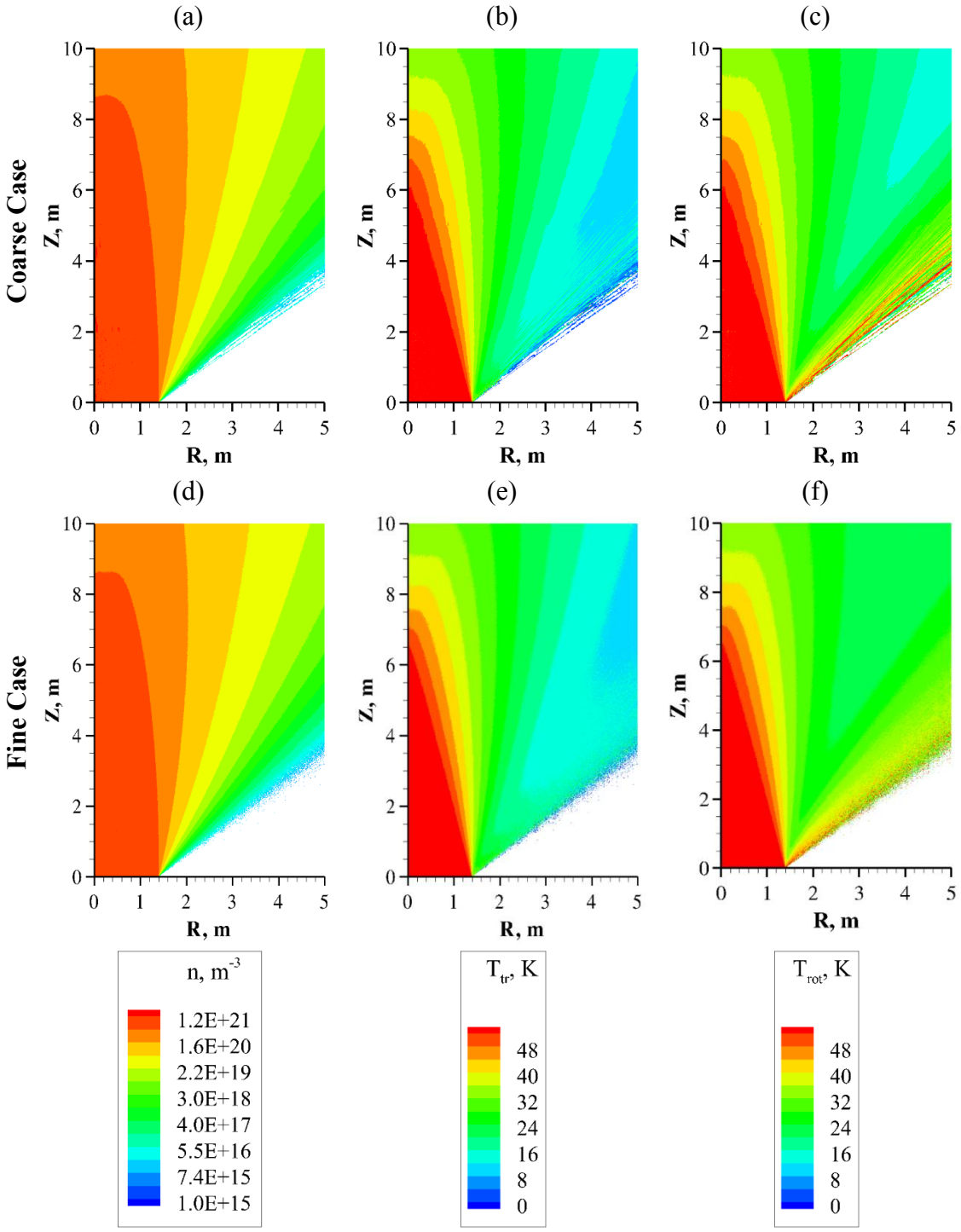

Figure D.1. Contours of gas number density (n), translational temperature (T_{tr}), and rotational temperature (T_{rot}) between the coarse (top row) and the fine (bottom row) cases.

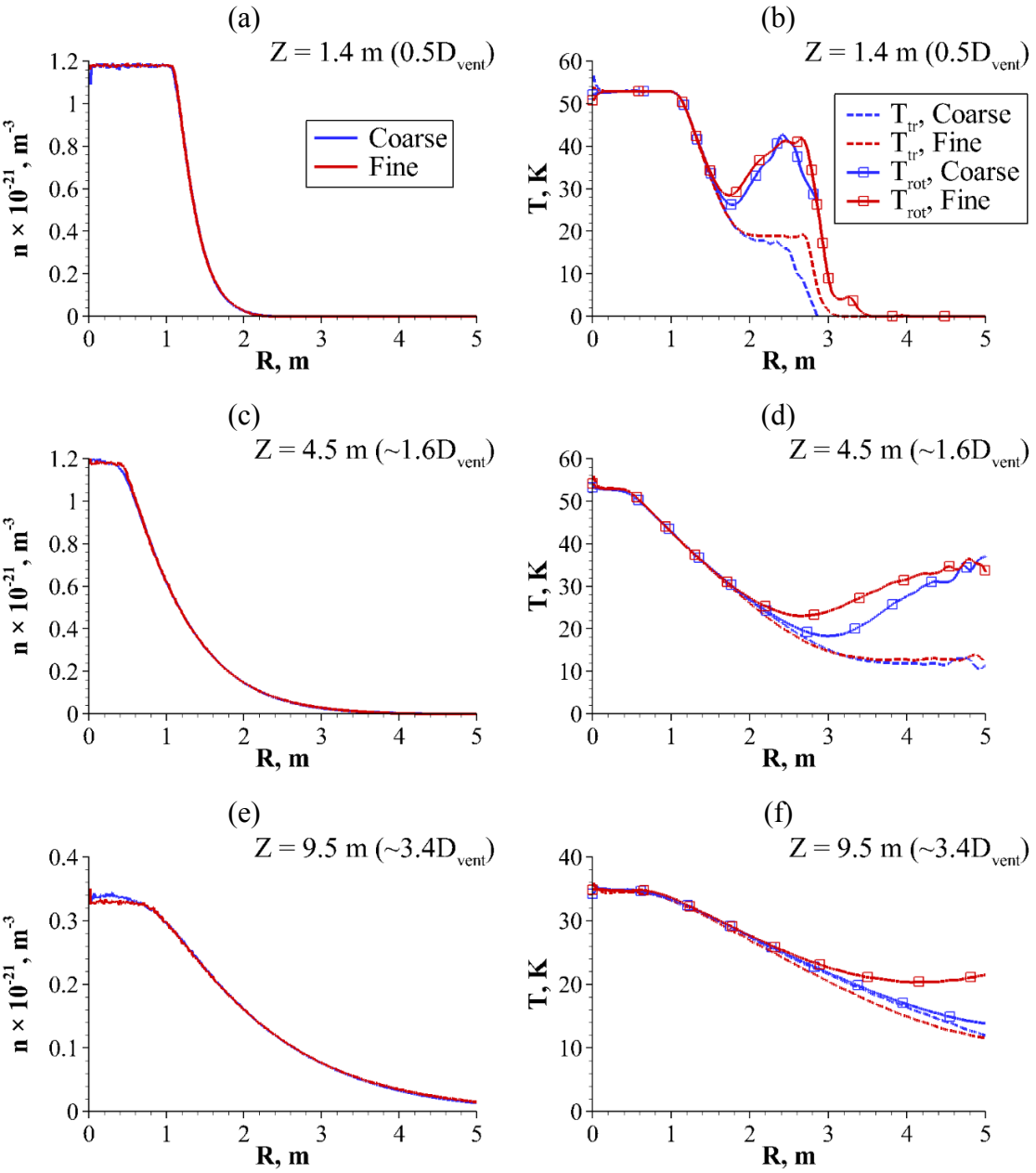

Figure D.2. Profiles of number density (n), translational temperature (T_{tr}) and rotational temperature (T_{rot}) across half the width of the jet between the coarse and the fine cases at three altitudes: Z = 1.4 m (0.5D_{vent}), 4.5 m (~1.6D_{vent}) and 9.5 m (~3.4D_{vent}).

D.2. VENT CONDITIONS FROM COMPUTATIONAL SUBSURFACE MODEL

As shown in Table 3.4, the DSMC calculations that take input from the computational subsurface model are also resolved in timestep but not in grid size everywhere in the domain for the first few stages. Consequently, we perform a grid convergence study for the first stage (5 m × 5 m × 1° wedge) where the flow is most collisional and thus it is most crucial that the grid size requirement be satisfied. Contours of n, T_{tr} and T_{rot} for two cases with different grid sizes, Δx = 0.01 m and 0.02 m, are shown in Figures D.3a–f. The timestep size is chosen to be 1 μs, and the average number of computational particles per cell is maintained between the two cases at ~10. As shown in Figures D.3a–f, there are no significant differences in the contours between the two cases, thus Δx = 0.02 m should be adequate.

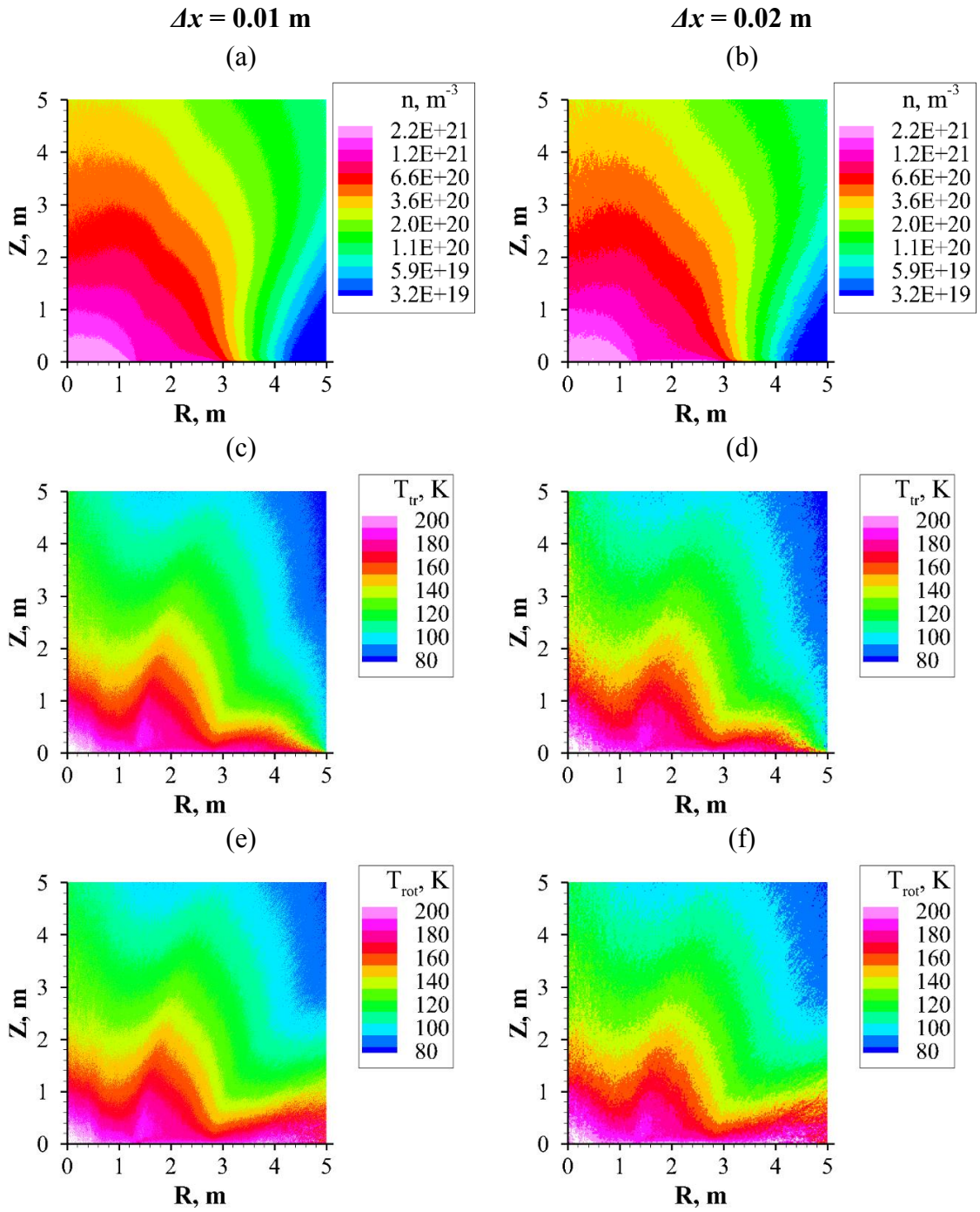

Figure D.3. Contours of gas number density (n), translational temperature (T_{tr}), and rotational temperature (T_{rot}) between two cases with different grid sizes, Δx = 0.01 m (left column) and 0.02 m (right column).

Appendix E.

Insertion Procedure for DSMC Particles into Free-Molecular Model

The collisional near-field directly above the vent is simulated using DSMC (see Section 3.3). Once collisions have ceased at higher altitudes, the DSMC output is passed on to the planetary-scale free-molecular model (see Section 3.4) that continues to propagate the plume out into space. The details on how the DSMC output is passed on to the free-molecular model are provided here.

Recall that the DSMC simulations are axisymmetric and thus are performed in a 1° wedge (see Figure 3.4a) located at the north pole. Moreover, the simulated jet is oriented in the local surface normal (vertical) direction. Once the flow becomes free-molecular, the DSMC particles (gas molecules and grains) are sampled and inserted into the free-molecular model at the eight jet sources identified by Spitale and Porco (2007) (see Table 3.5 for source locations and jet orientations). Prior to insertion, the positions and the velocities of the particles are rotated according to the location and local jet orientation of the source at which the particles are inserted. Both the DSMC and the free-molecular models use the same left-handed coordinate system with an origin at the center of Enceladus, as shown in Figure E.1.

Let the original position and velocity of a particle from the DSMC simulation be $\boldsymbol{r_{orig}} = (x_{orig}, y_{orig}, z_{orig})$ and $\boldsymbol{V_{orig}} = (u_{orig}, v_{orig}, w_{orig})$ respectively, as shown in Figure E.1. First, since the DSMC simulations are performed in a 1° wedge, the azimuthal position of the particle with respect to the local jet orientation is selected at random so as to produce a full 360° jet. The velocity of the particle is also converted accordingly. The transformed position, $\boldsymbol{r'}$, and velocity, $\boldsymbol{V'}$, of the particle are given by:

$$\boldsymbol{r}' = \begin{bmatrix} x' \\ y' \\ z' \end{bmatrix} = \begin{bmatrix} x_{orig}\cos(\theta_{rand}) + z_{orig}\sin(\theta_{rand}) \\ y_{orig} \\ -x_{orig}\sin(\theta_{rand}) + z_{orig}\cos(\theta_{rand}) \end{bmatrix} \tag{E.1}$$

$$\boldsymbol{V}' = \begin{bmatrix} u' \\ v' \\ w' \end{bmatrix} = \begin{bmatrix} u_{orig}\cos(\theta_{rand}) + w_{orig}\sin(\theta_{rand}) \\ v_{orig} \\ -u_{orig}\sin(\theta_{rand}) + w_{orig}\cos(\theta_{rand}) \end{bmatrix} \tag{E.2}$$

where θ_{rand} is a uniformly distributed random angle between 0 and 2π (in radians).

Next, the position and the velocity of the particle are rotated according to the local jet orientation of the source at which the particle is inserted. The local jet orientation is given by two angles: the zenith, θ_{zen}, and the azimuth, θ_{azim}. The definitions of these angles are given in the footnotes below Table 3.5. The transformed position, $\boldsymbol{r}''$, and velocity, $\boldsymbol{V}''$, of the particle are given by:

$$\boldsymbol{r}'' = \begin{bmatrix} x'' \\ y'' \\ z'' \end{bmatrix} = \begin{bmatrix} x'\cos\theta_2 + (y' - R_{Enc})\sin\theta_1\sin\theta_2 + z'\cos\theta_1\sin\theta_2 \\ (y' - R_{Enc})\cos\theta_1 - z'\sin\theta_1 \\ -x'\sin\theta_2 + (y' - R_{Enc})\sin\theta_1\cos\theta_2 + z'\cos\theta_1\cos\theta_2 \end{bmatrix} \tag{E.3}$$

$$\boldsymbol{V}'' = \begin{bmatrix} u'' \\ v'' \\ w'' \end{bmatrix} = \begin{bmatrix} u'\cos\theta_2 + v'\sin\theta_1\sin\theta_2 + w'\cos\theta_1\sin\theta_2 \\ v'\cos\theta_1 - w'\sin\theta_1 \\ -u'\sin\theta_2 + v'\sin\theta_1\cos\theta_2 + w'\cos\theta_1\cos\theta_2 \end{bmatrix} \tag{E.4}$$

where $\theta_1 = \theta_{zen}$, $\theta_2 = \theta_{azim}$ and R_{Enc} is the radius of Enceladus, 252.1 km.

Finally, the position and the velocity of the particle are rotated according to the location of the source at which the particle is inserted. The location of the source is given by latitude, θ_{lat}, and longitude, θ_{lon}, as defined in the footnotes below Table 3.5. Consequently, the final position, $\boldsymbol{r}'''$, and velocity, $\boldsymbol{V}'''$, of the particle at the jet source are given by:

$$\boldsymbol{r}''' = \begin{bmatrix} x''' \\ y''' \\ z''' \end{bmatrix} = \begin{bmatrix} x'' \cos\theta_3 + (y'' + R_{Enc}) \sin\theta_3 \sin\theta_4 - z'' \cos\theta_4 \sin\theta_3 \\ (y'' + R_{Enc})\cos\theta_4 + z''\sin\theta_4 \\ x'' \sin\theta_3 - (y'' + R_{Enc})\sin\theta_4\cos\theta_3 + z'' \cos\theta_3 \cos\theta_4 \end{bmatrix} \quad \text{(E.5)}$$

$$\boldsymbol{V}''' = \begin{bmatrix} u''' \\ v''' \\ w''' \end{bmatrix} = \begin{bmatrix} u'' \cos\theta_3 + v'' \sin\theta_3 \sin\theta_4 - w'' \cos\theta_4 \sin\theta_3 \\ v''\cos\theta_4 + w''\sin\theta_4 \\ u'' \sin\theta_3 - v''\sin\theta_4\cos\theta_3 + w'' \cos\theta_3 \cos\theta_4 \end{bmatrix} \quad \text{(E.6)}$$

where $\theta_3 = \pi - \theta_{lon}$ and $\theta_4 = \pi/2 - \theta_{lat}$.

In summary, Equations (E.1) through (E.6) are used to transform the original position and velocity of the particle, $\boldsymbol{r}_{orig}$ and $\boldsymbol{V}_{orig}$ respectively, resulting from a DSMC simulation in a 1° wedge located at the north pole and oriented in the local surface normal (vertical) direction into the position and velocity of the particle, $\boldsymbol{r}'''$ and $\boldsymbol{V}'''$ respectively, for a full 360° jet located elsewhere and not necessarily oriented in the local surface normal direction. In addition to accounting for the local jet orientation of the source, this procedure accounts for the spatial extent of the jet at the location of insertion (as opposed to simply inserting particles from a point source). A schematic of the entire insertion procedure is illustrated in Figure E.1.

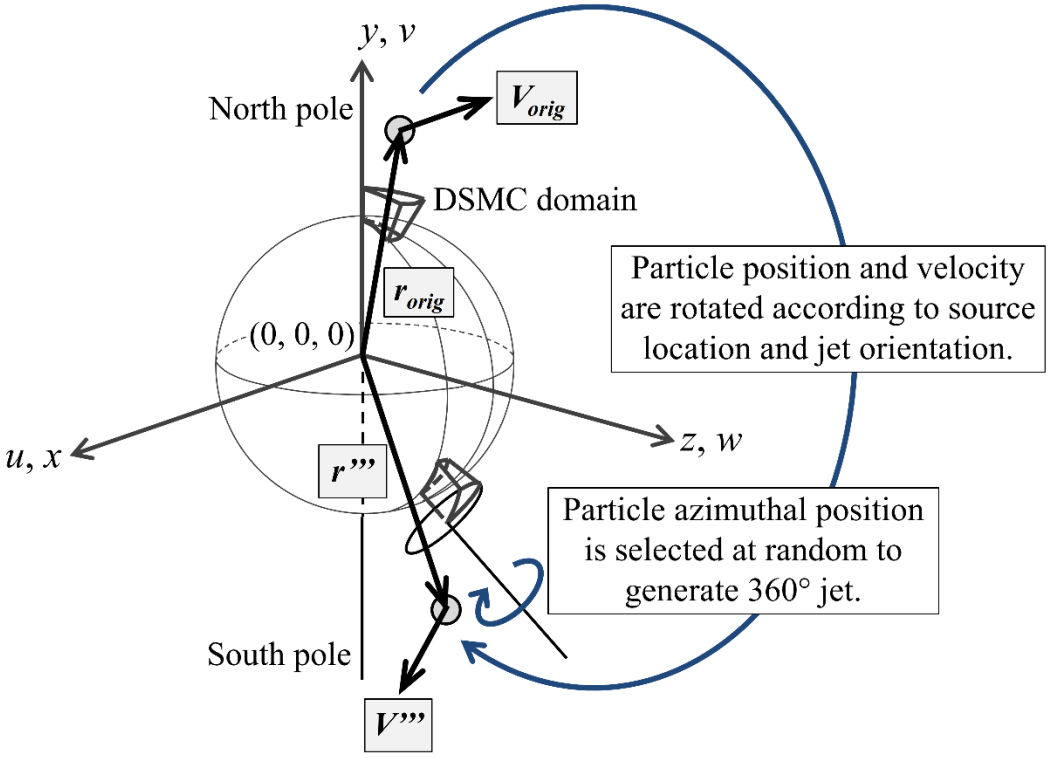

Figure E.1. Coordinate system of the DSMC and free-molecular models and schematic of insertion procedure for DSMC particles into the free-molecular model.

Appendix F.

Simulated E-ring Density Profiles near Enceladus

Here we explore the vertical and horizontal (radial) density profiles of our simulated E ring near Enceladus, as shown in Figures F.1a–b, for monodisperse grains of r_{grain} = 5 μm for three ejection velocities at the vent: V_{init} = 100 m/s, 400 m/s and 900 m/s. The total grain mass production rate, $\dot{M}_{grain}$, from Enceladus is the same for all three cases and has been arbitrarily set. The vertical and horizontal sampling cell sizes are ~600 km (~0.01R_S) and ~5300 km (~0.1R_S) respectively. Note that the sampling cell sizes used to obtain the E2 simulated grain density profiles in Section 7.4 are much smaller (see Section 3.5.2). We have also neglected various processes which may be important to the long-term dynamics of the E-ring grains (see Section 3.4).

As shown in Figure F.1a, the vertical density profiles of our simulated E ring are bi-modal, with a stronger peak at the south side (below the ring plane), for all three cases. This stronger southern peak is because the grains are ejected from the south pole of Enceladus. For V_{init} = 900 m/s, there are two peaks at the south side. The density profile is a superposition of the individual profiles from the eight jets used in our model. Most of the individual profiles also exhibit bi-modality, and the presence of the second peak near −0.22R_S is due to the individual profiles from Jets III and VII. While we will not pursue further why these jets differ from the others, it is interesting to note that these jets have the largest zenith angles, > 20º (see Table 3.5).

This bi-modality was also observed in E-ring simulations by Kempf *et al.* (2008) for single ejection velocities (see Figure 5 in their paper). Their simulations tracked the evolution of the grain charges and included the gravity of Saturn and all E-ring moons, the Lorentz force and solar radiation pressure. Based on *in-situ* CDA measurements, however,

they found that the E-ring vertical density profile for $r_{grain} \geq 1$ μm more closely resembled a Gaussian. They proposed that the bi-modality in their simulated profiles arose due to the single ejection velocities used, resulting in a narrow range of orbital inclinations. A distribution of ejection velocities might have smeared out the bi-modality in the individual profiles from each velocity in the CDA measurements.

The vertical extent of our simulated E ring increases with V_{init}. This is because the faster grains reach greater distances above and below the Saturn equatorial plane. However, they are more dispersed for the same $\dot{M}_{grain}$, resulting in lower densities. The distances between the two peaks for V_{init} = 100 m/s, 400 m/s and 900 m/s are ~3,000 km (~0.05R_S), ~10,000 km (~0.17R_S) and ~32,000 km (~0.53R_S) respectively. In comparison, the full-width-half-maximum (FWHM) of the E-ring vertical density profile near Enceladus measured by the CDA is (4362 ± 212) km for $r_{grain} \geq 1.6$ μm (Kempf *et al.*, 2008). This is comparable to the distance between the peaks for V_{init} = 100 m/s but is significantly smaller than those for V_{init} = 400 m/s and 900 m/s. Since the vertical extent of the ring is largely due to the plume (Kempf *et al.*, 2008), this may suggest that the larger escaping grains are ejected at slower V_{init}, which is consistent with several observations and predictions (Hedman *et al.*, 2009; Ingersoll and Ewald, 2011; Postberg *et al.*, 2011; Schmidt *et al.*, 2008).

On the other hand, the horizontal extent of our simulated E ring is less strongly affected by V_{init}, as shown in Figure F.1b. However, the peak density of the horizontal profile is higher for slower V_{init} because the faster grains are more dispersed out of the ring plane, as mentioned earlier. As shown in Figure F.1b, the peaks of the horizontal density profiles appear to be flat and truncated. This is not real but is an artifact of the crude resolution used in the horizontal direction (a factor of 10 more crude than the resolution

used in the vertical direction). A finer horizontal resolution would have resolved the peak better.

To investigate how the gravity of Enceladus affects the E-ring structure near Enceladus, we run our simulation longer after steady state is reached (for another ~30 years) with the particle creation and loss mechanisms turned off (see Section 3.5.2 for loss mechanisms considered). Consequently, the evolution of the E ring is now solely due to changes in the orbital dynamics of the grains under the gravitational fields of Saturn and Enceladus. This is only done for V_{init} = 400 m/s. As shown in Figure F.1a, we find that the bi-modality in the vertical profile has weakened. In fact, the longer the simulation is run, the weaker the bi-modality becomes. Moreover, the vertical extent of the ring has increased slightly and the density profile drops more gradually to zero at the edges. The densities are also lower. As shown in Figure F.1b, the densities of the horizontal profile are also lower, but the horizontal extent of the ring has increased significantly.

It appears that the gravity of Enceladus is scattering the grains away from the vertical axis passing through the center of Enceladus over the long term, resulting in reduced bi-modality in the vertical profile and a greater horizontal extent of the ring. Because the grains are more spread out in the horizontal direction, the densities are lower. We expect this effect to increase as V_{init} decreases because the slower grains would spend more time near Enceladus and thus be scattered more strongly.

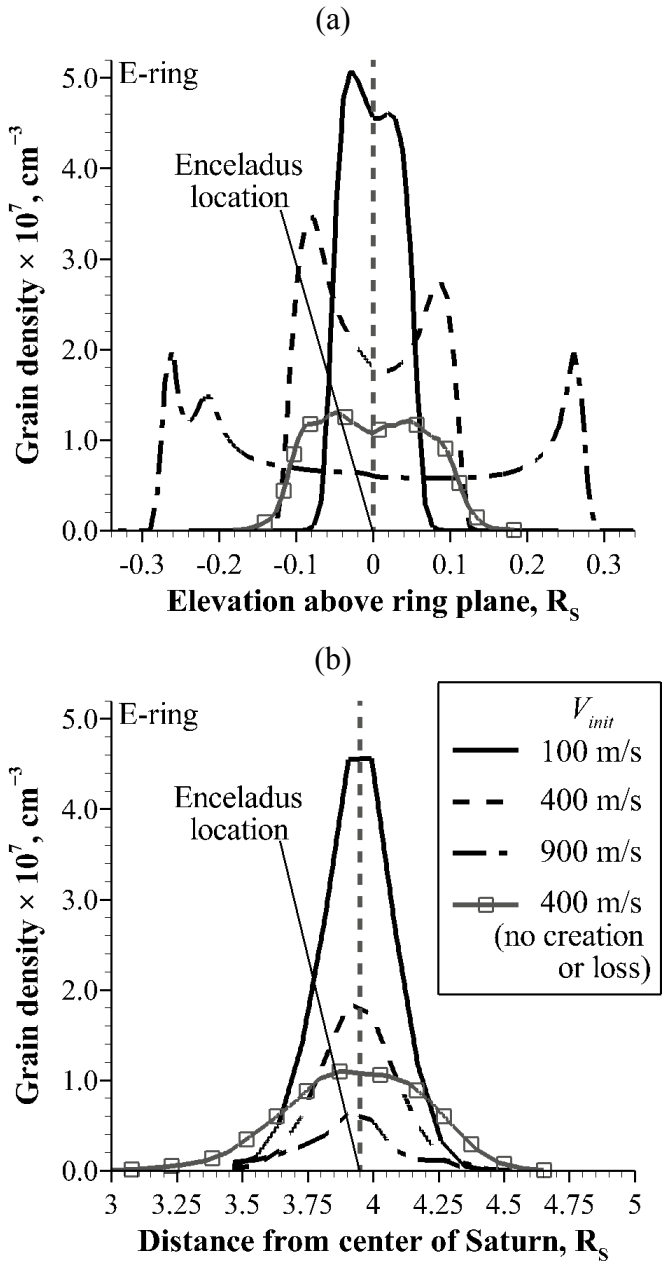

Figure F.1. (a) Vertical and (b) horizontal (radial) simulated E-ring density profiles for r_{grain} = 5 μm for initial grain velocities at the vent, V_{init} = 100 m/s, 400 m/s and 900 m/s. All result from the same total grain mass production rate, $\dot{M}_{grain}$, from Enceladus, which has been arbitrarily set. The radius of Saturn, R_S, and the distance of Enceladus from the center of Saturn are 60,330 km and 238,020 km (~3.95R_S) respectively. Both figures share the same symbols and line patterns. Note the linear scale on the y-axis.

Appendix G.

Derivation of Ultimate Speed of Adiabatic Expansion for Gas Mixture

Consider a *uniform* mixture of several gas species *at rest* and in *equilibrium* in a reservoir at temperature T_0, pressure p_0 and density ρ_0. This mixture is then allowed to expand into vacuum. It would achieve the maximum mean (bulk) speed possible when *all* its molecular random kinetic (thermal) and internal energy is converted into mean kinetic energy in an *adiabatic* process. This speed is called the ultimate speed of adiabatic expansion, V_{ult}, which is given by:

$$V_{ult} = \sqrt{2h_0} \tag{G.1}$$

where h_0 is the specific stagnation enthalpy of the mixture (per unit mass) in the reservoir and is defined as:

$$h_0 \triangleq e_0 + \frac{p_0}{\rho_0} \tag{G.2}$$

where e_0 is the specific energy of the mixture.

To obtain h_0, let us first derive e_0. By the principle of equipartition, the energy per molecule of species i, e_i', is given by:

$$e_i' = f_i \left(\frac{1}{2} k_b T_i\right) \tag{G.3}$$

where f_i is the total number of degrees of freedom (d.o.f) of *fully excited* molecular energy modes (e.g. translational, rotational and vibrational), k_b is the Boltzmann constant, and T_i is the temperature of species i. For instance, for a diatomic gas at low temperatures, only the translational and rotational modes are fully excited. Therefore, f_i would be 3 (translational) + 2 (rotational) = 5.

The total energy contained in gas species i is thus given by:

$$E_i = N_i e_i' = N_i f_i \left(\frac{1}{2} k_b T_i\right) \tag{G.4}$$

where N_i is the number of gas molecules of species i. Consequently, the total energy contained in the gas mixture is the sum of the total energy of each species:

$$E_0 = \sum_{i=1}^{N_s} E_i = \sum_{i=1}^{N_s} N_i f_i \left(\frac{1}{2} k_b T_i\right) \tag{G.5}$$

where the summation is over all the species present in the mixture, N_s. The total mass of molecules of species i is given by $M_i = N_i m_i$, where m_i is the molecular mass of species i. Therefore, the total mass of the gas mixture is given by:

$$M = \sum_{i=1}^{N_s} M_i = \sum_{i=1}^{N_s} N_i m_i \tag{G.6}$$

Equation (G.5) is rewritten in terms of specific gas constants of each species, $R_i = k_b/m_i$:

$$E_0 = \sum_{i=1}^{N_s} N_i m_i f_i \left(\frac{1}{2} R_i T_i\right) = \sum_{i=1}^{N_s} M_i f_i \left(\frac{1}{2} R_i T_i\right) \tag{G.7}$$

The specific energy of the mixture is obtained by dividing Equation (G.7) by Equation (G.6):

$$e_0 = \frac{E_0}{M} = \sum_{i=1}^{N_s} \frac{M_i}{M} f_i \left(\frac{1}{2} R_i T_i\right) = \sum_{i=1}^{N_s} \chi_i f_i \left(\frac{1}{2} R_i T_i\right) \tag{G.8}$$

where χ_i is the mass fraction of species i, defined as M_i/M. The pressure of the mixture is the sum of the partial pressures of all the species:

$$p_0 = \sum_{i=1}^{N_s} p_i = \sum_{i=1}^{N_s} \chi_i \rho_0 R_i T_i \tag{G.9}$$

Substituting Equations (G.8) and (G.9) into Equation (G.2):

$$h_0 = \sum_{i=1}^{N_s} \chi_i f_i \left(\frac{1}{2} R_i T_i\right) + \sum_{i=1}^{N_s} \chi_i R_i T_i = \sum_{i=1}^{N_s} \chi_i \left(\frac{f_i + 2}{2}\right) R_i T_i \tag{G.10}$$

Since the gas mixture exists in equilibrium, the temperatures of all species are equal, i.e. $T_i = T_0$ for all species i. Therefore, Equation (G.10) becomes:

$$h_0 = T_0 \left[\sum_{i=1}^{N_s} \chi_i \left(\frac{f_i + 2}{2}\right) R_i\right] \tag{G.11}$$

The term in the parentheses is the specific heat of the gas mixture at constant pressure:

$$c_p = \sum_{i=1}^{N_s} \chi_i \left(\frac{f_i + 2}{2}\right) R_i \tag{G.12}$$

Substitute Equation (G.11) into Equation (G.1):

$$V_{ult} = \sqrt{2T_0 \left[\sum_{i=1}^{N_s} \chi_i \left(\frac{f_i + 2}{2}\right) R_i\right]} = \sqrt{T_0 \left[\sum_{i=1}^{N_s} \chi_i (f_i + 2)\, R_i\right]} \tag{G.13}$$

Now, let us apply Equation (G.13) to a gas mixture consisting of water vapor and hydrogen at the triple-point temperature of water, $T_0 = 273.16$ K. At this temperature, only the translational and rotational modes are fully excited for either species. Therefore, $f_{H_2} = 3 + 2 = 5$ and $f_{H_2O} = 3 + 3 = 6$ (H_2O molecule is a triatomic with 3 rotational d.o.f. due to its bent geometry). The gas constants for H_2 and H_2O are ~4124 J/kg-K and ~462 J/kg-K respectively. The ultimate speed of the mixture, V_{ult}, as a function of hydrogen mass fraction, χ_{H_2}, is shown in Figure G.1. Consequently, a higher V_{ult} can be achieved when the gas is a mixture of water vapor and a lighter species such as hydrogen instead of simply pure water vapor. As shown in Figure G.1, a χ_{H_2} of ~23% is sufficient to produce $V_{ult} \approx$ 1600 m/s, which is the lower limit of the gas speeds inferred from UVIS observations

(Hansen *et al.*, 2011). The upper limit, ~2600 m/s, requires a χ_{H_2} of ~84%, thus the mixture is predominantly composed of hydrogen by mass. This seems to be implausible.

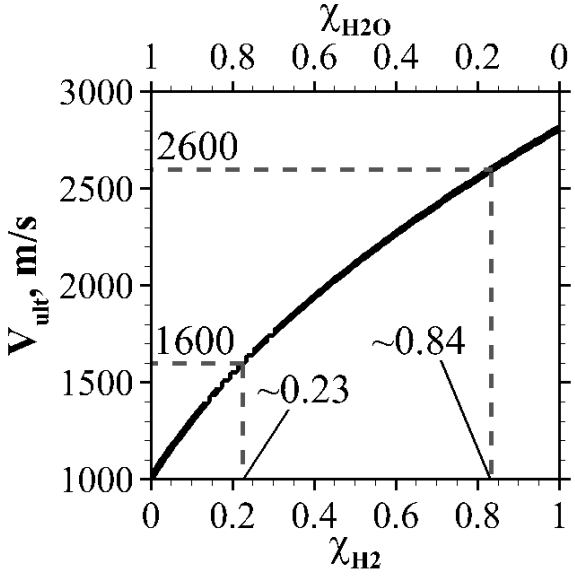

Figure G.1. Ultimate speed, V_{ult}, of gas mixture consisting of hydrogen and water vapor as function of mass fraction of hydrogen, χ_{H_2}. The x-axis at the top is the mass fraction of water vapor, $\chi_{H_2O} = 1 - \chi_{H_2}$.

Appendix H.

Distributions of Grain Radius Increments and Salinity due to Condensation above Vents

H.1. DERIVATIONS

Consider the vent conditions from the analytical subsurface model (see Table 3.1). As shown in Section 4.4, the flow is highly supersaturated just above the vent. As a result, the grains emerging from the vent would grow due to condensation. Moreover, if the grains emerge with some initial salt mass fraction, this fraction would change as the condensing vapor is salt-poor and would form a salt-poor outer shell around the salty cores, as shown in Figure H.1a.

Using the condensation model derived in Section 4.5.1, we derive the distributions of radius increments, Δr_{grain}, due to condensation and final salt mass fractions, β_f, for the grains emerging from the vent. Assume the following grain properties are given at the vent and only depend on the distance from the centerline, R, as shown in Figure H.1b:

$$r_0 = r_0(R)$$
$$\beta_0 = \beta_0(R)$$
$$n_{grain} = n_{grain}(R)$$
$$u_{grain} = u_{grain}(R)$$

where r_0 and β_0 are the initial grain radius and salt mass fraction respectively, and n_{grain} and u_{grain} are the grain number density and velocity respectively.

In addition to the assumptions made in Section 4.5.1, we also assume that:

1) The vent is circular, with diameter D_{vent}.
2) The flow is axisymmetric.
3) The gas properties (e.g. density, temperature and velocity) are uniform across the vent.
4) The initial grain salt mass fractions are very small, i.e. $\beta_0 << 1$.

5) The condensing vapor is *totally* devoid of salt ($\beta_{vapor} = 0$).

Assumption 4 should be valid as the upper limit on the grain salt mass fractions would be that of the subsurface salty ocean at ~2–20 g/kg or ~0.002–0.02 (Postberg *et al.*, 2009; Zolotov, 2007). As the grains travel up the subsurface channel, the salt-poor vapor would condense on them and reduce their salt mass fractions before they exit the vent.

First, we derive the distribution of Δr_{grain}. In Section 4.5.1, we have shown that Δr_{grain} does not depend on r_0 and have derived Δr_{grain} along the centerline ($R = 0$). Here, we extend this to the *entire* vent. First, let us consider only the growth occurring below the first expansion wave where the gas properties are uniform. Therefore, we only perform the integration in Equation (4.4) from the vent ($Z^* = Z/D_{vent} = 0$) to the first expansion wave ($Z^* = Z_{\text{wave}}/D_{vent}$):

$$\Delta r^*_{grain} \triangleq \frac{\Delta r_{grain}}{D_{vent}} = \frac{m}{4\rho_{ice}} \int_0^{\frac{Z_{wave}}{D_{vent}}} \frac{n_{gas}(Z^*)\bar{c}(Z^*)}{u_{gas}(Z^*)} dZ^*$$

$$\Delta r^*_{grain} = \frac{m}{4\rho_{ice}} \left[\frac{n_{gas}(0)\bar{c}(0)}{u_{gas}(0)}\right] \frac{Z_{wave}}{D_{vent}} \tag{H.1}$$

where $n_{gas}(0)$, $\bar{c}(0)$ and $u_{gas}(0)$ are the gas properties at the vent. As shown in Figure H.1a, the height of the first expansion wave from the vent, Z_{wave}, is a linear function of R. By geometry,

$$Z_{wave} = Z_0 \left(1 - \frac{2R}{D_{vent}}\right) \tag{H.2}$$

where Z_0 is the height at which the first expansion wave crosses the centerline and is given by:

$$Z_0 = \frac{D_{vent}}{2\tan(\mu_{vent})} \tag{H.3}$$

where μ_{vent} is the vent Mach angle, i.e. $\mu_{vent} = \sin^{-1}(1/Ma_{vent})$ (Anderson, 2003). Substitute Equations (H.2) and (H.3) into Equation (H.1) and obtain:

$$\Delta r^*_{grain} = \frac{m}{4\rho_{ice}}\left[\frac{n_{gas}(0)\bar{c}(0)}{u_{gas}(0)}\right]\frac{1}{2\tan(\mu_{vent})}\left(1-\frac{2R}{D_{vent}}\right) \tag{H.4}$$

Note that Δr^*_{grain} in Equation (H.4) only accounts for the growth below the first expansion wave. In Section 4.5.2, we determine that ~60% of the total growth along the *centerline* ($R = 0$) occurs below the first expansion wave for both $Ma_{vent} = 3$ and 5. Assuming this applies to the entire vent, we estimate the total Δr^*_{grain} over the entire vent by dividing the right-hand side of Equation (H.4) by 0.6 to obtain:

$$\Delta r^*_{grain} = \frac{5}{12}\frac{m}{\rho_{ice}}\left[\frac{n_{gas}(0)\bar{c}(0)}{u_{gas}(0)}\right]\frac{1}{2\tan(\mu_{vent})}\left(1-\frac{2R}{D_{vent}}\right)$$

$$\Delta r^*_{grain} = h(Ma_{vent})\left(1-\frac{2R}{D_{vent}}\right) \tag{H.5}$$

where $h(Ma_{vent})$ is Δr^*_{grain} at the center of the vent ($R = 0$) and is only a function of Ma_{vent}.

Note that Δr^*_{grain} is a linear function of R. The largest growth occurs along the centerline ($R = 0$) while there is no growth at the edges ($R = D_{vent}/2$). Grains at the center traverse the greatest distance before reaching the first expansion wave (see Figure H.1a), thus they stay the longest in the near-vent region where the gas density is the highest. As a result, they experience more collisions and grow larger. In contrast, grains at the edges immediately encounter the first expansion wave above which the gas density and collision rates drop rapidly, and they barely have a chance to grow.

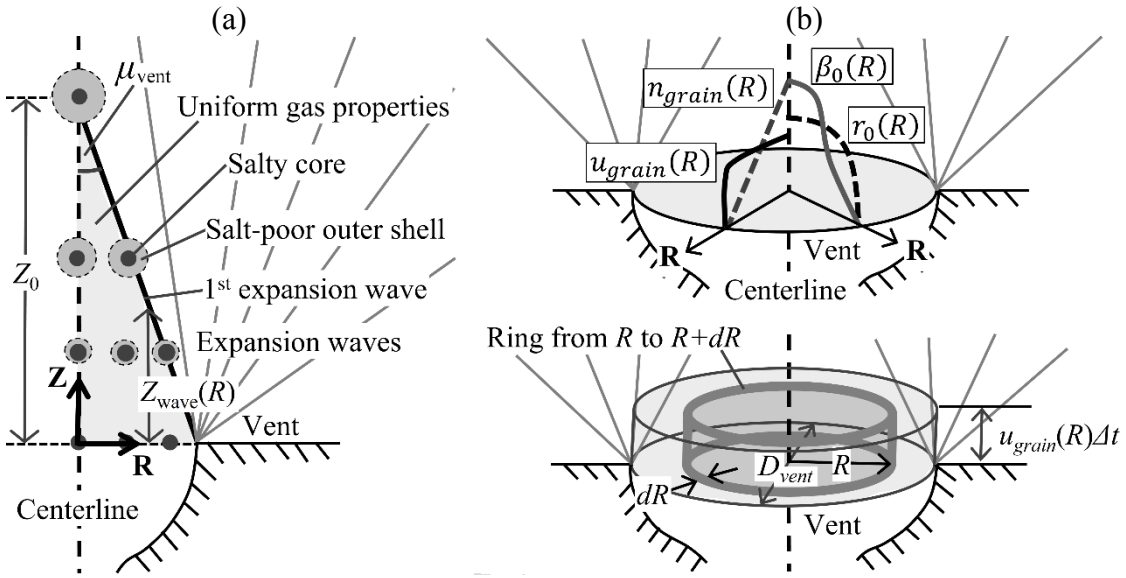

Figure H.1. (a) Grain growth due to condensation occurring above the vent. (b) Grain properties at the vent as a function of distance from the centerline, R, (top) and a ring from R to R+dR at the vent (bottom).

Next, we determine the number of grains emerging from the vent, which serve as the condensation cores. The number of grains emerging from a ring from R to $R+dR$, as shown in Figure H.1b, over an interval Δt, is given by:

$$dN_{R+dR} = n_{grain}(R)u_{grain}(R)\Delta t 2\pi R dR \tag{H.6}$$

The total number of grains emerging from the entire vent over an interval Δt is obtained by integrating Equation (H.6) from $R = 0$ to $R = D_{vent}/2$:

$$N_{total} = \int_0^{\frac{D_{vent}}{2}} n_{grain}(R)\, u_{grain}(R)\Delta t 2\pi R dR \tag{H.7}$$

To obtain the fraction of grains emerging from the ring from R to $R+dR$ over the total number of grains emerging from the entire vent over an interval Δt, we divide Equation (H.6) by Equation (H.7) to obtain:

$$f_R dR = \frac{dN_{R+dR}}{N_{total}} = \frac{n_{grain}(R) u_{grain}(R) R dR}{\int_0^{\frac{D_{vent}}{2}} n_{grain}(R)\, u_{grain}(R) R dR} \tag{H.8}$$

Now that we have the fraction of grains emerging from a ring from R to $R+dR$ and Δr^*_{grain} as a function of R, we can determine the fraction of grains emerging from the vent with normalized radius increment in the range Δr^*_{grain} to $\Delta r^*_{grain} + d(\Delta r^*_{grain})$ by solving for R and dR in terms of Δr^*_{grain} and $d(\Delta r^*_{grain})$ using Equation (H.5) and then substituting them into Equation (H.8). Doing so and simplifying, we obtain:

$$f_R dR = -\frac{n_{grain}(\Delta r^*_{grain}) u_{grain}(\Delta r^*_{grain}) \left(1 - \frac{\Delta r^*_{grain}}{h}\right) d(\Delta r^*_{grain})}{\int_0^h n_{grain}(\Delta r^*_{grain})\, u_{grain}(\Delta r^*_{grain}) \left(1 - \frac{\Delta r^*_{grain}}{h}\right) d(\Delta r^*_{grain})} \tag{H.9}$$

Due to the inverse nature of the relationship between Δr^*_{grain} and R, we take the negative of Equation (H.9) to be the fraction of grains emerging from the vent with normalized radius increment in the range Δr^*_{grain} to $\Delta r^*_{grain} + d(\Delta r^*_{grain})$ so that 1 is obtained instead of −1 when we integrate over Δr^*_{grain} from 0 to h:

$$f_{\Delta r^*_{grain}} d(\Delta r^*_{grain}) = -f_R dR$$

$$f_{\Delta r^*_{grain}} d(\Delta r^*_{grain}) = \frac{n_{grain}(\Delta r^*_{grain}) u_{grain}(\Delta r^*_{grain}) \left(1 - \frac{\Delta r^*_{grain}}{h}\right) d(\Delta r^*_{grain})}{\int_0^h n_{grain}(\Delta r^*_{grain})\, u_{grain}(\Delta r^*_{grain}) \left(1 - \frac{\Delta r^*_{grain}}{h}\right) d(\Delta r^*_{grain})} \tag{H.10}$$

Equation (H.10) is the distribution of normalized radius increments, Δr^*_{grain}, of the grains emerging from the vent due to condensation. The distribution of Δr_{grain} is obtained by replacing Δr^*_{grain} with $\Delta r_{grain}/D_{vent}$ and $d(\Delta r^*_{grain})$ with $d(\Delta r_{grain})/D_{vent}$ in Equation (H.10):

$$f_{\Delta r_{grain}} d(\Delta r_{grain}) = \frac{n_{grain}(\Delta r_{grain}) u_{grain}(\Delta r_{grain}) \left(1 - \frac{\Delta r_{grain}}{hD_{vent}}\right) d(\Delta r_{grain})}{\int_0^{hD_{vent}} n_{grain}(\Delta r_{grain})\, u_{grain}(\Delta r_{grain}) \left(1 - \frac{\Delta r_{grain}}{hD_{vent}}\right) d(\Delta r_{grain})} \tag{H.11}$$

Therefore, the distribution of Δr_{grain} depends on the vent size.

Next, we determine the distribution of final grain radii, r_f, after condensation has ceased. The final grain radius is given by: $r_f = r_0(R) + \Delta r_{grain}(R) = r_0(R) + \Delta r^*_{grain}(R) D_{vent} = \phi_{r_f}(R)$. Assuming that $\phi_{r_f}(R)$ is monotonic in R between 0 and $D_{vent}/2$ and invertible, we solve for R and dR in terms of r_f and dr_f:

$$R = \phi_{r_f}^{-1}(r_f) \qquad \text{(H.12)} \qquad dR = dr_f \Big/ \left(\frac{d\phi_{r_f}}{dR}\right) = \left(\frac{d\phi_{r_f}}{dR}\right)^{-1} dr_f \qquad \text{(H.13)}$$

where $\phi_{r_f}^{-1}$ represents the inverse of ϕ_{r_f}. To obtain the distribution of r_f, we substitute Equations (H.12) and (H.13) into Equation (H.8):

$$f_{r_f} dr_f = \frac{n_{grain}(r_f) u_{grain}(r_f) \phi_{r_f}^{-1}(r_f) \left(\frac{d\phi_{r_f}}{dR}\right)^{-1} dr_f}{\int_{r_{f,min}}^{r_{f,max}} n_{grain}(r_f) u_{grain}(r_f) \phi_{r_f}^{-1}(r_f) \left(\frac{d\phi_{r_f}}{dR}\right)^{-1} dr_f} \qquad \text{(H.14)}$$

Note that the sign of Equation (H.14) may have to be switched, as we did to obtain Equation (H.10), so that 1 is obtained instead of −1 when the distribution is integrated over all r_f.

Finally, we derive the distribution of final grain salt mass fractions, β_f, after condensation has ceased. The initial grain salt mass fraction, β_0, and mass, m_0, are given by:

$$\beta_0 = \frac{m_{salt}}{m_0} \qquad \text{(H.15)} \qquad m_0 = \frac{4}{3}\pi r_0^3 \rho_{ice} \qquad \text{(H.16)}$$

where m_{salt} is the mass of salt in the grain, which does not change upon emerging from the vent since the vapor is salt-poor, and ρ_{ice} is the density of ice (~920 kg/m^3). Equation (H.16) is reasonable because we assume that $\beta_0 << 1$, thus m_{salt} is negligible and the grain is mostly made of ice. Due to condensation, each grain accumulates an extra mass, Δm, given by:

$$\Delta m = \frac{4}{3}\pi\left(r_f^3 - r_0^3\right)\rho_{ice} = \frac{4}{3}\pi\left[\left(r_0 + \Delta r_{grain}\right)^3 - r_0^3\right]\rho_{ice}$$

$$\Delta m = \frac{4}{3}\pi\left(\Delta r_{grain}^3 + 3r_0^2\Delta r_{grain} + 3r_0\Delta r_{grain}^2\right)\rho_{ice} \tag{H.17}$$

The final grain salt mass fraction, β_f, is given by:

$$\beta_f = \frac{m_{salt}}{m_0 + \Delta m} = \frac{1}{\frac{1}{\beta_0} + \frac{\Delta m}{m_{salt}}} \tag{H.18}$$

Substituting Equations (H.15), (H.16) and (H.17) into Equation (H.18) and simplifying, we obtain:

$$\beta_f = \frac{\beta_0}{1 + \left(\frac{\Delta r_{grain}}{r_0}\right)^3 + 3\left(\frac{\Delta r_{grain}}{r_0}\right)^2 + 3\left(\frac{\Delta r_{grain}}{r_0}\right)} = \phi_{\beta_f}(R) \tag{H.19}$$

Therefore, β_f is only a function of R for a given Ma_{vent} and D_{vent}. Assuming that $\phi_{\beta_f}(R)$ is monotonic in R between 0 and $D_{vent}/2$ and invertible, we solve for R and dR in terms of β_f and $d\beta_f$:

$$R = \phi_{\beta_f}^{-1}(\beta_f) \tag{H.20}$$

$$dR = d\beta_f \Big/ \left(\frac{d\phi_{\beta_f}}{dR}\right) = \left(\frac{d\phi_{\beta_f}}{dR}\right)^{-1} d\beta_f \tag{H.21}$$

where $\phi_{\beta_f}^{-1}$ represents the inverse of ϕ_{β_f}. To obtain the distribution of β_f, we substitute Equations (H.20) and (H.21) into Equation (H.8):

$$f_{\beta_f} d\beta_f = \frac{n_{grain}(\beta_f) u_{grain}(\beta_f) \phi_{\beta_f}^{-1}(\beta_f) \left(\frac{d\phi_{\beta_f}}{dR}\right)^{-1} d\beta_f}{\int_{\beta_{f,min}}^{\beta_{f,max}} n_{grain}(\beta_f) u_{grain}(\beta_f) \phi_{\beta_f}^{-1}(\beta_f) \left(\frac{d\phi_{\beta_f}}{dR}\right)^{-1} d\beta_f} \tag{H.22}$$

Note that the sign of Equation (H.22) may have to be switched, as we did to obtain Equation (H.10), so that 1 is obtained instead of −1 when the distribution is integrated over all β_f.

It is worth noting the dependencies of the different distribution functions. From Equation (H.10), the distribution of normalized radius increments, $\Delta r_{grain}^* = \Delta r_{grain}/D_{vent}$, depends only on Ma_{vent}. From Equation (H.11), the distribution of radius

increments, Δr_{grain}, depends on Ma_{vent} and D_{vent}. The effect of vent size can be easily seen from examining Δr_{grain} along the centerline: $h(Ma_{vent})D_{vent}$. For a given Ma_{vent}, a larger vent results in a larger centerline Δr_{grain} due to the longer distance over which condensation would occur. From Equation (H.14), the distribution of final grain radii, r_f, depends on not only Ma_{vent} and D_{vent} but also r_0. From Equation (H.22), the distribution of final grain salt mass fractions, β_f, depends on Ma_{vent}, D_{vent}, r_0 and β_0.

H.2. CASE STUDY: UNIFORM GRAIN PROPERTIES AT VENT

Let us consider a simple case where the grain properties, r_0, β_0, n_{grain} and u_{grain}, are uniform across the vent and determine the distributions of Δr^*_{grain}, Δr_{grain}, r_f and β_f after condensation has ceased. From Equations (H.10), (H.11) and (H.14), we obtain:

$$f_{\Delta r^*_{grain}} d\left(\Delta r^*_{grain}\right) = \frac{2}{h}\left(1 - \frac{\Delta r^*_{grain}}{h}\right) d\left(\Delta r^*_{grain}\right) \tag{H.23}$$

$$f_{\Delta r_{grain}} d\left(\Delta r_{grain}\right) = \frac{2}{hD_{vent}}\left(1 - \frac{\Delta r_{grain}}{hD_{vent}}\right) d\left(\Delta r_{grain}\right) \tag{H.24}$$

$$f_{r_f} dr_f = \frac{2}{hD_{vent}}\left(1 - \frac{r_f - r_0}{hD_{vent}}\right) dr_f \tag{H.25}$$

To obtain f_{β_f}, we need to first find $\phi_{\beta_f}(R)$ by solving for Δr_{grain} using Equation (H.5) and substituting it into Equation (H.19) for a given Ma_{vent} and D_{vent}. Then, we have to determine its inverse, which is difficult to do analytically given the cubic nature of Equation (H.19). Therefore, we determine its inverse by directly plotting it, as shown in Figure H.2a for D_{vent} = 4 m, r_0 = 0.5 μm and β_0 = 0.02 for Ma_{vent} = 3 and 5. As shown in Figure H.2a, $\phi_{\beta_f}(R)$ is monotonic in R and is invertible (a one-to-one correspondence exists between β_f and R). While these results have been obtained for $\phi_{\beta_f}(R)$ for the specific set of parameter values given above, they hold for all sets of values.

We can now compute f_{β_f} numerically. To do so, we first select several values of R between 0 and $D_{vent}/2$ and calculate β_f and f_R for each value. We obtain β_f from Figure H.2a and f_R from Equation (H.8). Due to the one-to-one correspondence between β_f and R, we can directly set f_{β_f} to be equal to f_R for each corresponding pair of R and β_f. Once this is done for all R, we obtain the distribution for β_f. Finally, we normalize this distribution so that we obtain 1 when we integrate it over all β_f.

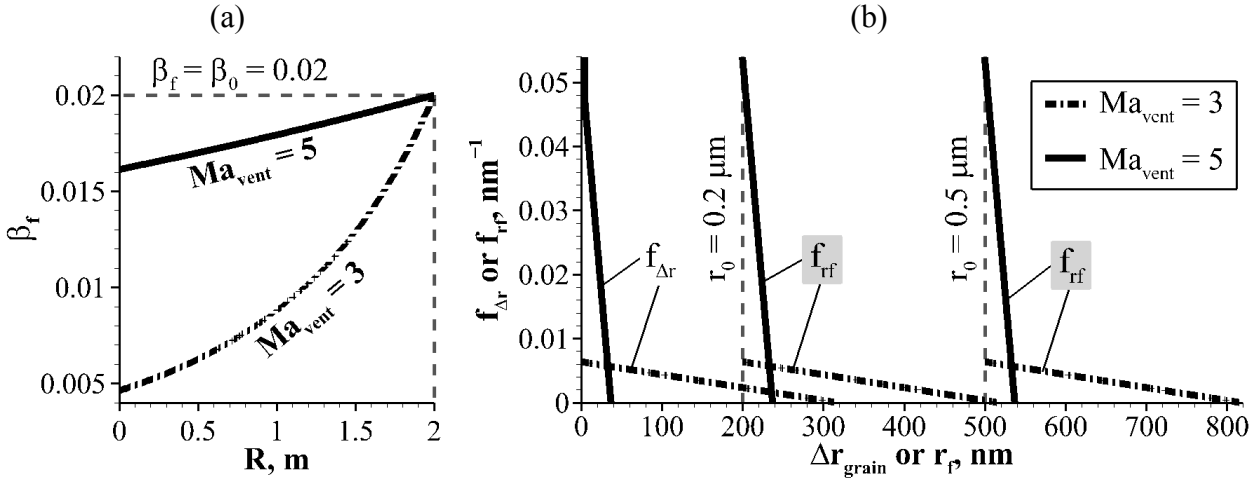

Figure H.2. (a) Final grain salt mass fraction, β_f, as a function of distance from the centerline, R, (i.e. $\beta_f = \phi_{\beta_f}(R)$) for D_{vent} = 4 m, r_0 = 0.5 μm and β_0 = 0.02 for Ma_{vent} = 3 and 5. (b) Distribution of grain radius increments, $f_{\Delta r}$, for D_{vent} = 4 m for Ma_{vent} = 3 and 5, and distribution of final radii, f_{r_f}, for the same D_{vent} and Ma_{vent} for initial grain radii, r_0 = 0.2 μm and 0.5 μm. The areas under the distributions have been normalized to 1.

As shown in Figure H.2a, $\beta_f = \beta_0 = 0.02$ at the edges of the vent ($R = D_{vent}/2 = 2$ m) as there is no condensation growth there (see Equation (H.5)). At the center of the vent (R = 0) where the growth is maximum, β_f reaches a minimum. Figure H.2a also shows how β_f varies with Ma_{vent}. For the same D_{vent}, r_0, and β_0, β_f is lower for Ma_{vent} = 3 compared to Ma_{vent} = 5 because of the greater condensation growth that occurs with Ma_{vent} = 3 (see

Figure 4.6b), thus more greatly diluting the grain salt content. We have not shown how β_f would vary with D_{vent}, r_0 or β_0, but we expect the following: a larger D_{vent} has the same effect as a lower Ma_{vent} (larger decrease in β_f) while a larger r_0 or β_0 has the same effect as a higher Ma_{vent} (smaller decrease in β_f).

Figure H.2b shows the distribution of Δr_{grain} for the grains emerging from a vent with D_{vent} = 4 m for Ma_{vent} = 3 and 5. As shown Figure H.1b, the number of grains emerging from each ring from R to $R+dR$ at the vent is proportional to R. Consequently, more grains emerge from closer to the edges of the vent (larger R) than from near the center (smaller R). Since the smallest growth occurs near the edges of the vent and the largest growth near the center, a large number of grains experience only minimal growth. This agrees with inverse trend exhibited by the distributions of Δr_{grain} in Figure H.2b.

Moreover, the distribution of Δr_{grain} for Ma_{vent} = 3 extends over a greater range of Δr_{grain} than that for Ma_{vent} = 5 because of the larger condensation growth that occurs with Ma_{vent} = 3. We have not shown how this distribution would vary with D_{vent}. A larger D_{vent} would also result in larger condensation growth, thus we expect a larger D_{vent} to have the same effect as a lower Ma_{vent}. Figure H.2b also shows the distributions of r_f for D_{vent} = 4 m for Ma_{vent} = 3 and 5 for r_0 = 0.2 μm and 0.5 μm. The distribution of r_f is simply the distribution of Δr_{grain} shifted by r_0. This is because Δr_{grain} is not a function of r_0.

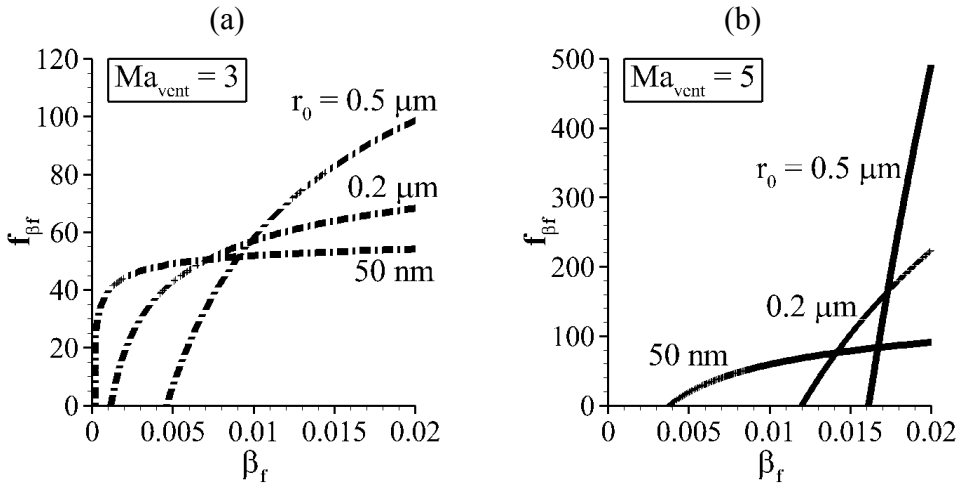

Figure H.3. Distributions of final grain salt mass fractions, f_{β_f}, for D_{vent} = 4 m and β_0 = 0.02 for initial grain radii, r_0 = 50 nm, 0.2 μm and 0.5 μm, for: (a) Ma_{vent} = 3 and (b) Ma_{vent} = 5. The areas under the distributions have been normalized to 1.

Figure H.3 shows the distributions of β_f for D_{vent} = 4 m and β_0 = 0.02 for Ma_{vent} = 3 and 5 for r_0 = 50 nm, 0.2 μm and 0.5 μm. The ring from R to $R+dR$ (see Figure H.1b) from which the most grains emerge is at the edges of the vent ($R = D_{vent}/2$ = 2 m) where there is no condensation growth and the grain salinity remains unchanged, thus the distribution of β_f is maximum at $\beta_f = \beta_0$ = 0.02. On the contrary, no grains emerge from the center of the vent (R = 0) where condensation growth is maximum and the grain salinity is most diluted, thus the distribution of β_f is zero where β_f reaches a minimum.

As r_0 increases, the distribution of β_f approaches a delta function at $\beta_f = \beta_0$ for a given Ma_{vent}, D_{vent} and β_0, i.e. nearly all the grains have $\beta_f \approx \beta_0$. This is because Δr_{grain} decreases relative to r_0 as r_0 increases for a given Ma_{vent} and D_{vent}. As a result, the grain salinity is hardly affected by condensation when r_0 is sufficiently large for a given Ma_{vent} and D_{vent}. This also occurs when going to a higher Ma_{vent}, which can be seen by comparing

Figures H.3a and H.3b, as a higher Ma_{vent} also results in a smaller Δr_{grain} relative to r_0 for a given D_{vent} and r_0.

We have only examined how the distribution of β_f varies with Ma_{vent} and r_0. A larger D_{vent} leads to larger condensation growth, thus we expect a larger D_{vent} to have the same effect on the distribution of β_f as a smaller r_0 or lower Ma_{vent}. On the other hand, a higher β_0 is expected to have the same effect on the distribution of β_f as a larger r_0 or higher Ma_{vent}. It is interesting to note that when r_0 is sufficiently small for a given Ma_{vent}, D_{vent} and β_0, the distribution of β_f approaches a horizontal line. This is more evident in Figure H.3a for $Ma_{vent} = 3$. This means that there are equal amounts of grains at each salt mass fraction after condensation has ceased.

Appendix I.

Analysis using 98 Jets

The plume model considered in this work only includes the eight jets identified by Spitale and Porco (2007). Recently, more than 98 jets have been identified (Porco *et al.*, 2014). Figure 2.5c shows 98 of the more clearly identified jets and it can be easily seen that most of the jets are located near or along the Tiger Stripes and are not quite oriented in the local surface normal direction. Their source locations and jet orientations are listed in Table 2 in Porco *et al.* (2014). Here, we report the results from a preliminary analysis of the plume model consisting of these 98 jets.

Figures I.1a–b show 2D contour plots colored by the fraction of the total H_2O density distribution, n_{plume}, made up by each jet along the E7 trajectory for the Mach-3 and Mach-5 vent conditions (see Table 3.1) from the analytical subsurface model. The E7 trajectory has been chosen because its INMS data provide the best constraint for the plume among the data sets considered. To generate the 2D plots, all 98 jets have been set to equal strengths, s_{Jet} = 1 kg/s, and the resulting 3D density fields from each jet are sampled to obtain the individual jet density distributions, n_{Jet}, along the E7 trajectory. As shown in Figures I.1a–b, most of the 98 jets appear to contribute about equally and there are no dominant jets within the range of the E7 INMS data considered for both vent conditions. With only 44 data points within that range, finding the *individual* jet strengths by fitting to the E7 INMS data such that χ^2 is minimized (see Section 7.1) is thus an under-constrained problem (i.e. there are more free parameters than constraining equations).

As a result, we may not be able to uniquely determine the individual jet strengths by fitting to the E7 INMS data. However, we have not considered the E3 and E5 INMS data. It is possible that the E3 and E5 trajectories took Cassini through the plume such that

only a subset of the 98 jets are intersected or have dominant contributions, thus their individual strengths can be constrained by fitting to these data sets. New INMS data sets from the E14, E17 and E18 trajectories may also be included in this analysis.

In future work, similar 2D contour plots may be generated for each trajectory to determine which jets are dominant along that particular trajectory. Then, if the number of dominant jets is less than or equal to the number of data points, their individual strengths may be constrained by fitting to the INMS data along that particular trajectory. Since the set of dominant jets will most likely vary between trajectories, the strengths of different groups of jets may be determined in this way. However, the strengths of the different groups of jets determined using the different data sets collected at different times may represent the state of the plume at different times as the plume appears to vary with time.

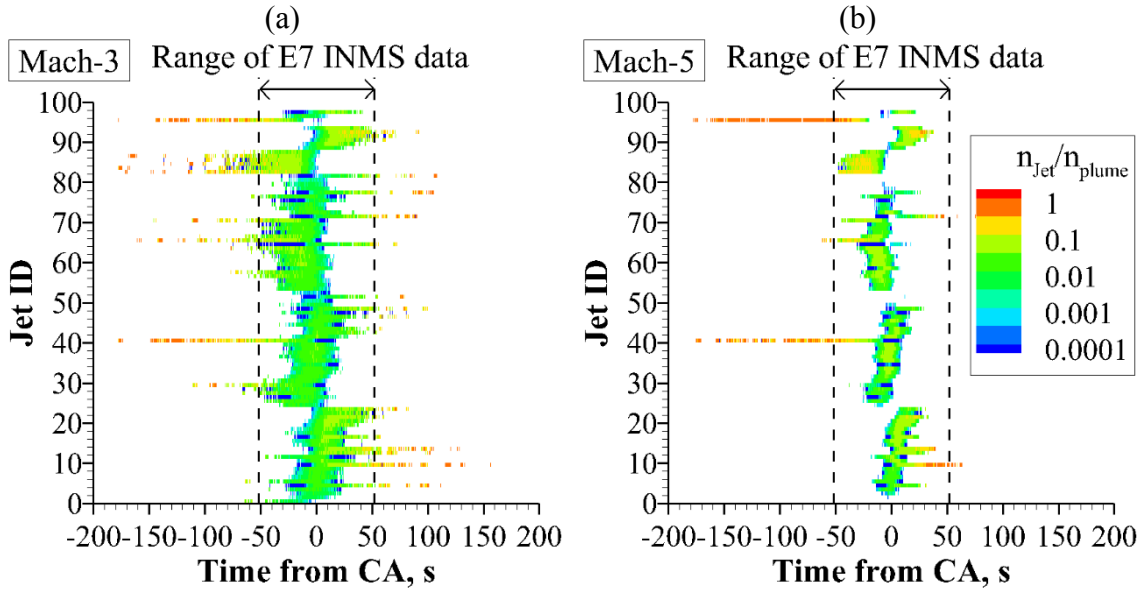

Figure I.1. 2D contour plots colored by the fraction of the total H_2O density distribution, n_{plume}, made up by each of the 98 jets given in Table 2 of Porco *et al.* (2014) along the E7 trajectory for: (a) Mach-3 and (b) Mach-5 vent conditions. On the x-axis is the time from closest approach (CA).

References

Abramov, O., Spencer, J.R., 2009. Endogenic heat from Enceladus' south polar fractures: New observations, and models of conductive surface heating. *Icarus* **199**, 189–196.

Anderson, J.D., 2003. Modern Compressible Flow with Historical Perspective. New York: McGraw-Hill.

Anilkumar, A.V., 1989. Experimental studies of high-speed dense dusty gases. PhD Dissertation, California Institute of Technology. 135 pp.

Baum, W.A., Kreidl, T., Westphal, J.A., Danielson, G.E., Seidelmann, P.K., Pascu, D., Currie, D.G., 1981. Saturn's E ring: I. CCD observations of March 1980. *Icarus* **47**, 84–96.

Bird, G.A., 1994. Molecular Gas Dynamics and the Direct Simulation of Gas Flows. New York: Oxford University Press.

Borner, A., Li, Z., Levin, D.A., 2013. Development of a molecular-dynamics-based cluster-heat-capacity model for study of homogeneous condensation in supersonic water-vapor expansions. *J. Chem. Phys.* **138**, 064302.

Bouquet, A., Mousis, O., Waite, J.H., Picaud, S., 2015. Possible evidence for a methane source in Enceladus' ocean. *Geophys. Res. Lett.* **42**, 1334–1339.

Brilliantov, N.V., Schmidt, J., Spahn, F., 2008. Geysers of Enceladus: Quantitative analysis of qualitative models. *Planet. Space Sci.* **56**, 1596–1606.

Brown, R.H., Clark, R.N., Buratti, B.J., Cruikshank, D.P., Barnes, J.W., Mastrapa, R.M.E., Bauer, J., Newman, S., Momary, T., Baines, K.H., Belluci, G., Capaccioni, F., Cerroni, P., Combes, M., Coradini, A., Drossart, P., Formisano, V., Jaumann, R., Langevin, Y., Matson, D.L., McCord, T.B., Nelson, R.M., Nicholson, P.D., Sicardy, B., Sotin, C., 2006. Composition and physical properties of Enceladus' surface. *Science* **311**, 1425–1428.

Burger, M.H., Sittler, E.C., Johnson, R.E., Smith, H.T., Tucker, O.J., Shematovich, V.I., 2007. Understanding the escape of water from Enceladus. *J. Geophys. Res*. **112**, A06219.

Burt, J.M., Boyd, I.D., 2004. Development of a two-way coupled model for two phase rarefied flows. 42nd AIAA Aerospace Sciences Meeting, Reno, NV. Jan. 5–8. AIAA 2004-1351.

Burt, J.M., Boyd, I.D., 2007. High-Altitude Plume Simulations for a Solid Propellant Rocket. *AIAA J.* **45**, 2872–2884.

Cassidy, T.A., Johnson, R.E., 2010. Collisional spreading of Enceladus' neutral cloud. *Icarus* **209**, 696–703.

Charvat, A., Abel, B., 2007. How to make big molecules fly out of liquid water: Applications, features and physics of laser assisted liquid phase dispersion mass spectrometry. *Phys. Chem. Chem. Phys.* **9**, 3335–3360.

Collins, G.C., Goodman, J.C., 2007. Enceladus' south polar sea. *Icarus* **189**, 72–82.

Crawford, G.D., Stevenson, D.J., 1988. Gas-driven water volcanism and the resurfacing of Europa. *Icarus* **73**, 66–79.

Crovisier, J., 1984. The water molecule in comets: fluorescence mechanisms and thermodynamics of the inner coma. *Astron. Astrophys.* **130**, 361–372.

Crowe, C.T., Schwarzkopf, J.D., Sommerfeld, M., Tsuji, Y., 2012. Multiphase flows with droplets and particles. Florida: CRC Press.

Degruyter, W., Manga, M., 2011. Cryoclastic origin of particles on the surface of Enceladus. *Geophys. Res. Lett.* **38**, L16201.

Dong, Y., Hill, T.W., 2014. Magnetospheric consequences of charged ice grains from th Enceladus plume. 47th AGU Annual Fall Meeting, San Francisco, CA. Dec. 15–19. SM51F-4314.

Dong, Y., Hill, T.W., Teolis, B.D., Magee, B.A., Waite, J.H., 2011. The water vapor plumes of Enceladus. *J. Geophys. Res*. **116**, A10204.

Dougherty, M.K., Khurana, K.K., Neubauer, F.M., Russell, C.T., Saur, J., Leisner, J.S., Burton, M.E., 2006. Identification of a dynamic atmosphere at Enceladus with the Cassini magnetometer. *Science* **311**, 1406–1409.

Esposito, L.W., Colwell, J.E., Larsen, K., McClintock, W.E., Stewart, A.I.F., Hallett, J.T., Shemansky, D.E., Ajello, J.M., Hansen, C.J., Hendrix, A.R., West, R.A., Keller, H.U., Korth, A., Pryor, W.R., Reulke, R., Yung, Y.L., 2005. Ultraviolet imaging spectroscopy shows an active Saturnian system. *Science* **307**, 1251–1255.

Fukusako, S., 1990. Thermophysical Properties of Ice, Snow, and Sea Ice. *Int. J. Thermophys.* **11**, 353–372.

Gallis, M.A., Torczynski, J.R., Rader, D.J., 2001. An approach for simulating the transport of spherical particles in a rarefied gas flow via the direct simulation Monte Carlo method. *Phys. Fluids* **13**, 3482–3492.

Glein, C.R., Shock, E.L., 2010. Sodium chloride as a geophysical probe of a subsurface ocean on Enceladus. *Geophys. Res. Lett.* **37**, L09204.

Goguen, J.D., Buratti, B.J., Brown, R.H., Clark, R.N., Nicholson, P.D., Hedman, M.M., Howell, R.R., Sotin, C., Cruikshank, D.P., Baines, K.H., Lawrence, K.J., Spencer, J.R., Blackburn, D.G., 2013. The temperature and width of an active fissure on Enceladus measured with Cassini VIMS during the 14 April 2012 South Pole flyover. *Icarus* **226**, 1128–1137.

Hansen, C.J., Esposito, L., Stewart, A.I.F., Colwell, J., Hendrix, A., Pryor, W., Shemansky, D., West, R., 2006. Enceladus' water vapor plume. *Science* **311**, 1422–1425.

Hansen, C.J., Esposito, L.W., Stewart, A.I.F., Meinke, B., Wallis, B., Colwell, J.E., Hendrix, A.R., Larsen, K., Pryor, W., Tian, F., 2008. Water vapour jets inside the plume of gas leaving Enceladus. *Nature* **456**, 477–479.

Hansen, C.J., Shemansky, D.E., Esposito, L.W., Stewart, A.I.F., Lewis, B.R., Colwell, J.E., Hendrix, A.R., West, R.A., Waite, J.H., Teolis, B., Magee, B.A., 2011. The composition and structure of the Enceladus plume. *Geophys. Res. Lett.* **38**, L11202.

Hedman, M.M., Burns, J.A., Hamilton, D.P., Showalter, M.R., 2012. The three-dimensional structure of Saturn's E ring. *Icarus* **217**, 322–338.

Hedman, M.M., Gosmeyer, C.M., Nicholson, P.D., Sotin, C., Brown, R.H., Clark, R.N., Baines, K.H., Buratti, B.J., Showalter, M.R., 2013. An observed correlation between plume activity and tidal stresses on Enceladus. *Nature* **500**, 182–184.

Hedman, M.M., Nicholson, P.D., Showalter, M.R., Brown, R.H., Buratti, B.J., Clark, R.N., 2009. Spectral observations of the Enceladus plume with Cassini-VIMS. *Astrohys. J.* **694**, 1749–1762.

Hillier, J.K., Green, S.F., McBride, N., Schwanethal, J.P., Postberg, F., Srama, R., Kempf, S., Moragas-Klostermeyer, G., McDonnell, J.A.M., Grun, E., 2007. The composition of Saturn's E ring. *Mon. Not. R. Astron. Soc.* **377**, 1588–1596.

Hobbs, P.V., 1974. Ice Physics. New York: Oxford University Press.

Horanyi, M., 1996. Charging Dust Dynamics in the Solar System. *Annu. Rev. Astron. Astrophys.* **34**, 383–418.

Horanyi, M., Burns, J.A., Hamilton, D.P., 1992. The dynamics of Saturn's E ring particles. *Icarus* **97**, 248–259.

Howett, C.J.A., Spencer, J.R., Pearl, J., Segura, M., 2011. High heat flow from Enceladus' south polar region measured using 10–600 cm^{-1} Cassini/CIRS data. *J. Geophys. Res*. **116**, E03003.

Hsu, H.-W., Postberg, F., Sekine, Y., Shibuya, T., Kempf, S., Horanyi, M., Juhasz, A., Altobelli, N., Suzuki, K., Masaki, Y., Kuwatani, T., Tachibana, S., Sirono, S., Moragas-Klostermeyer, G., Srama, R., 2015. Ongoing hydrothermal activities within Enceladus. *Nature* **519**, 207–210.

Hurford, T.A., Bills, B.G., Helfenstein, P., Greenberg, R., Hoppa, G.V., Hamilton, D.P., 2009. Geological implications of a physical libration on Enceladus. *Icarus* **203**, 541–552.

Hurford, T.A., Helfenstein, P., Hoppa, G.V., Greenberg, R., Bills, B.G., 2007. Eruptions arising from tidally controlled periodic openings of rifts on Enceladus. *Nature* **447**, 292–294.

Iess, L., Stevenson, D.J., Parisi, M., Hemingway, D., Jacobson, R.A., Lunine, J.I., Nimmo, F., Armstrong, J.W., Asmar, S.W., Ducci, M., Tortora, P., 2014. The gravity field and interior structure of Enceladus. *Science* **344**, 78–80.

Ingersoll, A.P., Ewald, S.P., 2011. Total particulate mass in Enceladus plumes and mass of Saturn's E ring inferred from Cassini ISS images. *Icarus* **216**, 492–506.

Ingersoll, A.P., Pankine, A.A., 2010. Subsurface heat transfer on Enceladus: Conditions under which melting occurs. *Icarus* **206**, 594–607.

Jaumann, R., Stephan, K., Hansen, G.B., Clark, R.N., Buratti, B.J., Brown, R.H., Baines, K.H., Newman, S.F., Bellucci, G., Filacchione, G., Coradini, A., Cruikshank, D.P., Griffith, C.A., Hibbitts, C.A., McCord, T.B., Nelson, R.M., Nicholson, P.D., Sotin, C., Wagner, R., 2008. Distribution of icy particles across Enceladus' surface as derived from Cassini-VIMS measurements. *Icarus* **193**, 407–419.

Johnson, R.E., 1990. Energetic charged-particle interactions with atmospheres and surfaces. New York: Springer-Verlag.

Johnson, R.E., Pospieszalska, M.K., Sittler Jr., E.C., Cheng, A.F., Lanzerotti, L.J., Sieveka, E.M., 1989. The neutral cloud and heavy ion inner torus at Saturn. *Icarus* **77**, 311–329.

Johnson, R.E., Smith, H.T., Tucker, O.J., Liu, M., Burger, M.H., Sittler, E.C., Tokar, R.L., 2006. The Enceladus and OH tori at Saturn. *Astrohys. J.* **644**, L137–L139.

Jones, G.H., Arridge, C.S., Coates, A.J., Lewis, G.R., Kanani, S., Wellbrock, A., Young, D.T., Crary, F.J., Tokar, R.L., Wilson, R.J., Hill, T.W., Johnson, R.E., Mitchell, D.G., Schmidt, J., Kempf, S., Beckmann, U., Russell, C.T., Jia, Y.D., Dougherty, M.K., Waite Jr., J.H., Magee, B.A., 2009. Fine jet structure of electrically charged grains in Enceladus' plume. *Geophys. Res. Lett.* **36**, L16204.

Jones, G.H., Roussos, E., Krupp, N., Paranicas, C., Woch, J., Lagg, A., Mitchell, D.G., Krimigis, S.M., Dougherty, M.K., 2006. Enceladus' varying imprint on the magnetosphere of Saturn. *Science* **311**, 1412–1415.

Juhasz, A., Horanyi, M., 2002. Saturn's E-ring: A dynamical approach. J. Geophys. Res. 107 (A6), 1066.

Juhasz, A., Horanyi, M., Morfill, G.E., 2007. Signatures of Enceladus in Saturn's E ring. *Geophys. Res. Lett.* **34**, L09104.

Jurac, S., McGrath, M.A., Johnson, R.E., Richardson, J.D., Vasyliunas, V.M., Eviatar, A., 2002. Saturn: Search for a missing water source. *Geophys. Res. Lett.* **29**, 2172.

Jurac, S., Richardson, J.D., 2005. A self-consistent model of plasma and neutrals at Saturn: Neutral cloud morphology. *J. Geophys. Res*. **110**, A09220.

Kempf, S., Beckmann, U., Moragas-Klostermeyer, G., Postberg, F., Srama, R., Economou, T., Schmidt, J., Spahn, F., Grun, E., 2008. The E ring in the vicinity of Enceladus I. Spatial distribution and properties of the ring particles. *Icarus* **193**, 420–437.

Kempf, S., Beckmann, U., Schmidt, J., 2010. How the Enceladus dust plume feeds Saturn's E ring. *Icarus* **206**, 446–457.

Kieffer, S.W., Lu, X., Bethke, C.M., Spencer, J.R., Marshak, S., Navrotsky, A., 2006. A Clathrate Reservoir Hypothesis for Enceladus' South Polar Plume. *Science* **314**, 1764–1766.

Kieffer, S.W., Lu, X., McFarquhar, G., Wohletz, K.H., 2009. A redetermination of the ice/vapor ratio of Enceladus' plumes: Implications for sublimation and the lack of a liquid water reservoir. *Icarus* **203**, 238–241.

Krivov, A.V., Sremcevic, M., Spahn, F., Dikarev, V.V., Kholshevnikov, K.V., 2003. Impact-generated dust clouds around planetary satellites: Spherically symmetric case. *Planet. Space Sci.* **51**, 251–269.

Kruger, H., Krivov, A.V., Hamilton, D.P., Grun, E., 1999. Detection of an impact-generated dust cloud around Ganymede. *Nature* **399**, 558–560.

Laufer, D., Pat-El, I., Bar-Nun, A., 2005. Experimental simulation of the formation of non-circular active depressions on Comet Wild-2 and of ice grain ejection from cometary surfaces. *Icarus* **178**, 248–252.

Lunine, J.I., Stevenson, D.J., 1985. Thermodynamics of clathrate hydrate at low and high pressures with application to the outer solar system. *Astrophys J Suppl S* **58**, 493–531.

Mack, C, 1967. Essentials of Statistics for Scientists and Technologists. New York: Plenum Press.

Matson, D.L., Castillo-Rogez, J.C., Davies, A.G., Johnson, T.V., 2012. Enceladus: A hypothesis for bringing both heat and chemicals to the surface. *Icarus* **221**, 53–62.

Matson, D.L., Castillo, J.C., Lunine, J., Johnson, T.V., 2007. Enceladus' plume: Compositional evidence for a hot interior. *Icarus* **187**, 569–573.

McDoniel, W.J., Goldstein, D.B., Varghese, P.L., Trafton, L.M., 2015. Three-dimensional simulation of gas and dust in Io's Pele plume. *Icarus*. Advance online publication. doi: 10.1016/j.icarus.2015.03.019.

McGrath, M.J., Siepmann, J.I, Kuo, I.W., Mundy, C.J., VandeVondele, J., Hutter, J., Mohamed, F., Krack, M., 2006. Simulating fluid-phase equilibria of water from first principles. *J. Phys. Chem. A* **110**, 640–646.

McKay, C.P., Porco, C.C., Atheide, T., Davis, W.L., Kral, T.A., 2008. The possible origin and persistence of life on Enceladus and detection of biomarkers in the plume. *Astrobiology* **8**, 909–919.

Meier, P., Kriegel, H., Motschmann, U., Schmidt, J., Spahn, F., Hill, T.W.. Dong, Y., Jones, G.H., 2014. A model of the spatial and size distribution of Enceladus' dust plume. *Planet. Space Sci*. **104**, 216–233.

Meyer, J., Wisdom, J., 2007. Tidal heating in Enceladus. *Icarus* **188**, 535–539.

Mitchell, C.J., Porco, C.C., Weiss, J.W., 2015. Tracking the geysers of Enceladus into Saturn's E ring. *Astron. J.* **149**:156, 16 pp.

Monnin, C., Chavagnac, V., Boulart, C., Ménez, B., Gérard, M., Gérard, E., Pisapia, C., Quéméneur, M., Erauso, G., Postec, A., Guentas-Dombrowski, L., Payri, C., Pelletier, B., 2014. Fluid chemistry of the low temperature hyperalkaline hydrothermal system of Prony Bay (New Caledonia). *Biogeosciences* **11**, 5687–5706.

Moore, C.H., 2011. Monte Carlo simulation of the Jovian plasma torus interaction with Io's atmosphere and the resultant aurora during eclipse. PhD Dissertation, The University of Texas at Austin. 274 pp.

Moore, C.H., Goldstein, D.B., Varghese, P.L., Trafton, L.M., Stewart, B., 2009. 1-D DSMC simulation of Io's atmospheric collapse and reformation during and after eclipse. *Icarus* **201**, 585–597.

Morris, A.B., 2012. Simulation of Rocket Plume Impingement and Dust Dispersal on the Lunar Surface. PhD Dissertation, The University of Texas at Austin. 236 pp.

Murphy, D.M., Koop, T., 2005. Review of the vapor pressures of ice and supercooled water for atmospheric applications. *Q. J. R. Meteorol. Soc.* **131**, 1539–1565.

Nanbu, K., 1986. Theoretical basis of the direct simulation Monte Carlo method. In: Rarefied Gas Dynamics: 15th International Symposium Proceedings 1, Teubner, Stuttgart, 369–383.

Nicholson, P.D., Showalter, M.R., Dones, L., French, R.G., Larson, S.M., Lissauer, J.J., McGhee, C.A., Seitzer, P., Siscardy, B., Danielson, G.E., 1996. Observations of Saturn's ring-plane crossings in August and November 1995. *Science* **272**, 509–515.

Nimmo, F., Gaidos, E., 2002. Thermal consequences of strike-slip motion on Europa. *J. Geophys. Res.* **107**, 5021.

Nimmo, F., Porco, C., Mitchell, C., 2014. Tidally modulated eruptions on Enceladus: Cassini ISS observations and models. *Astron. J.* **148**:46, 14 pp.

Nimmo, F., Spencer, J.R., Pappalardo, R.T., Mullen, M.E., 2007. Shear heating as the origin of the plumes and heat flux on Enceladus. *Nature* **447**, 289–291.

Pang, K.D., Voge, C.C., Rhoads, J.W., Ajello, J.M., 1984. The E ring of Saturn and satellite Enceladus. *J. Geophys. Res*. **89**, 9459–9470.

Parkinson, C.D., Liang, M., Yung, Y.L., Kirschivnk, J.L., 2008. Habitability of Enceladus: Planetary conditions for life. *Orig. Life Evol. Biosph.* **38**, 355–369.

Porco, C., DiNino, D., Nimmo, F., 2014. How the geysers, tidal stresses, and thermal emission across the south polar terrain of Enceladus are related. *Astron. J.* **148**:45, 24 pp.

Porco, C.C., Helfenstein, P., Thomas, P.C., Ingersoll, A.P., Wisdom, J., West, R., Neukum, G., Denk, T., Wagner, R., Roatsch, T., Kieffer, S., Turtle, E., McEwen, A., Johnson, T.V., Rathbun, J., Veverka, J., Wilson, D., Perry, J., Spitale, J., Brahic, A., Burns, J.A., DelGenio, A.D., Dones, L., Murray, C.D., Squyres, S., 2006. Cassini observes the active south pole of Enceladus. *Science* **311**, 1393–1401.

Postberg, F., Kempf, S., Hillier, J.K., Srama, R., Green, S.F., McBride, N., Grun, E., 2008. The E-ring in the vicinity of Enceladus: II. Probing the moon's interior—the composition of E-ring particles. *Icarus* **193**, 438–454.

Postberg, F., Kempf, S., Schmidt, J., Brilliantov, N., Beinsen, A., Abel, B., Buck, U., Srama, R., 2009. Sodium salts in E-ring ice grains from an ocean below the surface of Enceladus. *Nature* **459**, 1098–1101.

Postberg, F., Schmidt, J., Hillier, J., Kempf, S., Srama, R., 2011. A salt-water reservoir as the source of a compositionally stratified plume on Enceladus. *Nature* **474**, 620–622.

Prem, P., Artemieva, N.A., Goldstein, D.B., Varghese, P.L., Trafton, L.M., 2014. Transport of water in a transient impact-generated lunar atmosphere. *Icarus*. Advance online publication. doi:10.1016/j.icarus.2014.10.017.

Press, W.H., Teukolsky, S.A., Vetterling, W.T., Flannery, B.P., 1992. Numerical Recipes in C. New York: Cambridge University Press.

Prisbell, A., Marichalar, J., Lumpkin, F., LeBeau, G., 2011. Analysis of Plume Impingement Effects from Orion Crew Service Module Dual Reaction Control System Engine Firings. *AIP Conf. Proc.* **1333**, 595–600.

Prudencio, E., Cheung, S.H., 2012. Parallel adaptive multilevel sampling algorithms for the Bayesian Analysis of mathematical models. *Int. J. Uncertainty Quantification* **2**, 215–237.

Richardson, J.D., Eviatar, A., McGrath, M.A., Vasyliunas, V.M., 1998. OH in Saturn's magnetosphere: Observations and implications. *J. Geophys. Res*. **103**, 20245–20255.

Roberts, J.H., Nimmo, F., 2008. Near-surface heating on Enceladus and the south polar thermal anomaly. *Geophys. Res. Lett.* **35**, L09201.

Saur, J., Schilling, N., Neubauer, F.M., Strobel, D.F., Simon, S., Dougherty, M.K., Russell, C.T., Pappalardo, R.T., 2008. Evidence for temporal variability of Enceladus' gas jets: Modeling of Cassini observations. *Geophys. Res. Lett.* **35**, L20105.

Schmidt, J., Brilliantov, N., Spahn, F., Kempf, S., 2008. Slow dust in Enceladus' plume from condensation and wall collisions in tiger stripe fractures. *Nature* **451**, 685–688.

Schneider, N.M., Burger, M.H., Schaller, E.L., Brown, M.E., Johnson, R.E., Kargel, J.S., Dougherty, M.K., Achilleos, N.A., 2009. No sodium in the vapour plumes of Enceladus. *Nature* **459**, 1102–1104.

Shemansky, D.E., Matheson, P., Hall, D.T., Hu, H.-Y., Tripp, T.M., 1993. Detection of the hydroxyl radical in the Saturn magnetosphere. *Nature* **363**, 329–331.

Shkuratov, Y.G., Helfenstein, P., 2001. The opposition effect and the quasi-fractal structure of regolith: I. Theory. *Icarus* **152**, 96–116.

Showalter, M.R., Cuzzi, J.N., Larson, S.M., 1991. Structure and particle properties of Saturn's E Ring. *Icarus* **94**, 451–473.

Smith, H.T., Johnson, R.E., Perry, M.E., Mitchell, D.G., McNutt, R.L., Young, D.T., 2010. Enceladus plume variability and the neutral gas densities in Saturn's magnetosphere. *J. Geophys. Res.* **115**, A10252.

Smith, B.A., Soderblom, L., Beebe, R., Boyce, J., Briggs, G., Bunker, A., Collins, S.A., Hansen, C.J., Johnson, T.V., Mitchell, J.L., Terrile, R.J., Carr, M., Cook, A.F., Cuzzi, J., Pollack, J.B., Danielson, G.E., Ingersoll, A., Davies, M.E., Hunt, G.E., Masursky, H., Shoemaker, E., Morrison, D., Owen, T., Sagan, C., Veverka, J., Strom, R., Suomi, V.E., 1981. Encounter with Saturn: Voyager 1 imaging science results. *Science* **212**, 163–191.

Spahn, F., Albers, N., Horning, M., Kempf, S., Krivov, A.V., Makuch, M., Schmidt, J., Seiβ, M., Sremcevic, M., 2006a. E ring dust sources: Implications from Cassini's dust measurements. *Planet. Space Sci.* **54**, 1024–1032.

Spahn, F., Schmidt, J., Albers, N., Horning, M., Makuch, M., Seiβ, M., Kempf, S., Srama, R., Dikarev, V., Helfert, S., Moragas-Klostermeyer, G., Krivov, A.V., Sremcevic, M., Tuzzolino, A.J., Economou, T., Grun, E., 2006b. Cassini dust measurements at Enceladus and implications for the origin of the E ring. *Science* **311**, 1416–1418.

Spencer, J.R., Howett, C.J.A., Verbiscer, A., Hurford, T.A., Segura, M., Spencer, D.C., 2013. Enceladus heat flow from high spatial resolution thermal emission observations. Abstract. *European Planetary Science Congress*, 840, 1.

Spencer, J.R., Pearl, J.C., Segura, M., Flasar, F.M., Mamoutkine, A., Romani, P., Buratti, B.J., Hendrix, A.R., Spilker, L.J., Lopes, R.M.C., 2006. Cassini encounters Enceladus: Background and the discovery of a south polar hot spot. *Science* **311**, 1401–1405.

Spitale, J.N., Porco, C.C., 2007. Association of the jets of Enceladus with the warmest regions on its south-polar fractures. *Nature* **449**, 695–697.

Sremcevic, M., Krivov, A.V., Spahn, F., 2003. Impact-generated dust clouds around planetary satellites: Asymmetry effects. *Planet. Space Sci.* **51**, 455–471.

Stewart, B., 2010. Numerical simulations of the flow produced by a comet impact on the moon and its effects on ice deposition in cold traps. PhD Dissertation, The University of Texas at Austin. 357 pp.

Stewart, B.D., Pierazzo, E., Goldstein, D.B., Varghese, P.L., Trafton, L.M., 2011. Simulations of a comet impact on the Moon and associated ice deposition in polar cold traps. *Icarus* **215**, 1–16.

Strand, J.S., 2012. Statistical methods for the analysis of DSMC simulations of hypersonic shocks. PhD Dissertation, The University of Texas at Austin. 215 pp.

Tenishev, V., Combi, M.R., Teolis, B.D., Waite, J.H., 2010. An approach to numerical simulation of the gas distribution in the atmosphere of Enceladus. *J. Geophys. Res.* **115**, A09302.

Teolis, B.D., Perry, M.E., Magee, B.A., Westlake, J., Waite, J.H., 2010. Detection and measurement of ice grains and gas distribution in the Enceladus plume by Cassini's Ion Neutral Mass Spectrometer. *J. Geophys. Res*. **115**, A09222.

Tian, F., Stewart, A.I.F., Toon, O.B., Larsen, K.W., Esposito, L.W., 2007. Monte Carlo simulations of the water vapor plumes on Enceladus. *Icarus* **188**, 154–161.

Titov, E.V., Levin, D.A., 2007. Extension of the DSMC method to high pressure flows. *Int. J. Comput. Fluid D.* **21,** 351–368.

Tobie, G., Cadek, O., Sotin, C., 2008. Solid tidal friction above a liquid water reservoir as the origin of the south pole hotspot on Enceladus. *Icarus* **196**, 642–652.

Tokar, R.L., Johnson, R.E., Hill, T.W., Pontius, D.H., Kurth, W.S., Crary, F.J., Young, D.T., Thomsen, M.F., Reisenfeld, D.B., Coates, A.J., Lewis, G.R., Sittler, E.C., Gurnett, D.A., 2006. The interaction of the atmosphere of Enceladus with Saturn's plasma. *Science* **311**, 1409–1412.

Verbiscer, A., French, R., Showalter, M., Helfenstein, P., 2007. Enceladus: Cosmic graffiti artist caught in the act. *Science* **315**, 815.

Vincenti, W.G., Kruger, C.H., 1967. Introduction to Physical Gas Dynamics. Florida: Krieger Publishing Company.

Wagner, W., 1992. A convergence proof for Bird's direct simulation Monte Carlo method for the Boltzmann equation. *J. Stat. Phys.* **66**, 1011–1044.

Waite, J.H., Combi, M.R., Ip, W., Cravens, T.E., McNutt, R.L., Kasprzak, W., Yelle, R., Luhmann, J., Niemann, H., Gell, D., Magee, B., Fletcher, G., Lunine, J., Tseng, W., 2006. Cassini Ion and Neutral Mass Spectrometer: Enceladus plume composition and structure. *Science* **311**, 1419–1422.

Waite, J.H., Lewis, W.S., Magee, B.A., Lunine, J.I., McKinnon, W.B., Glein, C.R., Mousis, O., Young, D.T., Brockwell, T., Westlake, J., Nguyen, M.-J., Teolis, B.D., Niemann, H.B., McNutt, R.L., Perry, M., Ip, W.-H., 2009. Liquid water on Enceladus from observations of ammonia and ^{40}Ar in the plume. *Nature* **460**, 487–490.

Walker, A.C., 2012. A comprehensive numerical model of Io's chemically-reacting sublimation-driven atmosphere and its interaction with the Jovian plasma torus. PhD Dissertation, The University of Texas at Austin. 248 pp.

Walker, A.C., Gratiy, S.L., Goldstein, D.B., Moore, C.H., Varghese, P.L., Trafton, L.M., Levin, D.A., Steward, B., 2010. A comprehensive numerical simulation of Io's sublimation-driven atmosphere. *Icarus* **207**, 409–432.

Walker, A.C., Moore, C.H., Goldstein, D.B., Varghese, P.L., Trafton, L.M., 2012. A parametric study of Io's thermophysical surface properties and subsequent numerical atmospheric simulations based on the best fit parameters. *Icarus* **220**, 225–253.

Wexler, A., 1976. Vapor pressure formulation for ice. *J. Res. Nat. Bur. Stand.* **81A**, 5–20.

Yeoh, S.K., Chapman, T.A., Goldstein, D.B., Varghese, P.L., Trafton, L.M., 2015. On understanding the physics of the Enceladus south polar plume via numerical simulation. *Icarus* 253, 205–222.

Zhang, J., 2004. Simulation of gas dynamics, radiation and particulates in volcanic plumes on Io. PhD Dissertation, The University of Texas at Austin. 238 pp.

Zhang, J., Goldstein, D.B., Varghese, P.L., Gimelshein, N.E., Gimelshein, S.F., Levin, D.A., 2003. Simulation of gas dynamics and radiation in volcanic plumes on Io. *Icarus* **163**, 182–197.

Zhang, J., Goldstein, D.B., Varghese, P.L., Trafton, L.M., Moore, C., Miki, K., 2004. Numerical modeling of Ionian volcanic plumes with entrained particulates. *Icarus* **172**, 479–502.

Zolotov, M.Y., 2007. An oceanic composition on early and today's Enceladus. *Geophys. Res. Lett.* **34**, L23203.

Vita

Seng Keat Yeoh was born in Penang, Malaysia. He received his Bachelor and Master of Science in Engineering, both in Mechanical Engineering, from the University of Michigan at Ann Arbor in 2004 and 2006 respectively. He began his graduate studies in Mechanical Engineering at the University of Texas at Austin in the fall of 2007 before switching over to Aerospace Engineering in the fall of 2008. Since then, he has worked on modeling and understanding the plume of Enceladus under the supervision and guidance of Profs. Goldstein and Varghese at the Computational Fluid Physics Laboratory. During his free time, he enjoys running and playing all types of sports, especially soccer.

Email: skyeoh.utexas@gmail.com

This dissertation was typed by the author.